

1 **The Sensitivity to Oscillation Parameters**
2 **from a Simultaneous Beam and**
3 **Atmospheric Neutrino Analysis that**
4 **combines the T2K and SK Experiments**



6 Daniel Robert Clement Barrow
7 Magdalen College
8 University of Oxford

9 A thesis submitted for the degree of
10 *Doctor of Philosophy*
11 Michaelmas 2022

Abstract

12

13 Lorem ipsum dolor sit amet, consectetur adipiscing elit. Pellentesque sit amet
14 nibh volutpat, scelerisque nibh a, vehicula neque. Integer placerat nulla massa,
15 et vestibulum velit dignissim id. Ut eget nisi elementum, consectetur nibh in,
16 condimentum velit. Quisque sodales dui ut tempus mattis. Duis malesuada arcu
17 at ligula egestas egestas. Phasellus interdum odio at sapien fringilla scelerisque.
18 Mauris sagittis eleifend sapien, sit amet laoreet felis mollis quis. Pellentesque
19 dui ante, finibus eget blandit sit amet, tincidunt eu neque. Vivamus rutrum
20 dapibus ligula, ut imperdiet lectus tincidunt ac. Pellentesque ac lorem sed
21 diam egestas lobortis.

22 Suspendisse leo purus, efficitur mattis urna a, maximus molestie nisl. Aenean
23 porta semper tortor a vestibulum. Suspendisse viverra facilisis lorem, non
24 pretium erat lacinia a. Vestibulum tempus, quam vitae placerat porta, magna
25 risus euismod purus, in viverra lorem dui at metus. Sed ac sollicitudin nunc.
26 In maximus ipsum nunc, placerat maximus tortor gravida varius. Suspendisse
27 pretium, lorem at porttitor rhoncus, nulla urna condimentum tortor, sed suscipit
28 nisi metus ac risus.

29 Aenean sit amet enim quis lorem tristique commodo vitae ut lorem. Duis
30 vel tincidunt lacus. Sed massa velit, lacinia sed posuere vitae, malesuada vel
31 ante. Praesent a rhoncus leo. Etiam sed rutrum enim. Pellentesque lobortis
32 elementum augue, at suscipit justo malesuada at. Lorem ipsum dolor sit amet,
33 consectetur adipiscing elit. Praesent rhoncus convallis ex. Etiam commodo nunc
34 ex, non consequat diam consectetur ut. Pellentesque vitae est nec enim interdum
35 dapibus. Donec dapibus purus ipsum, eget tincidunt ex gravida eget. Donec
36 luctus nisi eu fringilla mollis. Donec eget lobortis diam.

37 Suspendisse finibus placerat dolor. Etiam ornare elementum ex ut vehicula.
38 Donec accumsan mattis erat. Quisque cursus fringilla diam, eget placerat neque
39 bibendum eu. Ut faucibus dui vitae dolor porta, at elementum ipsum semper.
40 Sed ultrices dui non arcu pellentesque placerat. Etiam posuere malesuada turpis,
41 nec malesuada tellus malesuada.

Acknowledgements

⁴³ Personal

⁴⁴ This is where you thank your advisor, colleagues, and family and friends.

⁴⁵ Lorem ipsum dolor sit amet, consectetur adipiscing elit. Vestibulum feugiat
⁴⁶ et est at accumsan. Praesent sed elit mattis, congue mi sed, porta ipsum. In
⁴⁷ non ullamcorper lacus. Quisque volutpat tempus ligula ac ultricies. Nam sed
⁴⁸ erat feugiat, elementum dolor sed, elementum neque. Aliquam eu iaculis est,
⁴⁹ a sollicitudin augue. Cras id lorem vel purus posuere tempor. Proin tincidunt,
⁵⁰ sapien non dictum aliquam, ex odio ornare mauris, ultrices viverra nisi magna
⁵¹ in lacus. Fusce aliquet molestie massa, ut fringilla purus rutrum consectetur.
⁵² Nam non nunc tincidunt, rutrum dui sit amet, ornare nunc. Donec cursus
⁵³ tortor vel odio molestie dignissim. Vivamus id mi erat. Duis porttitor diam
⁵⁴ tempor rutrum porttitor. Lorem ipsum dolor sit amet, consectetur adipiscing
⁵⁵ elit. Sed condimentum venenatis consectetur. Lorem ipsum dolor sit amet,
⁵⁶ consectetur adipiscing elit.

⁵⁷ Aenean sit amet lectus nec tellus viverra ultrices vitae commodo nunc. Mauris
⁵⁸ at maximus arcu. Aliquam varius congue orci et ultrices. In non ipsum vel
⁵⁹ est scelerisque efficitur in at augue. Nullam rhoncus orci velit. Duis ultricies
⁶⁰ accumsan feugiat. Etiam consectetur ornare velit et eleifend.

⁶¹ Suspendisse sed enim lacinia, pharetra neque ac, ultricies urna. Phasellus sit
⁶² amet cursus purus. Quisque non odio libero. Etiam iaculis odio a ex volutpat, eget
⁶³ pulvinar augue mollis. Mauris nibh lorem, mollis quis semper quis, consequat
⁶⁴ nec metus. Etiam dolor mi, cursus a ipsum aliquam, eleifend venenatis ipsum.
⁶⁵ Maecenas tempus, nibh eget scelerisque feugiat, leo nibh lobortis diam, id laoreet
⁶⁶ purus dolor eu mauris. Pellentesque habitant morbi tristique senectus et netus
⁶⁷ et malesuada fames ac turpis egestas. Nulla eget tortor eu arcu sagittis euismod
⁶⁸ fermentum id neque. In sit amet justo ligula. Donec rutrum ex a aliquet egestas.

⁶⁹ Institutional

⁷⁰ If you want to separate out your thanks for funding and institutional support,
⁷¹ I don't think there's any rule against it. Of course, you could also just remove
⁷² the subsections and do one big traditional acknowledgement section.

⁷³ Lorem ipsum dolor sit amet, consectetur adipiscing elit. Ut luctus tempor ex at
⁷⁴ pretium. Sed varius, mauris at dapibus lobortis, elit purus tempor neque, facilisis
⁷⁵ sollicitudin felis nunc a urna. Morbi mattis ante non augue blandit pulvinar.
⁷⁶ Quisque nec euismod mauris. Nulla et tellus eu nibh auctor malesuada quis
⁷⁷ imperdiet quam. Sed eget tincidunt velit. Cras molestie sem ipsum, at faucibus
⁷⁸ quam mattis vel. Quisque vel placerat orci, id tempor urna. Vivamus mollis,
⁷⁹ neque in aliquam consequat, dui sem volutpat lorem, sit amet tempor ipsum felis
⁸⁰ eget ante. Integer lacinia nulla vitae felis vulputate, at tincidunt ligula maximus.
⁸¹ Aenean venenatis dolor ante, euismod ultrices nibh mollis ac. Ut malesuada
⁸² aliquam urna, ac interdum magna malesuada posuere.

Contents

83

84	1 Introduction	1
85	2 Neutrino Oscillation Physics	2
86	2.1 Discovery of Neutrinos	3
87	2.2 Theory of Neutrino Oscillation	4
88	2.3 Neutrino Oscillation Measurements	8
89	2.4 Summary Of Oscillation Parameter Measurements	18
90	2.5 Overview of Oscillation Effects	19
91	3 T2K and SK Experiment Overview	27
92	3.1 The Super-Kamiokande Experiment	27
93	3.2 The Tokai to Kamioka Experiment	38
94	4 Bayesian Statistics and Markov Chain Monte Carlo Techniques	53
95	4.1 Bayesian Statistics	54
96	4.2 Monte Carlo Simulation	56
97	4.3 Understanding the MCMC Results	64
98	5 Simulation, Reconstruction, and Event Reduction	69
99	5.1 Simulation	69
100	5.2 Event Reconstruction at SK	75
101	5.3 Event Reduction at SK	86
102	6 Sample Selections and Systematics	91
103	6.1 Atmospheric Samples	93
104	6.2 Near Detector Beam Samples	99
105	6.3 Far Detector Beam Samples	102
106	6.4 Systematic Uncertainties	106
107	6.5 Likelihood Calculation	126
108	7 Oscillation Probability Calculation	130
109	7.1 Treatment of Fast Oscillations	131
110	7.2 Calculation Engine	138
111	7.3 Matter Density Profile	142
112	7.4 Production Height Averaging	147

113	8 Oscillation Analysis	150
114	8.1 Monte Carlo Prediction	151
115	8.2 Sensitivities	164
116	9 Conclusions and Outlook	213
117	Appendices	
118	A Atmospheric Sample Spectra	215
119	A.1 Binning	215
120	A.2 Fully Contained Sub-GeV Samples	215
121	A.3 Fully Contained Multi-GeV Samples	219
122	A.4 Fully Contained Multi-Ring Samples	220
123	A.5 Partially Contained Samples	221
124	A.6 Upward-Going Muon Samples	222

1

125

126

Introduction

2

¹²⁷

¹²⁸

Neutrino Oscillation Physics

¹²⁹ When first proposed, neutrinos were expected to be approximately massless
¹³⁰ fermions that only interact through weak and gravitational forces. This meant
¹³¹ they were very difficult to detect as they can pass through significant amounts
¹³² of matter without interacting. Despite this, experimental neutrino physics has
¹³³ developed many different detection techniques and observed neutrinos from
¹³⁴ both natural and artificial sources. In direct tension with Standard Model physics,
¹³⁵ neutrinos have been determined to oscillate between different lepton flavours,
¹³⁶ requiring them to have mass.

¹³⁷ The observation techniques which led to the discovery of the neutrino are doc-
¹³⁸ umented in section 2.1. The theory underpinning neutrino oscillation is described
¹³⁹ in section 2.2 and includes the approximations which can be made to simplify
¹⁴⁰ the understanding of neutrino oscillation in the two-flavour approximation. Past,
¹⁴¹ current, and future neutrino experiments are detailed in section 2.3, including the
¹⁴² reactor, atmospheric, and long-baseline accelerator neutrino sources that have
¹⁴³ been used to successfully constrain oscillation parameters. Finally, the current
¹⁴⁴ state of oscillation parameter measurements are summarised in section 2.4.

2.1 Discovery of Neutrinos

At the start of the 20th century, the electrons emitted from the β -decay of the nucleus were found to have a continuous energy spectrum [1, 2]. This observation seemingly broke the energy conservation invoked within that period's nuclear models. In 1930, Pauli provided a solution to this problem in the form of a new particle, the neutrino (originally termed "neutron"). It was theorized to be an electrically neutral spin-1/2 fermion with a mass smaller than that of the electron [3]. This neutrino was emitted with the electron in β -decay to alleviate the apparent breaking of energy conservation. As a predecessor of today's weak interaction model, Fermi's theory of β -decay developed the understanding by coupling the four constituent particles: electron, proton, neutron, and neutrino, into a quantitative model [4].

Whilst Pauli was not convinced of the ability to detect neutrinos, the first observations of the particle were made in the mid-1950s when neutrinos from a reactor were observed via the inverse β -decay (IBD) process, $\bar{\nu}_e + p \rightarrow n + e^+$ [5, 6]. The detector consisted of two parts: a neutrino interaction medium and a liquid scintillator. The interaction medium was built from two water tanks, loaded with cadmium chloride to allow for increased efficiency in the detection of neutron capture. The positron emitted from IBD annihilates, $e^+ + e^- \rightarrow 2\gamma$, generating a prompt signal and the neutron is captured on the cadmium via $n + ^{108}Cd \rightarrow ^{109*}Cd \rightarrow ^{109}Cd + \gamma$, producing a delayed signal. An increase in the coincidence rate was observed when the reactor was operating which was interpreted as interactions from neutrinos generated in the reactor.

After the discovery of the ν_e , the question of how many flavours of neutrino exist was asked. In 1962, a measurement of the ν_μ was conducted at the Brookhaven National Laboratory [7]. A proton beam was directed at a beryllium target, generating pions which then decayed via $\pi^\pm \rightarrow \mu^\pm + (\nu_\mu, \bar{\nu}_\mu)$, and the subsequent interactions of the ν_μ were observed. As the subsequent interaction of the neutrino generated muons rather than electrons, it was determined that

¹⁷⁴ the ν_μ was fundamentally different from ν_e . The final observation to be made
¹⁷⁵ was that of the ν_τ from the DONUT experiment [8]. Three neutrinos seem the
¹⁷⁶ obvious solution as it mirrors the known number of charged leptons (as they form
¹⁷⁷ weak isospin doublets) but there could be evidence of more. Several neutrino
¹⁷⁸ experiments have found anomalous results [9, 10] which could be attributed
¹⁷⁹ to “sterile” neutrinos. These hypothesised particles are not affected by gauge
¹⁸⁰ interactions in the Standard Model so their presence can only be inferred through
¹⁸¹ the observation of non-standard oscillation modes. However, cosmological
¹⁸² observations indicate the number of neutrino species $N_{eff} = 2.99 \pm 0.17$ [11], as
¹⁸³ measured from the cosmic microwave background power spectrum. LEP also
¹⁸⁴ measured the number of active neutrino flavours to be $N_\nu = 2.9840 \pm 0.0082$ [12]
¹⁸⁵ from measurements of the Z-decay width, but this does not strongly constrain
¹⁸⁶ the number of sterile neutrinos.

¹⁸⁷ 2.2 Theory of Neutrino Oscillation

¹⁸⁸ A neutrino generated with lepton flavour α can change into a different lepton
¹⁸⁹ flavour β after propagating some distance. This phenomenon is called neutrino
¹⁹⁰ oscillation and requires that neutrinos must have a non-zero mass. This behaviour
¹⁹¹ has been characterised by the Pontecorvo-Maki-Nakagawa-Sakata (PMNS) [13–
¹⁹² 15] mixing matrix which describes how the flavour and mass of neutrinos are
¹⁹³ associated. This is analogous to the Cabibbo-Kobayashi-Maskawa (CKM) [16]
¹⁹⁴ matrix measured in quark physics.

¹⁹⁵ 2.2.1 Three Flavour Oscillations

¹⁹⁶ The PMNS parameterisation defines three flavour eigenstates, ν_e , ν_μ and ν_τ
¹⁹⁷ (indexed ν_α), which are eigenstates of the weak interaction and three mass
¹⁹⁸ eigenstates, ν_1 , ν_2 and ν_3 (indexed ν_i). Each mass eigenstate is the superposition

¹⁹⁹ of all three flavour states,

$$|\nu_i\rangle = \sum_{\alpha} U_{\alpha i} |\nu_{\alpha}\rangle. \quad (2.1)$$

²⁰⁰ Where U is the 3×3 PMNS matrix which is unitary and connects the mass
²⁰¹ and flavour eigenstates.

²⁰² The weak interaction, when interacting via a W^{\pm} boson, couples to flavour
²⁰³ eigenstates so neutrinos interact with leptons of the same flavour. The prop-
²⁰⁴ agation of a neutrino flavour eigenstate, in a vacuum, can be re-written as a
²⁰⁵ plane-wave solution to the time-dependent Schrödinger equation,

$$|\nu_{\alpha}(t)\rangle = \sum_i U_{\alpha i}^{*} |\nu_i\rangle e^{-i\phi_i}. \quad (2.2)$$

²⁰⁶ The ϕ_i term can be expressed in terms of the energy, E_i , and magnitude of the
²⁰⁷ three momenta, p_i , of the neutrino, $\phi_i = E_i t - p_i x$ (t and x being time and position
²⁰⁸ coordinates). The probability of observing a neutrino of flavour eigenstate β from
²⁰⁹ one which originated as flavour α can be calculated as,

$$P(\nu_{\alpha} \rightarrow \nu_{\beta}) = |\langle \nu_{\beta} | \nu_{\alpha}(t) \rangle|^2 = \sum_{i,j} U_{\alpha i}^{*} U_{\beta i} U_{\alpha j} U_{\beta j}^{*} e^{-i(\phi_j - \phi_i)}. \quad (2.3)$$

²¹⁰ The term within the exponential can be represented as,

$$\phi_j - \phi_i = E_j t - E_i t - p_j x + p_i x. \quad (2.4)$$

²¹¹ For a relativistic particle, $E_i \gg m_i$, a Taylor series expansion means,

$$p_i = \sqrt{E_i^2 - m_i^2} \approx E_i - \frac{m_i^2}{2E_i}. \quad (2.5)$$

²¹² Making the approximations that neutrinos are relativistic, the mass eigenstates
²¹³ were created with the same energy and that $x = L$, where L is the distance
²¹⁴ travelled by the neutrino, Equation 2.4 then becomes

$$\phi_j - \phi_i = \frac{\Delta m_{ij}^2 L}{2E}, \quad (2.6)$$

where $\Delta m_{ij}^2 = m_i^2 - m_j^2$. This, combined with further use of unitarity relations results in Equation 2.3 becoming

$$\begin{aligned} P(\nu_\alpha \rightarrow \nu_\beta) &= \delta_{\alpha\beta} - 4 \sum_{i>j} \Re \left(U_{\alpha i}^* U_{\beta i} U_{\alpha j} U_{\beta j}^* \right) \sin^2 \left(\frac{\Delta m_{ij}^2 L}{4E} \right) \\ &\quad + (-) 2 \sum_{i>j} \Im \left(U_{\alpha i}^* U_{\beta i} U_{\alpha j} U_{\beta j}^* \right) \sin \left(\frac{\Delta m_{ij}^2 L}{2E} \right). \end{aligned} \quad (2.7)$$

Where $\delta_{\alpha\beta}$ is the Kronecker delta function and the negative sign on the last term is included for the oscillation probability of antineutrinos. As an important point to note, the observation of oscillation probability requires a non-zero value of Δm_{ij}^2 , which in turn requires that neutrinos have differing masses.

Typically, the PMNS matrix is parameterised into three mixing angles, a charge parity (CP) violating phase δ_{CP} , and two Majorana phases $\alpha_{1,2}$,

$$U = \underbrace{\begin{pmatrix} 1 & 0 & 0 \\ 0 & c_{23} & s_{23} \\ 0 & -s_{23} & c_{23} \end{pmatrix}}_{\text{Atmospheric, Accelerator}} \underbrace{\begin{pmatrix} c_{13} & 0 & s_{13} e^{-i\delta_{CP}} \\ 0 & 1 & 0 \\ -s_{13} e^{-i\delta_{CP}} & 0 & c_{13} \end{pmatrix}}_{\text{Reactor, Accelerator}} \times \underbrace{\begin{pmatrix} c_{12} & s_{12} & 0 \\ -s_{12} & c_{12} & 0 \\ 0 & 0 & 1 \end{pmatrix}}_{\text{Reactor, Solar}} \underbrace{\begin{pmatrix} e^{i\alpha_1/2} & 0 & 0 \\ 0 & e^{i\alpha_2/2} & 0 \\ 0 & 0 & 1 \end{pmatrix}}_{\text{Majorana}}. \quad (2.8)$$

Where $s_{ij} = \sin(\theta_{ij})$ and $c_{ij} = \cos(\theta_{ij})$. The oscillation parameters are often grouped: (1,2) as “solar”, (2,3) as “atmospheric” and (1,3) as “reactor”. Many neutrino experiments aim to measure the PMNS parameters from a wide array of origins, as is the purpose of this thesis.

The Majorana phase, $\alpha_{1,2}$, included within the fourth matrix in Equation 2.8 is only included for completeness. For an oscillation analysis experiment, any terms containing this phase disappear due to taking the expectation value of the PMNS matrix. Measurements of these phases can be performed by experiments searching for neutrino-less double β -decay [17].

232 A two-flavour approximation can be obtained when one assumes the third
233 mass eigenstate is degenerate with another. This results in the two-flavour
234 approximation being reasonable for understanding the features of the oscillation.
235 In this two-flavour case, the mixing matrix becomes,

$$U_{2\text{ Flav.}} = \begin{pmatrix} \cos(\theta) & \sin(\theta) \\ -\sin(\theta) & \cos(\theta) \end{pmatrix}. \quad (2.9)$$

236 This culminates in the oscillation probability,

$$\begin{aligned} P(\nu_\alpha \rightarrow \nu_\alpha) &= 1 - \sin^2(2\theta) \sin^2\left(\frac{\Delta m^2 L}{4E}\right), \\ P(\nu_\alpha \rightarrow \nu_\beta) &= \sin^2(2\theta) \sin^2\left(\frac{\Delta m^2 L}{4E}\right). \end{aligned} \quad (2.10)$$

237 Where $\alpha \neq \beta$. For a fixed neutrino energy, the oscillation probability is
238 a sinusoidal function depending upon the distance over which the neutrino
239 propagates. The frequency and amplitude of oscillation are dependent upon
240 $\Delta m^2/4E$ and $\sin^2 2\theta$, respectively. The oscillation probabilities presented thus far
241 assume $c = 1$, where c is the speed of light in a vacuum. In more familiar units, the
242 maximum oscillation probability for a fixed value of θ is given at $L[\text{km}] / E[\text{GeV}] \sim$
243 $1.27/\Delta m^2$. It is this calculation that determines the best L/E value for a given
244 experiment to be designed around for measurements of a specific value of Δm^2 .

245 2.2.2 The MSW Effect

246 The theory of neutrino oscillation in a vacuum has been described in subsec-
247 tion 2.2.1. However, the beam neutrinos and atmospheric neutrinos originating
248 from below the horizon propagate through the matter in the Earth. The coherent
249 scattering of neutrinos from a material target modifies the Hamiltonian of the
250 system which results in a change in the oscillation probability. This modification
251 is termed the Mikheyev-Smirnov-Wolfenstein (MSW) effect [18–20]. This occurs
252 because charged current scattering ($\nu_e + e^- \rightarrow \nu_e + e^-$, propagated by a W boson)
253 only affects electron neutrinos whereas the neutral current scattering ($\nu_l + l^- \rightarrow$

²⁵⁴ $\nu_l + l^-$, propagated by a Z^0 boson) interacts through all neutrino flavours equally.
²⁵⁵ In the two-flavour approximation, the effective mixing parameter becomes

$$\sin^2(2\theta) \rightarrow \sin^2(2\theta_m) = \frac{\sin^2(2\theta)}{(A/\Delta m^2 - \cos(2\theta))^2 + \sin^2(2\theta)}, \quad (2.11)$$

²⁵⁶ where $A = 2\sqrt{2}G_F N_e E$, N_e is the electron density of the medium and G_F
²⁵⁷ is Fermi's constant. It is clear that there exists a value of $A = \Delta m^2 \cos(2\theta)$ for
²⁵⁸ $\Delta m^2 > 0$, which results in a divergent mixing parameter, colloquially called the
²⁵⁹ matter resonance. This resonance regenerates the electron neutrino component of
²⁶⁰ the neutrino flux [18–20]. The density at which the resonance occurs is given by

$$N_e = \frac{\Delta m^2 \cos(2\theta)}{2\sqrt{2}G_F E}. \quad (2.12)$$

²⁶¹ At densities lower than this critical value, the oscillation probability will
²⁶² be much closer to that of vacuum oscillation. For antineutrinos, $N_e \rightarrow -N_e$
²⁶³ [21]. The resonance occurring from the MSW effect depends on the sign of Δm^2 .
²⁶⁴ Therefore, any neutrino oscillation experiment which observes neutrinos and
²⁶⁵ antineutrinos which have propagated through matter can have some sensitivity
²⁶⁶ to the ordering of the neutrino mass eigenstates.

²⁶⁷ 2.3 Neutrino Oscillation Measurements

²⁶⁸ As evidence of beyond Standard Model physics, the 2015 Nobel Prize in Physics
²⁶⁹ was awarded to the Super-Kamiokande (SK) [22] and Sudbury Neutrino Ob-
²⁷⁰ servatory (SNO) [23] collaborations for the first definitive observation of solar
²⁷¹ and atmospheric neutrino oscillation [24]. Since then, the field has seen a wide
²⁷² array of oscillation measurements from a variety of neutrino sources. As seen
²⁷³ in subsection 2.2.1, the neutrino oscillation probability is dependent on the ratio
²⁷⁴ of the propagation baseline, L , to the neutrino energy, E . It is this ratio that
²⁷⁵ determines the type of neutrino oscillation a particular experiment is sensitive to.

²⁷⁶ As illustrated in Figure 2.1, there are many neutrino sources that span a
²⁷⁷ wide range of energies. The least energetic neutrinos are from reactor and

²⁷⁸ terrestrial sources at $O(1)$ MeV whereas the most energetic neutrinos originate
²⁷⁹ from atmospheric and galactic neutrinos of $> O(1)$ TeV.

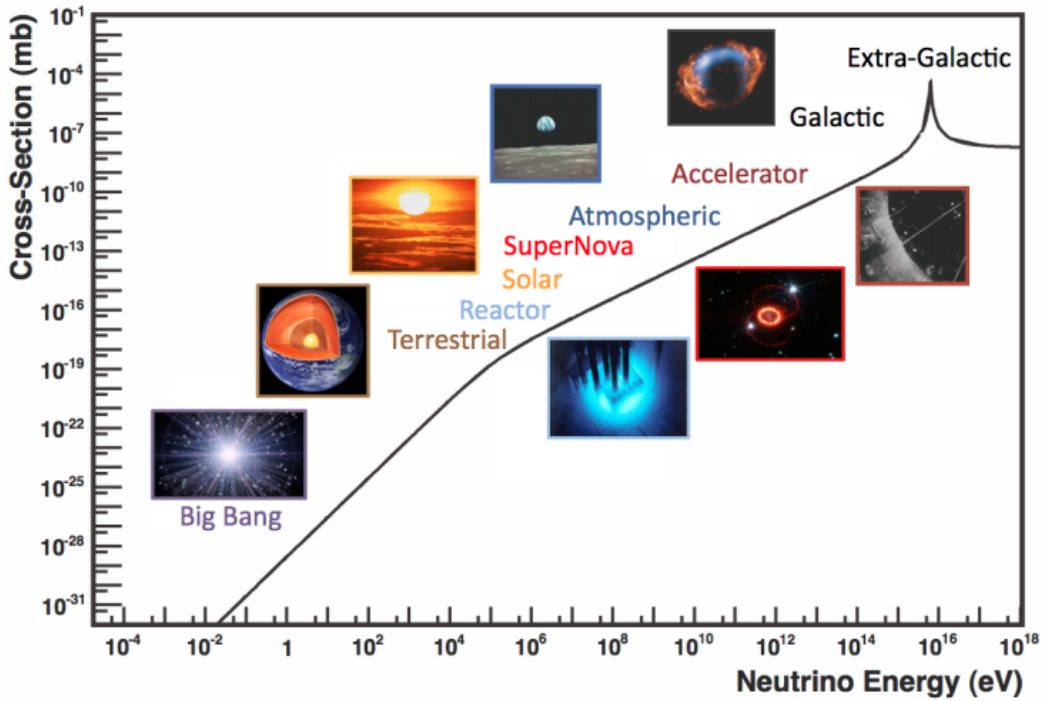


Figure 2.1: The electro-weak cross-section for $\bar{\nu}_e + e^- \rightarrow \bar{\nu}_e + e^-$ scattering on free electrons from various natural and man-made neutrino sources, as a function of neutrino energy. Taken from [25]

²⁸⁰ 2.3.1 Solar Neutrinos

²⁸¹ Solar neutrinos are emitted from fusion reaction chains at the centre of the Sun.
²⁸² The solar neutrino flux, given as a function of neutrino energy for different
²⁸³ fusion and decay chains, is illustrated in Figure 2.2. Whilst proton-proton fusion
²⁸⁴ generates the largest flux of neutrinos, the neutrinos are low energy and are
²⁸⁵ difficult to reconstruct due to the IBD interaction threshold of 1.8MeV [26].
²⁸⁶ Consequently, most experiments focus on the neutrinos from the decay of 8B
²⁸⁷ (via $^8B \rightarrow ^8Be^* + e^+ + \nu_e$), which are higher energy.

²⁸⁸ The first measurements of solar neutrinos observed a significant reduction in
²⁸⁹ the event rate compared to predictions from the Standard Solar Model [28, 29]. A
²⁹⁰ proposed solution to this “solar neutrino problem” was $\nu_e \leftrightarrow \nu_\mu$ oscillations in a

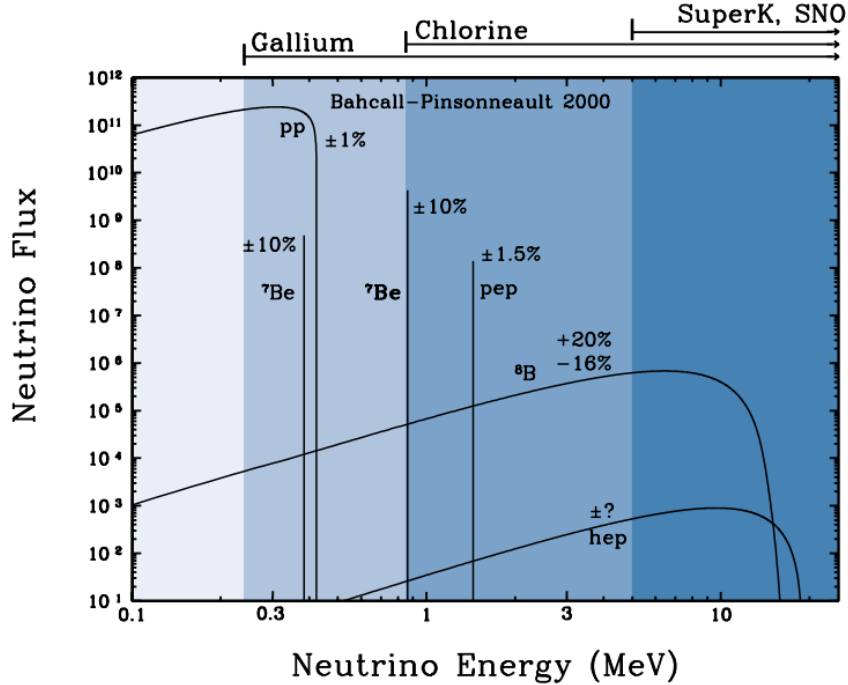


Figure 2.2: The solar neutrino flux as a function of neutrino energy for various fusion reactions and decay chains as predicted by the Standard Solar Model. Taken from [27].

291 precursory version of the PMNS model [30]. The Kamiokande [31], Gallex [32]
 292 and Sage [33] experiments confirmed the ~ 0.5 factor deficit of solar neutrinos.

293 The conclusive solution to this problem was determined by the SNO col-
 294 laboration [34]. Using a deuterium water target to observe 8B neutrinos, the
 295 event rate of charged current (CC), neutral current (NC), and elastic scattering
 296 (ES) interactions (Given in Equation 2.13) was simultaneously measured. CC
 297 events can only occur for electron neutrinos, whereas the NC channel is agnostic
 298 to neutrino flavour, and the ES reaction has a small excess sensitivity for the
 299 detection of electron neutrino interactions. This meant that there were direct
 300 measurements of the ν_e and ν_x neutrino flux. It was concluded that the CC and
 301 ES interaction rates were consistent with the deficit previously observed. Most
 302 importantly, the NC reaction rate was only consistent with the others under the

303 hypothesis of flavour transformation.

$$\begin{aligned} \nu_e + d &\rightarrow p + p + e^- & (CC) \\ \nu_x + d &\rightarrow p + n + \nu_x & (NC) \\ \nu_x + e^- &\rightarrow \nu_x + e^- & (ES) \end{aligned} \quad (2.13)$$

304 Since the SNO measurement, many experiments have since measured the
 305 neutrino flux of different interaction chains within the sun [35–37]. The most
 306 recent measurement was that of CNO-cycle neutrinos which were recently
 307 observed with 5σ significance by the Borexino collaboration [35].

308 2.3.2 Accelerator Neutrinos

309 The concept of using an artificial “neutrino beam” was first realised in 1962 [38].
 310 Since then, many experiments have adopted the same fundamental concepts.
 311 Typically, a proton beam is aimed at a target producing charged mesons that
 312 decay to neutrinos. The mesons can be sign-selected by the use of magnetic
 313 focusing horns to generate a neutrino or antineutrino beam. Pions are the primary
 314 mesons that decay and depending on the orientation of the magnetic field, a
 315 muon (anti-)neutrino beam is generated via $\pi^+ \rightarrow \mu^+ + \nu_\mu$ or $\pi^- \rightarrow \mu^- + \bar{\nu}_\mu$.
 316 The decay of muons and kaons results in an irreducible intrinsic electron neutrino
 317 background. In T2K, this background contamination is $O(< 1\%)$ [39]. There is
 318 also an approximately $\sim 5\%$ “wrong-sign” neutrino background of $\bar{\nu}_\mu$ generated
 319 via the same decays. As the beam is generated by proton interactions (rather
 320 than anti-proton interactions), the wrong-sign component in the antineutrino
 321 beam is larger when operating in neutrino mode.

322 Tuning the proton energy in the beam and using beam focusing techniques
 323 allows the neutrino energy to be set to a value that maximises the disappear-
 324 ance oscillation probability in the L/E term in Equation 2.10. This means that
 325 accelerator experiments are typically more sensitive to the mixing parameters as
 326 compared to a natural neutrino source. However, the disadvantage compared
 327 to atmospheric neutrino experiments is the cost of building a facility to provide

328 high-energy neutrinos, with a high flux, which is required for longer baselines.
 329 Consequently, there is typically less sensitivity to matter effects and the ordering
 330 of the neutrino mass eigenstates.

331 A neutrino experiment measures

$$R(\vec{x}) = \Phi(E_\nu) \times \sigma(E_\nu) \times \epsilon(\vec{x}) \times P(\nu_\alpha \rightarrow \nu_\beta), \quad (2.14)$$

332 where $R(\vec{x})$ is the event rate of neutrinos at position \vec{x} , $\Phi(E_\nu)$ is the flux of
 333 neutrinos with energy E_ν , $\sigma(E_\nu)$ is the cross-section of the neutrino interaction and
 334 $\epsilon(\vec{x})$ is the efficiency and resolution of the detector. In order to leverage the most
 335 out of an accelerator neutrino experiment, the flux and cross-section systematics
 336 need to be constrained. This is typically done via the use of a “near detector”,
 337 situated at a baseline of $O(1)$ km. This detector observes the unoscillated neutrino
 338 flux and constrains the parameters used within the flux and cross-section model.

339 The first accelerator experiments to precisely measure oscillation parameters
 340 were MINOS [40] and K2K [41]. These experiments confirmed the ν_μ disappear-
 341 ance seen in atmospheric neutrino experiments by finding consistent parameter
 342 values for $\sin^2(\theta_{23})$ and Δm_{32}^2 . The current generation of accelerator neutrino
 343 experiments, T2K and NO ν A extended this field by observing $\bar{\nu}_\mu \rightarrow \bar{\nu}_e$ and lead
 344 the sensitivity to atmospheric mixing parameters as seen in Figure 2.6 [42]. The
 345 two experiments differ in their peak neutrino energy, baseline, and detection tech-
 346 nique. The NO ν A experiment is situated at a baseline of 810km from the NuMI
 347 beamline which delivers 2GeV neutrinos. The T2K neutrino beam is peaked
 348 around 0.6GeV and propagates 295km [43]. Additionally, the NO ν A experiment
 349 uses functionally identical detectors (near and far) whereas T2K uses a plastic
 350 scintillator technique at the near detector and a water Cherenkov far detector.
 351 The future generation experiments DUNE [44] and Hyper-Kamiokande [45]
 352 will succeed these experiments as the high-precision era of neutrino oscillation
 353 parameter measurements develops.

354 Several anomalous results have been observed in the LSND [9] and Mini-
 355 BooNE [10] detectors which were designed with purposefully short baselines.

356 Parts of the neutrino community attributed these results to oscillations induced
357 by a fourth “sterile” neutrino [46] but several searches in other experiments,
358 MicroBooNE [47] and KARMEN [48], found no hints of additional neutrino
359 species. The solution to the anomalous results is still being determined.

360 2.3.3 Atmospheric Neutrinos

361 The interactions of primary cosmic ray protons in the Earth’s upper atmosphere
362 generate showers of energetic hadrons. These are mostly pions and kaons that
363 decay to produce a natural source of neutrinos spanning energies of MeV to
364 TeV [49]. The main decay is via,

$$\begin{aligned} \pi^\pm &\rightarrow \mu^\pm + (\nu_\mu, \bar{\nu}_\mu), \\ \mu^\pm &\rightarrow e^\pm + (\nu_e, \bar{\nu}_e) + (\nu_\mu, \bar{\nu}_\mu), \end{aligned} \tag{2.15}$$

365 such that for a single pion decay, three neutrinos can be produced. The
366 atmospheric neutrino flux energy spectra as predicted by the Bartol [50], Honda
367 [51–53], and FLUKA [54] models are illustrated in Figure 2.3. The flux distribution
368 peaks at an energy of $O(10)$ GeV. The uncertainties associated with these models
369 are dominated by the hadronic production of kaon and pions as well as the
370 primary cosmic flux.

371 Unlike long-baseline experiments which have a fixed baseline, the distance
372 atmospheric neutrinos propagate is dependent upon the zenith angle at which
373 they interact. This is illustrated in Figure 2.4. Neutrinos that are generated
374 directly above the detector ($\cos(\theta) = 1.0$) have a baseline equivalent to the
375 height of the atmosphere, whereas neutrinos that interact directly below the
376 detector ($\cos(\theta) = -1.0$) have to travel a length equal to the diameter of the Earth.
377 This means atmospheric neutrinos have a baseline that varies from $O(20)$ km to
378 $O(6 \times 10^3)$ km. Any neutrino generated at or below the horizon will be subject
379 to MSW matter resonance as they propagate through the Earth.

380 Figure 2.5 highlights the neutrino flux as a function of the zenith angle for
381 different slices of neutrino energy. For medium to high-energy neutrinos (and to



Figure 2.3: Left panel: The atmospheric neutrino flux for different neutrino flavours as a function of neutrino energy as predicted by the 2007 Honda model (“This work”) [51], the 2004 Honda model (“HKKM04”)[52], the Bartol model [50] and the FLUKA model [54]. Right panel: The ratio of the muon to electron neutrino flux as predicted by all the quoted models. Both figures taken from [51].

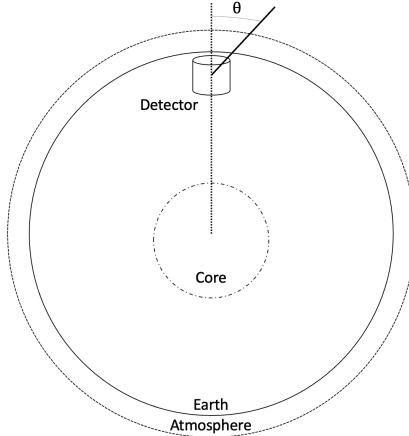


Figure 2.4: A diagram illustrating the definition of zenith angle as used in the Super Kamiokande experiment [55].

382 a lesser degree for low-energy neutrinos), the flux is approximately symmetric
 383 around $\cos(\theta) = 0$. To the accuracy of this approximation, the systematic
 384 uncertainties associated with atmospheric flux for comparing upward-going
 385 and down-going neutrino cancels. This allows the down-going events, which are

386 mostly insensitive to oscillation probabilities, to act as an unoscillated prediction
 387 (similar to a near detector in an accelerator neutrino experiment).



Figure 2.5: Prediction of ν_e , $\bar{\nu}_e$, ν_μ , $\bar{\nu}_\mu$ fluxes as a function of zenith angle as calculated by the HKKM model [53]. The left, middle and right panels represent three values of neutrino energy, 0.32GeV, 1.0GeV and 3.2GeV respectively. Predictions for other models including Bartol [50], Honda [51] and FLUKA [54] are given in [55].

388 Precursory hints of atmospheric neutrinos were observed in the mid-1960s
 389 searching for $\nu_\mu + X \rightarrow X^* + \mu^\pm$ [56]. This was succeeded by the IMB-3 [57]
 390 and Kamiokande [58] experiments which measured the double ratio of muon
 391 to electron neutrinos in data to Monte Carlo, $R(\nu_\mu/\nu_e) = (\mu/e)_{Data}/(\mu/e)_{MC}$.
 392 Both experiments were found to have a consistent deficit of muon neutrinos,
 393 with $R(\nu_\mu/\nu_e) = 0.67 \pm 0.17$ and $R(\nu_\mu/\nu_e) = 0.658 \pm 0.016 \pm 0.035$, respectively.
 394 Super-Kamiokande (SK) [55] extended this analysis by fitting oscillation pa-
 395 rameters in $P(\nu_\mu \rightarrow \nu_\tau)$ which found best fit parameters $\sin^2(2\theta) > 0.92$ and
 396 $1.5 \times 10^{-3} < \Delta m^2 < 3.4 \times 10^{-3}\text{eV}^2$.

397 Since then, atmospheric neutrino experiments have been making precision
 398 measurements of the $\sin^2(\theta_{23})$ and Δm^2_{32} oscillation parameters. Atmospheric
 399 neutrino oscillation is dominated by $P(\nu_\mu \rightarrow \nu_\tau)$, where SK observed a 4.6σ
 400 discovery of ν_τ appearance [59]. Figure 2.6 illustrates the current estimates on
 401 the atmospheric mixing parameters, from a wide range of atmospheric and
 402 accelerator neutrino observatories.



Figure 2.6: Constraints on the atmospheric oscillation parameters, $\sin^2(\theta_{23})$ and Δm_{32}^2 , from atmospheric and long-baseline experiments: SK [60], T2K [61], NOvA [62], IceCube [63] and MINOS [64]. Figure taken from [65].

2.3.4 Reactor Neutrinos

As illustrated in the first discovery of neutrinos (section 2.1), nuclear reactors are a very useful artificial source of electron antineutrinos. For reactors that use low-enriched uranium ^{235}U as fuel, the antineutrino flux is dominated by the β -decay fission of ^{235}U , ^{238}U , ^{239}Pu and ^{241}Pu [66] as illustrated in Figure 2.7.

Due to their low energy, reactor electron antineutrinos predominantly interact via the inverse β -decay (IBD) interaction. The typical signature contains two signals delayed by $O(200)\mu\text{s}$; firstly the prompt photons from positron annihilation, and secondly the photon emitted ($E_{tot}^\gamma = 2.2\text{MeV}$) from de-excitation after neutron capture on hydrogen. Searching for both signals improves the detector's ability to distinguish between background and signal events [68].

There are many short baseline experiments ($L \sim O(1)\text{km}$) that have measured the $\sin^2(\theta_{13})$ and Δm_{32}^2 oscillation parameters. Daya Bay [69], RENO [70] and Double Chooz [71] have all provided precise measurements, with the first discovery of a non-zero θ_{13} made by Daya Bay and RENO (and complemented by T2K [71]). The constraints on $\sin^2(\theta_{13})$ by the reactor experiments lead the field. They



Figure 2.7: Reactor electron antineutrino fluxes for ^{235}U (Black), ^{238}U (Green), ^{239}Pu (Purple), and ^{241}Pu (Orange) isotopes. The inverse β -decay cross-section (Blue) and corresponding measurable neutrino spectrum (Red) are also given. Top panel: Schematic of Inverse β -decay interaction including the eventual capture of the emitted neutron. This capture emits a γ -ray which provides a second signal of the event. Taken from [67].

are often used as external inputs to accelerator neutrino experiments to improve their sensitivity to δ_{CP} and mass hierarchy determination. JUNO-TAO [72], a small collaboration within the larger JUNO experiment, is a next-generation reactor experiment that aims to precisely measure the isotopic antineutrino yields from the different fission chains.

Kamland [73] is the only experiment to have observed reactor neutrinos using a long baseline (flux weighted averaged baseline of $L \sim 180\text{km}$) which allows it to have sensitivity to Δm_{21}^2 . Combined with the SK solar neutrino experiment, the combined analysis puts the most stringent constraint on Δm_{21}^2 [74].

2.4 Summary Of Oscillation Parameter Measurements

Since the first evidence of neutrino oscillations, numerous measurements of the mixing parameters have been made. Many experiments use neutrinos as a tool for the discovery of new physics (diffuse supernova background, neutrinoless double beta decay and others) so the PMNS parameters are summarised in the Particle Data Group (PDG) review tables. The analysis presented in this thesis focuses on the 2020 T2K oscillation analysis presented in [75] which the 2020 PDG constraints [76] were used. These constraints are outlined in Table 2.1.

Parameter	2020 Constraint
$\sin^2(\theta_{12})$	0.307 ± 0.013
Δm_{21}^2	$(7.53 \pm 0.18) \times 10^{-5} \text{ eV}^2$
$\sin^2(\theta_{13})$	$(2.18 \pm 0.07) \times 10^{-2}$
$\sin^2(\theta_{23})$ (I.H.)	0.547 ± 0.021
$\sin^2(\theta_{23})$ (N.H.)	0.545 ± 0.021
Δm_{32}^2 (I.H.)	$(-2.546^{+0.034}_{-0.040}) \times 10^{-3} \text{ eV}^2$
Δm_{32}^2 (N.H.)	$(2.453 \pm 0.034) \times 10^{-3} \text{ eV}^2$

Table 2.1: The 2020 Particle Data Group constraints of the oscillation parameters taken from [76]. The value of Δm_{32}^2 is given for both normal hierarchy (N.H.) and inverted hierarchy (I.H.) and $\sin^2(\theta_{23})$ is broken down by whether its value is below (Q1) or above (Q2) 0.5.

The $\sin^2(\theta_{13})$ measurement stems from the electron antineutrino disappearance, $P(\bar{\nu}_e \rightarrow \bar{\nu}_e)$, and is taken as the average best-fit from the combination of Daya Bay, Reno and Double Chooz. It is often used as a prior uncertainty within other neutrino oscillation experiments, typically termed the reactor constraint. The $\sin^2(\theta_{12})$ parameter is predominantly measured through electron neutrino disappearance, $P(\nu_e \rightarrow \nu_{\mu,\tau})$, in solar neutrino experiments. The long-baseline reactor neutrino experiment Kamland also has a sensitivity to this parameter and is used in a joint fit to solar data from SNO and SK, using the reactor constraint. Measurements of $\sin^2(\theta_{23})$ are made by long-baseline and atmospheric neutrino experiments. The PDG value is a joint fit of T2K, NO ν A, MINOS and IceCube DeepCore experiments. The latest T2K-only measurement, provided at Neutrino2020 and is the basis of this thesis, is given as $\sin^2(\theta_{23}) = 0.546^{+0.024}_{-0.046}$ [75].

The PDG constraint on Δm_{21}^2 is provided by the KamLAND experiment using solar and geoneutrino data. This measurement utilised a $\sin^2(\theta_{13})$ constraint from accelerator (T2K, MINOS) and reactor neutrino (Daya Bay, RENO, Double Chooz) experiments. Accelerator measurements make some of the most stringent constraints on Δm_{32}^2 although atmospheric experiments have more sensitivity to the mass hierarchy determination. The PDG performs a joint fit of accelerator and atmospheric data, in both normal and inverted hierarchies separately. The latest T2K-only result is $\Delta m_{32}^2 = 2.49^{+0.058}_{-0.082} \times 10^{-3} \text{ eV}^2$ favouring normal hierarchy [75]. The value of δ_{CP} is largely undetermined. CP-conserving values of 0 and π were rejected with $\sim 2\sigma$ intervals, as published in Nature, although more recent analyses have reduced the credible intervals to 90%. Since the 2020 PDG publication, there has been a new measurement of $\sin^2(\theta_{13}) = (2.20 \pm 0.07) \times 10^{-2}$ [77], alongside updated Δm_{32}^2 and $\sin^2(\theta_{23})$ measurements.

Throughout this thesis, several sample spectra predictions and contours are presented, which require oscillation parameters to be assumed. Table 2.2 defines two sets of oscillation parameters, with “Asimov A” set being close to the preferred values from a previous T2K-only fit [78] and “Asimov B” being CP-conserving and further from maximal θ_{23} mixing.

Parameter	Asimov A	Asimov B
Δm_{12}^2	$7.53 \times 10^{-5} \text{ eV}^2$	
Δm_{32}^2	$2.509 \times 10^{-3} \text{ eV}^2$	
$\sin^2(\theta_{12})$	0.304	
$\sin^2(\theta_{13})$	0.0219	
$\sin^2(\theta_{23})$	0.528	0.45
δ_{CP}	-1.601	0.0

Table 2.2: Reference values of the neutrino oscillation parameters for two different oscillation parameter sets.

2.5 Overview of Oscillation Effects

The analysis presented within this thesis focuses on the determination of oscillation parameters from atmospheric and beam neutrinos. Whilst subject to the

⁴⁶⁹ same oscillation formalism, the way in which the two samples have sensitivity
⁴⁷⁰ to the different oscillation parameters differs significantly.

⁴⁷¹ Atmospheric neutrinos have a varying baseline, or “path length” L , such that
⁴⁷² the distance each neutrino travels before interacting is dependent upon the zenith
⁴⁷³ angle, θ_Z . As primary cosmic rays can interact anywhere between the Earth’s
⁴⁷⁴ surface and $\sim 50\text{km}$ above that, the height, h , in the atmosphere at which the
⁴⁷⁵ neutrino was generated also affects the path length,

$$L = \sqrt{(R_E + h)^2 - R_E^2 (1 - \cos^2(\theta_Z))} - R_E \cos(\theta_Z). \quad (2.16)$$

⁴⁷⁶ DB: Ask Giles what he means about the horizontal issue and Layering in
⁴⁷⁷ the ProdH section

⁴⁷⁸ Where $R_E = 6,371\text{km}$ is the Earth’s radius. Consequently, the oscillation
⁴⁷⁹ probability is dependent upon two parameters, $\cos(\theta_Z)$ and E_ν .

⁴⁸⁰ The oscillation probability used within this analysis is based on [21]. The
⁴⁸¹ neutrino wavefunction in the vacuum Hamiltonian evolves in each layer of
⁴⁸² constant matter density via

$$i \frac{d\psi_j(t)}{dt} = \frac{m_j^2}{2E_\nu} \psi_j(t) - \sum_k \sqrt{2} G_F N_e U_{ej} U_{ke}^\dagger \psi_k(t), \quad (2.17)$$

⁴⁸³ where m_j^2 is the square of the j^{th} vacuum eigenstate mass, E_ν is the neutrino
⁴⁸⁴ energy, G_F is Fermi’s constant, N_e is the electron number density and U is the
⁴⁸⁵ PMNS matrix. The transformation $N_e \rightarrow -N_e$ and $\delta_{CP} \rightarrow -\delta_{CP}$ is applied for
⁴⁸⁶ antineutrino propagation. Thus, a model of the Earth’s density is required for
⁴⁸⁷ neutrino propagation. Following the official SK-only methodology [79], this
⁴⁸⁸ analysis uses the Preliminary Reference Earth Model (PREM) [80] which provides
⁴⁸⁹ piecewise cubic polynomials as a function of the Earth’s radius. This density
⁴⁹⁰ profile is illustrated in Figure 2.8. As the propagator requires layers of constant
⁴⁹¹ density, the SK methodology approximates the PREM model by using four layers
⁴⁹² of constant density [79], detailed in Table 2.3.



Figure 2.8: The density of the Earth given as a function of the radius, as given by the PREM model (Black), and the constant density four-layer approximation (Blue), as used in the official SK-only analysis.

Layer	Outer Radius [km]	Density [g/cm ³]	Chemical composition (Z/A)
Inner Core	1220	13	0.468 ± 0.029
Outer Core	3480	11.3	0.468 ± 0.029
Lower Mantle	5701	5.0	0.496
Transition Zone	6371	3.3	0.496

Table 2.3: Description of the four layers of the Earth invoked within the constant density approximation of the PREM model [80].

The atmospheric neutrino oscillation probabilities can be presented as two dimensional “oscillograms” as illustrated in Figure 2.9. The distinct discontinuities, as a function of $\cos(\theta_Z)$, are due to the discontinuous density in the PREM model.

Atmospheric neutrinos have sensitivity to δ_{CP} through the overall event rate. Figure 2.10 illustrates the difference in oscillation probability between CP-conserving ($\delta_{CP} = 0.$) and a CP-violating ($\delta_{CP} = -1.601$) value taken from Asimov A oscillation parameter set (Table 2.2). The result is a complicated oscillation pattern in the appearance probability for sub-GeV upgoing neutrinos. The detector does not have sufficient resolution to resolve these individual patterns so the sensitivity to δ_{CP} for atmospheric neutrinos comes via the overall normalisation of these events.

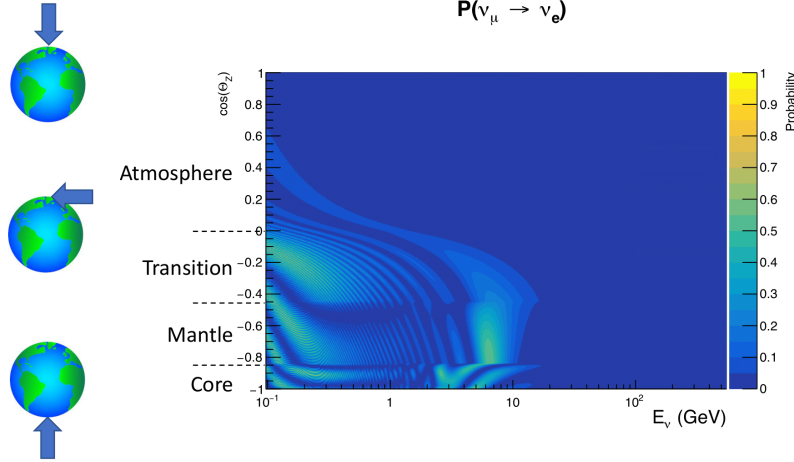


Figure 2.9: An “oscillogram” that depicts the $P(\nu_\mu \rightarrow \nu_e)$ oscillation probability as a function of neutrino energy and cosine of the zenith angle. The zenith angle is defined such that $\cos(\theta_Z) = 1.0$ represents neutrinos that travel from directly above the detector. The four-layer constant density PREM model approximation is used and Asimov A oscillation parameters are assumed (Table 2.2).

504 The presence of matter means that the effect δ_{CP} has on the oscillation prob-
 505 ability is not equal between neutrinos and antineutrinos. Furthermore, the
 506 interaction cross-section for neutrinos is larger than for antineutrinos so the two
 507 effects have to be disentangled. These effects are further convoluted by detector
 508 efficiencies as SK cannot distinguish neutrinos and antineutrinos well. All of
 509 these effects lead to a difference in the number of neutrinos detected compared
 510 to antineutrinos. This changes how the δ_{CP} normalisation term is observed,
 511 resulting in a very complex sensitivity to δ_{CP} .

512 The vacuum and matter oscillation probabilities for $P(\nu_e \rightarrow \nu_e)$ and $P(\bar{\nu}_e \rightarrow$
 513 $\bar{\nu}_e)$ are presented in Figure 2.11, where the PREM model has been assumed. The
 514 oscillation probability for both neutrinos and antineutrinos is affected in the
 515 presence of matter. However, the resonance effects around $O(5)\text{GeV}$ only occur
 516 for neutrinos in the normal mass hierarchy and antineutrinos in the inverse mass
 517 hierarchy. The exact position and amplitude of the resonance depend on $\sin^2(\theta_{23})$,
 518 further increasing the atmospheric neutrinos’ sensitivity to the parameter.

519 As the T2K beam flux is centered at the first oscillation maximum ($E_\nu =$

$$\mathbf{P}(\nu_\mu \rightarrow \nu_e; \delta_{CP} = -1.601) - \mathbf{P}(\nu_\mu \rightarrow \nu_e; \delta_{CP} = 0)$$

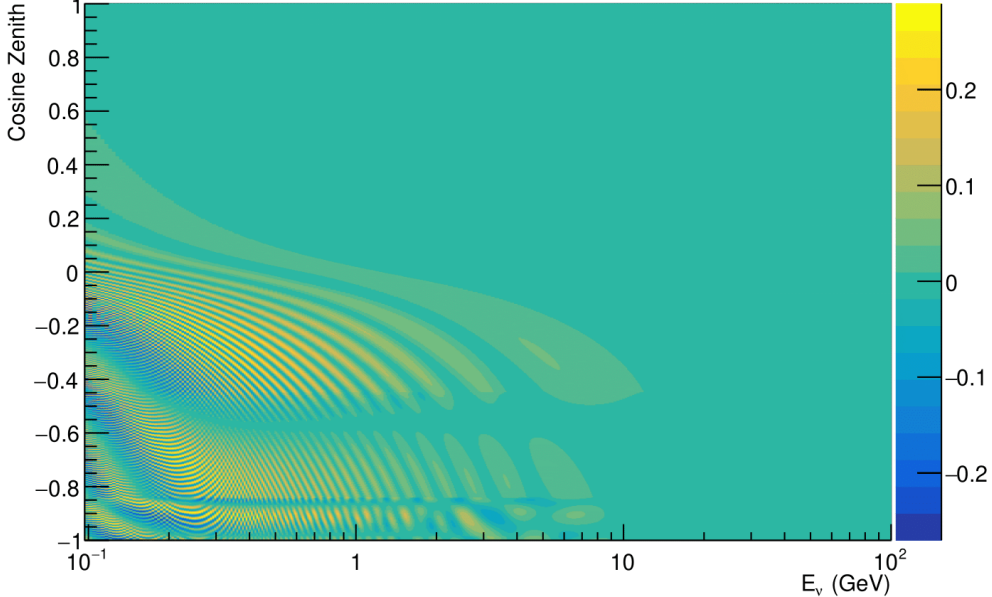


Figure 2.10: The effect of δ_{CP} for atmospheric neutrinos given in terms of the neutrino energy and zenith angle. This oscillogram compares the $P(\nu_\mu \rightarrow \nu_e)$ oscillation probability for a CP conserving ($\delta_{CP} = 0.0$) and a CP violating ($\delta_{CP} = -1.601$) value taken from the Asimov A parameter set. The other oscillation parameters assume the Asimov A oscillation parameter set given in Table 2.2.

520 0.6GeV) [43], the sensitivity to δ_{CP} is predominantly observed as a change in the
 521 event-rate of e-like samples in $\nu/\bar{\nu}$ modes. Figure 2.12 illustrates the $P(\nu_\mu \rightarrow \nu_e)$
 522 oscillation probability for a range of δ_{CP} values. A circular modulation of the
 523 first oscillation peak (in both magnitude and position) is observed when varying
 524 throughout the allowable values of δ_{CP} . The CP-conserving values of $\delta_{CP} = 0, \pi$
 525 have a lower(higher) oscillation maximum than the CP-violating values of $\delta_{CP} =$
 526 $-\pi/2 (\delta_{CP} = \pi/2)$. A sub-dominant shift in the energy of the oscillation peak is
 527 also present, which aids in separating the two CP-conserving values of δ_{CP} .

528 T2K's sensitivity to $\sin^2(\theta_{23})$ and Δm_{32}^2 is observed as a shape-based variation
 529 of the muon-like samples, as illustrated in Figure 2.12. The value of Δm_{32}^2 laterally
 530 shifts the position of the oscillation dip (around $E_\nu \sim 0.6\text{GeV}$) in the $P(\nu_\mu \rightarrow \nu_\mu)$
 531 oscillation probability. A variation of $\sin^2(\theta_{23})$ is predominantly observed as
 532 a vertical shift of the oscillation dip with second-order horizontal shifts being



Figure 2.11: An illustration of the matter-induced effects on the oscillation probability, given as a function of neutrino energy and zenith angle. The top row of panels gives the $P(\nu_e \rightarrow \nu_e)$ oscillation probability and the bottom row illustrates the $P(\bar{\nu}_e \rightarrow \bar{\nu}_e)$ oscillation probability. The left column highlights the oscillation probability in a vacuum, whereas the middle and right column represents the oscillation probabilities when the four-layer fixed density PREM model is assumed. All oscillation probabilities assume the “Asimov A” set given in Table 2.2, but importantly, the right column sets an inverted mass hierarchy. The “matter resonance” effects at $E_\nu \sim 5\text{GeV}$ can be seen in the $P(\nu_e \rightarrow \nu_e)$ for normal mass hierarchy and $P(\bar{\nu}_e \rightarrow \bar{\nu}_e)$ for inverted hierarchy.

533 due to matter effects. The beam neutrinos have limited sensitivity to matter
 534 effects due to the relatively shorter baseline as well as the Earth’s mantle being
 535 a relatively low-density material (as compared to the Earth’s core). For some
 536 values of δ_{CP} , the degeneracy in the number of e-like events allows the mass
 537 hierarchy to be broken. This leads to a δ_{CP} -dependent mass hierarchy sensitivity
 538 which can be seen in Figure 2.13.

539 Whilst all oscillation channels should be included for completeness, the

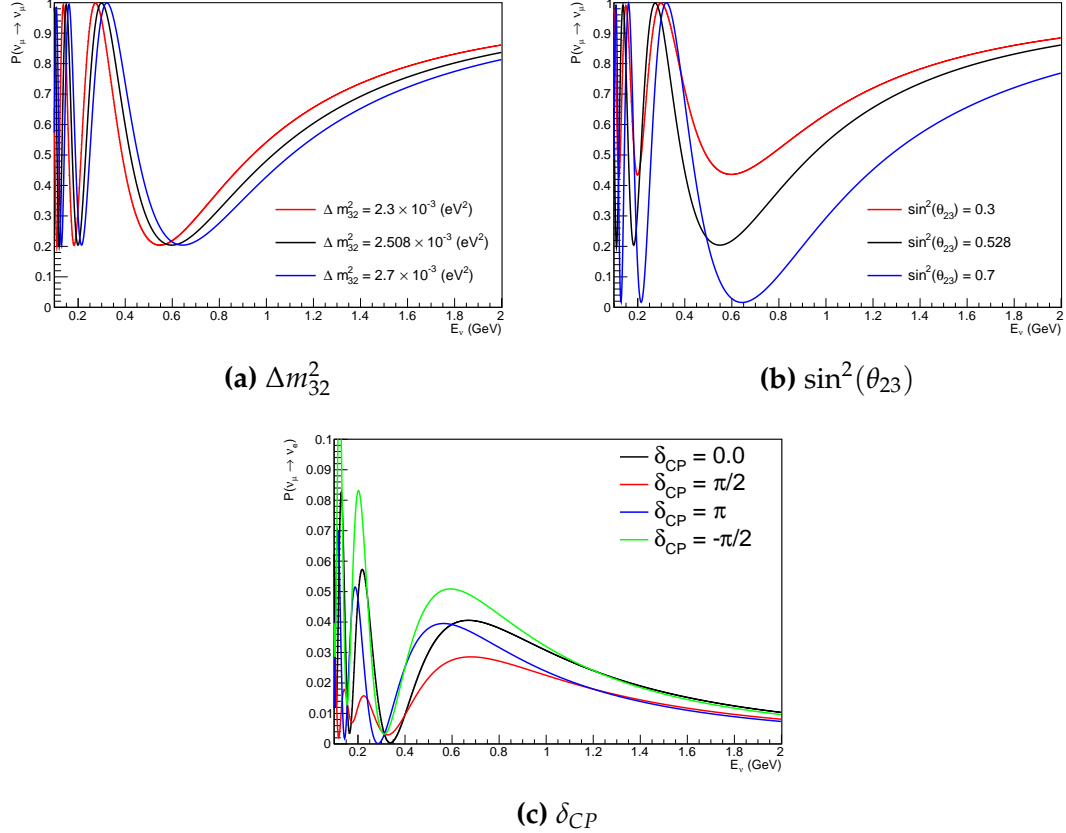


Figure 2.12: The oscillation probability for beam neutrino events given as a function of neutrino energy. All oscillation parameters assume the “Asimov A” set given in Table 2.2 unless otherwise stated. Each panel represents a change in one of the oscillation parameters whilst keeping the remaining parameters fixed.

computational resources required to run a fit are limited and any reasonable approximations which reduce the number of oscillation probability calculations that need to be made should be applied. The $\nu_e \rightarrow \nu_{e,\mu,\tau}$ (and antineutrino equivalent) oscillations can be ignored for beam neutrinos as the $\nu_e/\bar{\nu}_e$ fluxes are approximately two orders of magnitude smaller than the corresponding $\nu_\mu/\bar{\nu}_\mu$ flux. Furthermore, as the peak neutrino energy of the beam is well below the threshold for charged current tau production ($E_\nu = 3.5$ GeV [59]), only a small proportion of the neutrinos produced in the beam have the required energy. For the few neutrinos that have sufficient energy, the oscillation probability is very small due to their energy being well above the oscillation maximum (small value of L/E). Whilst these approximations have been made for the beam



Figure 2.13: The number of electron-like events in the FHC and RHC operating mode of the beam, as a function of the oscillation probabilities. Both normal hierarchy (Solid) and inverse hierarchy (Dashed) values of Δm_{32}^2 are given.

551 neutrinos, the atmospheric flux of ν_e is of the same order of magnitude as the ν_μ
 552 flux and the energy distribution of atmospheric neutrinos extends well above
 553 the tau production threshold. These events can have non-negligible oscillation
 554 probabilities due to the further distance they travel.

3

555

556

T2K and SK Experiment Overview

557 As the successor of the Kamiokande experiment, the Super-Kamiokande (SK)
558 collaboration has been leading atmospheric neutrino oscillation analyses for
559 over two decades. The detector has provided some of the strongest constraints
560 on proton decay and the first precise measurements of the Δm_{32}^2 and $\sin^2(\theta_{23})$
561 neutrino oscillation parameters. The history, detection technique, and operation
562 of the SK detector is described in section 3.1.

563 The Tokai-to-Kamioka (T2K) experiment was one of the first long-baseline
564 experiments to use both neutrino and antineutrino beams to precisely measure
565 charge parity violation within the neutrino sector. The T2K experiment observed
566 the first hints of a non-zero $\sin^2(\theta_{13})$ measurement and continues to lead the
567 field with the constraints it provides on $\sin^2(\theta_{13})$, $\sin^2(\theta_{23})$, Δm_{32}^2 and δ_{CP} . In
568 section 3.2, the techniques that T2K use to generate the neutrino beam and
569 constrain systematic parameter through near detector constraints are described.

570 3.1 The Super-Kamiokande Experiment

571 The SK experiment began taking data in 1996 [81] and has had many modifi-
572 cations throughout its operation. There have been seven defined periods of
573 data taking as noted in Table 3.1. Data taking began in SK-I which ran for five

574 years. Between the SK-I and SK-II periods, approximately 55% of the PMTs were
 575 damaged during maintenance [82]. Those that survived were equally distributed
 576 throughout the detector in the SK-II era, which resulted in a reduced 19% photo-
 577 coverage. From SK-III onwards, repairs to the detector meant the full suite of
 578 PMTs was operational recovering the 40% photo-coverage. Before the start of
 579 SK-IV, the data acquisition and electronic systems were upgraded. Between
 580 SK-IV and SK-V, a significant effort was placed into tank open maintenance and
 581 repair/replacement of defective PMTs in preparation for the Gadolinium upgrade;
 582 a task for which the author of this thesis was required. Consequently, the detector
 583 conditions were significantly changed from this point. SK-VI marked the start of
 584 the SK-Gd era, with the detector being doped with gadolinium at a concentration
 585 of 0.01% by concentration. SK-VII, which started during the writing of this thesis,
 586 has increased the gadolinium concentration to 0.03% for continued operation [83].

587 The oscillation analysis presented within this thesis focuses on the SK-IV
 588 period of running and the data taken within it. This follows from the recent
 589 SK analysis presented in [84]. Therefore, the information presented within this
 590 section focuses on that period.

Period	Start Date	End Date	Live-time (days)
I	April 1996	July 2001	1489.19
II	October 2002	October 2005	798.59
III	July 2006	September 2008	518.08
IV	September 2008	May 2018	3244.4
V	January 2019	July 2020	461.02
VI	July 2020	May 2022	583.3
VII	May 2022	Ongoing	N/A

Table 3.1: The various SK periods and their respective live-time. The SK-VI live-time is calculated until 1st April 2022. SK-VII started during the writing of this thesis.

591 3.1.1 The SK Detector

592 The basic structure of the Super-Kamiokande (SK) detector is a cylindrical tank
 593 with a diameter 39.3m and height 41.1m filled with ultrapure water [82]. A
 594 diagram of the significant components of the SK detector is given in Figure 3.1.

595 The SK detector is situated in the Kamioka mine in Gifu, Japan. The mine
 596 is underground with roughly 1km rock overburden (2.7km water equivalent
 597 overburden) [85]. At this depth, the rate of cosmic ray muons is significantly
 598 decreased to a value of $\sim 2\text{Hz}$ (net rate) [86]. The top of the tank is covered
 599 with stainless steel which is designed as a working platform for maintenance,
 600 calibration, and location for high voltage and data acquisition electronics.



Figure 3.1: A schematic diagram of the Super-Kamiokande Detector. Taken from [87].

601 A smaller cylindrical structure (36.2m diameter, 33.8m height) is situated
 602 inside the tank, with an approximate 2m gap between this structure and the outer
 603 tank wall. The purpose of this structure is to support the photomultiplier tubes
 604 (PMTs). The volume inside and outside the support structure is referred to as the
 605 inner detector (ID) and outer detector (OD), respectively. In the SK-IV era, the
 606 ID and OD are instrumented by 11,129 50cm and 1,885 20cm PMTs respectively
 607 [82]. The ID contains a 32kton mass of water. Many analyses performed at SK
 608 use a “fiducial volume” defined by the volume of water inside the ID excluding
 609 some distance to the ID wall. This reduces the volume of the detector which is
 610 sensitive to neutrino events but reduces radioactive backgrounds and allows for

611 better reconstruction performance. The nominal fiducial volume is defined as the
612 area contained inside 2m from the ID wall for a total of 22.5kton water [88].

613 The two regions of the detector (ID and OD) are optically separated with
614 opaque black plastic hung from the support structure. The purpose of this is
615 to determine whether an event entered or exited the ID. This allows cosmic ray
616 muons and partially contained events to be tagged and separated from neutrino
617 events entirely contained within the ID. This black plastic is also used to cover
618 the area between the ID PMTs to reduce photon reflection from the ID walls.
619 Opposite to this, the OD is lined with a reflective material to allow photons to
620 reflect around inside the OD until collected by one of the PMTs. Furthermore,
621 each OD PMT is optically coupled with $50 \times 50\text{cm}$ plates of wavelength shifting
622 acrylic which increases the efficiency of light collection [85].

623 In the SK-IV data-taking period, the photocathode coverage of the detector, or
624 the fraction of the ID wall instrumented with PMTs, is $\sim 40\%$ [85]. The PMTs have
625 a quantum efficiency (the ratio of detected electrons to incident photons) of $\sim 21\%$
626 for photons with wavelengths of $360\text{nm} < \lambda < 390\text{nm}$ [89, 90]. The proportion
627 of photoelectrons that produce a signal in the dynode of a PMT, termed the
628 collection efficiency, is $> 70\%$ [85]. The PMTs used within SK are most sensitive
629 to photons with wavelength $300\text{nm} \leq \lambda \leq 600\text{nm}$ [85]. One disadvantage of
630 using PMTs as the detection media is that the Earth's geomagnetic field can
631 modify its response. Therefore, a set of compensation coils is built around the
632 inner surface of the detector to mitigate this effect [86].

633 The SK detector is filled with ultrapure water, which in a perfect world, con-
634 tains no impurities. However, bacteria and organic compounds can significantly
635 degrade the water quality. This decreases the attenuation length, which reduces
636 the total number of photons that hit a PMT. To combat this, a sophisticated water
637 treatment system has been developed [85, 91]. UV lights, mechanical filters, and
638 membrane degasifiers are used to reduce the bacteria, suspended particulates,
639 and radioactive materials from the water. The flow of water within the tank
640 is also critical as it can remove stagnant bacterial growth or build-up of dust

641 on the surfaces within the tank. Gravity drifts impurities in the water towards
642 the bottom of the tank which, if left uncontrolled, can create asymmetric water
643 conditions between the top and bottom of the tank. Typically, the water entering
644 the tank is cooled below the ambient temperature of the tank to control convection
645 and inhibit bacteria growth. Furthermore, the rate of dark noise hits within PMTs
646 is sensitive to the PMT temperature [92]. Therefore controlling the temperature
647 gradients within the tank is beneficial for stable measurements.

648 SK-VI is the first phase of the SK experiment to use gadolinium dopants
649 within the ultrapure water [83]. As such, the SK water system had to be replaced
650 to avoid removing the gadolinium concentrate from the ultrapure water [93]. For
651 an inverse β -decay (IBD) interaction on a water target, the emitted neutron is
652 thermally captured on hydrogen. This process releases a 2.2MeV γ ray which is
653 difficult to detect as the resulting Compton scattered electrons are very close to the
654 Cherenkov threshold, limiting detection capability. Thermal capture of neutrons
655 on gadolinium generates γ rays with higher energy (8MeV [68]) meaning they
656 are more easily detected and reconstructed. SK-VI has 0.01% Gd loading (0.02%
657 gadolinium sulphate by mass) which causes \approx 50% of neutrons emitted by IBD to
658 be captured on gadolinium[94, 95] . Whilst predominantly useful for low energy
659 analyses, Gd loading allows better $\nu/\bar{\nu}$ separation for atmospheric neutrino
660 event selections [96]. Efforts are currently in place to increase the gadolinium
661 concentrate to 0.03% for \approx 75% neutron capture efficiency on gadolinium [97].
662 The final stage of loading targets 0.1% concentrate for \approx 90% neutron capture
663 efficiency on gadolinium.

664 3.1.2 Calibration

665 The calibration of the SK detector is documented in [82] and summarised below.
666 The analysis presented within this thesis is dependent upon ‘high energy events’
667 (Charged particles with $O(> 100)$ MeV momenta). These are events that are
668 expected to generate a larger number of photons such that each PMT will
669 be hit with multiple photons. The reconstruction of these events depends

upon the charge deposited within each PMT and the timing response of each individual PMT. Therefore, the most relevant calibration techniques to this thesis are outlined.

Before installation, 420 PMTs were calibrated to have identical charge responses and then distributed throughout the tank in a cross-shape pattern (As illustrated by Figure 3.2). These are used as a standardised measure for the rest of the PMTs installed at similar geometric positions within SK to be calibrated against. To perform this calibration, a xenon lamp is located at the center of the SK tank which flashes uniform light at 1Hz. This allows for geometrical effects, water quality variation, and timing effects to be measured in situ throughout normal data-taking periods.

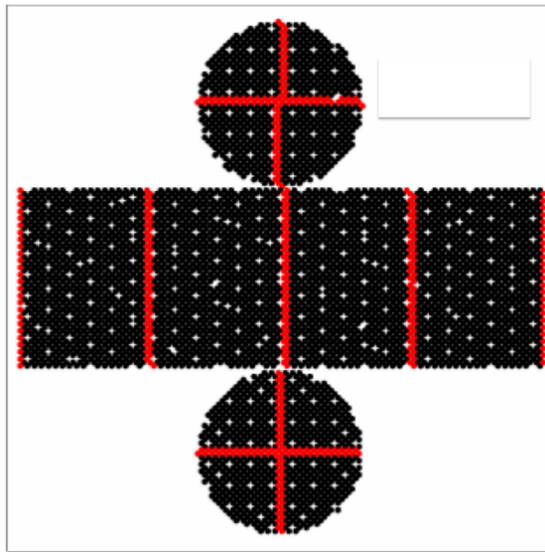


Figure 3.2: The location of “standard PMTs” (red) inside the SK detector. Taken from [82].

When specifically performing calibration of the detector (in out-of-data taking mode), the water in the tank was circulated to avoid top/bottom asymmetric water quality. Any non-uniformity within the tank significantly affects the PMT hit probability through scattering or absorption. This becomes a dominant effect for very low-intensity light sources that are designed such that only one photon is incident upon a given PMT.

687 The gain of a PMT is defined as the ratio of the total charge of the signal
 688 produced compared to the charge of photoelectrons emitted by the photocathodes
 689 within the PMT. To calibrate the signal of each PMT, the “relative” and “absolute”
 690 gain values are measured. The relative gain is the variation of gain among each
 691 of the PMTs whereas the absolute gain is the average gain of all PMTs.

692 The relative gain is calibrated as follows. A laser is used to generate two
 693 measurements: a high-intensity flash that illuminates every PMT with a sufficient
 694 number of photons, and a low-intensity flash in which only a small number
 695 of PMTs collect light. The first measurement creates an average charge, $Q_{obs}(i)$
 696 on PMT i , whereas the second measurement ensures that each hit PMT only
 697 generates a single photoelectron. For the low-intensity measurement, the number
 698 of times each PMT records a charge larger than 1/4 photoelectrons, $N_{obs}(i)$, is
 699 counted. The values measured can be expressed as

$$\begin{aligned} Q_{obs}(i) &\propto I_H \times f(i) \times \epsilon(i) \times G(i), \\ N_{obs}(i) &\propto I_L \times f(i) \times \epsilon(i). \end{aligned} \tag{3.1}$$

700 Where I_H and I_L is the intensity of the high and low flashes, $f(i)$ is the
 701 acceptance efficiency of the i^{th} PMT, $\epsilon(i)$ is the product of the quantum and
 702 collection efficiency of the i^{th} PMT and $G(i)$ is the gain of the i^{th} PMT. The relative
 703 gain for each PMT can be determined by taking the ratio of these quantities.

704 The absolute gain calibration is performed by observing fixed energy γ -rays
 705 of $E_\gamma \sim 9\text{MeV}$ emitted isotropically from neutron capture on a NiCf source
 706 situated at the center of the detector. This generates a photon yield of about 0.004
 707 photoelectrons/PMT/event, meaning that $> 99\%$ of PMT signals are generated
 708 from single photoelectrons. A charge distribution is generated by performing
 709 this calibration over all PMTs, and the average value of this distribution is taken
 710 to be the absolute gain value.

711 As mentioned in subsection 3.1.1, the average quantum and collection effi-
 712 ciency for the SK detector PMTs is $\sim 21\%$ and $> 70\%$ respectively. However,
 713 these values do differ between each PMT and need to be calibrated accordingly.

714 Consequently, the NiCf source is also used to calibrate the “quantum \times collection”
715 efficiency (denoted “QE”) value of each PMT. The NiCf low-intensity source is
716 used as the PMT hit probability is proportional to the QE ($N_{obs}(i) \propto \epsilon(i)$ in
717 Equation 3.1). A Monte Carlo prediction which includes photon absorption,
718 scattering, and reflection is made to estimate the number of photons incident on
719 each PMT and the ratio of the number of predicted to observed hits is calculated.
720 The difference is attributed to the QE efficiency of that PMT. This technique is
721 extended to calculate the relative QE efficiency by normalizing the average of
722 all PMTs which removes the dependence on the light intensity.

723 Due to differing cable lengths and readout electronics, the timing response
724 between a photon hitting the PMT and the signal being captured by the data
725 acquisition can be different between each PMT. Due to threshold triggers (De-
726 scribed in subsection 3.1.3), the time at which a pulse reaches a threshold is
727 dependent upon the size of the pulse. This is known as the ‘time-walk’ effect
728 and also needs to be accounted for in each PMT. To calibrate the timing response,
729 a pulse of light with width 0.2ns is emitted into the detector through a diffuser.
730 Two-dimensional distributions of time and pulse height (or charge) are made
731 for each PMT and are used to calibrate the timing response. This is performed
732 in-situ during data taking with the light source pulsing at 0.03Hz.

733 The top/bottom water quality asymmetry is measured using the NiCf calibra-
734 tion data and cross-referencing these results to the “standard PMTs”. The water
735 attenuation length is continuously measured by the rate of vertically-downgoing
736 cosmic-ray muons which enter via the top of the tank.

737 Dark noise is where a PMT registers a pulse that is consistent with a single
738 photoelectron emitted from photon detection despite the PMT being in complete
739 darkness. This is predominately caused by two processes. Firstly there is
740 intrinsic dark noise which is where photoelectrons gain enough thermal energy
741 to be emitted from the photocathode, and secondly, the radioactive decay of
742 contaminants inside the structure of the PMT. Typical dark noise rate for PMTs
743 used within SK are $O(3)\text{kHz}$ [85]. This is lower than the expected number of

744 photons generated for a ‘high energy event’ (As described in subsection 3.1.4)
745 but instability in this value can cause biases in reconstruction. Dark noise is
746 related to the gain of a PMT and is calibrated using hits inside a time window
747 recorded before an event trigger [98].

748 3.1.3 Data Acquisition and Triggering

749 As the analysis presented in this thesis will only use the SK-IV period of the
750 SK experiment so this subsection focuses on the relevant points of the data
751 acquisition and triggering systems to that SK period. The earlier data acquisition
752 and triggering systems are documented in [99, 100].

753 Before the SK-IV period started, the existing front-end electronics were re-
754 placed with “QTC-Based Electronics with Ethernet, QBEE” systems [101]. When
755 the QBEE observes a signal above a 1/4 photoelectron threshold, the charge-to-
756 time (QTC) converter generates a rectangular pulse. The start of the rectangular
757 pulse indicates the time at which the analog photoelectron signal was received
758 and the width of the pulse indicates the total charge integrated throughout the
759 signal. This is then digitized by time-to-digital converters and sent to the “front-
760 end” PCs. The digitized signal from every QBEE is then chronologically ordered
761 and sent to the “merger” PCs. It is the merger PCs that apply the software trigger.
762 Any triggered events are passed to the “organizer” PC. This sorts the data stream
763 of multiple merger PCs into chronologically ordered events, which are then saved
764 to disk. The schematic of data flow from PMTs to disk is illustrated in Figure 3.3.

765 The software trigger (described in [103]) operates by determining the number
766 of PMT hits within a 200ns sliding window, N_{200} . This window coincides with
767 the maximum time that a Cherenkov photon would take to traverse the length
768 of the SK tank [100]. For lower energy events that generate fewer photons, this
769 technique is useful for eliminating background processes like dark noise and
770 radioactive decay which would be expected to be separated in time. When the
771 value of N_{200} exceeds some pre-defined threshold, a software trigger is issued.
772 There are several trigger thresholds used within the SK-IV period which are

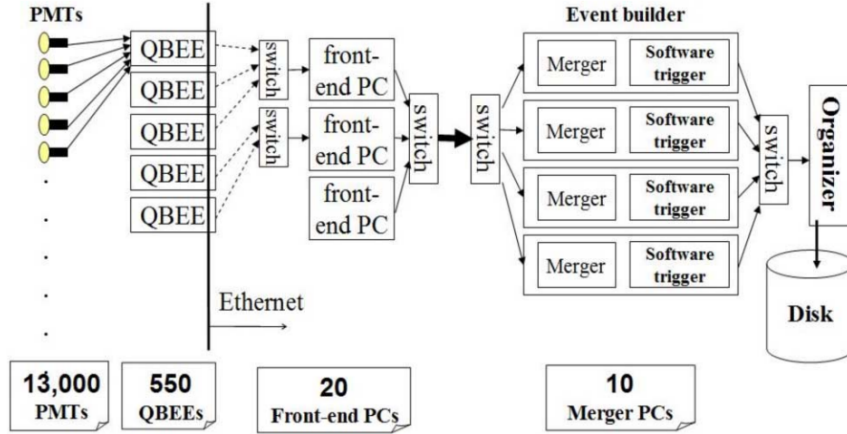


Figure 3.3: Schematic view of the data flow through the data acquisition and online system. Taken from [102].

773 detailed in Table 3.2. If one of these thresholds is met, the PMT hits within an
 774 extended time window are also read out and saved to disk. In the special case
 775 of an event that exceeds the SHE trigger but does not exceed the OD trigger,
 776 the AFT trigger looks for delayed coincidences of 2.2MeV gamma rays emitted
 777 from neutron capture in a $535\mu\text{s}$ window after the SHE trigger. A similar but
 778 more complex “Wideband Intelligent Trigger (WIT)” has been deployed and
 779 is described in [104].

Trigger	Acronym	Condition	Extended time window (μs)
Super Low Energy	SLE	>34/31 hits	1.3
Low Energy	LE	>47 hits	40
High Energy	HE	>50 hits	40
Super High Energy	SHE	>70/58 hits	40
Outer Detector	OD	>22 hits in OD	N/A

Table 3.2: The trigger thresholds and extended time windows saved around an event which were utilised throughout the SK-IV period. The exact thresholds can change and the values listed here represent the thresholds at the start and end of the SK-IV period.

780 3.1.4 Cherenkov Radiation

781 Cherenkov light is emitted from any highly energetic charged particle traveling
 782 with relativistic velocity, β , greater than the local speed of light in a medium [105].

783 Cherenkov light is formed at the surface of a cone with a characteristic pitch angle,

$$\cos(\theta) = \frac{1}{\beta n}. \quad (3.2)$$

784 Where n is the refractive index of the medium. Consequently, the Cherenkov
 785 momentum threshold, P_{thres} , is dependent upon the mass, m , of the charged
 786 particle moving through the medium,

$$P_{thres} = \frac{m}{\sqrt{n^2 - 1}}. \quad (3.3)$$

787 For water, where $n = 1.33$, the Cherenkov threshold momentum and energy
 788 for various particles are given in Table 3.3. In contrast, γ -rays are detected
 789 indirectly via the combination of photons generated by Compton scattering
 790 and pair production. The threshold for detection in the SK detector is typically
 791 higher than the threshold for photon production. This is due to the fact that the
 792 attenuation of photons in the water means that typically $\sim 75\%$ of Cherenkov
 793 photons reach the ID PMTs. Then the collection and quantum efficiencies
 794 described in subsection 3.1.1 result in the number of detected photons being
 795 lower than the number of photons which reach the PMTs.

Particle	Threshold Momentum (MeV)	Threshold Energy (MeV)
Electron	0.5828	0.7751
Muon	120.5	160.3
Pion	159.2	211.7
Proton	1070.0	1423.1

Table 3.3: The threshold momentum and total energy for a particle to generate Cherenkov light in ultrapure water, as calculated in Equation 3.2 in ultrapure water which has refractive index $n = 1.33$.

796 The Frank-Tamm equation [106] describes the relationship between the num-
 797 ber of Cherenkov photons generated per unit length, dN/dx , the wavelength of
 798 the photons generated, λ , and the relativistic velocity of the charged particle,

$$\frac{d^2N}{dxd\lambda} = 2\pi\alpha \left(1 - \frac{1}{n^2\beta^2}\right) \frac{1}{\lambda^2}. \quad (3.4)$$

799 where α is the fine structure constant. For a 100MeV momentum electron,
 800 approximately 330 photons will be produced per centimeter in the $300\text{nm} \leq \lambda \leq$
 801 700nm region which the ID PMTs are most sensitive to [85].

802 3.2 The Tokai to Kamioka Experiment

803 The Tokai to Kamioka (T2K) experiment is a long-baseline neutrino oscillation
 804 experiment located in Japan. Proposed in the early 2000s [107, 108] to replace
 805 K2K [109], T2K was designed to observe electron neutrino appearance whilst
 806 precisely measuring the oscillation parameters associated with muon neutrino
 807 disappearance [110]. The experiment consists of a neutrino beam generated
 808 at the Japan Proton Accelerator Research Complex (J-PARC), a suite of near
 809 detectors situated 280m from the beam target, and the Super Kamiokande far
 810 detector positioned at a 295km baseline. The cross-section view of the T2K
 811 experiment is drawn in Figure 3.4.

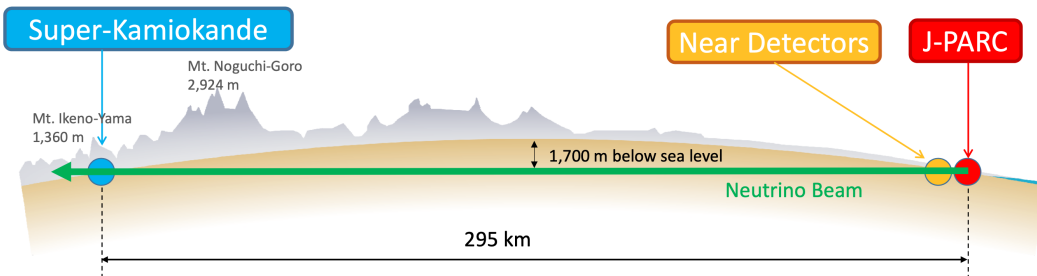


Figure 3.4: The cross-section view of the Tokai to Kamioka experiment illustrating the beam generation facility at J-PARC, the near detector situated at a baseline of 280m and the Super Kamiokande far detector situated 295km from the beam target.

812 The T2K collaboration makes world-leading measurements of the $\sin^2(\theta_{23})$,
 813 Δm_{32}^2 , and δ_{CP} oscillation parameters. Improvements in the precision and accu-
 814 racy of parameter estimates are still being made by including new data samples
 815 and developing the models which describe the neutrino interactions and detector
 816 responses [111]. Electron neutrino appearance was first observed at T2K in 2014
 817 [112] with 7.3σ significance.

818 The near detectors provide constraints on the beam flux and cross-section
 819 model parameters used within the oscillation analysis by observing the unoscil-
 820 lated neutrino beam. There are a host of detectors situated in the near detector hall
 821 (As illustrated in Figure 3.5): ND280 (subsection 3.2.3), INGRID (subsection 3.2.4),
 822 NINJA [113], WAGASCI [114], and Baby-MIND [115]. The latter three are not
 823 currently used within the oscillation analysis presented in this thesis.

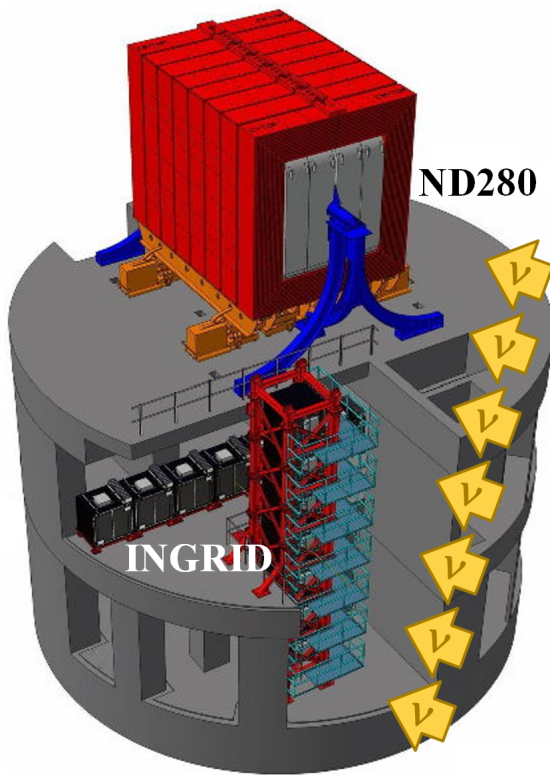


Figure 3.5: The near detector suite for the T2K experiment showing the ND280 and INGRID detectors. The distance between the detectors and the beam target is 280m.

824 Whilst this thesis presents the ND280 in terms of its purpose for the oscillation
 825 analysis, the detector can also make many cross-section measurements at neutrino
 826 energies of $O(1)$ GeV for the different targets within the detector [116, 117]. These
 827 measurements are of equal importance as they can lead the way in determining
 828 the model parameters used in the interaction models for the future high-precision
 829 era of neutrino physics.

3.2.1 Analysis Overview

There are two independent fitters, MaCh3 and BANFF, which perform the near detector fit. MaCh3 uses a bayesian Markov Chain Monte Carlo fitting technique, whereas BANFF uses a frequentist gradient descent technique. The output of each fitter is compared as a method of cross-checking the behaviour of the two fitters. This is done by comparing: the Monte Carlo predictions using various tunes, the likelihood that is calculated in each fitter and the post-fit constraint associated with every parameter used in the fit. Once validated, the output converted into a covariance matrix to describe the error and correlations between all the flux and cross-section parameters. This is then propagated to the far-detector oscillation analysis group.

The far detector group has three independent fitters: P-Theta, VALOR and MaCh3. The first two fitters use a hybrid frequentist fitting technique where the likelihood is minimised with respect to the parameters of interest and marginalised over all other parameters. These fitters use the covariance provided by the near detector fitters as a basis for implementing the near detector constraints. The MaCh3 fitter uses a simultaneous fit of all near and far detector samples. This removes any Gaussian assumptions when making the covariance matrix from the near detector results. The results for all three fitters are compares using a technique similar to the validation of the near detector fitters.

There are three particular tunes of the T2K flux and low energy cross section model typically considered. Firstly, the “generated” tune which is the set of dial values with which the Monte Carlo was generated. Secondly, the set of dial values which are taken from external data measurements and used as inputs. These are the “pre-fit” dial values. The reason these two sets of dial values are different is that the external data measurements are continually updated but it is very computationally intensive to regenerate a Monte Carlo prediction after each update. The final tune is the “post-fit”, “post-ND fit” or “post-BANFF” dial values. These are the values taken from the constraints provided by the near detector.

3.2.2 The Neutrino Beam

The neutrino beam used within the T2K experiment is described in [39, 43] and summarised below. The accelerator facility at J-PARC is composed of two sections; the primary and secondary beamlines. Figure 3.6 illustrates a schematic of the beamline, focusing mostly on the components of the secondary beamline. The primary beamline has three accelerators that progressively accelerate protons; a linear accelerator, a rapid-cycling synchrotron, and the main-ring (MR) synchrotron. Once fully accelerated by the MR, the protons have a kinetic energy of 30GeV. Eight bunches of these protons, separated by 500ns, are extracted per “spill” from the MR and directed towards a graphite target (a rod of length 91.4cm and diameter 2.6cm). Spills are extracted at 0.5Hz with $\sim 3 \times 10^{14}$ protons contained per spill.

The secondary beamline consists of three main components: the target station, the decay volume, and the beam dump. The target station is comprised of the target, beam monitors, and three magnetic focusing horns. The proton beam interacts with the graphite target to form a secondary beam of mostly pions and kaons. The secondary beam travels through a 96m long decay volume, generating neutrinos through the following decays [39],

$$\begin{array}{ll}
\pi^+ \rightarrow \mu^+ + \nu_\mu & \pi^- \rightarrow \mu^- + \bar{\nu}_\mu \\
K^+ \rightarrow \mu^+ + \nu_\mu & K^- \rightarrow \mu^- + \bar{\nu}_\mu \\
\rightarrow \pi^0 + e^+ + \nu_e & \rightarrow \pi^0 + e^- + \bar{\nu}_e \\
\rightarrow \pi^0 + \mu^+ + \nu_\mu & \rightarrow \pi^0 + \mu^- + \bar{\nu}_\mu \\
K_L^0 \rightarrow \pi^- + e^+ + \nu_e & K_L^0 \rightarrow \pi^+ + e^- + \bar{\nu}_e \\
\rightarrow \pi^- + \mu^+ + \nu_\mu & \rightarrow \pi^+ + \mu^- + \bar{\nu}_\mu \\
\mu^+ \rightarrow e^+ + \bar{\nu}_\mu + \nu_e & \mu^- \rightarrow e^- + \nu_\mu + \bar{\nu}_e.
\end{array}$$

The electrically charged component of the secondary beam is focused towards the far detector by the three magnetic horns. These horns direct charged particles of a particular polarity towards SK whilst defocusing the oppositely charged particles. This allows a mostly neutrino or mostly antineutrino beam to be used within the experiment, denoted as “forward horn current (FHC)” or “reverse horn current (RHC)” respectively.

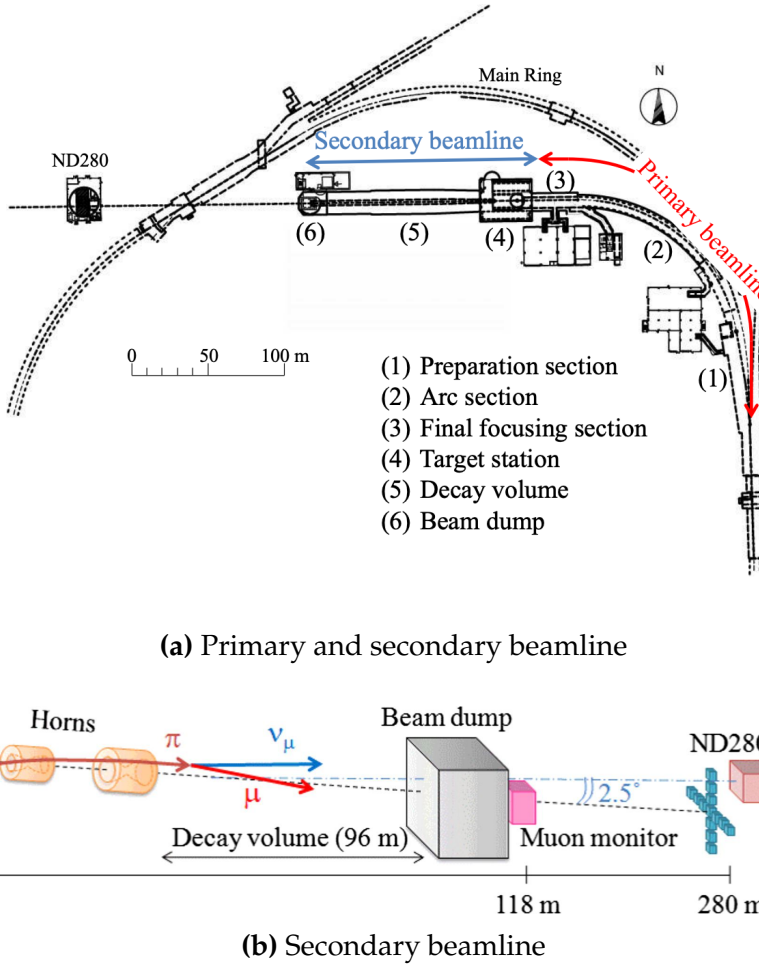


Figure 3.6: Top panel: Bird's eye view of the most relevant part of primary and secondary beamline used within the T2K experiment. The primary beamline is the main-ring proton synchrotron, kicker magnet, and graphite target. The secondary beamline consists of the three focusing horns, decay volume, and beam dump. Figure taken from [43]. Bottom panel: The side-view of the secondary beamline including the focusing horns, beam dump and neutrino detectors. Figure taken from [118].

885 Figure 3.7 illustrates the different contributions to the FHC and RHC neutrino
 886 flux. The low energy flux is dominated by the decay of pions whereas kaon
 887 decay becomes the dominant source of neutrinos for $E_\nu > 3\text{GeV}$. The “wrong-
 888 sign” component, which is the $\bar{\nu}_\mu$ background in a ν_μ beam, and the intrinsic
 889 irreducible ν_e background, are predominantly due to muon decay for $E_\nu <$
 890 2GeV . As the antineutrino production cross-section is smaller than the neutrino
 891 cross-section, the wrong-sign component is more dominant in the RHC beam
 892 as compared to that in the FHC beam.



Figure 3.7: The Monte Carlo prediction of the energy spectrum for each flavour of neutrino (ν_e , $\bar{\nu}_e$, ν_μ and $\bar{\nu}_\mu$) in the neutrino dominated beam FHC mode (Left) and antineutrino dominated beam RHC mode (Right) expected at SK. Taken from [119].

893 The beam dump, situated at the end of the decay volume, stops all charged
 894 particles other than highly energetic muons ($p_\mu > 5\text{GeV}$). The MuMon detector
 895 monitors the penetrating muons to determine the beam direction and inten-
 896 sity which is used to constrain some of the beam flux systematics within the
 897 analysis [118, 120].

898 The T2K experiment uses an off-axis beam to narrow the neutrino energy
 899 distribution. This was the first implementation of this technique in a long-
 900 baseline neutrino oscillation experiment after its original proposal [121]. Pion
 901 decay, $\pi \rightarrow \mu + \nu_\mu$, is a two-body decay. Consequently, the neutrino energy,
 902 E_ν , can be determined based on the pion energy, E_π , and the angle at which
 903 the neutrino is emitted, θ ,

$$E_\nu = \frac{m_\pi^2 - m_\mu^2}{2(E_\pi - p_\pi \cos(\theta))}, \quad (3.5)$$

904 where m_π and m_μ are the mass of the pion and muon respectively. For a fixed
 905 energy pion, the neutrino energy distribution is dependent upon the angle at
 906 which the neutrinos are observed from the initial pion beam direction. For the
 907 295km baseline at T2K, $E_\nu = 0.6\text{GeV}$ maximises the electron neutrino appearance
 908 probability, $P(\nu_\mu \rightarrow \nu_e)$, whilst minimising the muon disappearance probability,

909 $P(\nu_\mu \rightarrow \nu_\mu)$. Figure 3.8 illustrates the neutrino energy distribution for a range of
 910 off-axis angles, as well as the oscillation probabilities most relevant to T2K.

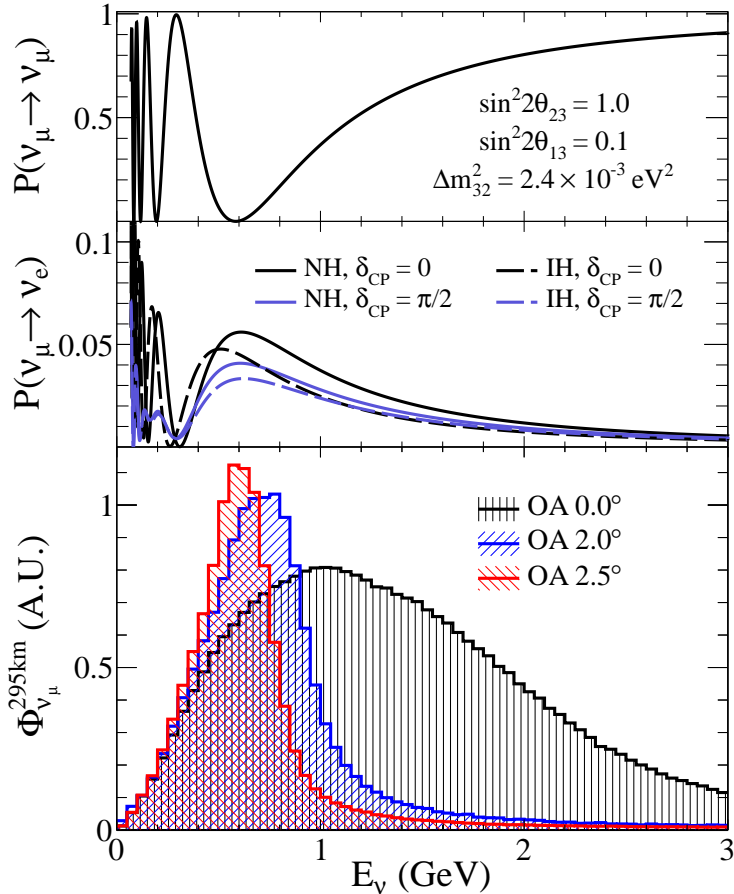


Figure 3.8: Top panel: T2K muon neutrino disappearance probability as a function of neutrino energy. Middle panel: T2K electron neutrino appearance probability as a function of neutrino energy. Bottom panel: The neutrino flux distribution for three different off-axis angles (Arbitrary units) as a function of neutrino energy.

911 3.2.3 The Near Detector at 280m

912 Whilst all the near detectors are situated in the same “pit” located at 280m from
 913 the beamline, the “ND280” detector is the off-axis detector which is situated at
 914 the same off-axis angle as the Super-Kamiokande far detector. It has two primary
 915 functions; firstly it measures the neutrino flux and secondly, it counts the event
 916 rates of different types of neutrino interactions. Both of these constrain the flux
 917 and cross-section systematics invoked within the model for a more accurate
 918 prediction of the expected event rate at the far detector.



Figure 3.9: The components of the ND280 detector. The neutrino beam travels from left to right. Taken from [43].

As illustrated in Figure 3.9, the ND280 detector consists of several sub-detectors. The most important part of the detector for this analysis is the tracker region. This is comprised of two-time projection chambers (TPCs) sandwiched between three fine grain detectors (FGDs). The FGDs contain both hydrocarbon plastics and water targets for neutrino interactions and provide track reconstruction near the interaction vertex. The emitted charged particles can then propagate into the TPCs which provide particle identification and momentum reconstruction. The FGDs and TPCs are further described in subsubsection 3.2.3.1 and subsubsection 3.2.3.2 respectively. The electromagnetic calorimeter (ECAL) encapsulates the tracker region alongside the π^0 detector (P0D). The ECAL measures the deposited energy from photons emitted from interactions within the FGD. The P0D constrains the cross-section of neutral current interactions which generate neutral pions, which is one of the largest backgrounds in the electron neutrino appearance oscillation channel. The P0D and ECAL detectors are detailed in subsubsection 3.2.3.3 and subsubsection 3.2.3.4 respectively. The entire detector is located within a large yoke magnet which produces a 0.2T magnetic field.

935 field. This design of the magnet also includes a scintillating detector called the
936 side muon range detector (SMRD), which is used to track high-angle muons as
937 well as acting as a cosmic veto. The SMRD is described in subsubsection 3.2.3.5.

938 **3.2.3.1 Fine Grained Detectors**

939 The T2K tracker region is comprised of two fine-grained detectors (FGD) and
940 three Time Projection Chambers (TPC). A detailed description of the FGD design,
941 construction, and assembly is found in [122] and summarised below. The FGDS
942 are the primary target for neutrino interactions with a mass of 1.1 tonnes per FGD.
943 Alongside this, the FGDS are designed to be able to track short-range particles
944 which do not exit the FGD. Typically, short-range particles are low momentum
945 and are observed as tracks that deposit a large amount of energy per unit length.
946 This means the FGD needs good granularity to resolve these particles. The
947 FGDS have the best timing resolution ($\sim 3\text{ns}$) of any of the sub-detectors of the
948 ND280 detector. As such, the FGDS are used for time of flight measurements
949 to distinguish forward-going positively charged particles from backward-going
950 negatively charged particles. Finally, any tracks which pass through multiple
951 sub-detectors are required to be track matched to the FGD.

952 Both FGDS are made from square scintillator planes of side length 186cm and
953 width 2.02cm. Each plane consists of two layers of 192 scintillator bars in an
954 X or Y orientation. A wavelength-shifting fiber is threaded through the center
955 of each bar and is read out by a multi-pixel photon counter (MPPC). FGD1 is
956 the most upstream of the two FGDS and contains 15 planes of carbon plastic
957 scintillator which is a common target in external neutrino scattering data. As
958 the far detector is a pure water target, 7 of the 15 scintillator planes in FGD2
959 have been replaced with a hybrid water-scintillator target. Due to the complexity
960 of the nucleus, nuclear effects can not be extrapolated between different nuclei.
961 Therefore having the ability to take data on one target which is the same as
962 external data and another target which is the same as the far detector target is
963 beneficial for reliable model parameter estimates.

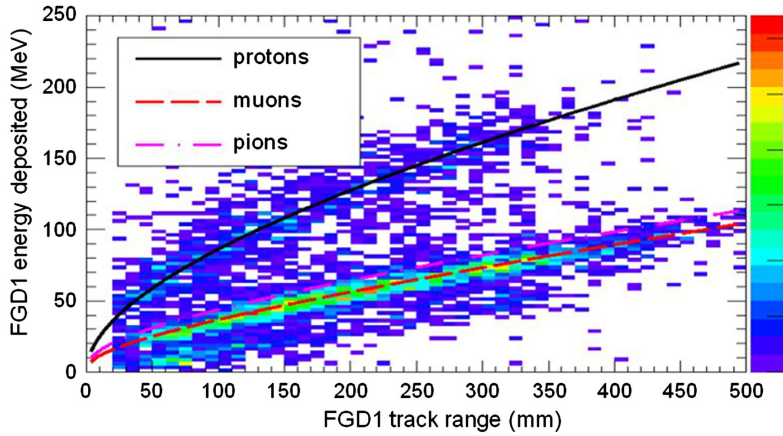


Figure 3.10: Comparison of data to Monte Carlo prediction of integrated deposited energy as a function of track length for particles that stopped in FGD1. Taken from [122].

964 The integrated deposited energy is used for particle identification. The FGD
965 can distinguish protons from other charged particles by comparing the integrated
966 deposited energy from data to Monte Carlo prediction as seen in Figure 3.10.

967 3.2.3.2 Time Projection Chambers

968 The majority of particle identification and momentum measurements within
969 ND280 are provided by three Time Projection Chambers (TPCs) [123]. The
970 TPCs are located on either side of the FGDs. They are located inside of the
971 magnetic field meaning the momentum of a charged particle can be determined
972 from the bending of the track.

973 Each TPC module consists of two gas-tight boxes, as shown in Figure 3.11,
974 which are made of non-magnetic material. The outer box is filled with CO₂ which
975 acts as an electrical insulator between the inner box and the ground. The inner box
976 forms the field cage which produces a uniform electric drift field of $\sim 275\text{V/cm}$
977 and is filled with an argon gas mixture. Charged particles moving through this
978 gas mixture ionize the gas and the ionised charge is drifted towards micromegas
979 detectors which measure the ionization charge. The time and position information
980 in the readout allows a three-dimensional image of the neutrino interaction.

981 The particle identification of tracks that pass through the TPCs is performed
982 using dE/dx measurements. Figure 3.12 illustrates the data to Monte Carlo



Figure 3.11: Schematic design of a Time Projection Chamber detector. Taken from [123].

983 distributions of the energy lost by a charged particle passing through the TPC as
 984 a function of the reconstructed particle momentum. The resolution is $7.8 \pm 0.2\%$
 985 meaning that electrons and muons can be distinguished. This allows reliable
 986 measurements of the intrinsic ν_e component of the beam.

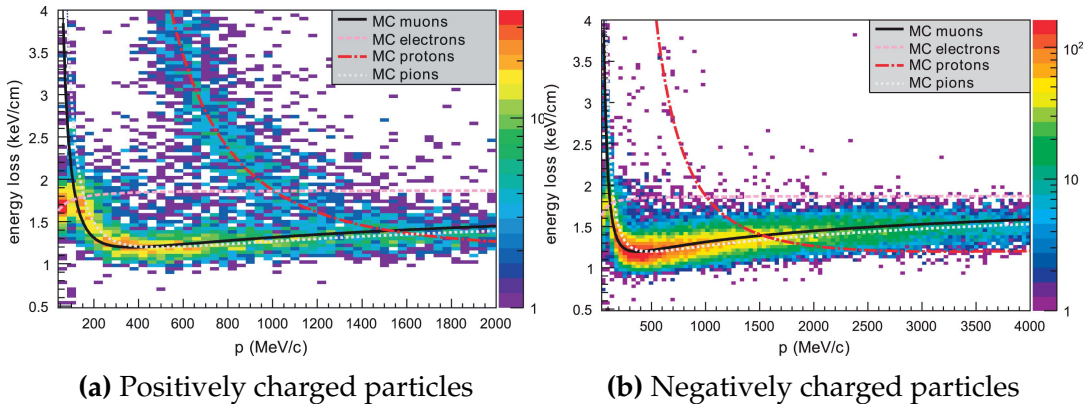


Figure 3.12: The distribution of energy loss as a function of reconstructed momentum for charged particles passing through the TPC, comparing data to Monte Carlo prediction. Taken from [123].

987 **3.2.3.3 π^0 Detector**

988 If one of the γ -rays from a $\pi^0 \rightarrow 2\gamma$ decay is missed at the far detector, the
 989 reconstruction will determine that event to be a charge current ν_e -like event.
 990 This is one of the main backgrounds hindering the electron neutrino appearance

991 searches. The π^0 detector (P0D) measures the cross-section of the neutral current
 992 induced neutral pion production on a water target to constrain this background.

993 The P0D is a cube of approximately 2.5m length consisting of layers of scin-
 994 tillating bars, brass and lead sheets, and water bags as illustrated in Figure 3.13.
 995 Two electromagnetic calorimeters are positioned at the most upstream and most
 996 downstream position in the sub-detector and the water target is situated in
 997 between them. The scintillator layers are built from two triangular bars orientated
 998 in opposite directions to form a rectangular layer. Each triangular scintillator bar
 999 is threaded with optical fiber which is read out by MPPCs. The high-Z brass and
 1000 lead regions produce electron showers from the photons emitted in π^0 decay.

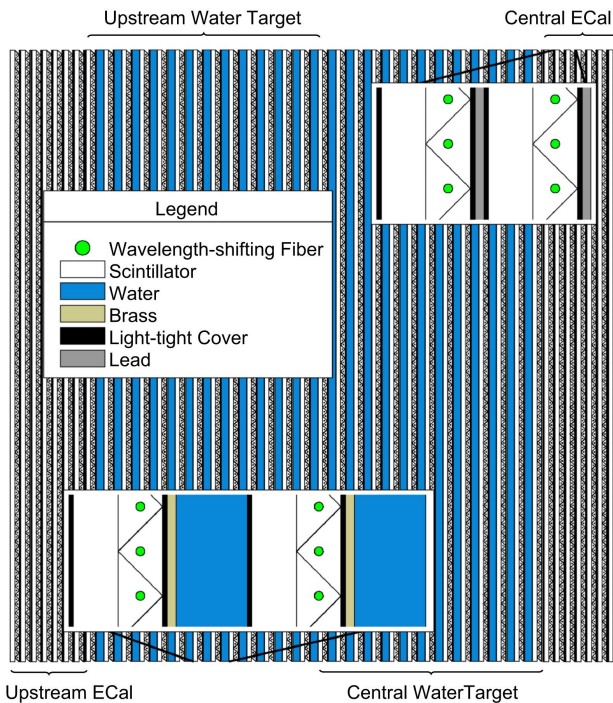


Figure 3.13: A schematic of the P0D side-view. Taken from [124].

1001 The sub-detector can generate measurements of NC1 π^0 cross-sections on a
 1002 water target by measuring the event rate both with and without the water target,
 1003 with the cross-section on a water target being determined as the difference. The to-
 1004 tal active mass is 16.1 tonnes when filled with water and 13.3 tonnes when empty.

1005 3.2.3.4 Electromagnetic Calorimeter

1006 The electromagnetic calorimeter [125] (ECal) encapsulates the P0D and tracking
1007 sub-detectors. Its primary purpose is to aid π^0 reconstruction from any interac-
1008 tion in the tracker. To do this, it measures the energy and direction of photon
1009 showers from $\pi^0 \rightarrow 2\gamma$ decay. It can also distinguish pion and muon tracks
1010 depending on the shape of the photon shower deposited.

1011 The ECal is comprised of three sections; the P0D ECal which surrounds the
1012 P0D, the barrel ECal which encompasses the tracking region, and the downstream
1013 ECal which is situated downstream of the tracker region. The barrel and down-
1014 stream ECals are tracking calorimeters that focus on electromagnetic showers
1015 from high-angle particles emitted from the tracking sub-detectors. Particularly in
1016 the TPC, high-angle tracks (those which travel perpendicularly to the beam-axis)
1017 can travel along a single scintillator bar resulting in very few hits. The width of
1018 the barrel and downstream ECal corresponds to ~ 11 electron radiation lengths
1019 to ensure a significant amount of the π^0 energy is contained. As the P0D has
1020 its own calorimetry which reconstructs showers, the P0D ECal determines the
1021 energy which escapes the P0D.

1022 Each ECal is constructed of multiple layers of scintillating bars sandwiched
1023 between lead sheets. The scintillating bars are threaded with optical fiber and read
1024 out by MPPCs. Each sequential layer of the scintillator is orientated perpendicular
1025 to the previous which allows a three-dimensional event reconstruction. The
1026 target mass of the P0D ECal, barrel ECal, and downstream ECal are 1.50, 4.80,
1027 and 6.62 tonnes respectively.

1028 3.2.3.5 Side Muon Range Detector

1029 As illustrated in Figure 3.9, the ECal, FGDs, P0D, and TPCs are enclosed within
1030 the UA1 magnet. Reconditioned after use in the UA1 [126] and NOMAD [127]
1031 experiments, this magnet provides a uniform horizontal magnetic field of 0.2T
1032 with an uncertainty of 2×10^{-4} T.

1033 Built into the UA1 magnet, the side muon range detector (SMRD)[128] monitors
1034 high-energy muons which leave the tracking region and permeate through
1035 the ECal. It additionally acts as a cosmic muon veto and trigger.

1036 **3.2.4 The Interactive Neutrino GRID**

1037 The Interactive Neutrino GRID (INGRID) detector is situated within the same
1038 “pit” as the other near detectors. It is aligned with the beam in the “on-axis”
1039 position and measures the beam direction, spread, and intensity. The detector
1040 was originally designed with 16 identical modules [43] (two modules have since
1041 been decommissioned) and a “proton” module. The design of the detector is 14
1042 modules oriented in a cross with length and height 10m × 10m, as illustrated
1043 in Figure 3.14.

1044 Each module is composed of iron sheets interlaced with eleven tracking
1045 scintillator planes for a total target mass of 7.1 tonnes per module. The scintillator
1046 design is an X-Y pattern of 24 bars in both orientations, where each bar contains
1047 wave-length shifting fibers which are connected to multi-pixel photon counters
1048 (MPPCs). Each module is encapsulated inside veto planes to aid the rejection
1049 of charged particles entering the module.

1050 The proton module is different from the other modules in that it consists
1051 of entirely scintillator planes with no iron target. The scintillator bars are also
1052 smaller than those used in the other modules to increase the granularity of
1053 the detector and improve tracking capabilities. The module sits in the center
1054 of the beamline and is designed to give precise measurements of quasi-elastic
1055 charged current interactions to evaluate the performance of the Monte Carlo
1056 simulation of the beamline.

1057 The INGRID detector can measure the beam direction to an uncertainty of
1058 0.4mrad and the beam centre within a resolution of 10cm [43]. The beam direction
1059 in both the vertical and horizontal directions is discussed in [129] and it is found
1060 to be in good agreement with the MUMON monitor described in subsection 3.2.2.



Figure 3.14: Left panel: The Interactive Neutrino GRID on-axis Detector. 14 modules are arranged in a cross-shape configuration, with the center modules being directly aligned with the on-axis beam. Right panel: The layout of a single module of the INGRID detector. Both figures are recreated from [43].

4

1061

1062

1063

Bayesian Statistics and Markov Chain Monte Carlo Techniques

1064 This thesis presents a Bayesian oscillation analysis. To extract the oscillation
1065 parameters, a Markov Chain Monte Carlo (MCMC) method is used. This chapter
1066 explains the theory of how parameter estimates can be determined using this
1067 technique and condenses the material found in the literature [130–133].

1068 The oscillation parameter determination presented here is built upon a si-
1069 multaneous fit to neutrino beam data in the near detector, beam data at SK, and
1070 atmospheric data at SK. In total, there are four oscillation parameters of interest
1071 ($\sin^2(\theta_{23})$, $\sin^2(\theta_{13})$, Δm_{32}^2 , and δ_{CP}), two oscillation parameters to which this
1072 study will not be sensitive ($\sin^2(\theta_{12})$, Δm_{21}^2) and many nuisance parameters that
1073 control the systematic uncertainty models.

1074 This analysis uses a Monte Carlo technique to generate a multi-dimensional
1075 probability distribution across all of the model parameters used in the fit. To
1076 determine an estimate for each parameter, this multi-dimensional object is in-
1077 tegrated over all other parameters. This process is called Marginalisation and
1078 is described in subsection 4.3.1. Monte Carlo techniques approximate the prob-
1079 ability distribution of each parameter within the limit of generating infinite
1080 samples. As ever, generating a large number of samples is time and resource-

1081 dependent. Therefore, an MCMC technique is utilised within this analysis to
1082 reduce the required number of steps to sufficiently sample the parameter space.
1083 This technique is described in further detail in subsection 4.2.1.

1084 The Bayesian analysis techniques used within this thesis are built within the
1085 MaCh3 framework [134]. This uses a custom MCMC library package exclusively
1086 supported and developed by the MaCh3 collaborators (which includes the author
1087 of this thesis).

1088 4.1 Bayesian Statistics

1089 Bayesian inference treats observable data, D , and model parameters, $\vec{\theta}$, on equal
1090 footing such that a probability model of both data and parameters is required.
1091 This is the joint probability distribution $P(D, \vec{\theta})$ and can be described by the
1092 prior distribution for model parameters $P(\vec{\theta})$ and the likelihood of the data given
1093 the model parameters $P(D|\vec{\theta})$,

$$P(D, \vec{\theta}) = P(D|\vec{\theta})P(\vec{\theta}). \quad (4.1)$$

1094 The prior distribution, $P(\vec{\theta})$, describes all previous knowledge about the
1095 parameters within the model. For example, if the risk of developing health
1096 problems is known to increase with age, the prior distribution would describe the
1097 increase. For the purpose of this analysis, the prior distribution is typically
1098 the best-fit values taken from external data measurements with a Gaussian
1099 uncertainty. The prior distribution can also contain correlations between model
1100 parameters. In an analysis using Monte Carlo techniques, the likelihood of
1101 measuring some data assuming some set of model parameters is calculated
1102 by comparing the Monte Carlo prediction generated at that particular set of
1103 model parameters to the data.

1104 It is parameter estimation that is important for this analysis and as such, Bayes'
1105 theorem [135] is applied to calculate the probability for each parameter to have a

1106 certain value given the observed data, $P(\vec{\theta}|D)$, which is known as the posterior
1107 distribution (often termed the posterior). This can be expressed as

$$P(\vec{\theta}|D) = \frac{P(D|\vec{\theta})P(\vec{\theta})}{\int P(D|\vec{\theta})P(\vec{\theta})d\vec{\theta}}. \quad (4.2)$$

1108 The denominator in Equation 4.2 is the integral of the joint probability distri-
1109 bution over all values of all parameters used within the fit. For brevity, the
1110 posterior distribution is

$$P(\vec{\theta}|D) \propto P(D|\vec{\theta})P(\vec{\theta}). \quad (4.3)$$

1111 For the purposes of this analysis, it is acceptable to neglect the normalisation
1112 term and focus on this proportional relationship.

1113 4.1.1 Application of Prior Knowledge

1114 The posterior distribution is proportional to the prior uncertainty applied to
1115 each parameter, as illustrated by Equation 4.3. This means that it is possible
1116 to change the prior after the posterior distribution has been determined. The
1117 prior uncertainty of a particular parameter can be ‘divided’ out of the posterior
1118 distribution and the resulting distribution can be reweighted using the new
1119 prior uncertainty that is to be applied. The methodology and implementation
1120 of changing the prior follows that described in [136].

1121 An example implementation that is useful for this analysis is the application
1122 of the “reactor constraint”. As discussed in section 2.4, an external constraint
1123 on $\sin^2(\theta_{13})$ is determined from measurements taken from reactor experiments.
1124 However, the sensitivities from just using the T2K and SK samples is equally
1125 as important. Without this technique, two fits would have to be run, doubling
1126 the required resources. Therefore, the key benefit for this analysis is the fact that
1127 only a single ‘fit’ has to be performed and can be used to build the two posterior
1128 distributions of the with and without reactor constraint applied.

1129 4.2 Monte Carlo Simulation

1130 Monte Carlo techniques are used to numerically solve a complex problem that
1131 does not necessarily have an analytical solution. These techniques rely on
1132 building a large ensemble of samples from an unknown distribution and then
1133 using the ensemble to approximate the properties of the distribution.

1134 An example that uses Monte Carlo techniques is to calculate the area under-
1135 neath a curve. For example, take the problem of calculating the area under a
1136 straight line with gradient $M = 0.4$ and intercept $C = 1.0$. Analytically, one can
1137 calculate the area under the line is equal to 30 units for $0 \leq x \leq 10$. Using Monte
1138 Carlo techniques, one can calculate the area under this line by throwing many
1139 random values for the x and y components of each sample and then calculating
1140 whether that point falls below the line. The area can then be calculated by the
1141 ratio of points below the line to the total number of samples thrown multiplied by
1142 the total area in which samples were scattered. The study is shown in Figure 4.1
1143 highlights this technique and finds the area under the curve to be 29.9 compared
1144 to an analytical solution of 30.0. The deviation of the numerical to analytical
1145 solution can be attributed to the number of samples used in the study. The
1146 accuracy of the approximation in which the properties of the Monte Carlo samples
1147 replicate those of the desired distribution is dependent on the number of samples
1148 used. Replicating this study with a differing number of Monte Carlo samples
1149 used in each study (As shown in Figure 4.2) highlights how the Monte Carlo
1150 techniques are only accurate within the limit of a high number of samples.

1151 Whilst the above example has an analytical solution, these techniques are just
1152 as applicable to complex solutions. Clearly, any numerical solution is only as
1153 useful as its efficiency. As discussed, the accuracy of the Monte Carlo technique is
1154 dependent upon the number of samples generated to approximate the properties
1155 of the distribution. Furthermore, if the positions at which the samples are
1156 evaluated are not ‘cleverly’ picked, the efficiency of the Monte Carlo technique
1157 significantly drops. Given the example in Figure 4.1, if the region in which the

1158 samples are scattered significantly extends passed the region of interest, many
1159 calculations will be calculated but do not add to the ability of the Monte Carlo
1160 technique to achieve the correct result. For instance, any sample evaluated at
1161 a $y \geq 5$ could be removed without affecting the final result. This does bring in
1162 an aspect of the ‘chicken and egg’ problem in that to achieve efficient sampling,
1163 one needs to know the distribution beforehand.

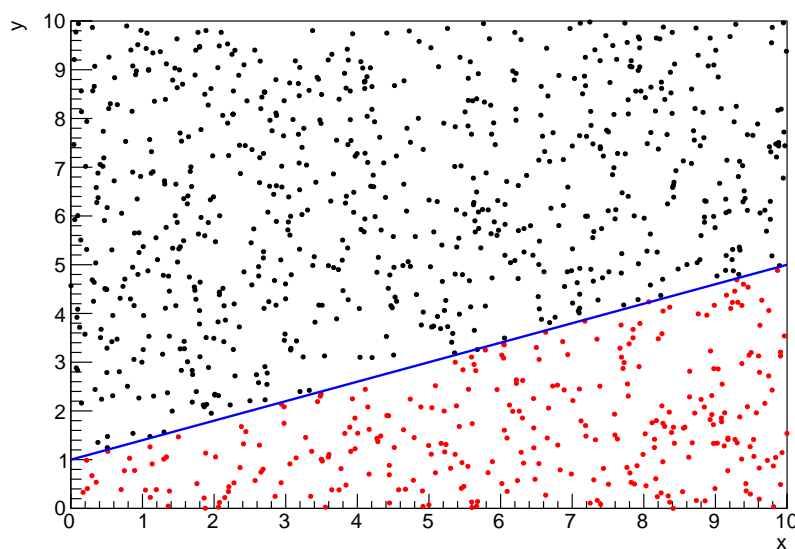


Figure 4.1: Example of using Monte Carlo techniques to find the area under the blue line. The gradient and intercept of the line are 0.4 and 1.0 respectively. The area found to be under the curve using one thousand samples is 29.9 units.

1164 4.2.1 Markov Chain Monte Carlo

1165 This analysis utilises a multi-dimensional probability distribution, with some
1166 dimensions being significantly more constrained than others. These constraints
1167 can be from prior knowledge of parameter distributions from external data or
1168 un-physical regions in which parameters can not exist. To maximise the efficiency
1169 of building the posterior distribution, a Markov Chain Monte Carlo (MCMC)
1170 technique is used. This employs a Markov chain to select the points at which
1171 to sample the posterior distribution. It performs a semi-random stochastic walk
1172 through the allowable parameter space. This builds a posterior distribution

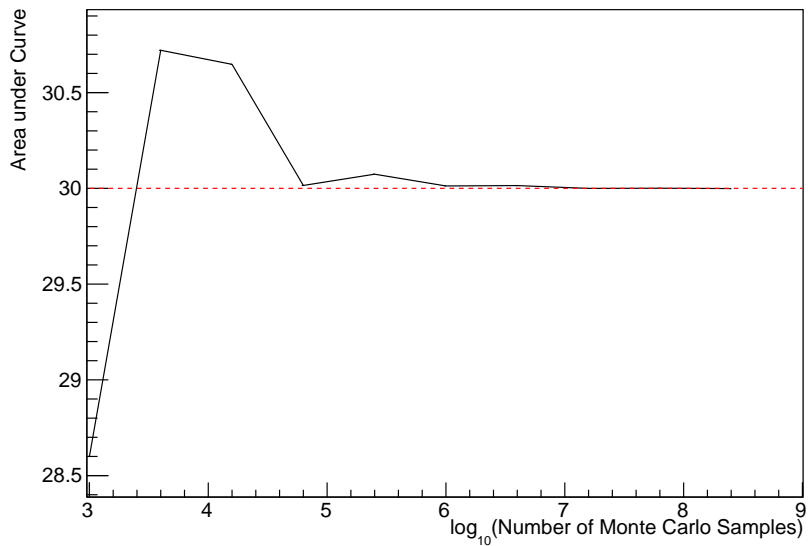


Figure 4.2: The area under a line of gradient 0.4 and intercept 1.0 for the range $0 \leq x \leq 10$ as calculated using Monte Carlo techniques as a function of the number of samples used in each repetition. The analytical solution to the area is 30 units as given by the red line.

1173 which has the property that the density of sampled points is proportional to the
 1174 probability density of that parameter. This means that the samples produced by
 1175 this technique are not statistically independent but they will cover the space
 1176 of the distribution.

1177 A Markov chain functions by selecting the position of step \vec{x}_{i+1} based on the
 1178 position of \vec{x}_i . The space in which the Markov chain selects samples is dependent
 1179 upon the total number of parameters utilised within the fit, where a discrete point
 1180 in this space is described by the N-dimensional space \vec{x} . In a perfectly operating
 1181 Markov chain, the position of the next step depends solely on the previous step
 1182 and not on the further history of the chain (\vec{x}_0, \vec{x}_1 , etc.). However, in solving
 1183 the multi-dimensionality of the fit used within this analysis, each step becomes
 1184 correlated with several of the steps preceding itself. Providing the MCMC chain is
 1185 well optimised, it will begin to converge towards a unique stationary distribution.
 1186 The period between the chain's initial starting point and the convergence to the
 1187 unique stationary distribution is colloquially known as the burn-in period. Once
 1188 the chain reaches the stationary distribution, all points sampled after that point

1189 will look like samples from that distribution.

1190 Further details of the theories underpinning MCMC techniques are discussed
1191 in [131] but can be summarised by the requirement that the chain satisfies the
1192 three ‘regularity conditions’:

- 1193 • Irreducibility: From every position in the parameter space \vec{x} , there must
1194 exist a non-zero probability for every other position in the parameter space
1195 to be reached.
- 1196 • Recurrence: Once the chain arrives at the stationary distribution, every step
1197 following from that position must be samples from the same stationary
1198 distribution.
- 1199 • Aperiodicity: The chain must not repeat the same sequence of steps at any
1200 point throughout the sampling period.

1201 The output of the chain after burn-in (i.e. the sampled points after the chain
1202 has reached the stationary distribution) can be used to approximate the posterior
1203 distribution and model parameters $\vec{\theta}$. To achieve the requirement that the unique
1204 stationary distribution found by the chain be the posterior distribution, one
1205 can use the Metropolis-Hastings algorithm. This guides the stochastic process
1206 depending on the likelihood of the current proposed step compared to that
1207 of the previous step.

1208 4.2.2 Metropolis-Hastings Algorithm

1209 As a requirement for MCMCs, the Markov chain implemented in this technique
1210 must have a unique stationary distribution that is equivalent to the posterior
1211 distribution. To ensure this requirement and that the regularity conditions are
1212 met, this analysis utilises the Metropolis-Hastings (MH) algorithm [137, 138].
1213 For the i^{th} step in the chain, the MH algorithm determines the position in the
1214 parameter space to which the chain moves to based on the current step, \vec{x}_i , and
1215 the proposed step, \vec{y}_{i+1} . The proposed step is randomly selected from some

1216 proposal function $f(\vec{x}_{i+1}|\vec{x}_i)$, which depends solely on the current step (ie. not
1217 the further history of the chain). The next step in the chain \vec{x}_{i+1} can be either the
1218 current step or the proposed step determined by whether the proposed step is
1219 accepted or rejected. To decide if the proposed step is selected, the acceptance
1220 probability, $\alpha(\vec{x}_i, \vec{y}_i)$, is calculated as

$$\alpha(\vec{x}_i, \vec{y}_{i+1}) = \min\left(1, \frac{P(\vec{y}_{i+1}|D)f(\vec{x}_i|\vec{y}_{i+1})}{P(\vec{x}_i|D)f(\vec{y}_{i+1}|\vec{x}_i)}\right). \quad (4.4)$$

1221 Where $P(\vec{y}_{i+1}|D)$ is the posterior distribution as introduced in section 4.1. To
1222 simplify this calculation, the proposal function is required to be symmetric such
1223 that $f(\vec{x}_i|\vec{y}_{i+1}) = f(\vec{y}_{i+1}|\vec{x}_i)$. In practice, a multi-variate Gaussian distribution
1224 centered on \vec{x}_i is used to throw parameter proposals. This reduces Equation 4.4 to

$$\alpha(\vec{x}_i, \vec{y}_{i+1}) = \min\left(1, \frac{P(\vec{y}_{i+1}|D)}{P(\vec{x}_i|D)}\right). \quad (4.5)$$

1225 DB: Figure out what Giles means

1226 After calculating this quantity, a random number, β , is generated uniformly
1227 between 0 and 1. If $\beta \leq \alpha(\vec{x}_i, \vec{y}_{i+1})$, the proposed step is accepted. Otherwise,
1228 the chain sets the next step equal to the current step. This procedure is repeated
1229 for subsequent steps. This can be interpreted as if the posterior probability
1230 of the proposed step is greater than that of the current step, ($P(\vec{y}_{i+1}|D) \geq$
1231 $P(\vec{x}_i|D)$), the proposed step will always be accepted. If the opposite is true,
1232 ($P(\vec{y}_{i+1}|D) \leq P(\vec{x}_i|D)$), the proposed step will be accepted with probability
1233 $P(\vec{x}_i|D)/P(\vec{y}_{i+1}|D)$. This ensures that the Markov chain does not get trapped
1234 in any local minima in the potentially non-Gaussian posterior distribution. The
1235 outcome of this technique is that the density of steps taken in a discrete region
1236 is directly proportional to the probability density in that region.

1237 4.2.3 MCMC Optimisation

1238 As discussed in subsection 4.2.2, the proposal function invoked within the MH
1239 algorithm can take any form and the chain will still converge to the stationary
1240 distribution. At each set of proposed parameter values, a prediction of the same

1241 spectra has to be generated which requires significant computational resources.
1242 Therefore, the number of steps taken before the unique stationary distribution
1243 is found should be minimised as only steps after convergence add information
1244 to the oscillation analysis. Furthermore, the chain should entirely cover the
1245 allowable parameter space to ensure that all values have been considered. Tuning
1246 the distance that the proposal function jumps between steps on a parameter-by-
1247 parameter basis can both minimise the length of the burn-in period and ensure
1248 that the correlation between step \vec{x}_i and \vec{x}_j is sufficiently small.

1249 The effect of changing the width of the proposal function is highlighted in
1250 Figure 4.3. Three scenarios, each with the same underlying stationary distribution
1251 (A Gaussian of width 1.0 and mean 0.), are presented. The only difference between
1252 the three scenarios is the width of the proposal function, colloquially known as
1253 the ‘step size σ ’. Each scenario starts at an initial parameter value of 10.0 which
1254 would be considered an extreme variation. For the case where $\sigma = 0.1$, it is
1255 clear to see that the chain takes a long time to reach the expected region of the
1256 parameter. This indicates that this chain would have a large burn-in period and
1257 does not converge to the stationary distribution until step ~ 500 . Furthermore,
1258 whilst the chain does move towards the expected region, each step is significantly
1259 correlated with the previous. Considering the case where $\sigma = 5.0$, the chain
1260 approaches the expected parameter region almost instantly meaning that the
1261 burn-in period is not significant. However, there are clearly large regions of steps
1262 where the chain does not move. This is likely due to the chain proposing steps
1263 in the tails of the distribution which have a low probability of being accepted.
1264 Consequently, this chain would take a significant number of steps to fully span
1265 the allowable parameter region. For the final scenario, where $\sigma = 0.5$, you can
1266 see a relatively small burn-in period of approximately 100 steps. Once the chain
1267 reaches the stationary distribution, it moves throughout the expected region of
1268 parameter values many times, sufficiently sampling the full parameter region.
1269 This example is a single parameter varying across a continuous distribution and
1270 does not fully reflect the difficulties in the many-hundred multi-variate parameter

1271 distribution used within this analysis. However, it does give a conceptual idea of
1272 the importance of selecting the proposal function and associated step size.



Figure 4.3: Three MCMC chains, each with a stationary distribution equal to a Gaussian centered at 0 and width 1 (As indicated by the black dotted lines). All of the chains use a Gaussian proposal function but have different widths (or ‘step size σ ’). The top panel has $\sigma = 0.1$, middle panel has $\sigma = 0.5$ and the bottom panel has $\sigma = 5.0$.

1273 As discussed, step size tuning directly correlates to the average step accep-
1274 tance rate. If the step size is too small, many steps will be accepted but the
1275 chain moves slowly. If the opposite is true, many steps will be rejected as the
1276 chain proposes steps in the tails of the distribution. Discussion in [139] suggests
1277 that the ‘ideal’ acceptance rate of a high dimension MCMC chain should be

₁₂₇₈ approximately $\sim 25\%$. An “ideal” step size [139] of

$$\sigma = \frac{2.4}{N_p}, \quad (4.6)$$

₁₂₇₉ where N_p is the number of parameters included in the MCMC fit. However,
₁₂₈₀ the complex correlations between systematics mean that some parameters have
₁₂₈₁ to be hand-tuned and many efforts have been taken to select a set of parameter-
₁₂₈₂ by-parameter step sizes to approximately reach the ideal acceptance rate.

₁₂₈₃ Figure 4.4 highlights the likelihood as calculated by the fit in subsection 8.2.4
₁₂₈₄ as a function of the number of steps in each chain. In practice, many independent
₁₂₈₅ MCMC chains are run simultaneously to parallelise the task of performing the
₁₂₈₆ fit. This figure overlays the distribution found in each chain. As seen, the
₁₂₈₇ likelihood decreases from its initial value and converges towards a stationary
₁₂₈₈ distribution after $\sim 1 \times 10^5$ steps.

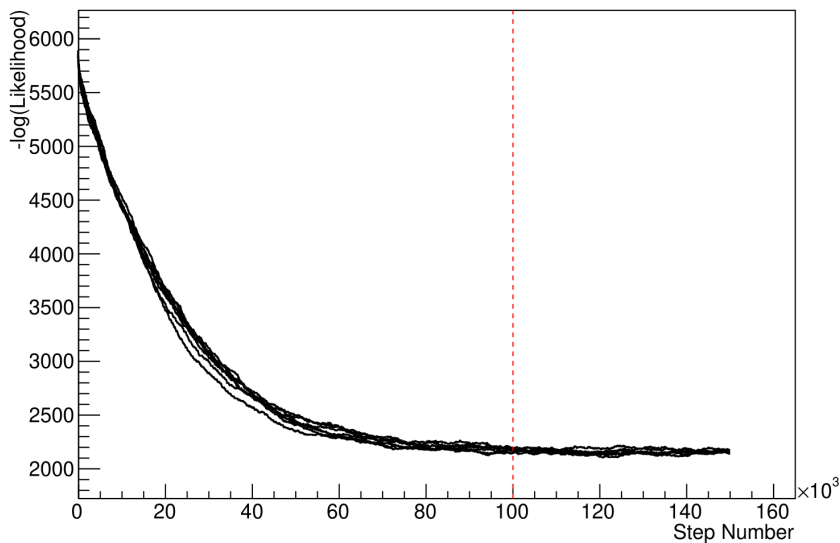


Figure 4.4: The log-likelihood from the fit detailed in subsection 8.2.4 as a function of the number of steps accumulated in each fit. Many independent MCMC chains were run in parallel and overlaid on this plot. The red line indicates the 1×10^5 step burn-in period after which the log-likelihood becomes stable.

₁₂₈₉ Multiple configurations of this analysis have been performed throughout this
₁₂₉₀ thesis where different samples or systematics have been used. For all of these con-
₁₂₉₁ figurations, it was found that a burnin period of 1×10^5 was sufficient in all cases.

1292 4.3 Understanding the MCMC Results

1293 The previous sections have described how to generate the posterior probability
1294 distribution using Bayesian MCMC techniques. However, this analysis focuses
1295 on oscillation parameter determination. The posterior distribution output from
1296 the chain is a high-dimension object, with as many dimensions as there are
1297 parameters included in the oscillation analysis. However, this multi-dimensional
1298 object is difficult to conceptualize so parameter estimations are often presented
1299 in one or two-dimensional projections of this probability distribution. To do
1300 this, marginalisation techniques are invoked.

1301 4.3.1 Marginalisation

1302 The output of the MCMC chain is a highly dimensional probability distribution
1303 which is very difficult to interpret. From the standpoint of an oscillation analysis
1304 experiment, the one or two-dimensional ‘projections’ of the oscillation parameters
1305 of interest are most relevant. Despite this, the best fit values and uncertainties on
1306 the oscillation parameters of interest should correctly encapsulate the correlations
1307 to the other systematic uncertainties (colloquially called ‘nuisance’ parameters).
1308 For this joint beam and atmospheric analysis, the oscillation parameters of
1309 interest are $\sin^2(\theta_{23})$, $\sin^2(\theta_{13})$, Δm_{32}^2 , and δ_{CP} . All other parameters (includ-
1310 ing the oscillation parameters this fit is insensitive to) are deemed nuisance
1311 parameters. To generate these projections, the posterior distribution is integrated
1312 over all nuisance parameters. This is called marginalisation. This technique
1313 also explains why it is acceptable to neglect the normalisation constant of the
1314 posterior distribution, which was discussed in section 4.1.

1315 A simple example of the marginalisation technique is to imagine the scenario
1316 where two coins are flipped. To determine the probability that the first coin
1317 returned a ‘head’, the exact result of the second coin flip is disregarded and
1318 simply integrated over. For the parameters of interest, $\vec{\theta}_i$, the marginalised

1319 posterior is calculated by integrating over the nuisance parameters, $\vec{\theta}_n$. In this
1320 case, Equation 4.2 becomes

$$P(\vec{\theta}_i|D) = \frac{\int P(D|\vec{\theta}_i, \vec{\theta}_n)P(\vec{\theta}_i, \vec{\theta}_n)d\vec{\theta}_n}{\int P(D|\vec{\theta})P(\vec{\theta})d\vec{\theta}}. \quad (4.7)$$

1321 Where $P(\vec{\theta}_i, \vec{\theta}_n)$ encodes the prior knowledge about the uncertainty and
1322 correlations between the parameters of interest and the nuisance parameters.
1323 In practice, this is simply taking the one or two-dimensional projection of the
1324 multi-dimensional probability distribution.

1325 While in principle an easy solution to a complex problem, correlations be-
1326 tween the interesting and nuisance parameters can bias the marginalised results.
1327 A similar effect is found when the parameters being marginalised over have
1328 non-Gaussian probability distributions. For example, Figure 4.5 highlights the
1329 marginalisation bias in the probability distribution found for a parameter when
1330 requiring a correlated parameter to have a positive parameter value. Due to
1331 the complex nature of the oscillation parameter fit presented in this thesis, there
1332 are correlations occurring between the oscillation parameters of interest and the
1333 other nuisance parameters included in the fit.



Figure 4.5: Left: The two-dimensional probability distribution for two correlated parameters x and y . The red distribution shows the two-dimensional probability distribution when $0 \leq x \leq 5$. Right: The marginalised probability distribution for the y parameter found when requiring the x to be bound between $-5 \leq x \leq 5$ and $0 \leq x \leq 5$ for the black and red distribution, respectively.

4.3.2 Parameter Estimation and Credible Intervals

The purpose of this analysis is to determine the best fit values for the oscillation parameters that the beam and atmospheric samples are sensitive to: $\sin^2(\theta_{23})$, $\sin^2(\theta_{13})$, Δm_{32}^2 , and δ_{CP} . The posterior probability density, taken from the output MCMC chain, is binned in these parameters. The parameter best-fit point is then taken to be the value that has the highest posterior probability. This is performed in both one and two-dimensional projections.

However, the single best-fit point in a given parameter is not of much use on its own. The uncertainty on the best-fit point must also be presented using credible intervals. The definition of the 1σ credible interval is that there is 68% belief that the parameter is within those bounds. For a more generalised definition, the credible interval is the region, R , of the posterior distribution that contains a specific fraction of the total probability, such that

$$\int_R P(\theta|D)d\theta = \alpha. \quad (4.8)$$

Where θ is the parameter being evaluated. This technique then calculates the $\alpha \times 100\%$ credible interval.

In practice, this analysis uses the highest posterior density (HPD) credible intervals which are calculated through the following method. First, the probability distribution is area-normalised such that it has an integrated area equal to 1.0. The bins of probability are then summed from the highest to lowest until the sum exceeds the 1σ level (0.68 in this example). This process is repeated for a range of credible intervals, notably the 1σ , 2σ and 3σ along with other levels where the critical values for each level can be found in [76]. This process can be repeated for the two-dimensional probability distributions by creating two-dimensional contours of credible intervals rather than a one-dimensional result.

1358 4.3.3 Bayesian Model Comparisons

1359 Due to the matter resonance, this analysis has some sensitivity to the mass
 1360 hierarchy of neutrino states (whether Δm_{32}^2 is positive or negative) and the
 1361 octant of $\sin^2(\theta_{23})$. The Bayesian approach utilised within this analysis gives an
 1362 intuitive method of model comparison by determining which hypothesis is most
 1363 favourable. Taking the ratio of Equation 4.3 for the two hypotheses of normal
 1364 hierarchy, NH , and inverted hierarchy, IH , gives

$$\frac{P(\vec{\theta}_{NH}|D)}{P(\vec{\theta}_{IH}|D)} = \frac{P(D|\vec{\theta}_{NH})}{P(D|\vec{\theta}_{IH})} \times \frac{P(\vec{\theta}_{NH})}{P(\vec{\theta}_{IH})}. \quad (4.9)$$

1365 The middle term defines the Bayes factor, $B(NH/IH)$, which is a data-driven
 1366 interpretation of how strong the data prefers one hierarchy to the other. For this
 1367 analysis, equal priors on both mass hierarchy hypotheses are chosen ($P(\vec{\theta}_{NH}) =$
 1368 $P(\vec{\theta}_{IH}) = 0.5$). In practice, the MCMC chain proposes a value of $|\Delta m_{32}^2|$ and
 1369 then applies a 50% probability that the value is sign flipped. Consequently,
 1370 the Bayes factor can be calculated from the ratio of the probability density in
 1371 either hypothesis. This equates to counting the number of steps taken in the
 1372 normal and inverted hierarchies and taking the ratio. The same approach can be
 1373 taken to compare the upper octant (UO) compared to the lower octant (LO)
 1374 hypothesis of $\sin^2(\theta_{23})$.

$\log_{10}(B_{AB})$	B_{AB}	Strength of Preference
< 0.0	< 1	No preference for hypothesis A (Supports hypothesis B)
0.0 – 0.5	1.0 – 3.16	Preference for hypothesis A is weak
0.5 – 1.0	3.16 – 10.0	Preference for hypothesis A is substantial
1.0 – 1.5	10.0 – 31.6	Preference for hypothesis A is strong
1.5 – 2.0	31.6 – 100.0	Preference for hypothesis A is very strong
> 2.0	> 100.0	Decisive preference for hypothesis A

Table 4.1: Jeffreys scale for strength of preference for two models A and B as a function of the calculated Bayes factor ($B_{AB} = B(A/B)$) between the two models [140]. The original scale is given in terms of $\log_{10}(B(A/B))$ but converted to linear scale for easy comparison throughout this thesis.

1375 Whilst the value of the Bayes factor should always be shown, the Jeffreys scale
 1376 [140] (highlighted in Table 4.1) gives an indication of the strength of preference

1377 for one model compared to the other. Other interpretations of the strength of
1378 preference of a model exist, e.g. the Kass and Raferty Scale [141].

1379 4.3.4 Comparison of MCMC Output to Expectation

1380 To ensure the fit is performing well, a best-fit spectrum is produced using the
1381 posterior probability distribution and compared with the data, allowing easy
1382 by-eye comparisons to be made. A simple method of doing this is to perform a
1383 comparison in the fitting parameters (For instance, the reconstructed neutrino
1384 energy and lepton direction for T2K far detector beam samples) of the spectra
1385 generated by the MCMC chain to ‘data’. This ‘data’ could be true data or some
1386 variation of Monte Carlo prediction. This allows easy comparison of the MCMC
1387 probability distribution to the data. To perform this, N steps from the post-burnin
1388 MCMC chain are randomly selected. From these, the Monte Carlo prediction
1389 at each step is generated by reweighting the model parameters to the values
1390 specified at that step. Due to the probability density being directly correlated
1391 with the density of steps in a certain region, parameter values close to the best
1392 fit value are most likely to be selected.

1393 In practice, for each bin of the fitting parameters has a probability distribution
1394 of event rates, with one entry per sampled MCMC step. This distribution is
1395 binned where the bin with the highest probability is selected as the mean and an
1396 error on the width of this probability distribution is calculated using the approach
1397 highlighted in subsection 4.3.2. Consequently, the best fit distribution in the fit
1398 parameter is not necessarily that which would be attained by reweighting the
1399 Monte Carlo prediction to the most probable parameter values.

1400 A similar study can be performed to illustrate the freedom of the model
1401 parameter space prior to the fit. This can be done by throwing parameter values
1402 from the prior uncertainty of each parameter.

5

1403

1404

1405

Simulation, Reconstruction, and Event Reduction

1406 As a crucial part of the oscillation analysis, an accurate prediction of the expected
1407 neutrino spectrum at the far detector is required. This includes modeling the
1408 flux generation, neutrino interactions, and detector effects. All of the simulation
1409 packages required to do this are briefly described in section 5.1. The reconstruc-
1410 tion of neutrino events in the far detector, including the `fitQun` algorithm, is
1411 documented in section 5.2. This also includes data quality checks of the SK-V
1412 data which the author performed for the T2K oscillation analysis presented at the
1413 Neutrino 2020 conference [75]. Finally, section 5.3 describes the steps taken in the
1414 SK detector to trigger on events of interest whilst removing the comparatively
1415 large rate of cosmic ray muon events.

1416 5.1 Simulation

1417 In order to generate a Monte Carlo prediction of the expected event rate at
1418 the far detector, all the processes in the beam and atmospheric fluxes, neutrino
1419 interaction, and detector need to be modeled.

1420 5.1.1 Neutrino Flux

1421 The beamline simulation consists of three distinct parts: the initial hadron
 1422 interaction modeled by FLUKA [142], the target station geometry and particle
 1423 tracking performed by JNUBEAM, [143, 144] and any hadronic re-interactions
 1424 simulated by GCALOR [145]. The primary hadronic interactions are $O(10)\text{GeV}$,
 1425 where FLUKA matches external cross-section data better than GCALOR [146].
 1426 However, FLUKA is not very adaptable so a small simulation is built to model
 1427 the interactions in the target and the output is then passed to JNUBEAM and
 1428 GCALOR for propagation. The hadronic interactions are tuned to data from the
 1429 NA61/SHINE [147–149] and HARP [150] experiments. The tuning is done by
 1430 reweighting the FLUKA and GCALOR predictions to match the external data
 1431 multiplicity and cross-section measurements, based on final state particle kine-
 1432 matics [146]. The culmination of this simulation package generates the predicted
 1433 flux for neutrino and antineutrino beam modes which are illustrated in Figure 3.7.

1434 The atmospheric neutrino flux is simulated by the HKKM model [51, 53]. The
 1435 primary cosmic ray flux is tuned to AMS [151] and BESS [152] data assuming
 1436 the US-standard atmosphere '76 [153] density profile and includes geomagnetic
 1437 field effects. The primary cosmic rays interact to generate pions and muons.
 1438 The interaction of these secondary particles to generate neutrinos is handled by
 1439 DPMJET-III [154] for energies above 32GeV and JAM [53, 155] for energies below
 1440 that value [49]. These hadronic interactions are tuned to BESS and L3 data [156,
 1441 157] using the same methodology as the tuning of the beamline simulation. The
 1442 energy and cosine zenith predictions of $\nu_e, \bar{\nu}_e, \nu_\mu, \bar{\nu}_\mu$ flux are given in Figure 2.3
 1443 and Figure 2.5, respectively. The flux is approximately symmetrical and peaked
 1444 around the horizon ($\cos(\theta_Z) = 0.0$). This is because horizontally-going pions
 1445 and kaons can travel further than their vertically-going counterparts resulting
 1446 in a larger probability of decaying to neutrinos. The symmetry is broken in
 1447 lower-energy neutrinos due to geomagnetic effects, which modify the track of the
 1448 primary cosmic rays. Updates to the HKKM model are currently ongoing [158].

5.1.2 Neutrino Interaction

Once a flux prediction has been made for all three detectors, NEUT 5.4.0 [159, 160] models the interactions of the neutrinos in the detectors. For the purposes of this analysis, quasi-elastic (QE), meson exchange (MEC), single meson production (PROD), coherent pion production (COH), and deep inelastic scattering (DIS) interactions are simulated. These interaction categories can be further broken down by whether they were propagated via a W^\pm boson in Charged Current (CC) interactions or via a Z^0 boson in Neutral Current (NC) interactions. CC interactions have a charged lepton in the final state, which can be flavour-tagged in reconstruction to determine the flavour of the neutrino. In contrast, NC interactions have a neutrino in the final state so no flavour information can be determined from the observables left in the detector after an interaction. This is the reason why neutrinos that interact through NC modes are assumed to not oscillate within this analysis. Both CC and NC interactions are modeled for all the above interaction categories, other than MEC interactions which are only modeled for CC events.

As illustrated in Figure 5.1, CCQE interactions dominate the cross-section of neutrino interactions around $E_\nu \sim 0.5\text{GeV}$. The NEUT implementation adopts the Llewellyn Smith [161] model for neutrino-nucleus interactions, where the nuclear ground state of any bound nucleons (neutrino-oxygen interactions) is approximated by a spectral-function [162] model that simulates the effects of Fermi momentum and Pauli blocking. The cross-section of QE interactions is controlled by vector and axial-vector form factors parameterised by the BBBA05 [163] model and a dipole form factor with $M_A^{QE} = 1.21\text{GeV}$ fit to external data [164], respectively. NEUT implements the Valencia [165] model to simulate MEC events, where two nucleons and two holes in the nuclear target are produced (often called 2p2h interactions).

For neutrinos of energy $O(1)\text{GeV}$, PROD interactions become dominant. These predominantly produce charged and neutral pions although γ , kaon,



Figure 5.1: The NEUT prediction of the ν_μ -H₂O cross-section overlaid on the T2K ν_μ flux. The charged current (black, solid) and neutral current (black, dashed) inclusive, charged current quasi-elastic (blue, solid), charged current 2p2h (blue, dashed), charged current single pion production (pink), and charged current multi- π and DIS (Purple) cross-sections are illustrated. Figure taken from [159].

and η production is also considered. To simulate these interactions, the Berger-Sehgal [166] model is implemented within NEUT. It simulates the excitation of a nucleon from a neutrino interaction, production of an intermediate baryon, and the subsequent decay to a single meson or γ . Pions can also be produced through COH interactions, which occur when the incoming neutrino interacts with the entire oxygen nucleus leaving a single pion outside of the nucleus. NEUT utilises the Berger-Sehgal [167] model to simulate these COH interactions.

DIS and multi- π producing interactions become the most dominant for energies $> O(5)$ GeV. PYTHIA [168] is used to simulate any interaction with invariant mass $W > 2\text{GeV}/c^2$, which produces at least one meson. For any interaction which produces at least two mesons but has $W < 2\text{GeV}/c^2$, the

¹⁴⁸⁹ Bronner model is used [169]. Both of these models use Parton distribution
¹⁴⁹⁰ functions based on the Bodek-Yang model [170–172].

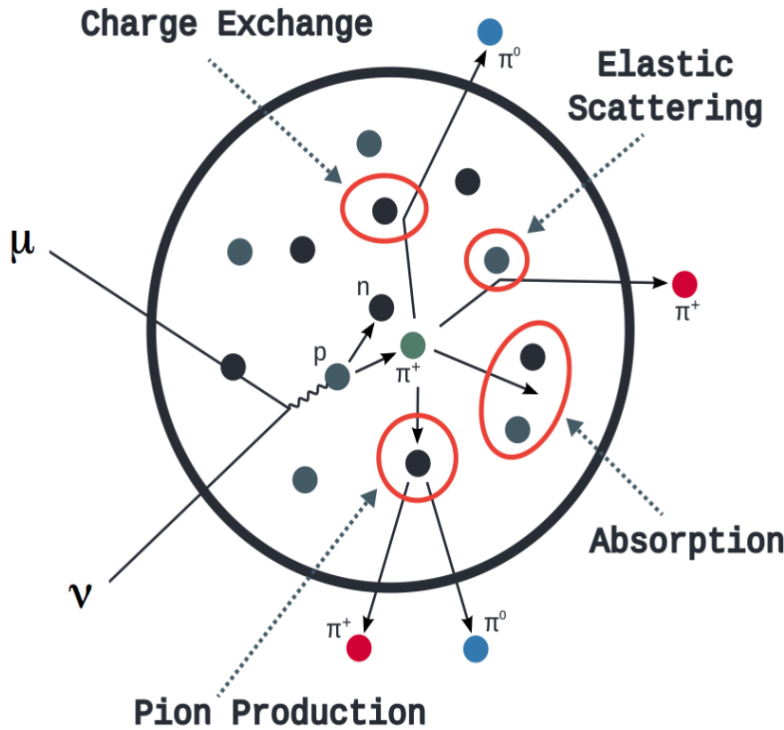


Figure 5.2: Illustration of the various processes which a pion can undergo before exiting the nucleus. Taken from [173].

¹⁴⁹¹ Any pion that is produced within the nucleus can re-interact through final
¹⁴⁹² state interactions before it exits, as illustrated by the scattering, absorption,
¹⁴⁹³ production, and exchange interactions in Figure 5.2. These re-interactions alter
¹⁴⁹⁴ the observable particles within the detector. For instance, if the charged pion
¹⁴⁹⁵ from a CC PROD interaction is absorbed, the observables would mimic a CC QE
¹⁴⁹⁶ interaction. To simulate these effects, NEUT uses a semi-classical intranuclear
¹⁴⁹⁷ cascade model [159]. This cascade functions by stepping the pion through the
¹⁴⁹⁸ nucleus in fixed-length steps equivalent to $dx = R_N/100$, where R_N is the radius
¹⁴⁹⁹ of the nucleus. At each step, the simulation allows the pion to interact through
¹⁵⁰⁰ scattering, charged exchange, absorption, or production with an interaction-
¹⁵⁰¹ dependent probability calculated from a fit to external data [174]. This cascade
¹⁵⁰² continues until the pion is absorbed or exits the nucleus.

5.1.3 Detector

Once the final state particle kinematics have been determined by NEUT, they are passed into the detector simulation. The near detectors, ND280 and INGRID, are simulated using a GEANT4 package [43, 175] to simulate the detector geometry, particle tracking, and energy deposition. The response of the detectors is simulated using the elecSim package [43].

The far detector simulation is based upon the original Kamiokande experiment software which uses the GEANT3-based SKDETSIM [43, 176] package. This simulates the interactions of particles in the water as well as Cherenkov light production. The water quality and PMT calibration measurements detailed in subsection 3.1.2 are also used within this simulation to make accurate predictions of the detector response.

Any event which generates optical photons that occurs in SK will be observed by the PMT array, where each PMT records the time and accumulated charge. This recorded information is shown in event displays similar to those illustrated in Figure 5.3 for simulated Monte Carlo events. To be useful for physics analyses, this series of PMT hit information needs to be reconstructed to determine the number and identity of particles and their kinematics (or track parameters): four-vertex, direction, and momentum. The reconstruction uses the fact that the charge and timing distribution of photons generated by a particular particle in an event is dependent upon its initial kinematics. Electron and muon rings are distinguished by their “fuzziness”. Muons are heavier and less affected by scattering or showering meaning they typically produce “crisp” rings. Electrons are more likely to interact via electromagnetic showering or scattering which results in larger variations of their direction from the initial direction. Consequently, electrons typically produce “fuzzier” rings compared to muons.



Figure 5.3: Event displays from Monte Carlo simulation at Super Kamiokande illustrating the “crisp” ring from a muon and the typically “fuzzy” electron ring. Each pixel represents a PMT and the color scheme denotes the accumulated charge deposited on that PMT. Figures taken from [177].

5.2 Event Reconstruction at SK

For the purposes of this analysis, the `fitQun` reconstruction algorithm [178] is utilised. Its core function is to compare a prediction of the accumulated charged and timing distribution from each PMT, generated for a particular particle identity and track parameters, to that observed in the neutrino event. It determines the preferred values by maximising a likelihood function (or minimising a log-likelihood function) which includes information from PMTs which were hit and those that were not hit. The `fitQun` algorithm is based on the key concepts of the MiniBooNE reconstruction algorithm [179].

The `fitQun` algorithm improves upon the previous `APFit` algorithm [180] which has been used for many previous SK analyses. `APFit` fits the vertex from timing information and then fits the direction of the particle from PMT hits within a 43 deg Cherenkov cone (assuming an ultra-relativistic particle) using a fitting estimator. A Hough transformation is used to find the radius of a ring (related to the momentum through Equation 3.2) as well as the number of rings contained within the event. The analysis presented here uses the `fitQun` algorithm as it improves both the accuracy of the fit parameters and the rejection of neutral

1546 current π^0 events as compared to APFit [181, 182].

1547 Any event in SK can consist of prompt (or primary) and decay (or secondary)
1548 particles. For example, a charged current muon neutrino interaction can gen-
1549 erate two particles that have the potential of generating Cherenkov photons
1550 (assuming the proton is below the Cherenkov threshold): the prompt muon,
1551 and the secondary decay-electron from the muon, approximately $2\mu\text{s}$ later. To
1552 reconstruct all particles within an event, it is divided into time clusters which are
1553 called “subevents”. Subevents after the primary subevent are considered to
1554 be decay electrons.

1555 The main steps of the `fitQun` reconstruction algorithm are:

- 1556 • **Vertex pre-fitting:** An estimate of the vertex is made using a goodness-of-fit
1557 metric based on PMT hit times
- 1558 • **Peak finding:** The initial time of each subevent is determined by clustering
1559 events by time residuals
- 1560 • **Single-ring fits:** Given the pre-fit vertex and estimated time of interaction,
1561 a maximum likelihood technique searches for a single particle generating
1562 light. Electron, muon, charged pion, and proton hypotheses are considered
- 1563 • **Multi-ring fits:** Seeded from the single-ring fits, hypotheses with multiple
1564 light-producing particles are considered using the same maximum likeli-
1565 hood technique. Electron-like or charged pion-like rings are added until
1566 the likelihood stops improving

1567 To find all the subevents in an event, a vertex goodness metric is calculated
1568 for some vertex position \vec{x} and time t ,

$$G(\vec{x}, t) = \sum_i^{\text{hit PMTs}} \exp \left(-\frac{1}{2} \left(\frac{T_{Res}^i(\vec{x}, t)}{\sigma} \right)^2 \right), \quad (5.1)$$

1569 where

$$T_{Res}^i(\vec{x}, t) = t^i - t - |R_{PMT}^i - \vec{x}| / c_n, \quad (5.2)$$

1570 is the residual hit time. It is the difference in time between the PMT hit time
 1571 t^i , of the i^{th} PMT, and the expected time of the PMT hit if the photon was at
 1572 the vertex. R_{PMT}^i is the position of the i^{th} PMT, c_n is the speed of light in water
 1573 and $\sigma = 4\text{ns}$ which is comparable to the time resolution of the PMT. When the
 1574 proposed fit values of time and vertex are close to the true values, $T_{Res}^i(\vec{x}, t)$ tends
 1575 to zero resulting in subevents appearing as spikes in the goodness metric. The
 1576 proposed fit vertex and time are grid-scanned, and the values which maximise
 1577 the goodness metric are selected as the “pre-fit vertex”. Whilst this predicts a
 1578 vertex for use in the clustering algorithm, the final vertex is fit using the higher-
 1579 precision maximum likelihood method described below.

1580 Once the pre-fit vertex has been determined, the goodness metric is scanned as
 1581 a function of t to determine the number of subevents. A peak-finding algorithm
 1582 is then used on the goodness metric, requiring the goodness metric to exceed
 1583 some threshold and drop below a reduced threshold before any subsequent
 1584 additional peaks are considered. The thresholds are set such that the rate of
 1585 false peak finding is minimised while still attaining good data to Monte Carlo
 1586 agreement. To improve performance, the pre-fit vertex for each delayed subevent
 1587 is re-calculated after PMT hits from the previous subevent are masked. This
 1588 improves the decay-electron tagging performance. Once all subevents have
 1589 been determined, the time window around each subevent is then defined by the
 1590 earliest and latest time which satisfies $-180 < T_{Res}^i < 800\text{ns}$. The subevents and
 1591 associated time windows are then used as seeds for further reconstruction.

1592 For a given subevent, the `fitQun` algorithm constructs a likelihood based on
 1593 the accumulated charge q_i and time information t_i from the i^{th} PMT,

$$L(\Gamma, \vec{\theta}) = \prod_j^{\text{unhit}} P_j(\text{unhit}|\Gamma, \vec{\theta}) \prod_i^{\text{hit}} \{1 - P_i(\text{unhit}|\Gamma, \vec{\theta})\} f_q(q_i|\Gamma, \vec{\theta}) f_t(t_i|\Gamma, \vec{\theta}). \quad (5.3)$$

1594 Where $\vec{\theta}$ defines the track parameters; vertex position, direction vector and
 1595 momenta, and Γ represents the particle hypothesis. $P_i(\text{unhit}|\Gamma, \vec{\theta})$ is the proba-
 1596 bility of the i^{th} tube to not register a hit given the track parameters and particle
 1597 hypothesis. The charge likelihood, $f_q(q_i|\Gamma, \vec{\theta})$, and time likelihood, $f_t(t_i|\Gamma, \vec{\theta})$,
 1598 represents the probability density function of observing charge q_i and time t_i on
 1599 the i^{th} PMT given the specified track parameters and particle hypothesis.

1600 The predicted charge is calculated based on contributions from both the
 1601 direct light and the scattered light. The direct light contribution is determined
 1602 based on the integration of the Cherenkov photon profile along the track. PMT
 1603 angular acceptance, water quality, and calibration measurements discussed in
 1604 subsection 3.1.2 are included to accurately predict the charge probability density
 1605 at each PMT. The scattered and reflected light is calculated in a similar way,
 1606 although it includes a scattering function that depends on the vertex of the
 1607 particle and the position of the PMT. The charge likelihood is calculated by
 1608 comparing the prediction to the observed charge in the PMT which is tuned
 1609 to the PMT simulation.

1610 The time likelihood is approximated to depend on the vertex \vec{x} , direction \vec{d} ,
 1611 and time t of the track as well as the particle hypothesis. The expected time
 1612 for PMT hits is calculated by assuming unscattered photons being emitted from
 1613 the midpoint of the track, S_{mid} ,

$$t_{\text{exp}}^i = t + S_{\text{mid}}/c + |R_{\text{PMT}}^i - \vec{x} - S_{\text{mid}}\vec{d}|/c_n, \quad (5.4)$$

1614 where c is the speed of light in a vacuum. The time likelihood is then expressed
 1615 in terms of the residual difference between the PMT hit time and the expected
 1616 hit time, $t_{\text{Res}}^i = t^i - t_{\text{exp}}^i$. The particle hypothesis and momentum also affect the
 1617 Cherenkov photon distribution. These parameters modify the shape of the time
 1618 likelihood density since in reality not all photons are emitted at the midpoint of
 1619 the track. As with the charge likelihood, the contributions from both the direct
 1620 and scattered light to the time likelihood density are calculated separately, which
 1621 are both calculated from particle gun Monte Carlo studies.

The track parameters and particle identity which maximise $L(\Gamma, \vec{\theta})$ are defined as the best-fit parameters. In practice MINUIT [183] is used to minimise the value of $-\ln L(\Gamma, \vec{\theta})$. The `fitQun` algorithm considers an electron-like, muon-like, and charged pion-like hypothesis for events with a single final state particle, denoted “single-ring events”. The particle’s identity is determined by taking the ratio of the likelihood of each of the hypotheses. For instance, electrons and muons are distinguished by considering the value of $\ln(L(e, \vec{\theta}_e)/L(\mu, \vec{\theta}_\mu))$ in comparison to the reconstructed momentum of the electron hypothesis, as illustrated by Figure 5.4. The coefficients of the discriminator between electron-like and muon-like events are determined from Monte Carlo studies [178]. Similar distributions exist for distinguishing electron-like events from π^0 -like events, and muon-like events from pion-like events. The cuts are defined as,

$$\begin{aligned} \text{Electron/Muon} : & \ln(L_e/L_\mu) > 0.2 \times p_e^{rec} [\text{MeV}], \\ \text{Electron}/\pi^0 : & \ln(L_e/L_{\pi^0}) < 175 - 0.875 \times m_{\gamma\gamma} [\text{MeV}], \\ \text{Muon/Pion} : & \ln(L_\mu/L_{\pi^\pm}) < 0.15 \times p_\mu^{rec} [\text{MeV}], \end{aligned} \quad (5.5)$$

as taken from [184], where p_e^{rec} and p_μ^{rec} are the reconstructed momentum of the single-ring electron and muon fits, respectively. $m_{\gamma\gamma}$ represents the reconstructed invariant mass of the two photons emitted from π^0 decay. Typically, the distance between a particular entry in these two-dimensional distributions and the cut-line is termed the PID parameter and is illustrated in Figure 5.5.

The `fitQun` algorithm also considers a π^0 hypothesis. To do this, it performs a fit looking for two standard electron-hypothesis tracks which point to the same four-vertex. This assumes the electron tracks are generated from photon-conversion so the electron tracks actually appear offset from the proposed π^0 vertex. For these fits, the conversion length, direction, and momentum of each photon are also considered as track parameters which are then fit in the same methodology as the standard single-ring hypotheses.

Whilst lower energy events are predominantly single-ring events, higher energy neutrino events can generate final states with multiple particles which

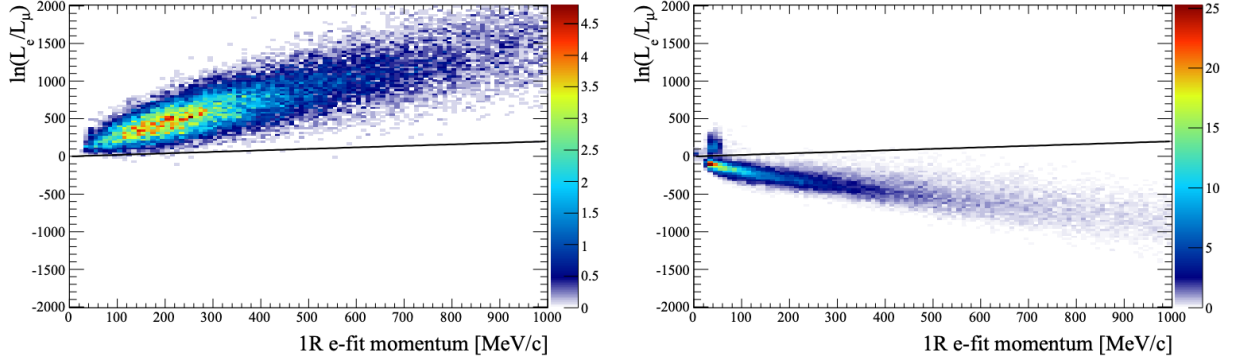


Figure 5.4: The difference of the electron-like and muon-like log-likelihood compared to the reconstructed single-ring fit momentum for atmospheric ν_e (left) and ν_μ (right) samples. The black line represents the cut used to discriminate electron-like and muon-like events, with coefficients obtained from Monte Carlo studies. Figures from [178].

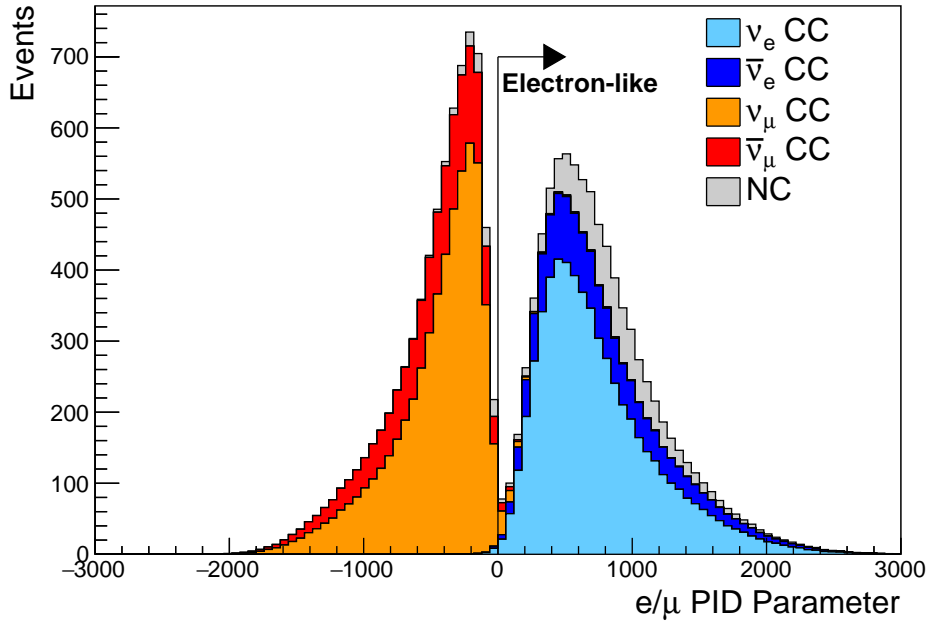


Figure 5.5: The electron/muon PID separation parameter for all sub-GeV single-ring events in SK-IV. The charged current (CC) component is broken down in four flavours of neutrino (ν_μ , $\bar{\nu}_\mu$, ν_e and $\bar{\nu}_e$). Events with positive values of the parameter are determined to be electron-like.

1648 generate Cherenkov photons. These “multi-ring” hypotheses are also considered
 1649 in the `fitQun` algorithm. When calculating the charge likelihood density, the
 1650 predicted charge associated with each ring is calculated separately and then
 1651 summed to calculate the total accumulated charge on each PMT. Similarly, the
 1652 time likelihood for the multi-ring hypothesis is calculated assuming each ring

is independent. Each track is time-ordered based on the time of flight from the center of the track to the PMT and the direct light from any ring incident on the PMT is assumed to arrive before any scattered light. To reduce computational resource usage, the multi-ring fits only consider electron-like and charged pion-like rings as the pion fit can be used as a proxy for a muon fit due to their similar mass. Due to the pions ability to interact through the strong force, they are more likely to hard-scatter. That means a single charged pion can produce multiple rings in different directions. There is an additional freedom, the fraction of kinetic energy lost in a single ring segment, which is added into the `fitQun` pion fit to cover this difference. Pion and muon rings are indistinguishable when this fraction tends to unity.

Multi-ring fits proceed by proposing another ring to the previous fit and then fitting the parameters in the method described above. Typically, multi-ring fits have the largest likelihood because of the additional degrees of freedom introduced. A likelihood value is calculated for the n -ring and $(n + 1)$ -ring hypotheses, where the additional ring is only included if the likelihood value is above 9.35, based on Monte Carlo studies in [185].

5.2.1 Validation of Reconstruction in SK-V

Understanding how the modelling of the detector conditions and stability effects the reconstruction is critical for ensuring accurate measurements. It is important to note that the detector systematics used in the 2020 T2K-only [75] oscillation analysis are determined using data-to-Monte Carlo comparisons of the SK-IV data [186]. Due to tank-open maintenance occurring between SK-IV and SK-V, the dark rate of each PMT was observed to increase in SK-V due to light exposure for a significant time during the repairs. This increase can be seen in Figure 5.6. Run-10 of the T2K experiment was conducted in the SK-V period, so the consistency of SK-IV and SK-V data needs to be studied to determine whether the SK-IV-defined systematics can be applied to the run-10 data. Consequently, the author of this thesis assessed the quality of `fitQun` event reconstruction for SK-V data.

This comparison study was performed using the stopping muon data set for both the SK-IV and SK-V periods. This data sample is used due to the high rate of interactions ($O(200)$ events per hour) as well as having similar energies to muons from CCQE ν_μ interactions from beam interactions. The rate of cosmic muons does depend on the solar activity cycle [187] but has been neglected in this comparison study. This is because the shape of the distributions is most important for the purposes of being compared to the detector systematics. The SK-IV and SK-V data samples consist of 2398.42 and 626.719 hours of data which equates to 686k and 192k events respectively. These samples do not correspond to the full data sets of either period but do contain enough events to be systematics limited rather than statistics limited.

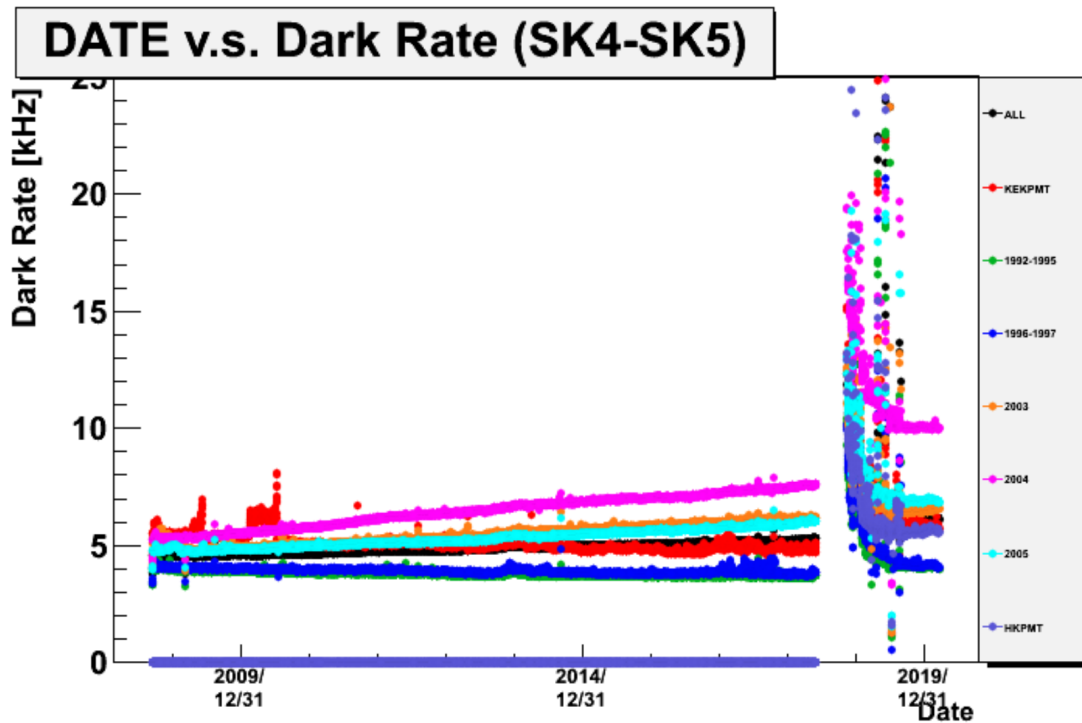


Figure 5.6: The variation of the measured dark rate as a function of date, broken down by PMT type. The SK-IV and SK-V periods span September 2008 to May 2018 and January 2019 to July 2020, respectively. The break in measurement in 2018 corresponds to the period of tank repair and refurbishment. Figure adapted from [186].

The predicted charge calculated in the `fitQun` algorithm includes a contribution from the photoelectron emission due to dark noise. Therefore, the increase

in the SK-V dark rate needs to be accounted for. In practice, the average dark rate in each SK period is calculated and used as an input in the reconstruction. This is calculated by averaging the dark rate per run for each period separately, using the calibration measurements detailed in subsection 3.1.2. The average dark rate from SK-IV and SK-V were found to be 4.57kHz and 6.30kHz, respectively. The charges associated with the muon and decay electron subevents are illustrated in Figure 5.7. The photoelectron emission from dark noise is more significant for events that have lower energy. This is because this contribution becomes more comparable to the number of photoelectrons emitted from incident photons in lower-energy events. This behaviour is observed in the data, where the charge deposited by the muon subevent is mostly unaffected by the increase in dark rate, whilst the charge associated with the decay-electron is clearly affected.

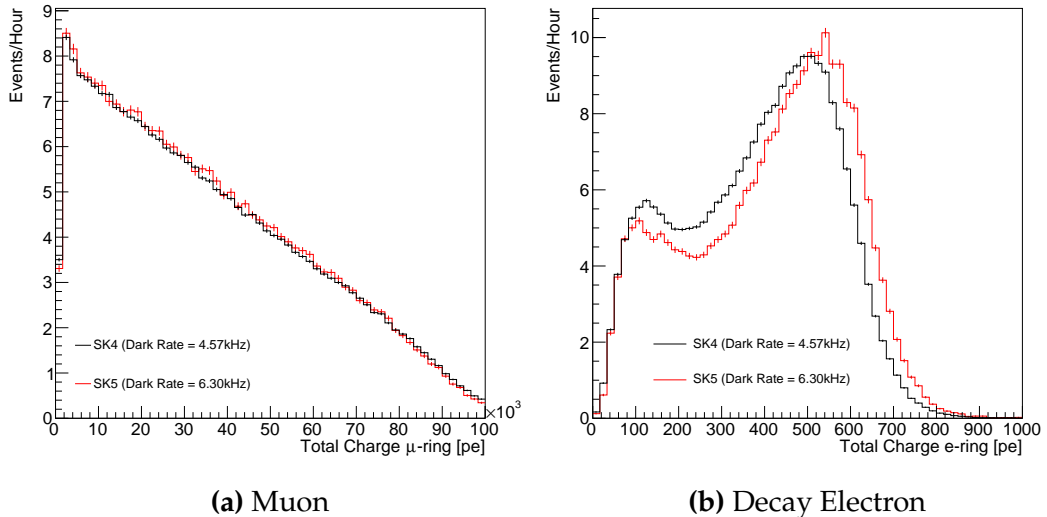


Figure 5.7: Comparison of the measured raw charge deposited per event from the stopping muon data samples between SK-IV (Blue) and SK-V (Red), split by the primary muon subevent (left) and the associated decay electron subevent (right).

The energy scale systematic is estimated from data-to-Monte Carlo differences in the stopping muon sample in [188] and found to be 2.1%. To determine the consistency of SK-IV and SK-V with respect to the energy scale systematic, the muon momentum distribution is compared between the two SK periods. As the total number of Cherenkov photons is integrated across the track length,

₁₇₁₂ the reconstructed momentum divided by track length (or range) is compared
₁₇₁₃ between SK-IV and SK-V as illustrated in Figure 5.8.

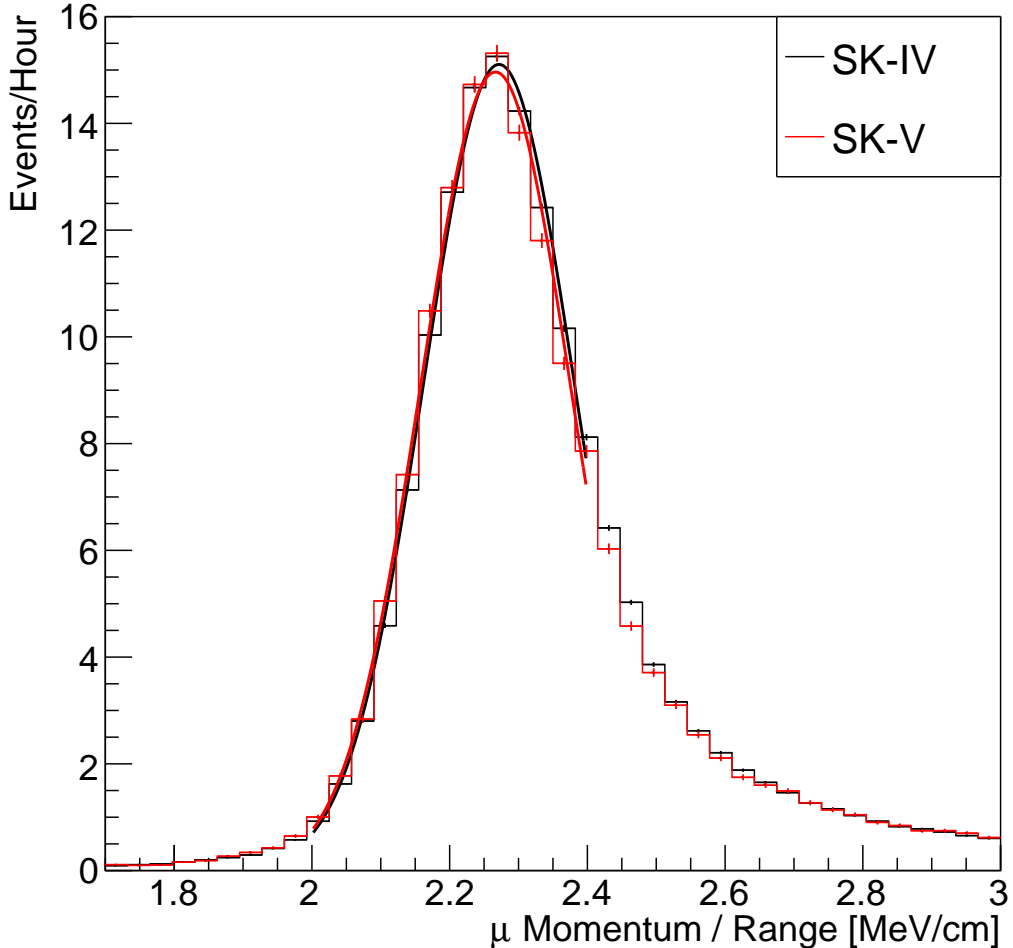


Figure 5.8: The distribution of the reconstructed momentum from the muon ring divided by the distance between the reconstructed muon and decay electron vertices as found in the stopping muon data sets of SK-IV (Black) and SK-IV (Red). Only events with one tagged decay electron are considered. A Gaussian fit is considered in the range [2.0, 2.4] MeV/cm and illustrated as the solid curve.

₁₇₁₄ The consistency between these muon distributions has been computed in two
₁₇₁₅ ways. Firstly, a Gaussian is fit to the peak of each distribution separately, whose
₁₇₁₆ mean is found to be (2.272 ± 0.003) MeV/cm and (2.267 ± 0.006) MeV/cm for SK-
₁₇₁₇ IV and SK-V respectively. The ratio of these is equal to 1.002 ± 0.003 . The means of
₁₇₁₈ the Gaussian fits are consistent with the expected stopping power of a minimum

ionising muon for a target material (water) with $Z/A \sim 0.5$ [189]. The second consistency check is performed by introducing a nuisance parameter, α , which modifies the SK-V distribution. The value of α which minimises the χ^2 value between the SK-IV and SK-V is determined by scanning across a range of values. This is repeated by applying the nuisance parameter as both a multiplicative factor and an additive shift. The χ^2 distributions for different values of α is illustrated in Figure 5.9. The values which minimise the χ^2 are found to be 0.0052 and 1.0024 for the additive and multiplicative implementations, respectively. No evidence of shifts larger than the 2.1% uncertainty on the energy scale systematic has been found in the reconstructed momentum distribution of SK-IV and SK-V.

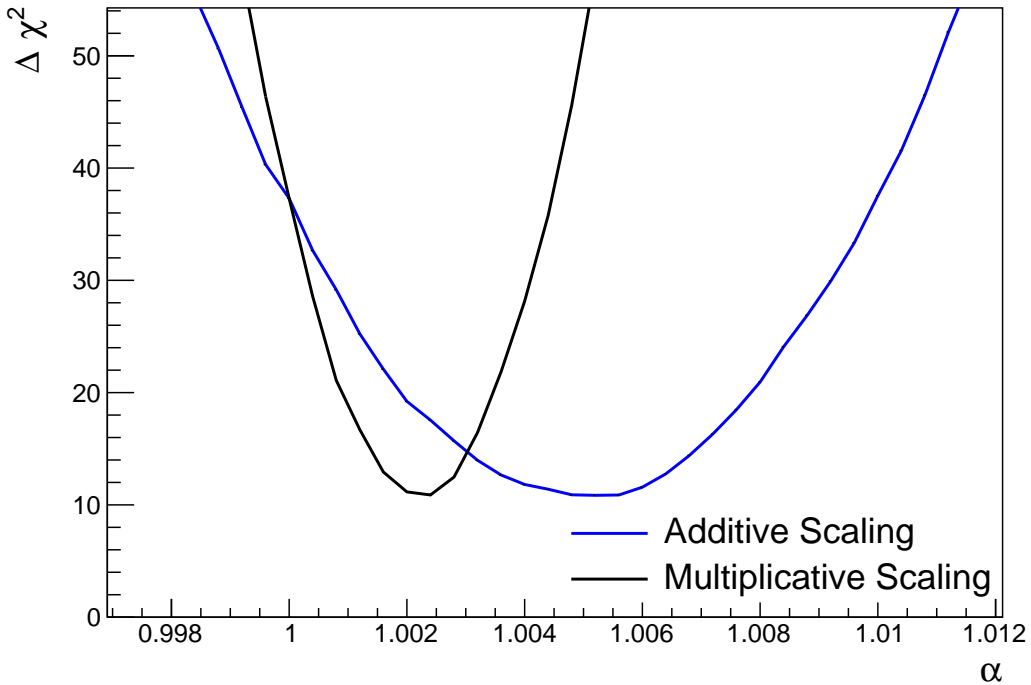


Figure 5.9: The χ^2 difference between the SK-IV and SK-V reconstructed muon momentum divided by range when the SK-V is modified by the scaling parameter α . Both additive (Blue) and multiplicative (Black) scaling factors have been considered. In practice, the additive scaling factor actually uses the value of $(\alpha - 1.0)$ but is illustrated like this so the results can be shown on the same axis range.

1729 5.3 Event Reduction at SK

1730 In normal data-taking operations, the SK detector observes many background
1731 events alongside the beam and atmospheric neutrino signal events of physics
1732 interest for this thesis. Cosmic ray muons and flasher events, which are the spon-
1733 taneous discharge of a given PMT, contribute the largest amount of background
1734 events in the energy range relevant to this thesis. Therefore the data recorded
1735 is reduced with the aim of removing these background events. The reduction
1736 process is detailed in [55, 88] and briefly summarised below.

1737 Atmospheric neutrino events observed in the SK detector are categorised
1738 into three different types of samples: fully contained (FC), partially contained
1739 (PC) and up-going muon (Up- μ), using PMT hit signatures in the inner and
1740 outer detector (ID and OD, respectively). To identify FC neutrino events, it is
1741 required that the neutrino interacts inside the fiducial volume of the ID and that
1742 no significant OD activity is observed. For this analysis, an event is defined to be
1743 in the fiducial volume provided the event vertex is at least 0.5m away from the
1744 ID walls. PC events have the same ID requirements but can have a larger signal
1745 present inside the OD. Typically, only high energy muons from ν_μ interactions can
1746 penetrate the ID wall. The Up- μ sample contains events where muons are created
1747 from neutrino interactions in the OD water or rock below the tank. They then
1748 propagate upwards through the detector. Downward-going muons generated
1749 from neutrino interactions above the tank are neglected because of the difficulty
1750 in separating their signature from the cosmic muon shower background. The
1751 sample categories are visually depicted in Figure 5.10.

1752 Based on the event characteristics, as defined by the `fitQun` event reconstruc-
1753 tion software, the FC events are categorised by

- 1754 • **Visible Energy:** equal to the sum of the reconstructed kinetic energy of
1755 particles above the Cerenkov threshold for all rings present in the event.
1756 The purpose is to separate events into sub-GeV and multi-GeV categories.

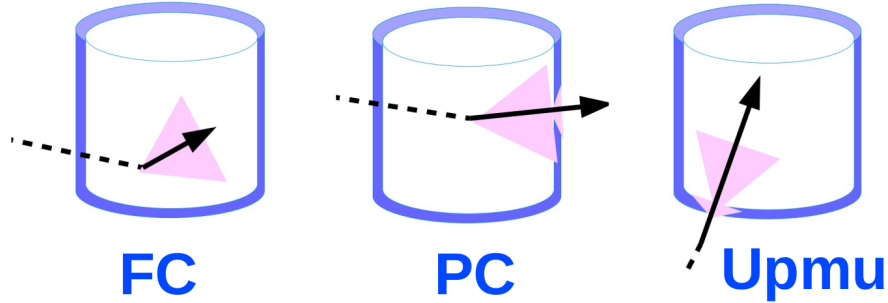


Figure 5.10: A depiction of the topology patterns for fully-contained (FC), partially-contained (PC), and up-going muon ($\text{Up-}\mu$) samples included in this analysis.

- **Number of observed Cerenkov rings.** The purpose is to separate single-ring and multi-ring events, where single-ring events predominantly consist of quasi-elastic interactions and multi-ring events are typically resonant pion production or deep inelastic scattering events.
- **Particle identification parameter of the most energetic ring:** A value determined from the maximum likelihood value based on `fitQun`'s electron, muon, or pion hypothesis. The purpose is to separate electron-like and muon-like events.
- **Number of decay electrons:** The purpose is to separate quasi-elastic events (which have one decay electron emitted from the muon decay) and resonant pion production events (which have two decay electrons emitted from the muon and pion).

The PC and Up- μ categories are broken down into “through-going” and “stopping” samples depending on whether the muon leaves the detector. This is because the PC stopping events deposit the entire energy of the interaction into the detector, resulting in better reconstruction. The energy of events that exit the detector has to be estimated, with a typically worse resolution, which introduces much larger systematic uncertainties. Through-going Up- μ samples are further broken down by whether any hadronic showering was observed in the event which typically indicates DIS interactions. The expected neutrino energy for the different categories is given in Figure 5.11. FC sub-GeV and multi-GeV events

¹⁷⁷⁸ peak around 0.7GeV and 3GeV respectively, with slightly different peak energies
¹⁷⁷⁹ for ν_e and ν_μ oscillation channels. PC and Up- μ are almost entirely comprised
¹⁷⁸⁰ of ν_μ events and peak around 7GeV and 100GeV, respectively.

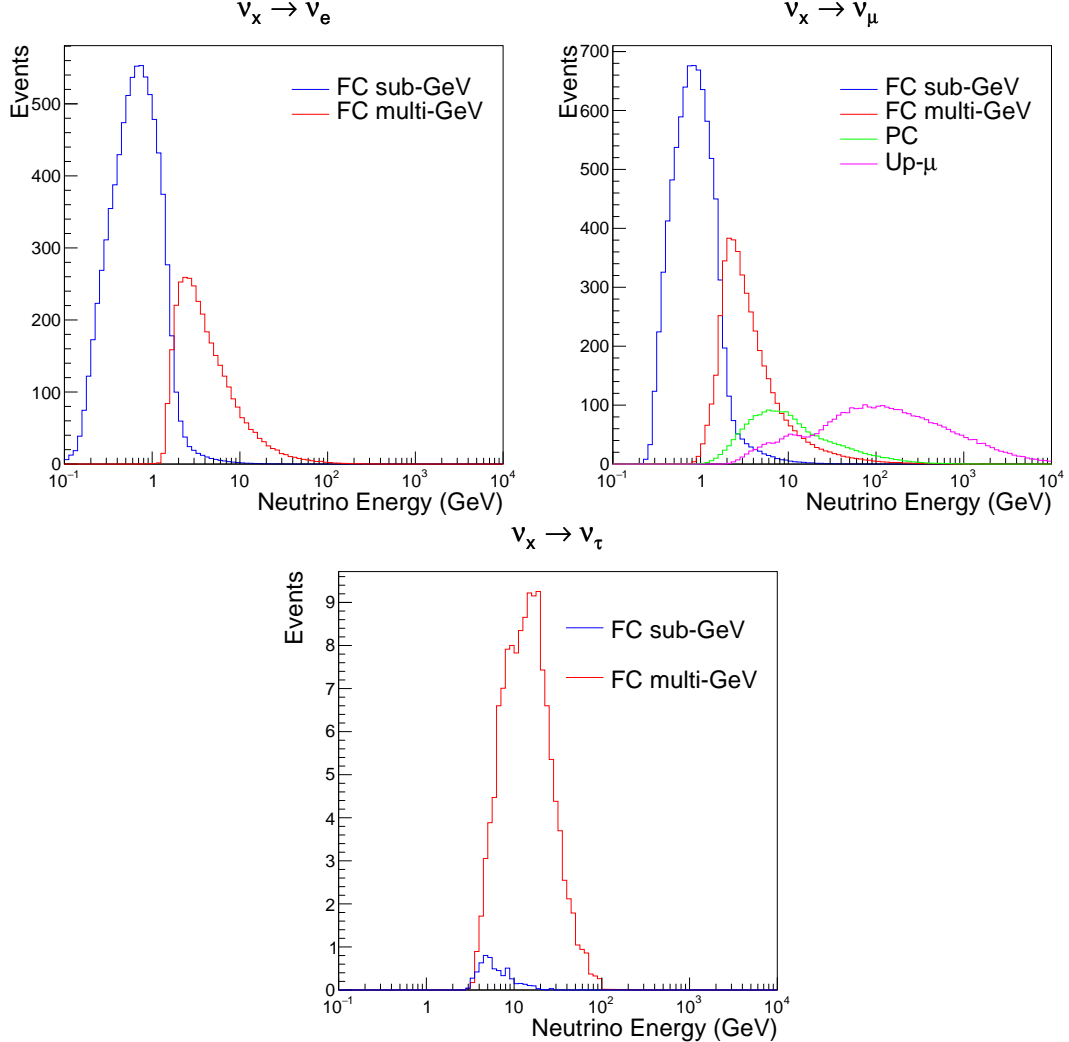


Figure 5.11: The predicted neutrino flux of the fully contained (FC) sub-GeV and multi-GeV, partially contained (PC), and upward-going muon (Up- μ) events. The prediction is broken down by the $\nu_x \rightarrow \nu_e$ prediction (top left), $\nu_x \rightarrow \nu_\mu$ prediction (top right) and $\nu_x \rightarrow \nu_\tau$ prediction (bottom). ν_x represents the flavours of neutrinos produced in the cosmic ray showers (electron and muon). Asimov A oscillation parameters are assumed (given in Table 2.2).

¹⁷⁸¹ The first two steps in the FC reconstruction remove the majority of cosmic
¹⁷⁸² ray muons by requiring a significant amount of ID activity compared to that
¹⁷⁸³ measured in the OD. Events that pass this cut are typically very high momentum
¹⁷⁸⁴ muons or events that leave very little activity in the OD. Consequently, a third

reduction step is then applied to select cosmic-ray muons that pass the initial reduction step. A purpose-built cosmic muon fitter is used to determine the entrance (or exit) position of the muon and a cut is applied to OD activity contained within 8m of this position. Flasher events are removed in the fourth reduction step which is based on the close proximity of PMT hits surrounding the PMT producing the flash. Events that pass all these reduction steps are reconstructed with the APFit algorithm. The fifth step of the reduction uses information from the more precise fitter to repeat the previous two steps with tighter cuts. Muons below the Cherenkov threshold can not generate optical photons in the ID but the associated decay electron can due to its lower mass. These are the types of events targeted in the fifth reduction step. The final cuts require the event vertex to be within the fiducial volume (0.5m from the wall although the nominal distance is 2.0m), visible energy $E_{vis} > 30\text{MeV}$ and fewer than 16 hits within the higher energy OD cluster. The culmination of the fully contained reduction results in 8.09 events/day in the nominal fiducial volume [84]. The uncertainty in the reconstruction is calculated by comparing Monte Carlo prediction to data. The largest discrepancy is found to be 1.3% in the fourth reduction step.

The PC and Up- μ events are processed through their own reduction processes detailed in [55]. Both of these samples are reconstructed with the APFit algorithm rather than `fiTQun`. This is because the efficiency of reconstructing events that leave the detector has not been sufficiently studied for reliable systematic uncertainties with `fiTQun`. The PC and Up- μ samples acquire events at approximately 0.66 and 1.44 events/day.

Beam neutrinos events undergo the same reduction steps as FC events and are then subject to further cuts [190]. The GPS system that links the timing between the beam facility and SK needs to be operating correctly and there should be no activity within the detector in the previous $100\mu\text{s}$ before the trigger. The events then need to triggered between $-2\mu\text{s}$ and $10\mu\text{s}$ of the expected spill timing.

1814 The beam neutrino samples are not split by visible energy since their energy
 1815 range is smaller than the atmospheric neutrino events. Following the T2K
 1816 analysis in [75], only single-ring beam neutrino events are considered. Similar to
 1817 atmospheric event selection, the number of decay electrons is used as a proxy for
 1818 distinguishing CCQE and CCRES events. The expected neutrino energy, broken
 1819 down by the number of decay electrons, is given in Figure 5.12.

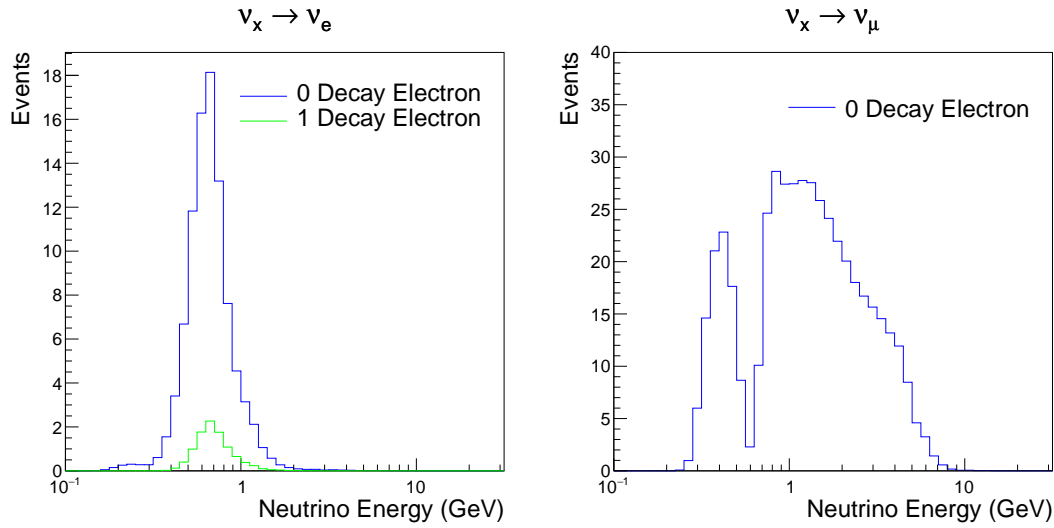


Figure 5.12: The predicted flux of beam neutrinos, as a function of neutrino energy. The predictions are broken down by the number of decay electrons associated with the particular events. Asimov A oscillation parameters are assumed (given in Table 2.2).

6

1820

1821

Sample Selections and Systematics

1822 The oscillation analysis presented within this thesis is built upon a simultaneous
1823 fit to atmospheric data at SK, neutrino beam data in the near detector, and
1824 beam data measured at SK. This is the first simultaneous oscillation analysis
1825 of beam and atmospheric samples supported by the T2K and SK collaborations.
1826 Notably, the author of this thesis has been responsible for the building and
1827 developing the MaCh3 framework to support all sets of samples simultaneously.
1828 The definitions of the samples are documented in section 6.1, section 6.2, and
1829 section 6.3, respectively. The data collected and used within this analysis is
1830 detailed in Table 6.1. The near and far detector data corresponds to T2K runs
1831 2-9 and runs 1-10, respectively. The accumulated POT and beam power for runs
1832 1 – 10 are illustrated in Figure 6.1.

Data Type	Total
Near Detector FHC	1.15×10^{21} POT
Near Detector RHC	8.34×10^{20} POT
Far Detector FHC	1.97×10^{21} POT
Far Detector RHC	1.63×10^{21} POT
Atmospheric SK-IV	3244.4 days

Table 6.1: The amount of data collected in each detector used within this analysis. The data collected at the near and far detector, for both neutrino beam (FHC) and antineutrino beam (RHC), is measured as the number of protons on target (POT).

The difference in POT recorded at the near and far detector is due to the difference in downtime. The SK detector is very stable with almost 100% of data recorded during beam operation. Due to various technical and operational issues, the downtime of the near detector is significantly higher due to its more complex design and operating requirements.

The systematic parameters invoked within the flux, detector, and interaction models used within this analysis are documented in section 6.4. The standard configuration of the joint beam and atmospheric data fit utilises far detector systematics provided in the official inputs from the two experiments. Additionally, a correlated detector model which fits the parameters used in sample selections to data has been developed and documented in subsection 6.4.5.

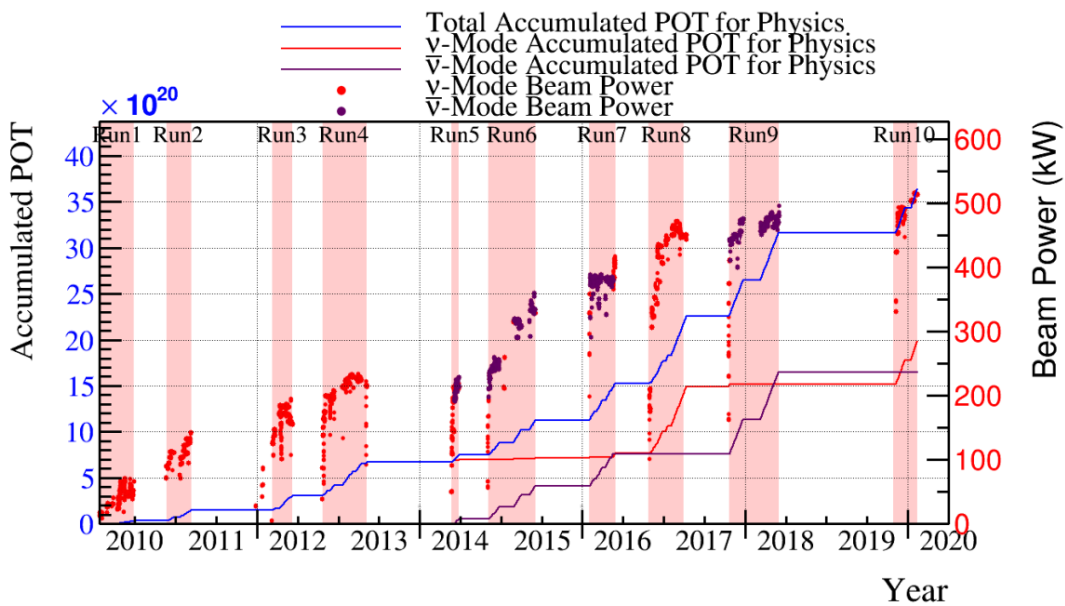


Figure 6.1: The accumulated beam data, measured as the number of protons on target (POT). The total data (blue) is given which comprises of the neutrino beam (red) and antineutrino (purple) components. The beam power for neutrino and antineutrino beams is given as the markers using the same colour scheme. The timescale runs from Run 1 which started in January 2010 until Run 10 which ended in February 2020. The ratio of accumulated data in neutrino and antineutrino beam is 54.7% : 45.3%.

1844 6.1 Atmospheric Samples

1845 The atmospheric event selection follows the official SK-IV analysis presented
1846 in [88] and is documented below. The Monte Carlo prediction used within this
1847 analysis corresponds to 500 years worth of neutrino events, which is scaled down
1848 to match the SK-IV livetime of 3244.4 days.

1849 The fully contained (FC), partially contained (PC), and upward going muon
1850 events ($\text{up-}\mu$) which pass the reduction cuts discussed in section 5.3 are further
1851 broken down into different samples based on reconstruction information. This
1852 section details the samples used within this oscillation analysis, alongside the
1853 chosen binning.

1854 FC events are first separated by the visible energy deposited within the
1855 detector. This is calculated as the sum of the reconstructed kinetic energy
1856 above the Cherenkov threshold for all rings present in the event. Events are
1857 separated by whether they were above or below $E_{\text{vis}} = 1.33\text{GeV}$. This separates
1858 “subGeV” and “multiGeV” events. Typically, lower energy events consist of
1859 charged current quasi-elastic (CCQE) interactions which are better understood
1860 and simpler to reconstruct resulting in smaller systematic uncertainties. Events
1861 are further separated by the number of rings associated with the event due to
1862 similar reasoning. As the oscillation probability is dependant upon the flavour
1863 of neutrino, electron and muon events are separated using a similar likelihood
1864 method to that discussed in section 5.2. To reduce computational resources
1865 required for the reconstruction, only electron and pion hypotheses are considered
1866 so this separation cut depends on the ratio of the electron to pion likelihoods,
1867 $\log(L_e/L_\pi)$. Finally, the number of decay electrons is used to classify events.
1868 Charged current resonant pion production (CCRES) interactions generate a final-
1869 state pion. This can decay, mostly likely through a muon, into a decay electron.
1870 Therefore any electron-like event with one decay electron or muon-like event
1871 with two decay electrons was most likely produced by a CCRES interaction.
1872 Consequently, the number of decay electrons can be used to distinguish CCQE

¹⁸⁷³ and CCRES interaction modes. Ultimately, FC subGeV events are separated
¹⁸⁷⁴ into the samples listed in Table 6.2.

Sample Name	Description
SubGeV- <i>e</i> like-0dcy	Single ring <i>e</i> -like events with zero decay electrons
SubGeV- <i>e</i> like-1dcy	Single ring <i>e</i> -like events with one or more decay electrons
SubGeV- <i>μ</i> like-0dcy	Single ring <i>μ</i> -like events with zero decay electrons
SubGeV- <i>μ</i> like-1dcy	Single ring <i>μ</i> -like events with one decay electrons
SubGeV- <i>μ</i> like-2dcy	Single ring <i>μ</i> -like events with two or more decay electrons
SubGeV- <i>π</i> 0like	Two <i>e</i> -like ring events with zero decay electrons and reconstructed π^0 mass $85 \leq m_{\pi^0} < 215$ MeV

Table 6.2: The fully contained subGeV samples, defined as events with visible energy $E_{vis} < 1.33$ GeV, used within this oscillation analysis.

¹⁸⁷⁵ In addition to the cuts discussed above, multiGeV samples also have addi-
¹⁸⁷⁶ tional cuts to separate samples which target neutrino and antineutrino events.
¹⁸⁷⁷ As discussed in section 2.5, the matter resonance only occurs for neutrinos in the
¹⁸⁷⁸ normal hierarchy and antineutrinos in the inverted mass hierarchy. Therefore,
¹⁸⁷⁹ having flavour-enriched samples aids in the determination of the mass hierarchy.
¹⁸⁸⁰ For a CCRES interaction,

$$\begin{aligned}
 \bar{\nu}_e + N &\rightarrow e^+ + N' + \pi^-, \\
 \nu_e + N &\rightarrow e^- + N' + \pi^+ \\
 &\quad \downarrow \mu^+ + \nu_\mu \\
 &\quad \downarrow e^+ + \nu_e + \bar{\nu}_\mu.
 \end{aligned} \tag{6.1}$$

¹⁸⁸¹ The π^- emitted from a $\bar{\nu}_e$ interaction is more likely to be captured by an
¹⁸⁸² oxygen nucleus than the π^+ from ν_e interactions [191]. These pions then decay,
¹⁸⁸³ mostly through muons, to electrons. Therefore the number of tagged decay
¹⁸⁸⁴ electrons associated with an event gives an indication of whether the interaction
¹⁸⁸⁵ was due to a neutrino or antineutrino: zero for $\bar{\nu}_e$ events, and one for ν_e events.
¹⁸⁸⁶ The ability to separate neutrino from antineutrino events is illustrated in Table 6.4,
¹⁸⁸⁷ where the MultiGeV-*e*like-nue has 78% purity of CC neutrino interactions with
¹⁸⁸⁸ only 7% antineutrino background, the rest consisting of NC backgrounds.

1889 The number of decay electrons discriminator works reasonably well for single-
 1890 ring events. However, this is not the case for multi-ring events. A multiGeV
 1891 multiring electron-like (MME) likelihood cut was introduced in [192, 193]. This
 1892 is a two-stage likelihood selection cut. Four observables are used in the first
 1893 likelihood cut to distinguish $CC\nu_e$ and $CC\bar{\nu}_e$ events from background:

- 1894 • The number of decay electrons
 1895 • The maximum distance between the vertex of the neutrino and the decay
 1896 electrons
 1897 • The energy deposited by the highest energy ring
 1898 • The particle identification of that highest energy ring

1899 Background events consist of $CC\nu_\mu$ and NC interactions. Typically, the
 1900 majority of the energy in these background events is carried by the hadronic
 1901 system. Additionally, muons tend to travel further than the pions from $CC\nu_e$
 1902 before decaying. Thus, the parameters used within the likelihood cut target these
 1903 typical background interaction kinematics.

Sample Name	Description
MultiGeV-elike-nue	Single ring e -like events with zero decay electrons
MultiGeV-elike-nuebar	Single ring e -like events with one or more decay electrons
MultiGeV-mulike	Single ring μ -like events
MultiRing-elike-nue	Two or more ring events with leading energy e -like ring and passed both MME and $\nu/\bar{\nu}$ separation cuts
MultiRing-elike-nuebar	Two or more ring events with leading energy e -like ring and passed MME and failed $\nu/\bar{\nu}$ separation cuts
MultiRing-mulike	Two or more ring events with leading energy μ -like ring and only requires $E_{vis} > 0.6\text{GeV}$
MultiRing-Other1	Two or more ring events with leading energy e -like ring and failed the MME likelihood cut

Table 6.3: The fully contained multiGeV samples used within this oscillation analysis. Both the sample name and description are given.

1904 Neutrino and antineutrino events are then separated by a second likelihood
 1905 method ($\nu/\bar{\nu}$ separation) detailed in [60]. This uses the number of decay electrons,

1906 the number of reconstructed rings, and the event’s transverse momentum. The
1907 last two parameters are used because higher-energy samples tend to have more
1908 pions produced above the Cherenkov threshold which results in more rings
1909 compared to an antineutrino interaction. Furthermore, the angular distribution
1910 also tends to be more forward peaked in antineutrino interactions as compared
1911 to neutrino interactions [88]. These FC multiGeV sample definitions are de-
1912 tailed in Table 6.3.

1913 The PC and up- μ samples are split by the amount of energy deposited within
1914 the outer detector, into “stopping” and “through-going” samples. If an event
1915 leaves the detector, the energy it takes with it has to be estimated which increases
1916 the systematic uncertainty compared to events entirely contained within the
1917 inner detector. This estimation is particularly poor at high energies, thus the
1918 up- μ through-going events are not binned in reconstructed momentum. The
1919 through-going up- μ are further separated by the presence of any electromagnetic
1920 showering in the event, as the assumption of non-showering muon does not give
1921 reliable reconstruction for these types of events [55]. In total, 13 FC, 2 PC, and
1922 3 up- μ atmospheric samples are included within this analysis.

1923 The atmospheric samples are binned in direct observables: reconstructed
1924 lepton momentum and direction, as given by Table A.1. The distribution of
1925 the reconstructed lepton momentum (for samples that only have one bin in
1926 reconstructed zenith angle) and reconstructed direction for each atmospheric
1927 sample used within this analysis is illustrated in Figure 6.2. The by-mode
1928 breakdown of each of the atmospheric samples is given in Appendix A.

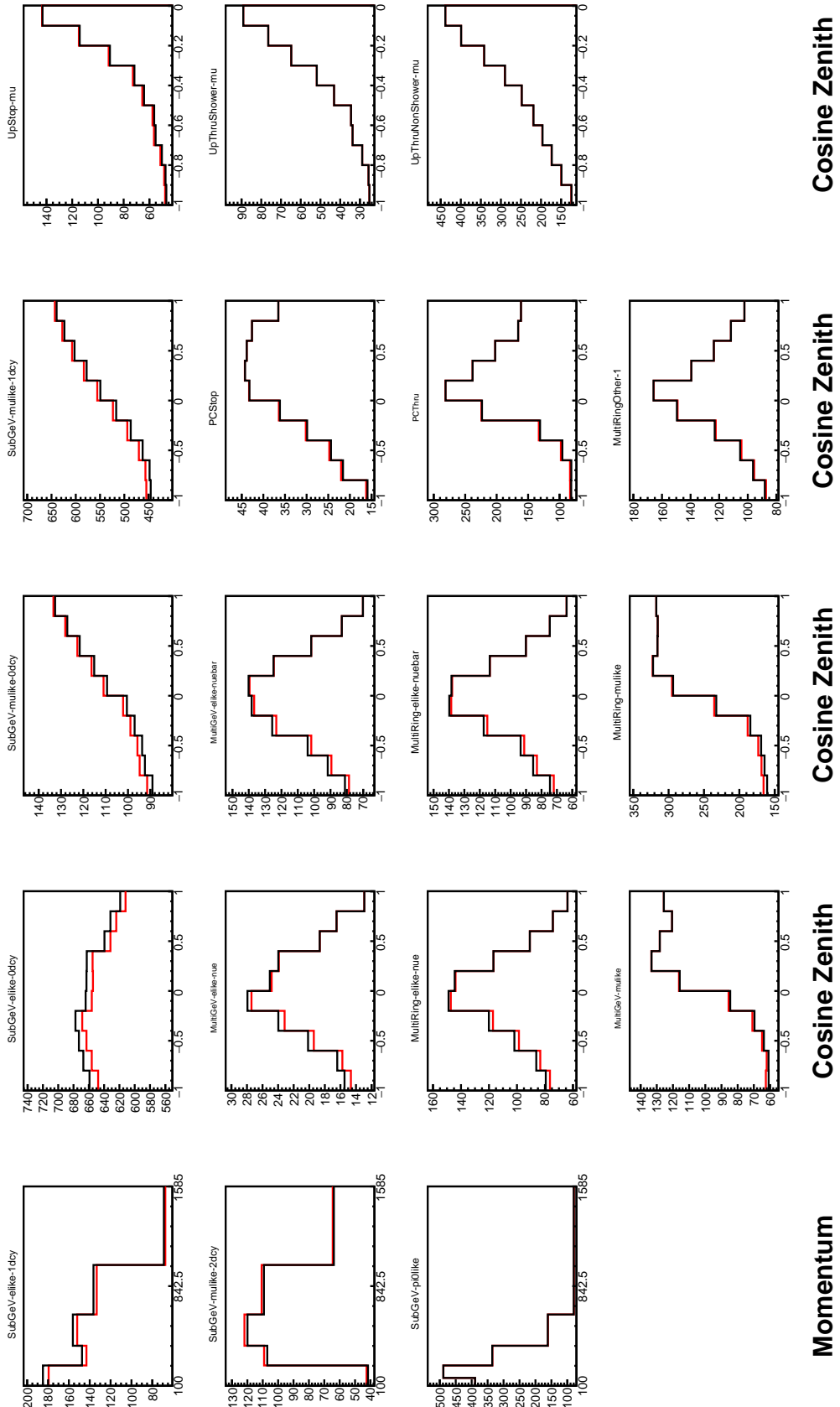


Figure 6.2: Comparison of the SK-IV atmospheric samples between predictions made with the CP-violating Asimov A (Black) and CP-conserving Asimov B (Red) oscillation parameter sets (given in Table 2.2). The subGeV samples CCRES and π^0 -like samples are given in their reconstructed lepton momentum. All other samples are presented in their reconstructed zenith angle projection.

Sample	$CC\nu_e$	$CC\bar{\nu}_e$	$CC(\nu_\mu + \bar{\nu}_\mu)$	$CC(\nu_\tau + \bar{\nu}_\tau)$	NC
SubGeV- <i>elike</i> -0dcy	72.17	23.3	0.724	0.033	3.77
SubGeV- <i>elike</i> -1dcy	86.81	1.773	7.002	0.062	4.351
SubGeV- <i>mulike</i> -0dcy	1.003	0.380	90.07	0.036	8.511
SubGeV- <i>mulike</i> -1dcy	0.023	0.	98.46	0.029	1.484
SubGeV- <i>mulike</i> -2dcy	0.012	0.	99.25	0.030	0.711
SubGeV- <i>pi0like</i>	6.923	2.368	0.928	0.011	89.77
MultiGeV- <i>elike</i> -nue	78.18	7.041	3.439	1.886	9.451
MultiGeV- <i>elike</i> -nuebar	56.68	37.81	0.174	0.614	4.718
MultiGeV- <i>mulike</i>	0.024	0.005	99.67	0.245	0.058
MultiRing- <i>elike</i> -nue	59.32	12.39	4.906	3.385	20
MultiRing- <i>elike</i> -nuebar	52.39	31.03	1.854	1.585	13.14
MultiRing- <i>mulike</i>	0.673	0.080	97.33	0.342	1.578
MultiRingOther-1	27.98	2.366	34.93	4.946	29.78
PCStop	8.216	3.118	84.45	0.	4.214
PCThru	0.564	0.207	98.65	0.	0.576
UpStop-mu	0.829	0.370	98.51	0.	0.289
UpThruNonShower-mu	0.206	0.073	99.62	0.	0.103
UpThruShower-mu	0.128	0.054	99.69	0.	0.132

Table 6.4: The purity of each atmospheric sample used within this analysis, broken down by charged current (CC) and neutral current (NC) interactions and which neutrino flavour interacted within the detector. Each row sums to 100% by definition. Asimov A oscillation parameter sets are assumed (given in Table 2.2). Electron neutrino and antineutrino events are separated to illustrate the ability of the separation likelihood cuts used within the multiGeV and multiring sample selections.

1929 6.2 Near Detector Beam Samples

1930 The near detector sample selections are documented in detail within [194] and
1931 summarised below. Samples are selected based upon which of the two Fine
1932 Grained Detector (FGD) the vertex is reconstructed in as well as the operating
1933 mode of the beam: FHC or RHC. Wrong-sign neutrino background samples are
1934 considered in the RHC mode in order to add additional constraints on model
1935 parameters. Samples from the wrong-sign component of the FHC beam mode
1936 are not included as they are statistically insignificant compared to those samples
1937 already listed.

1938 The reconstruction algorithm uses a clustering algorithm to group hits within
1939 the TPC. It then adds information from the upstream FGD to form a track
1940 that passes through both sub-detectors. In FHC(RHC), the highest momentum
1941 negative(positive) curvature track is defined as the muon candidate. Before
1942 being assigned a sample, these candidate muon events must pass CC-inclusive
1943 cuts, as defined in [195]:

- 1944 • Event Timing: The DAQ must be operational and the event must occur
1945 within the expected beam time window consistent with the beam spill
- 1946 • TPC Requirement: The muon-candidate track path must intercept one or
1947 more TPCs
- 1948 • Fiducial volume: The event must originate from within the fiducial volume
1949 defined in [196]
- 1950 • Upstream Background: Remove events that have muon tracks that originate
1951 upstream of the FGDs by requiring no high-momentum tracks within
1952 150mm upstream of the candidate vertex. Additionally, events that occur
1953 within the downstream FGD are vetoed if a secondary track starts within
1954 the upstream FGD

- 1955 • Broken track removal: All candidates where the muon candidate is broken
1956 in two are removed

- 1957 • Muon PID: Measurements of dE/dx in a TPC are used to distinguish muon-
1958 like events, from electron-like or proton-like, using a likelihood cut

1959 In addition to these cuts, RHC neutrino events also have to undergo the
1960 following cuts to aid in the separation of neutrino and antineutrino [197]:

- 1961 • TPC Requirement: The track path must intercept TPC2
1962 • Positive Track: The highest momentum track must have a positive recon-
1963 structed charge
1964 • TPC1 Veto: Remove any events originating upstream of TPC1

1965 Once all CC-inclusive events have been determined, they are further split
1966 by pion multiplicity: CC0 π , CC1 π , and CCOther. This breakdown targets the
1967 specific interaction modes CCQE, CCRES, and other CC background interactions,
1968 respectively. Pions in the TPCs and FGDs are selected by requiring a second track
1969 to be observed, which is separate from the muon track and is in the same beam
1970 spill window and sub-detector. If the pion originated within a FGD, it must also
1971 pass through the sequential downstream TPC (TPC2 for FGD1, TPC3 for FGD2).

1972 CC0 π , CC1 π , and CCOther samples are defined with the following cuts:

1973 **DB: Understand pion cuts at ND**

- 1974 • ν_μ CC0 π **Selection:** No electrons in TPC and no charged pions or decay
1975 electrons within the TPC or FGD

- 1976 • ν_μ CC1 π **Selection:** Exactly one charged pion in either the TPC or FGD,
1977 where the number of charged pions in the FGD is equal to the number of
1978 decay electrons

- 1979 • ν_μ CCOther **Selection:** All events which are not classified into the above
1980 two selections

Counting the three selections for each FGD in FHC and RHC running, including the wrong-sign background in RHC, 18 near detector samples are used within this analysis. These samples are binned in reconstructed lepton momentum (illustrated in Figure 6.3) and direction with respect to the beam. The binning is chosen such that each event has at least 20 Monte Carlo events in each bin [196]. This is to ensure that the bins are coarse enough to ensure the reduction of statistical errors, whilst also being fine enough to sample the high-resolution peak regions. The exact binning is detailed in [196].

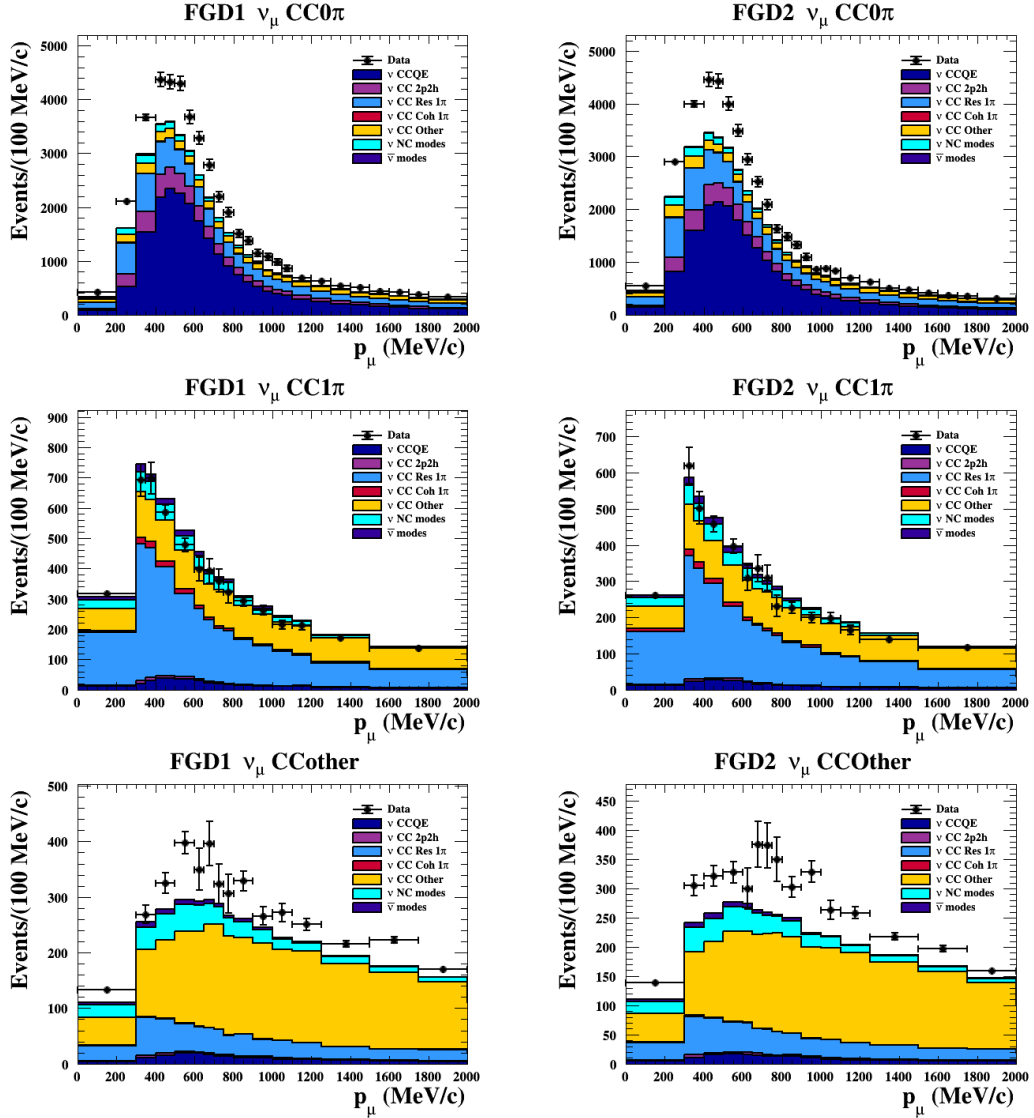


Figure 6.3: The nominal Monte Carlo predictions compared to data for the FGD1 and FGD2 samples in neutrino beam mode, broken down into the $CC\nu_\mu 0\pi$, $CC\nu_\mu 1\pi$ and $CC\nu_\mu$ Other categories. Figures taken from [194].

1989 6.3 Far Detector Beam Samples

1990 The beam neutrino events which occur at the SK detector, which pass the
 1991 reduction cuts detailed in section 5.3, are separated based on whether the beam
 1992 was operating in FHC or RHC mode. The events are then separated into three
 1993 samples: electron-like ($1Re$), muon-like ($1R\mu$), and $CC1\pi^+$ -like ($1Re1de$) which
 1994 are observed as electron-like events with an associated decay electron [186].
 1995 As discussed in section 6.1, positively charged pions emitted from neutrino
 1996 interactions are more likely to produce decay electrons than negatively charged
 1997 pions. Consequently, the $CC1\pi^+$ -like sample is only selected when the beam is
 1998 operating in FHC mode. Therefore, five beam samples measured at SK are
 1999 used in this analysis.

2000 The fiducial volume definition for beam samples is slightly different from that
 2001 used for the atmospheric samples. It uses both the distance to the closest wall
 2002 (`dWall`) and the distance to the wall along the trajectory of the particle (`toWall`).
 2003 This allows events that originate close to the wall but are facing into the tank to be
 2004 included within the analysis, which would have otherwise been removed. These
 2005 additional events are beneficial for a statistics-limited experiment. The exact
 2006 cut values for both `dWall` and `toWall` are different for each of the three types of
 2007 sample and are optimised based on T2K sensitivity to δ_{CP} [184, 198]. They are:

2008 **1Re event selection** For an event to be classified as a $1Re$ -like, the event must sat-
 2009 isfy:

- 2010 • Fully-contained and have $dWall > 80\text{cm}$ and $toWall > 170\text{cm}$
- 2011 • Total of one ring which is reconstructed as electron-like with reconstructed
 2012 momentum $P_e > 100\text{MeV}$
- 2013 • Zero decay electrons are associated with the event
- 2014 • Passes π^0 rejection cut discussed in section 5.2

2015 The zero decay electron cut removes non-CCQE interactions and the π^0
 2016 rejection cut is designed to remove neutral current π^0 background events which
 2017 can be easily reconstructed as 1Re-like events.

2018 The zero decay electron cut removes non-CCQE interactions and the π^0
 2019 rejection cut is designed to remove neutral current π^0 background events which
 2020 can be easily reconstructed as 1Re-like events.

2021 **CC1 π^+ event selection** This event selection is very similar to that of the 1Re
 2022 sample. The only differences are that the `dWall` and `toWall` criteria are changed
 2023 to $> 50\text{cm}$ and $> 270\text{cm}$, respectively, and exactly one decay electron is required
 2024 from the π^+ decay.

2025 **1R μ event selection** A 1R μ -like event is determined by the following cuts:

- 2026 • Fully-contained and have `dWall` $> 50\text{cm}$ and `toWall` $> 250\text{cm}$
- 2027 • Total of one ring which is reconstructed as muon-like with reconstructed
 2028 momentum $P_\mu > 200\text{MeV}$
- 2029 • Fewer than two decay electrons are associated with the event
- 2030 • Passes π^+ rejection cut discussed in section 5.2

2031 All of these samples are binned in reconstructed neutrino energy. This is
 2032 possible under a particular interaction mode assumption, as the direction from
 2033 the source is known extremely well. For the 1Re-like and 1R μ -like samples,

$$E_\nu^{rec} = \frac{(M_N - V_{nuc})E_l - m_l^2/2 + M_N V_{nuc} - V_{nuc}^2/2 + (M_P^2 + M_N^2)/2}{M_N - V_{nuc} - E_l + P_l \cos(\theta_{beam})}. \quad (6.2)$$

2034 Where M_N , M_P and m_l are the masses of the neutron, proton and outgoing
 2035 lepton, respectively. $V_{nuc} = 27\text{MeV}$ is the binding energy of the oxygen nucleus
 2036 [186], θ_{beam} is the angle between the beam and the direction of the outgoing
 2037 lepton, and E_l and P_l are the energy and momentum of that outgoing lepton.

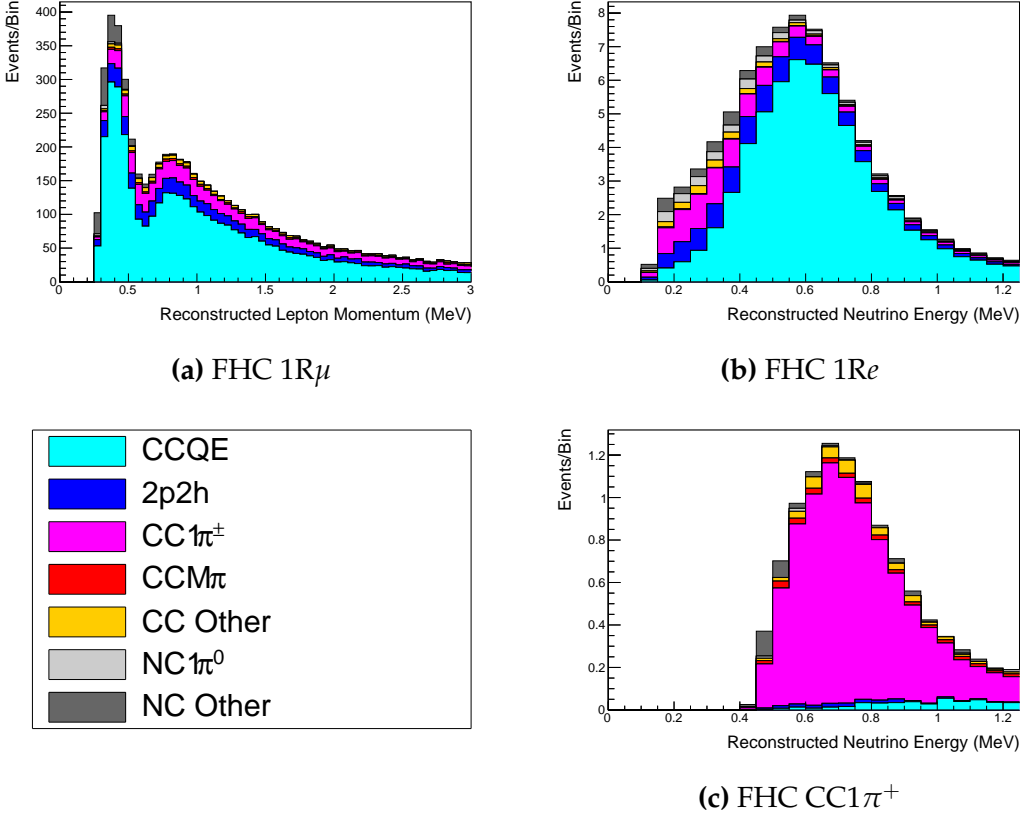


Figure 6.4: The reconstructed neutrino energy, as defined by Equation 6.2 and Equation 6.3, for the 1R μ -like, 1Re-like, and CC1 π^+ -like samples. The AsimovA oscillation parameters are assumed (given in Table 2.2). These samples are the FHC mode samples. For ease of viewing, the 1R μ sample only shows the $0 \leq E_\nu^{rec} < 3.0\text{GeV}$ but the binning extends to 30.0GeV.

2038 The reconstructed neutrino energy of the CC1 π^+ -like events also accounts
 2039 for the delta resonance produced within the interaction,

$$E_\nu^{rec} = \frac{2M_N E_l + M_{\Delta^{++}}^2 - M_N^2 - m_l^2}{2(M_N - E_l + P_l \cos(\theta_{beam}))}. \quad (6.3)$$

2040 Where $M_{\Delta^{++}}$ is the mass of the delta baryon. Binding energy effects are not
 2041 considered as a two-body process, with the delta baryon, is assumed. This follows
 2042 the T2K oscillation analysis presented in [75], although recent developments of
 2043 the interaction model in the latest T2K oscillation analysis do include effects
 2044 from binding energy in this calculation [199].

2045 The reconstructed neutrino energy for the FHC samples is illustrated in
 2046 Figure 6.4. As expected, the 1R μ -like and 1Re-like samples are heavily dominated

2047 by CCQE interactions, with smaller contributions from 2p2h meson exchange and
 2048 resonant pion production interactions. The CC1 π^+ -like sample predominantly
 2049 consists of charged current resonant pion production interactions. The 1Re-like
 2050 and CC1 π^+ -like samples are also binned by the angle between the neutrino beam
 2051 and the reconstructed lepton momentum. This is to aid in charged current and
 2052 neutral current separation, as indicated in Figure 6.5. This is because the neutral
 2053 current backgrounds are predominantly due to π^0 -decays, which decay into two
 2054 γ rays. The opening angle of which (alongside the different final state kinematics)
 2055 can produce a slightly broader angular distribution compared to the final state
 2056 particles originating from charged current ν_e interactions.

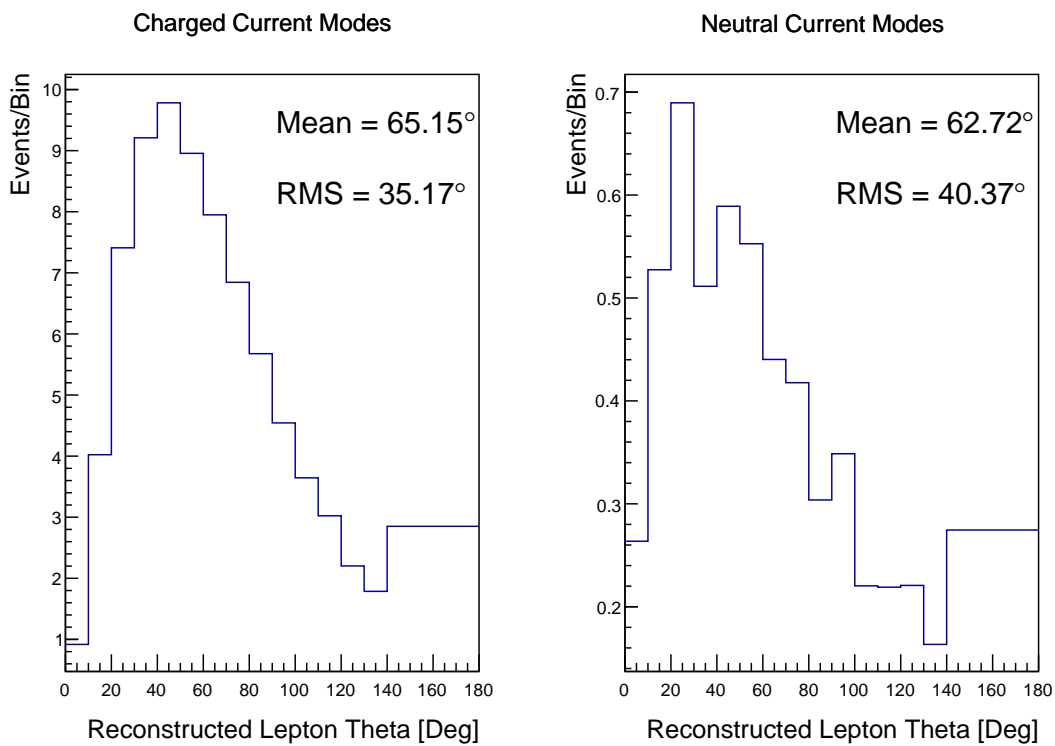


Figure 6.5: The distribution of the angle between the neutrino beam direction and the reconstructed final state lepton, for the FHC 1Re-like sample. The distribution is broken down by neutrino interaction mode into charged current (left) and neutral current (right) components. Asimov A oscillation parameter sets are assumed (given in Table 2.2). The RMS of the charged and neutral current plots are 35.17° and 40.37° , respectively.

2057 6.4 Systematic Uncertainties

2058 The systematic model parameters for this analysis are split into groups, or blocks,
2059 depending on their purpose. They consist of flux uncertainties, neutrino-matter
2060 interaction systematics, and detector efficiencies. There are also uncertainties on
2061 the oscillation parameters to which this analysis is not sensitive, namely Δm_{21}^2
2062 and $\sin^2(\theta_{12})$. These oscillation parameter uncertainties are taken from the 2020
2063 PDG measurements [76]. As described in chapter 4, each model parameter used
2064 within this analysis requires a prior uncertainty. This is provided via separate
2065 covariance matrices for each block. The covariance matrices can include prior
2066 correlations between parameters within a single block, but the separate treatment
2067 means prior correlations can not be included for parameters in different groups.
2068 Some parameters in these models have no reasonably motivated uncertainties
2069 and are assigned flat priors which do not modify the likelihood penalty. In
2070 practice, these flat prior parameters are actually assigned a Gaussian with a
2071 very large width to ensure the covariance matrix is positive definite. They are
2072 then checked at run time to determine if they contribute to the likelihood. The
2073 flux, neutrino interaction, and detector modeling simulations have already been
2074 discussed in section 5.1 and section 5.2. The uncertainties invoked within each
2075 of these models are described below.

2076 6.4.1 Beam Flux

2077 The neutrino beam flux systematics are based upon the uncertainty in the mod-
2078 eling of the components of the beam simulation. This includes the model of
2079 hadron productions and reinteractions, the shape, intensity, and alignment of
2080 the beam with respect to the target, and the uniformity of the magnetic field
2081 produced by the horn, alongside other effects. The uncertainty, as a function
2082 of neutrino energy, is illustrated in Figure 6.6 which includes a depiction of
2083 the total uncertainty as well as the contribution from individual components.
2084 The uncertainty around the peak of the energy distribution ($E_\nu \sim 0.6\text{GeV}$) is

2085 dominated by uncertainties in the beam profile and alignment. Outside of this
2086 region, uncertainties on hadron production dominate the error.

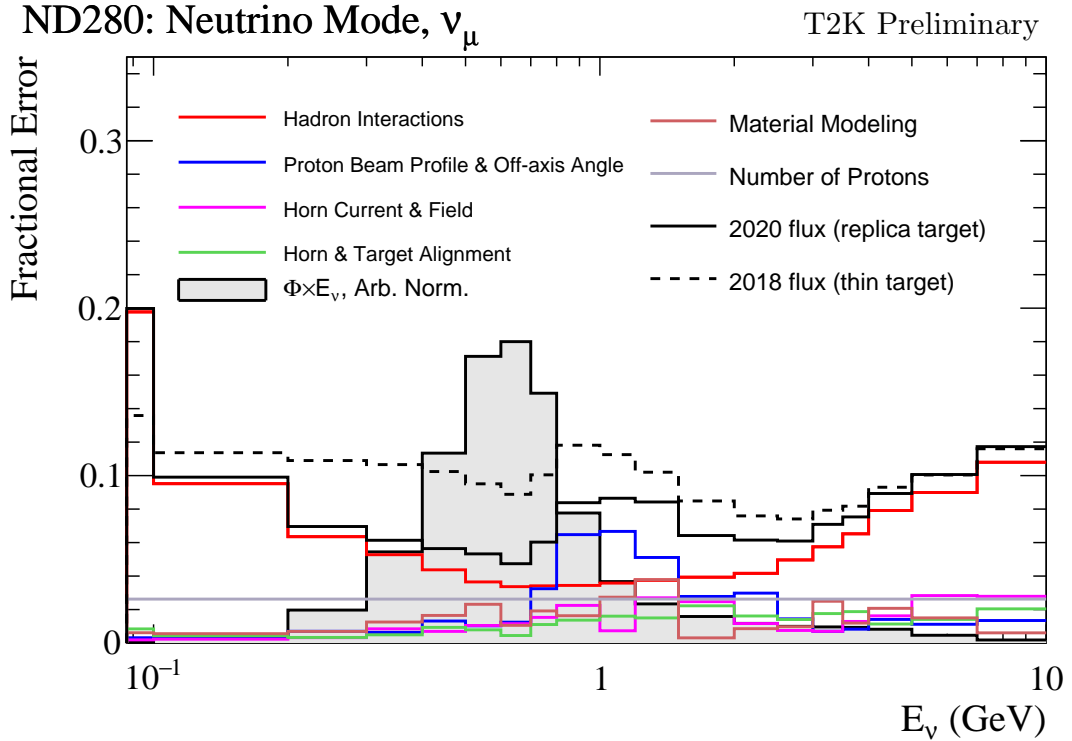


Figure 6.6: The total uncertainty evaluated on the near detector ν_μ flux prediction constrained by the replica-target data, illustrated as a function of neutrino energy. The solid(dashed) line indicates the uncertainty used within this analysis(the T2K 2018 analysis [200]). The solid histogram indicates the neutrino flux as a function of energy. Figure taken from [201].

2087 The beam flux uncertainties are described by one hundred parameters. They
2088 are split between the ND280 and SK detectors and binned by neutrino flavour:
2089 ν_μ , $\bar{\nu}_\mu$, ν_e and $\bar{\nu}_e$. The response is then broken down as a function of neutrino
2090 energy. The bin density in the neutrino energy is the same for the ν_μ in FHC
2091 and $\bar{\nu}_\mu$ in RHC beams, and narrows for neutrino energies close to the oscillation
2092 maximum of $E_\nu = 0.6\text{GeV}$. This binning is specified in Table 6.5. All of these
2093 systematic uncertainties are applied as normalisation parameters with Gaussian
2094 priors centered at 1.0 and error specified from a covariance matrix provided
2095 by the T2K beam group [201].

Neutrino Flavour	Sign	Neutrino Energy Bin Edges (GeV)
μ	Right	0., 0.4, 0.5, 0.6, 0.7, 1., 1.5, 2.5, 3.5, 5., 7., 30.
μ	Wrong	0., 0.7, 1., 1.5, 2.5, 30.
e	Right	0., 0.5, 0.7, 0.8, 1.5, 2.5, 4., 30.
e	Wrong	0., 2.5, 30.

Table 6.5: The neutrino energy binning for the different neutrino flavours. “Right” sign indicates neutrinos in the FHC beam and antineutrinos in the RHC beam. “Wrong” sign indicates antineutrinos in the FHC beam and neutrinos in the RHC beam. The binning of the detector response is identical for the FHC and RHC modes as well as at ND280 and SK.

2096 6.4.2 Atmospheric Flux

2097 The atmospheric neutrino flux is modeled by the HKKM model [51]. 16 systematic
 2098 uncertainties are applied to control the normalisation of each neutrino flavour,
 2099 energy, and direction. They are summarised below:

- 2100 • **Absolute Normalisation:** The overall normalisation of each neutrino flavour
 2101 is controlled by two independent systematic uncertainties, for $E_\nu < 1\text{GeV}$
 2102 and $E_\nu > 1\text{GeV}$, respectively. This is driven mostly by hadronic interaction
 2103 uncertainties for the production of pions and kaons [51]. The strength of
 2104 the response is dependent upon the neutrino energy. The uncertainty is
 2105 parameterized following Figure 11 in [51].
- 2106 • **Relative Normalisation:** Uncertainties on the ratio of $(\nu_\mu + \bar{\nu}_\mu) / (\nu_e + \bar{\nu}_e)$
 2107 are controlled by the difference between the HKKM model [51], FLUKA
 2108 [54] and Bartol models [50]. Three independent parameters are applied in
 2109 the energy ranges: $E_\nu < 1\text{GeV}$, $1\text{GeV} < E_\nu < 10\text{GeV}$, and $E_\nu > 10\text{GeV}$.
- 2110 • **$\nu/\bar{\nu}$ Normalisation:** The uncertainties in the π^+/π^- (and kaon equivalent)
 2111 production uncertainties in the flux of $\nu/\bar{\nu}$. The response is applied using
 2112 the same methodology as the relative normalisation parameters.
- 2113 • **Up/Down and Vertical/Horizontal Ratio:** Similar to the above two sys-
 2114 tematics, the difference between the HKKM, FLUKA, and Bartol model

2115 predictions, as a function of $\cos(\theta_Z)$, is used to control the normalisation of
 2116 events as a function of zenith angle.

- 2117 • **K/π Ratio:** Higher energy neutrinos ($E_\nu > 10\text{GeV}$) mostly originate in
 2118 kaon decay. Measurements of the ratio of K/π production [202] are used to
 2119 control the systematic uncertainty of the expected ratio of pion and kaon
 2120 production.
- 2121 • **Solar Activity:** As the 11-year solar cycle can affect the Earth's magnetic
 2122 field, the flux of primary cosmic rays varies across the same period. The
 2123 uncertainty is calculated by taking a ± 1 year variation, equating to a 10%
 2124 uncertainty for the SK-IV period.
- 2125 • **Atmospheric Density:** The height of the interaction of the primary cosmic
 2126 rays is dependent upon the atmospheric density. The HKKM assumes the
 2127 US standard 1976 [153] profile. This systematic controls the uncertainty in
 2128 that model.

2129 The total uncertainty is dominated by the absolute and relative normalisation
 2130 parameters. The effect of which is illustrated in Figure 6.7. Generally, the
 2131 uncertainty is large at low energy, reducing to $O(10\%)$ around the peak of the
 2132 flux distribution and then increasing once the neutrino energy exceeds 10GeV.

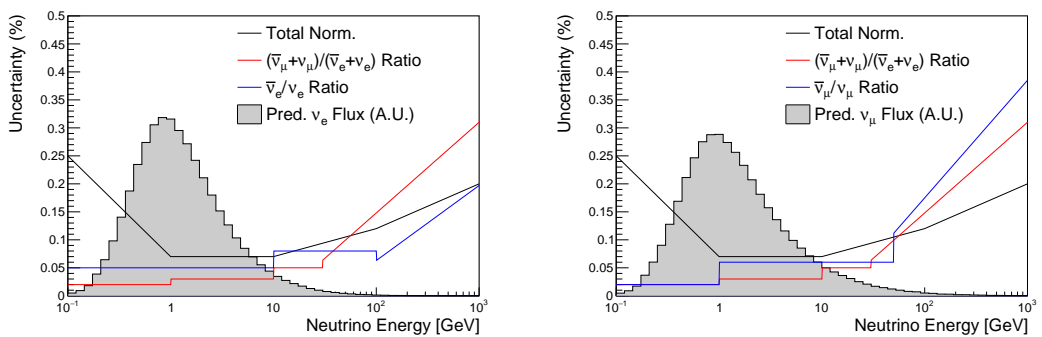


Figure 6.7: The uncertainty evaluated on the atmospheric ν_e (left) and ν_μ (right) flux predictions. The absolute normalisation and flavour ratio uncertainties are given. The solid histogram indicates the neutrino flux as a function of energy.

2133 Updates to the HKKM and Bartol models are underway [158] to use a similar
2134 tuning technique to that used in the beam flux predictions. After those updates,
2135 it may be possible to include correlations in the hadron production uncertainty
2136 systematics for beam and atmospheric flux predictions.

2137 6.4.3 Neutrino Interaction

2138 Neutrino interactions in the detectors are modeled by NEUT. The two indepen-
2139 dent oscillation analyses, T2K-only [203] and the SK-only [60], have developed
2140 separate interaction models. To maximise sensitivity out of this simultaneous
2141 beam and atmospheric analysis, a correlated interaction model has been defined
2142 in [204]. Where applicable, correlations allow the systematic uncertainties applied
2143 to the atmospheric samples to be constrained by near detector neutrino beam
2144 measurements. This can lead to stronger sensitivity to oscillation parameters
2145 as compared to an uncorrelated model.

2146 The low-energy T2K systematic model has a more sophisticated treatment
2147 of CCQE, 2p2h, and CCRES uncertainties, where extensive comparisons of
2148 this model have been performed to external data [203]. However, the model
2149 is not designed for high-energy atmospheric events, like those illustrated in
2150 Figure 5.11. Therefore the high energy systematic model from the SK-only
2151 analysis is implemented for the relevant multi-GeV, PC, and up- μ samples.
2152 The T2K CCQE model is more sophisticated so it has been implemented for
2153 all samples within this analysis, where separate low-energy and high-energy
2154 dials have been implemented. The low-energy dials are constrained by the near
2155 detector measurements and are uncorrelated to their high-energy counterparts.
2156 The author of this thesis was responsible for implementing and validating the
2157 combined cross-section model as documented in [204, 205].

2158 The high energy systematic model includes parameters developed from
2159 comparisons of Nieves and Rein-Seghal models which affect resonant pion
2160 producing interactions, comparisons of the GRV98 and CKMT models which
2161 control DIS interactions, and hadron multiplicity measurements which modulate

the normalisation of multi-pion producing events. The uncertainty on the ν_τ cross-section is particularly large and is controlled by a 25% normalisation uncertainty. These uncertainties are applied via normalisation or shape parameters. The former linearly scales the weight of all affected Monte-Carlo events, whereas the latter can increase or decrease a particular event's weight depending on its neutrino energy and mode of interaction. The response of the shape parameters is defined by third-order polynomial splines which return a weight for a particular neutrino energy. To reduce computational resources for the far detector fit, the response is binned by neutrino energy and sample binning: lepton momentum and cosine zenith binning for atmospheric splined responses and reconstructed neutrino energy and direction binning for beam samples. In total, 17 normalisation and 15 shape parameters are included in the high-energy model within this analysis.

Figure 6.8 indicates the predicted neutrino energy distribution for both beam and subGeV atmospheric samples. There is clearly significant overlap in neutrino energy between the subGeV atmospheric and beam samples, allowing similar kinematics in the final state particles. Figure 6.9 illustrates the fractional contribution of the different interaction modes per sample.

Comparing beam and atmospheric samples which target CCQE interactions (S.G. e-like 0de, S.G. μ -like [0,1]de, [FHC,RHC] 1R μ -like and [FHC,RHC] 1R e-like samples), there is a very similar contribution of CCQE, CC 2p2h, and CC1 π^\pm interactions. The samples which target CC1 π^\pm interactions, (S.G. e-like 0de, S.G. μ -like 2de and FHC 1R+1d.e e-like) also consist of very similar mode interactions.

As a consequence of the similarity in energy and mode contributions, correlating the systematic model between the beam and subGeV atmospheric samples ensures that this analysis attains the largest sensitivity to oscillation parameters while still ensuring neutrino interaction systematics are correctly accounted for. Due to its more sophisticated CCQE and 2p2h model, the T2K systematic model was chosen as the basis of the correlated model.

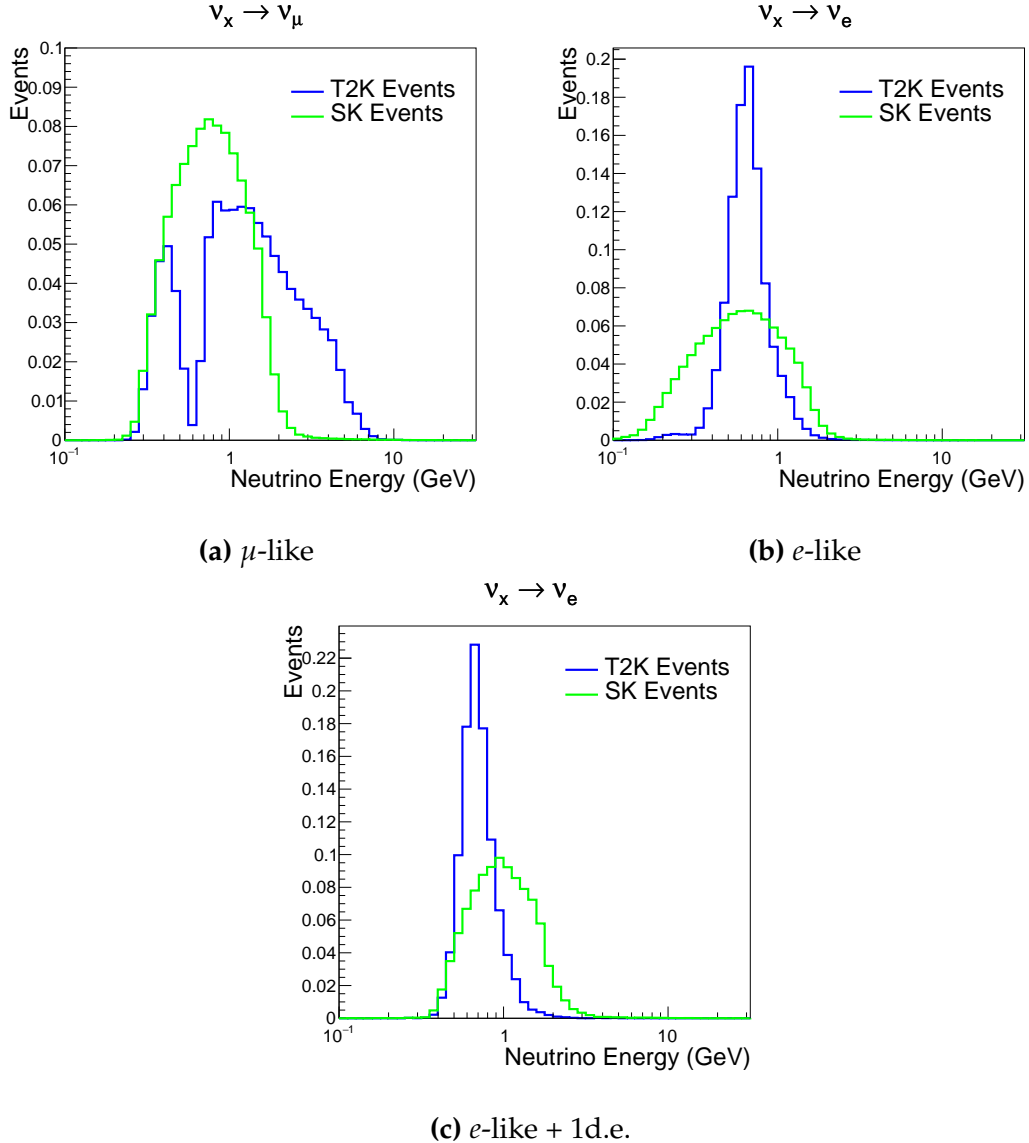


Figure 6.8: The predicted neutrino energy distribution for subGeV atmospheric and beam samples. FHC and RHC beam samples are summed together Asimov A oscillation parameters are assumed (given in Table 2.2). Beam and atmospheric samples with similar cuts are compared against one another.

2192 The T2K systematic model [203] is applied in a similar methodology to the
 2193 SK model parameters. It consists of 19 shape parameters and 24 normalisation
 2194 parameters. Four additional parameters, which model the uncertainty in the
 2195 binding energy, are applied in a way to shift the momentum of the lepton emitted
 2196 from a nucleus. This controls the uncertainty specified on the 27MeV binding
 2197 energy assumed within Equation 6.2. The majority of these parameters are

	CC QE	CC 2p2h	CC $1\pi^\pm$	CC $M\pi$	CC Other	NC $1\pi^0$	NC $1\pi^\pm$	NC $M\pi$	NC Coh.	NC Other
FHC 1R+1d.e. e-like	0.04	0.02	0.83	0.03	0.04	0.01	0.01	0.01	0.00	0.01
RHC 1R e-like	0.62	0.12	0.11	0.01	0.02	0.06	0.01	0.01	0.01	0.04
FHC 1R e-like	0.68	0.12	0.10	0.00	0.02	0.04	0.01	0.00	0.00	0.02
RHC 1R μ -like	0.62	0.13	0.17	0.02	0.03	0.00	0.02	0.00	0.00	0.00
FHC 1R μ -like	0.62	0.12	0.16	0.02	0.03	0.00	0.03	0.00	0.00	0.00
S.G. π^0 -like	0.05	0.01	0.02	0.00	0.01	0.68	0.06	0.07	0.06	0.04
S.G. μ -like 2de	0.04	0.01	0.80	0.10	0.04	0.00	0.00	0.00	0.00	0.00
S.G. μ -like 1de	0.72	0.11	0.12	0.01	0.02	0.00	0.01	0.00	0.00	0.00
S.G. μ -like 0de	0.68	0.11	0.10	0.01	0.02	0.01	0.05	0.01	0.00	0.02
S.G. e-like 1de	0.05	0.01	0.75	0.10	0.05	0.00	0.01	0.02	0.00	0.01
S.G. e-like 0de	0.73	0.11	0.10	0.01	0.02	0.02	0.00	0.00	0.00	0.00

Figure 6.9: The interaction mode contribution of each sample given as a fraction of the total event rate in that sample. Asimov A oscillation parameters are assumed (given in Table 2.2). The Charged Current (CC) modes are broken into quasi-elastic (QE), 2p2h, resonant charged pion production ($1\pi^\pm$), multi-pion production ($M\pi$), and other interaction categories. Neutral Current (NC) interaction modes are given in interaction mode categories: π^0 production, resonant charged pion production, multi-pion production, and others.

2198 assigned a Gaussian prior uncertainty. Those that have no reasonably motivated
 2199 uncertainty, or those which have not been fit to external data, are assigned a
 2200 flat prior which does not affect the penalty term.

2201 On top of the combination of the SK and T2K interaction models, several
 2202 other parameters have been specifically developed for the joint oscillation anal-
 2203 ysis. The majority of the atmospheric samples' δ_{CP} sensitivity comes from the
 2204 normalisation of subGeV electron-like events. These are modeled using a spectral
 2205 function to approximate the nuclear ground state. However, the near detector is
 2206 not able to constrain the model so an additional systematic is introduced which
 2207 models an alternative Continuous Random Phase Approximation (CRPA) nuclear
 2208 ground state. This dial approximates the event weights if a CRPA model had

been assumed rather than a spectral function. This dial only applies to ν_e and $\bar{\nu}_e$ as the near detector does not constraint ν_e cross-section measurements. It is applied as a shape parameter.

Further additions to the model have been introduced due to the inclusion of the subGeV π^0 atmospheric sample. This particularly targets charged current and neutral current π^0 producing interactions to help constrain the systematic uncertainties. Therefore, an uncertainty that affects neutral current resonant π^0 production is incorporated into this analysis. Comparisons of NEUT's NC resonant pion production predictions have been made to MiniBooNE [206] data and a consistent 16% to 21% underprediction is observed [204]. Consequently, a conservative 30% normalisation parameter is invoked.

Down-going events are mostly insensitive to oscillation parameters and can act similar to the near detector within an accelerator experiment (Details will be discussed in chapter 7). This region of phase space can act as a sideband and allows the cross-section model and near detector constraint to be studied. The distribution of events in this region is calculated using the technique outlined in subsection 4.3.4. The results are illustrated in Figure 6.10. For CCQE-targeting samples, the application of the near detector constraint is well within the statistical fluctuation of the down-going data. This means there is no significant tension is observed between the data and the Monte Carlo prediction after the near detector constraint is applied. This is not the case for samples with target CCRES interactions. The electron-like data is consistent with the constrained prediction at high reconstructed momenta but diverges at lower momentum, whereas the muon-like sample is under-predicted throughout the range of momenta. To combat this disagreement, an additional cross-section systematic dial, specifically designed to inflate the low pion momentum systematics was developed in [204]. This is a shape parameter implemented through a splined response.

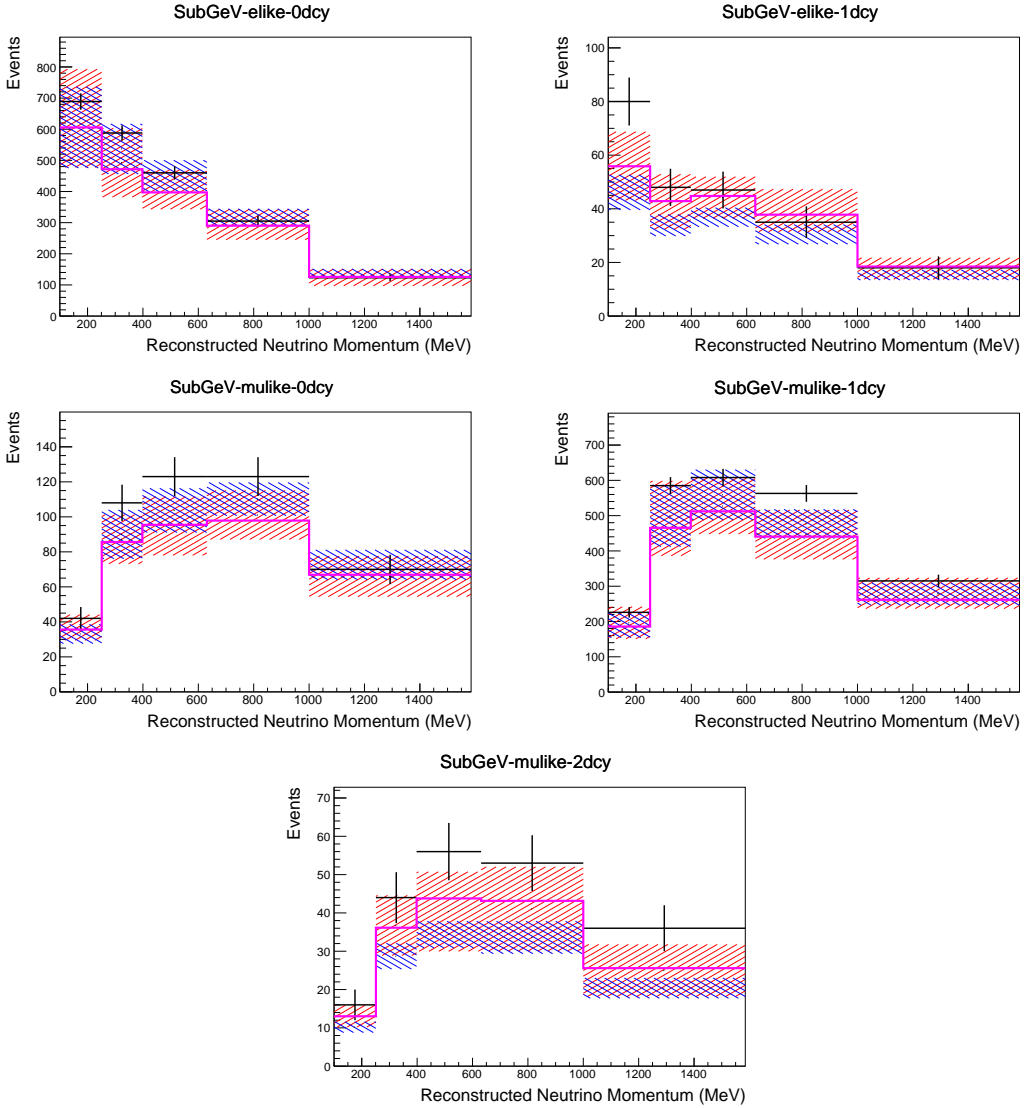


Figure 6.10: Down-going atmospheric subGeV single-ring samples comparing the mean and error of the pre-fit and post-fit Monte Carlo predictions in red and blue, respectively. The magenta histogram illustrates the Monte Carlo prediction using the generated dial values. The black points illustrate the down-going data with statistical errors given. The mean and errors of the Monte Carlo predictions are calculated by the techniques documented in subsection 4.3.4. The pre-fit spectrum is calculated by throwing the cross-section and atmospheric flux dial values from the pre-fit covariance matrix. The post-fit spectrum is calculated by sampling the cross-section dial values from an ND fit MCMC chain, whilst still throwing the atmospheric flux dials from the pre-fit covariance.

2236 6.4.4 Near Detector

2237 The systematics applied due to uncertainties arising from the response of the near
 2238 detector is documented in [132]. The response is described by 574 normalisation
 2239 parameters binned in the selected sample as well as momentum and angle,

2240 P_μ and $\cos(\theta_\mu)$, of the final-state muon. These are applied via a covariance
2241 matrix with each parameter being assigned a Gaussian prior from that covariance
2242 matrix. These normalisation parameters are built from underlying systematics,
2243 e.g. pion secondary interaction systematics, which are randomly thrown and
2244 the variation in each $P_\mu \times \cos(\theta_\mu)$ bin is determined. Two thousand throws are
2245 evaluated and a covariance matrix response is created. This allows significant
2246 correlations between FGD1 and FGD2 samples, as well as adjacent $P_\mu \times \cos(\theta_\mu)$
2247 bins. Statistical uncertainties are accounted for by including fluctuations of each
2248 event's weight from a Poisson distribution.

2249 Similar to the cross-section systematics, MaCh3 and BANFF are used to
2250 constrain the uncertainty of these systematics through independent validations.
2251 Each fitter generates a post-fit covariance matrix which is compared and passed
2252 to the far-detector oscillation analysis working group. As the analysis presented
2253 within this thesis uses the MaCh3 framework, a joint oscillation analysis fit of all
2254 three sets of samples and their respective systematics is performed.

2255 6.4.5 Far Detector

2256 Two configurations of the far detector systematic model implementation have
2257 been considered. Firstly, the far detector systematic uncertainties for beam and
2258 atmospheric samples are taken from their respective analysis inputs, denoted
2259 “official inputs” analysis, with no correlations assumed between the beam and at-
2260 mospheric samples. The beam- and atmospheric-specific inputs are documented
2261 in subsubsection 6.4.5.1 and subsubsection 6.4.5.2. Secondly, an alternative
2262 detector model has been developed which correlates the response of the SK
2263 detector systematics between the beam and atmospheric samples. Here, the
2264 distribution of parameters used for applying event cuts (e.g. electron-muon
2265 PID separation) is modified within the fit. It follows a similar methodology to
2266 the beam far detector systematics implementation but performs a joint fit of
2267 the beam and atmospheric data. This alternative implementation is detailed
2268 in subsubsection 6.4.5.3.

2269 **6.4.5.1 Beam Samples**

2270 There are 45 systematics which describe the response of the far detector to
2271 beam events [186], split into 44 normalisation parameters and one energy scale
2272 systematic. The energy scale systematic is applied as a multiplicative scaling
2273 of the reconstructed neutrino energy. It is estimated from data-to-Monte Carlo
2274 differences in the stopping muon sample in [188] and found to be 2.1%. The
2275 normalisation parameters are assigned a Gaussian error centered at one with
2276 width taken from a covariance matrix. A detailed breakdown of the generation
2277 of the covariance matrix is found in [198]. To build the covariance matrix, a fit
2278 is performed on atmospheric data which has been selected using beam sample
2279 selection cuts. These cuts use the variables, L^i , where the index i is detailed in
2280 Table 6.6. Each L^i is a smear, α , and shift, β parameter such that,

$$L_j^i \rightarrow \bar{L}_j^i = \alpha_j^i L + \beta_j^i \quad (6.4)$$

2281 Where L_j^i (\bar{L}_j^i) correspond to nominal(varied) PID cut parameters given in
2282 Table 6.6. The shift and smear parameters are nuisance parameters with no prior
2283 constraints. They are binned by final-state topology, j , where the binning is given
2284 in Table 6.7. The final-state topology binning is because the detector will respond
2285 differently to events that have one or multiple rings. For example, the detector
2286 will be able to distinguish single-ring events better than two overlapping ring
2287 events, resulting in different systematic uncertainty for one-ring events compared
2288 to two-ring events. This approach is used to allow the cut parameter distributions
2289 to be modified within the fit, allowing for better data to Monte Carlo agreement.

Cut Variable	Parameter Name
0	<code>fitQun e/mu PID</code>
1	<code>fitQun e/pi0 PID</code>
2	<code>fitQun mu/pi PID</code>
3	<code>fitQun Ring-Counting Parameter</code>

Table 6.6: List of cut variables that are included within the shift/smear fit documented in [198].

Category	Description
1e	Only one electron above Cherenkov threshold in the final state
1 μ	Only one muon above Cherenkov threshold in the final state
1e+other	One electron and one or more other charged particles above Cherenkov threshold in the final state
1 μ +other	One muon and one or more other charged particles above Cherenkov threshold in the final state
1 π^0	Only one π^0 in the final state
1 π^\pm or 1p	Only one hadron (typically charged pion or proton) in the final state
Other	Any other final state

Table 6.7: Reconstructed event topology categories on which the SK detector systematics [198] are based.

2290 The mis-modeling of π^0 events is also considered. If one of the two rings
 2291 from a π^0 event is missed, this will be reconstructed as a CC ν_e -like event. This
 2292 is one of the largest systematics hindering the electron neutrino appearance
 2293 analyses. Consequently, additional systematics have been introduced to con-
 2294 strain the mis-modeling of π^0 events in SK, binned by reconstructed neutrino
 2295 energy. To evaluate this systematic uncertainty, a set of “hybrid- π^0 ” samples is
 2296 constructed. These events are built by overlaying one electron-like ring from
 2297 the SK atmospheric neutrino samples or decay electron ring from a stopping
 2298 cosmic ray muon with one simulated photon ring. Both rings are chosen so
 2299 that momenta and opening angle follow the decay kinematics of NC π^0 events
 2300 from the T2K-MC. Hybrid- π^0 Monte Carlo samples with both rings from the
 2301 SK Monte Carlo are produced to compare with the hybrid- π^0 data samples and
 2302 the difference in the fraction of events that pass the ν_e selection criteria is used
 2303 to assign the systematic errors. In order to investigate any data to Monte Carlo
 2304 differences that may originate from either the higher energy ring or lower energy
 2305 ring, two samples are built; a sample in which the electron constitutes the higher
 2306 energy ring from the π^0 decay (called the primary sample) and another one in
 2307 which it constitutes the lower energy ring (called the secondary sample). The
 2308 standard T2K ν_e fitQun event selection criteria are used to select events.

2309 Final contributions to the covariance matrix are determined by supplemen-
 2310 tary uncertainties obtained by comparing stopping muon data to Monte Carlo

prediction, as first introduced in section 5.2. The efficiency of tagging decay electrons is estimated by the stopping muon data to Monte Carlo differences by comparing the number of one decay electron events to the number of events with one or fewer decay electrons. Similarly, the rate at which fake decay electrons are reconstructed by `fiTQun` is estimated by comparing the number of two decay electron events to the number of events with one or two reconstructed decay electrons. The two sources of systematics are added in quadrature weighted by the number of events with one true decay electron yielding a 0.2% systematic uncertainty. A fiducial volume systematic of $\pm 2.5\text{cm}$ which corresponds to a 0.5% shift in the normalisation of events is also applied. Additional normalisation uncertainties based on neutrino flavour and interaction mode are also defined in [186, 207, 208].

Two additional sources of uncertainty are included: secondary and photoneuclear interactions. These are estimated by varying the underlying parameters are building a distribution of sample event rates. These contributions are then added in quadrature to the above covariance matrix. The final uncertainty on the SK detector systematics are provided in Figure 6.11.

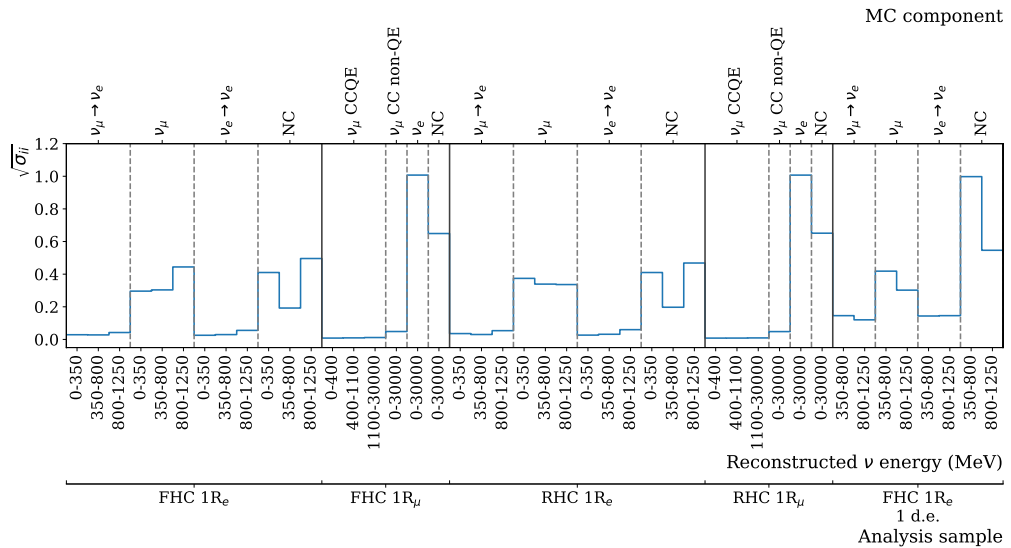


Figure 6.11: The uncertainty on each of the 44 parameters describing the SK detector systematics (The energy scale systematic is neglected). The parameters are split by sample, oscillation channel, interaction mode and reconstructed neutrino energy.

2328 6.4.5.2 Atmospheric Samples

2329 The detector systematics for atmospheric samples, documented in [88], are split
2330 into two sub-groups: those which are related to particle identification and ring
2331 counting systematics, and those which are related to calibration, separation,
2332 and reduction uncertainties.

2333 The particle identification systematics consist of five parameters. The ring sep-
2334 aration systematic enforces an anti-correlated response between the single-ring
2335 and multi-ring samples. This is implemented as a fractional increase/decrease
2336 in the overall normalisation of each sample, depending on the distance to the
2337 nearest wall from an event's vertex. The coefficients of the normalisation are
2338 estimated prior to the fit and depend on the particular atmospheric sample. Two
2339 electron-muon separation systematics are included within this model which
2340 anti-correlates the response of the electron-like and muon-like samples: one for
2341 single-ring events and another for multi-ring events.

2342 The multi-ring electron-like separation likelihood, discussed in section 6.1,
2343 encodes the ability of the detector to separate neutrino from anti-neutrino events.
2344 Two normalisation parameters vary the relative normalisation of multi-ring ν_e
2345 and $\bar{\nu}_e$ samples whilst keeping a consistent overall event rate.

2346 There are 22 systematics related to calibration measurements, including effects
2347 from backgrounds, reduction, and showering effects. They are documented in
2348 [88] and are briefly summarised in Table 6.8. They are applied via normalisation
2349 parameters, with the separation systematics requiring the conservation of event
2350 rate across all samples.

2351 6.4.5.3 Correlated Detector Model

2352 A complete uncertainty model of the SK detector would be able to determine
2353 the systematic shift on the sample spectra for a variation of the underlying
2354 parameters, e.g. PMT angular acceptance. However, this is computationally
2355 intensive, requiring Monte Carlo predictions to be made for each plausible
2356 variation. Consequently, an effective parameter model has been utilised for

Index	Description
0	Partially contained reduction
1	Fully contained reduction
2	Separation of fully contained and partially contained events
3	Separation of stopping and through-going partially contained events in top of detector
4	Separation of stopping and through-going partially contained events in barrel of detector
5	Separation of stopping and through-going partially contained events in bottom of detector
6	Background due to cosmic rays
7	Background due to flasher events
8	Vertex systematic moving events into and out of fiducial volume
9	Upward going muon event reduction
10	Separation of stopping and through-going in upward going muon events
11	Energy systematic in upward going muon events
12	Reconstruction of the path length of upward going muon events
13	Separation of showering and non-showering upward going muon events
14	Background of stopping upward going muon events
15	Background of non-showering through-going upward going muon events
16	Background of showering through-going upward going muon events
17	Efficiency of tagging two rings from π^0 decay
18	Efficiency of decay electron tagging
19	Background from downgoing cosmic muons
20	Asymmetry of energy deposition in tank
21	Energy scale deposition

Table 6.8: Sources of systematic errors specified within the grouped into the “calibration” systematics model.

2357 a correlated detector model following from the T2K-only model implementation
 2358 documented in subsubsection 6.4.5.1. It correlates the detector systematics
 2359 between the far-detector beam and subGeV atmospheric samples due to their
 2360 similar energies and interaction types. As there are no equivalent beam samples,
 2361 the multi-GeV, multiring, PC, and Up- μ samples will be subject to the particle
 2362 identification systematics implementation as described in subsubsection 6.4.5.2
 2363 rather than using this correlated detector model. The calibration systematics also
 2364 described in the aforementioned chapter still apply to all atmospheric samples.
 2365 The correlated detector model utilises the same smear and shift parameters
 2366 documented in subsubsection 6.4.5.1, split by final state topology. Beyond this,

2367 the shift and smear parameters are split by visible energy deposited within the
 2368 detector, with binning specified in Table 6.9. This is because atmospheric events
 2369 are categorised by subGeV and multi-GeV events based on visible energy, so
 2370 this splitting is required when correlating the systematic model for beam and
 2371 atmospheric events. Alongside the technical requirement, higher energy events
 2372 will be better reconstructed due to fractionally less noise within the detector. As
 2373 a result of the inclusion of visible energy binning, Equation 6.4 becomes

$$L_{jk}^i \rightarrow \bar{L}_{jk}^i = \alpha_{jk}^i L + \beta_{jk}^i, \quad (6.5)$$

2374 where k is the visible energy bin.

Index	Range (MeV)
0	$30 \geq E_{vis} > 300$
1	$300 \geq E_{vis} > 700$
2	$700 \geq E_{vis} > 1330$
3	$E_{vis} \geq 1330$

Table 6.9: Visible energy binning for which the correlated SK detector systematics are based

2375 The implementation of this systematic model takes the events reconstructed
 2376 values of the cut parameters, modifies them by the particular shift and smear
 2377 parameter for that event, and then re-applies event selection. This causes event
 2378 migration, which is a new feature incorporated into the MaCh3 framework which
 2379 is only achievable due to the event-by-event reweighting scheme.

2380 Particular care has to be taken when varying the ring counting parameter.
 2381 This is because the number of rings is a finite value (one-ring, two-ring, etc.)
 2382 which can not be continuously varied through this shift and smear technique.
 2383 Consequently a continuous ring counting parameter, RC_i , is calculated for the
 2384 i^{th} event, following the definition in [185]: the preferred likelihoods from all
 2385 considered one-ring (L_{1R}) and two-ring (L_{2R}) fits are determined. The difference

2386 is computed as $\Delta_{LLH} = \log(L_{1R}) - \log(L_{2R})$. The ring counting parameter is
 2387 then defined as

$$RC_i = \text{sgn}(\Delta_{LLH}) \times \sqrt{|\Delta_{LLH}|}, \quad (6.6)$$

2388 where $\text{sgn}(x) = x/|x|$. This ring counting parameter corresponds to an
 2389 intermediate likelihood value used within the `fitQun` algorithm to decide the
 2390 number of rings associated with a particular event. However, fake-ring merging
 2391 algorithms are applied after this likelihood value is used. Consequently, this
 2392 ring counting parameter does not always exactly correspond to the number of
 2393 reconstructed rings. This can be seen in Figure 6.12.

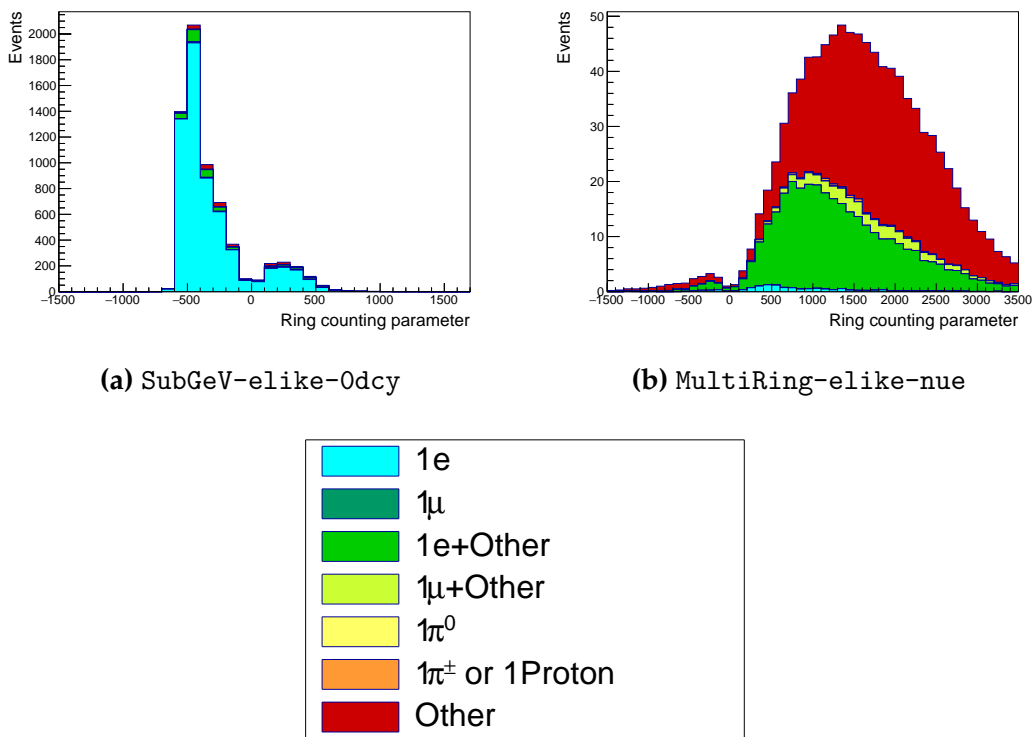


Figure 6.12: The ring counting parameter as defined in Equation 6.6 for the SubGeV-elike-0dcy and MultiRing-elike-nue samples.

2394 As the `fitQun` algorithm does not provide a likelihood value after the fake-
 2395 ring algorithms have been applied, the ring counting parameter distribution is
 2396 correlated to the final number of reconstructed rings through “maps”. These

2397 are two-dimensional distributions of the ring counting parameter and the final
 2398 number of reconstructed rings. An example is illustrated in Figure 6.13. In
 2399 principle, the `fitQun` reconstruction algorithm should be re-run after the variation
 2400 in the ring counting parameter. However, this is not computationally viable.
 2401 Therefore the “maps” are used as a reweighting template.

2402 The maps are split by final state topology and true neutrino flavour and
 2403 all `fitQun`-reconstructed Monte Carlo events are used to fill them. The maps
 2404 are row-normalised to represent the probability of X rings for a given RC_i
 2405 value. Prior to the oscillation fit, an event’s nominal weight is calculated as
 2406 $W^i(N_{Rings}^i, L_{jk}^i)$, where N_{Rings}^i is the reconstructed number of rings for the i^{th}
 2407 event and $W^i(x, y)$ is the bin content in map associated with the i^{th} event, where
 2408 x number of rings and y is ring counting parameter. Then during the fit, the
 2409 value of $R = W^i(N_{Rings}^i, \bar{L}_{jk}^i) / W^i(N_{Rings}^i, L_{jk}^i)$ is calculated as the event weight
 2410 for the i^{th} event. This is the only cut variable that uses a reweighting technique
 2411 rather than event migration.

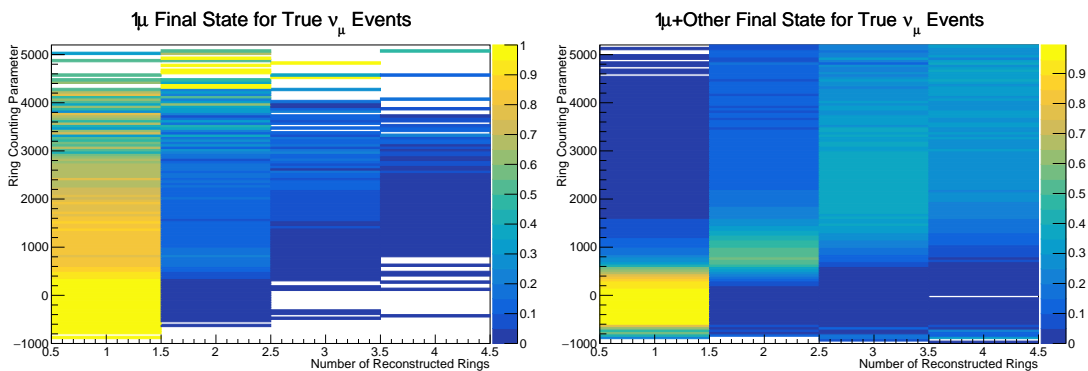


Figure 6.13: The ring counting parameter, defined in Equation 6.6, as a function of the number of reconstructed rings as found by the `fitQun` reconstruction algorithm. Left: true ν_μ events with only one muon above the Cherenkov threshold in the final state. Right: true ν_μ events with one muon and at least one other charged particle above the Cherenkov threshold in the final state.

2412 The π^0 systematics introduced in subsection 6.4.4 are applied via a covariance
 2413 matrix. This is not possible in the alternative model as no covariance matrix
 2414 is used. Thus, the implementation of the π^0 systematics has been modified.
 2415 The inputs from the hybrid π^0 sample are included via the use of “ χ^2 maps”,

which are two-dimensional histograms in α_{jk}^i and β_{jk}^i parameters over some range. Illustrative examples of the χ^2 maps are given in Figure 6.14. Due to their nature, the shift and smear parameters are typically very correlated. A map is produced for each cut parameter given in Table 6.6 and for each visible energy bin given in Table 6.9.

The maps are filled through the χ^2 comparison of the hybrid π^0 Monte Carlo and data in the particle identification parameters documented in Table 6.6. The Monte Carlo distribution is modified by the α_{jk}^i and β_{jk}^i scaling, whilst cross-section and flux nuisance parameters are thrown from their prior uncertainties. The χ^2 between the scaled Monte Carlo and data is calculated and the relevant point in the χ^2 map is filled.

The implementation within this alternative detector model is to add the bin contents of the maps, for the relevant values of the α_{jk}^i and β_{jk}^i parameters, to the likelihood penalty. Only $1\pi^0$ final state topology shift and smear parameters use this prior uncertainty.

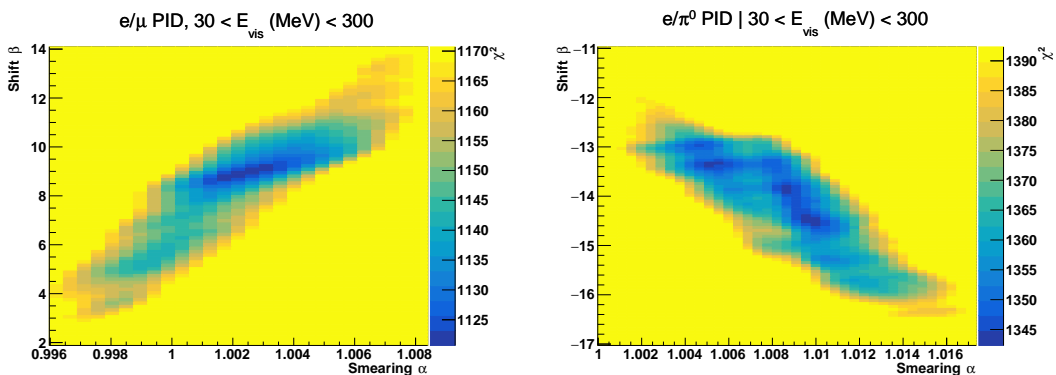


Figure 6.14: The χ^2 between the hybrid- π^0 Monte Carlo and data samples, as a function of smear (α) and shift (β) parameters, for events which have $1\pi^0$ final state topology. Left: Electron-muon separation PID parameter for events with $30 \leq E_{\text{vis}}(\text{MeV}) < 300$. Right: Electron- π^0 separation PID parameter for events with $30 \leq E_{\text{vis}}(\text{MeV}) < 300$.

Similarly, the implementation of the supplementary systematics documented in subsubsection 6.4.5.1 needs to be modified. A new framework [209] was built in tandem with the T2K-SK working group [186] so the additional parameters can be incorporated into the MaCh3 framework. These are applied as normalisation parameters, depending on the particular interaction mode, number of tagged

2436 decay electrons, and whether the primary particle generated Cherenkov light.
 2437 They are assigned Gaussian uncertainties with widths described by a covariance
 2438 matrix. Furthermore, the secondary interaction and photo-nuclear effects need to
 2439 be accounted for in this detector model using a different implementation than
 2440 that in subsubsection 6.4.5.1. This was done by including a shape parameter for of
 2441 each of the secondary interactions and the photo-nuclear systematic parameters.

2442 There are a total of 224 α_{jk}^i and β_{jk}^i parameters, of which 32 have prior
 2443 constraints from the hybrid π^0 samples.

2444 One final complexity of this correlated detector model is that the two sets
 2445 of samples, beam and subGeV atmospheric, use slightly different parameters
 2446 to distinguish electron and muon-like events. The T2K samples use the value
 2447 of $\log(L_e/L_\mu)$ whereas the atmospheric samples use the value of $\log(L_e/L_\pi)$,
 2448 where L_X is the likelihood for hypothesis X. This is because the T2K fits use
 2449 single-ring fiTQun fitting techniques, whereas multi-ring fits are applied to the
 2450 atmospheric samples where only the electron and pion hypothesis are considered.
 2451 The correlation between the two likelihood ratios is illustrated in Figure 6.15. As
 2452 discussed in section 5.2, the pion hypothesis is a very good approximation of the
 2453 muon hypothesis due to their similar mass. Consequently, using the same shift
 2454 and smear parameters correlated between the beam and subGeV atmospheric
 2455 samples is deemed a good approximation.

2456 6.5 Likelihood Calculation

2457 This analysis performs a joint oscillation parameter fit of the ND280 beam
 2458 samples, the T2K far detector beam samples, and the SK atmospheric samples
 2459 introduced in this chapter.

2460 Once the Monte Carlo predictions of each beam and atmospheric sample
 2461 have been built, a likelihood needs to be constructed. This is done by comparing
 2462 the binned Monte Carlo prediction to binned data. The Monte Carlo prediction
 2463 is calculated at a particular point, $\vec{\theta}$, in the model parameter space such that
 2464 $N_i^{MC} = N_i^{MC}(\vec{\theta})$, where N_i represents the bin content of the i^{th} bin. The data

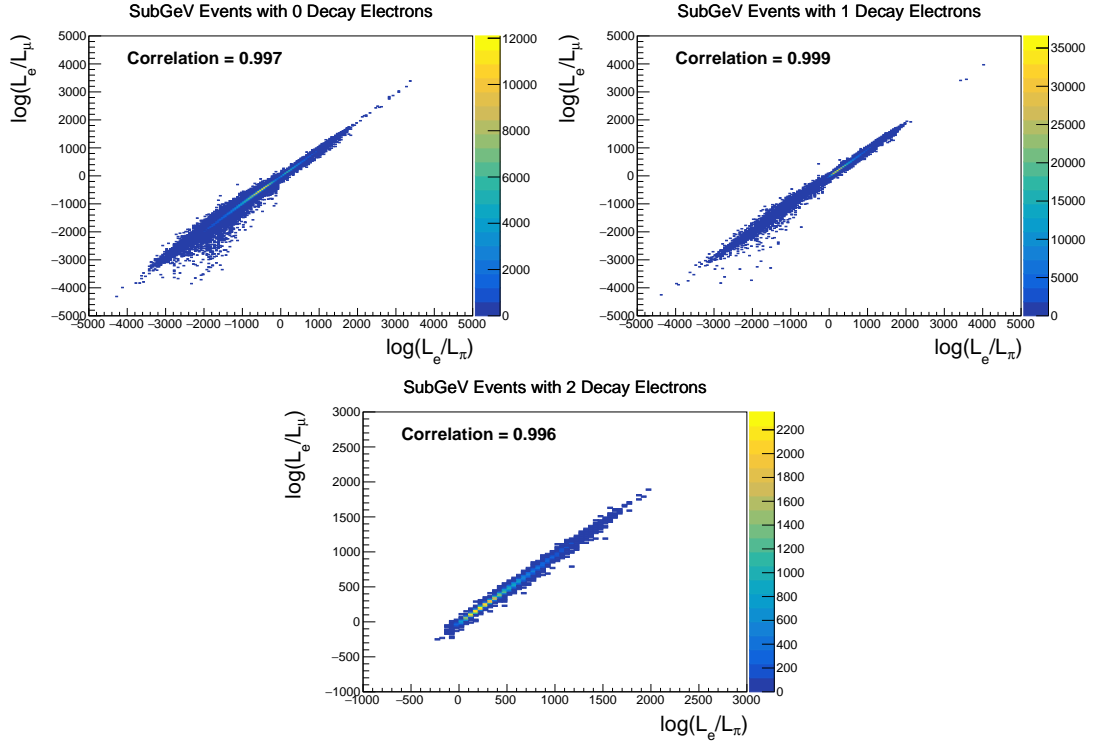


Figure 6.15: The distribution of $\log(L_e/L_\mu)$ compared to $\log(L_e/L_\pi)$ for subGeV events with zero (top left), one (top right) or two (bottom) decay electrons. The correlation in the distribution is calculated as 0.997, 0.999 and 0.996, respectively.

and Monte Carlo spectra are represented by N_i^D and N_i^{MC} , respectively. The bin contents for the beam near detector, beam far detector and atmospheric samples are denoted with ND , FD , and Atm , respectively. The binning index, i , runs over all the bins within a sample. Taking the FHC1Rmu far detector sample as an example, the binning index runs over all the reconstructed neutrino energy bins. The likelihood calculation between the data and the Monte Carlo prediction for a particular bin follows a Poisson distribution, where the data is treated as a fluctuation of the simulation.

The data can consist of either real data or an ‘Asimov’ Monte Carlo prediction, which is typically used for sensitivity studies and denoted ‘Asimov data’. The process for building Asimov data is as follows. The Monte Carlo prediction is reweighted using a particular set of oscillation parameters (potentially those listed in Table 2.2) and systematic parameter tune. The resulting spectra for each sample is then defined to be the Asimov data for that sample. Whilst this results

2479 in unphysical non-integer data predictions, it eliminates statistical fluctuations
 2480 from the data. Therefore, the results of a fit to Asimov data should not include any
 2481 biases from statistical fluctuations. Furthermore, these results should produce
 2482 posterior probability distributions consistent with the parameters which were
 2483 used to make the data prediction. That is to say, the fit results should return the
 2484 known parameters. Any biases seen would be attributed to correlations between
 2485 each oscillation parameter and correlations between oscillation and systematic
 2486 parameters. Consequently, Asimov fit results present the maximum precision
 2487 at which the oscillation parameters could be measured to.

2488 Following the T2K analysis presented in [75], the likelihood contribution for
 2489 the near detector samples also includes a Monte Carlo statistical uncertainty term,
 2490 derived from the Barlow and Beeston statistical treatment [210, 211]. In addition
 2491 to treating the data as a Poisson fluctuation of the Monte Carlo prediction, it
 2492 includes a contribution to the likelihood that which treats the generated Monte
 2493 Carlo prediction as a statistical fluctuation of the actual true simulation assuming
 2494 an infinite amount of statistics had been created. The technical implementation
 2495 of this additional likelihood term is documented in [194] and briefly summarised
 2496 as follows. The term is defined as,

$$\frac{(\beta_i - 1)^2}{2\sigma_{\beta_i}^2}, \quad (6.7)$$

2497 where β_i represents a scaling parameter for the i^{th} bin that relates the bin
 2498 content for the amount of Monte Carlo actually generated N_i^{MC} to the bin content
 2499 if an infinite amount of Monte Carlo statistics had been generated $N_{i,true}^{MC}$, such
 2500 that $N_{i,true}^{MC} = \beta_i \times N_i^{MC}$. In the case where a sufficient amount of Monte Carlo
 2501 statistics had been generated, $\beta_i = 1$. An analytical solution for β_i is given in
 2502 [194]. Additionally, $\sigma_{\beta_i} = \sqrt{\sum_i w_i^2 / N_i^{MC}}$ where $\sqrt{\sum_i w_i^2}$ represents the sum of
 2503 the square of the weights of the Monte Carlo events which fall into bin i .

2504 An additional contribution to the likelihood comes from the variation of
 2505 the systematic model parameters. For those parameters with well-motivated
 2506 uncertainty estimates, a covariance matrix, V , describes the prior knowledge of

each parameter as well as any correlations between the parameters. Due to a technical implementation, a single covariance matrix describes each “block” of model parameters, e.g. beam flux systematics. The covariance matrix associated with the k^{th} block is denoted V^k . This substitution results in $\vec{\theta} = \sum_k^{N_b} \vec{\theta}^k$ and $V = \sum_k^{N_b} V^k$ where N_b denotes the number of blocks. A single covariance matrix is provided for: the oscillation parameters, the beam flux parameters, the atmospheric flux parameters, the neutrino interaction systematics, the near detector parameters, the beam far detector systematics, and the atmospheric far detector systematics. The number of parameters in the k^{th} block is defined as $n(k)$.

The equation for the likelihood \mathcal{L} includes all the terms discussed above. It is defined as,

$$\begin{aligned}
-\ln(\mathcal{L}) = & \\
& \sum_i^{\text{NDbins}} N_i^{\text{ND},MC}(\vec{\theta}) - N_i^{\text{ND},D} + N_i^{\text{ND},D} \times \ln \left[N_i^{\text{ND},D} / N_i^{\text{ND},MC}(\vec{\theta}) \right] + \frac{(\beta_i - 1)^2}{2\sigma_{\beta_i}^2} \\
& + \sum_i^{\text{FDbins}} N_i^{\text{FD},MC}(\vec{\theta}) - N_i^{\text{FD},D} + N_i^{\text{FD},D} \times \ln \left[N_i^{\text{FD},D} / N_i^{\text{FD},MC}(\vec{\theta}) \right] \\
& + \sum_i^{\text{Atmbins}} N_i^{\text{Atm},MC}(\vec{\theta}) - N_i^{\text{Atm},D} + N_i^{\text{Atm},D} \times \ln \left[N_i^{\text{Atm},D} / N_i^{\text{Atm},MC}(\vec{\theta}) \right] \\
& + \frac{1}{2} \sum_k^{N_b} \sum_i^{n(k)} \sum_j^{n(k)} (\vec{\theta}^k)_i (V^k)_{ij}^{-1} (\vec{\theta}^k)_j.
\end{aligned} \tag{6.8}$$

The negative log-likelihood value is determined at each step of the MCMC to build the posterior distribution defined in chapter 4. This value is minimised when the Monte Carlo prediction tends towards the data spectrum.

7

2521

2522

Oscillation Probability Calculation

2523 It is important to understand how and where the sensitivity to the oscillation parameters comes from for both atmospheric and beam samples. An
2524 overview of how these samples respond to changes in δ_{CP} , Δm_{32}^2 , and $\sin^2(\theta_{23})$
2525 is given in section 2.5. This section also explains the additional complexities
2526 involved when performing an atmospheric neutrino analysis as compared to
2527 a beam-only analysis.

2529 Without additional techniques, atmospheric sub-GeV upward-going neutrinos ($E_\nu < 1.33\text{GeV}, \cos(\theta_Z) < 0.$) can artificially inflate the sensitivity to δ_{CP}
2530 due to the quickly varying oscillation probability in this region. Therefore, a
2531 “sub-sampling” approach has been developed to reduce these biases ensuring
2532 accurate and reliable sensitivity measurements. This technique ensures that small-
2533 scale unresolvable features of the oscillation probability have been averaged over
2534 whilst the large-scale features in the oscillation probability are unaffected. The
2535 documentation and validation of this technique are found in section 7.1. The
2536 oscillation probability calculation is computationally intensive due to the large
2537 number of matrix multiplications needed. Consequently, the CUDAProb3 imple-
2538 mentation choice made within the fitting framework, as detailed in section 7.2,
2539 ensures that the analysis can be done in a timely manner.

Whilst the beam neutrinos are assumed to propagate through a constant density slab of material, the density variations through the Earth result in more complex oscillation patterns for atmospheric neutrinos. Furthermore, the uncertainty in the electron density can modify the oscillation probability for the denser core layers of the Earth. The model of the Earth used within this analysis is detailed in section 7.3. This includes information about the official SK-only methodology as well as improvements that have been made to remove some of the approximations used in that analysis. Another complexity of atmospheric neutrino oscillation studies is that the height of production in the atmosphere is not known on an event-by-event basis. An analytical averaging technique that approximates the uncertainty of the oscillation probability has been followed, with the author of this thesis being responsible for the implementation and validation. This implementation of an external technique is described in section 7.4.

7.1 Treatment of Fast Oscillations

As shown in Figure 7.1, atmospheric neutrino oscillations have a significantly more complex structure for upgoing neutrinos with energy below 1GeV. This is because the L/E dependence of the oscillation probability in this region induces rapid variations for small changes in L or E . As discussed in section 2.5, this is also the region in which atmospheric neutrinos have sensitivity to δ_{CP} . In practice, the direction of the neutrino is inferred from the direction of the final state particles traveling in the detector. The correlation between these two directions can be particularly weak for low-energy neutrino interactions. This creates a distinct difference from the beam neutrinos where the position of the source is very precisely known.

As a consequence of the unresolvable structure, an event rate consistent with the averaged oscillation probability is observed in the subGeV upgoing region. This creates a computational problem: A significantly large amount of Monte Carlo statistics would be required to accurately predict the number of events if Monte Carlo averaging was the only technique used. This section describes

2570 the ‘sub-sampling’ approach developed for this analysis and compares it to the
2571 methodology used within the SK-only analysis.

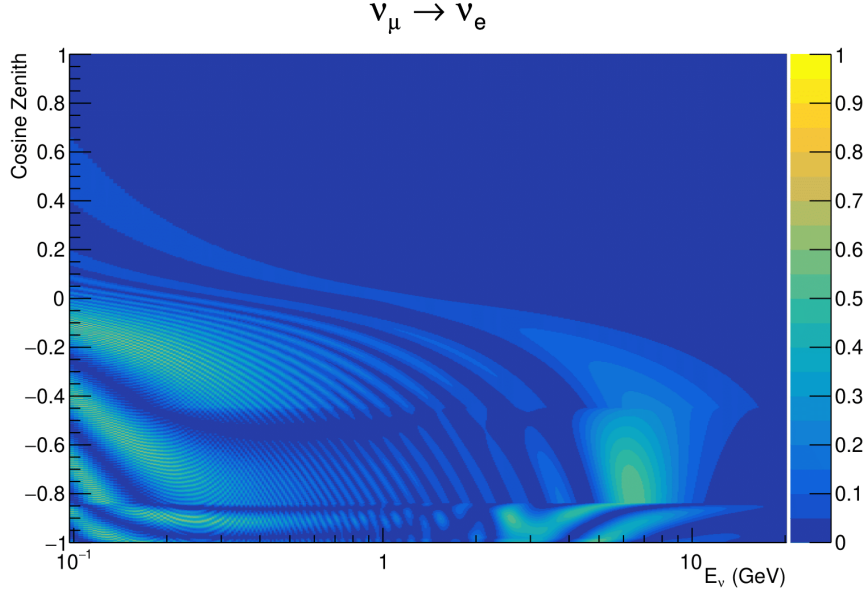


Figure 7.1: The oscillation probability $P(\nu_\mu \rightarrow \nu_e)$, given as a function of neutrino energy and zenith angle, which highlights an example of the “fast” oscillations in the sub-GeV upgoing region.

2572 The official SK-only analysis uses the osc3++ oscillation parameter fitter
2573 [79]. To perform the fast oscillation averaging, it uses a ‘nearest-neighbour’
2574 technique. For a given Monte Carlo neutrino event, the nearest twenty Monte
2575 Carlo neighbours in reconstructed lepton momentum and zenith angle are
2576 found and a distribution of their neutrino energies is built. The RMS, σ , of
2577 this distribution is then used to compute an average oscillation probability for
2578 the given neutrino Monte Carlo event.

2579 For the i^{th} event, the oscillation weight is calculated as

$$W_i = \frac{1}{5}P(E_i, \bar{L}_i) + \frac{1}{5}\sum_{\beta=-1, -0.5, 0.5, 1} P(E_i + \beta\sigma_i, L_\beta), \quad (7.1)$$

2580 where $P(E, L)$ is the oscillation probability calculation for neutrino energy E
2581 and path length L and the two path lengths, \bar{L}_i and L_β are described below. All
2582 of the oscillation probability calculations are performed with a fixed zenith angle
2583 such that the same density profile is used. The uncertainty in the production

2584 height is controlled by using an “average” production height, \bar{L}_i , which represents
2585 the average path length computed using twenty production heights taken from
2586 the Honda flux model’s prediction [53]. These inputs are provided in 5% intervals
2587 of the cumulative distribution function. The value of \bar{L}_i is calculated as:

$$\bar{L}_i = \frac{1}{20} \sum_{j=1}^{20} \sqrt{(R_E + h_j)^2 - R_E^2 (1 - \cos^2 \theta_i)} - R_E \cos \theta_i. \quad (7.2)$$

2588 Where R_E is the Earth’s radius and θ_i is the zenith angle of the i^{th} event.
2589 The production heights h_j represent the $(j \times 5)^{th}$ percentile of the cumulative
2590 distribution function. L_β values (where the values of β are given in Equa-
2591 tion 7.1) are similarly calculated but instead use different combinations of four
2592 production heights,

$$\begin{aligned} L_{-1.0} &= \frac{1}{4} L(45, 50, 55, 60), \\ L_{-0.5} &= \frac{1}{4} L(35, 40, 65, 70), \\ L_{+0.5} &= \frac{1}{4} L(25, 30, 75, 68), \\ L_{+1.0} &= \frac{1}{4} L(15, 20, 85, 89). \end{aligned} \quad (7.3)$$

2593 Where $L(i, j, k, l)$ represents the sum of the path lengths with fixed
2594 zenith angle and production heights corresponding to the i^{th} , j^{th} , k^{th} and l^{th}
2595 percentile of the cumulative distribution function. The values that are taken
2596 as β (and values for L_β) are chosen to smooth the oscillation contours in Δm_{32}^2
2597 without incurring loss of sensitivity [212].

2598 This averaging technique works because of the inference between the zenith
2599 angle and the reconstructed direction of final state particles in the detector. For
2600 low-energy neutrinos, where the resolution of the true neutrino direction is poor,
2601 σ_i will be large, resulting in significant averaging effects. Contrary to this, the
2602 inferred direction of high-energy neutrinos will be much closer to the true value,
2603 meaning that σ_i will be smaller, culminating in small averaging effects.

In practice, these calculations are performed prior to the fit as only oscillation parameters at fixed points are considered. The MCMC technique used in this thesis requires oscillation probabilities to be evaluated at arbitrary parameter values, not known *a priori*. Calculating the five oscillation probabilities per event required by the SK technique is computationally infeasible, so a different averaging technique is used. However, the concept of the averaging technique can be taken from it.

To perform a similar averaging as the SK analysis, a sub-sampling approach using binned oscillograms has been devised. A coarsely binned oscillogram is defined in $\cos(\theta_Z)$ and E_ν . For a given set of oscillation parameters, a single oscillation probability will be assigned to each coarse bin. This value will then apply to all Monte Carlo events which fall into that bin. To assign these oscillation probabilities, the probability is calculated at $N \times N$ points on a grid within a particular bin. This ensemble of oscillation probabilities is averaged to define the coarse bin's oscillation probability, assuming a flat prior in E_ν and $\cos(\theta_Z)$ within the bin. Figure 7.2 illustrates the $N = 2$ example where the assigned value to a coarse bin is the average of the four fine bins which fall in that coarse bin. Whilst the coarse bin edges do not have to be linear on either axis, the sub-division of the fine bins is linear within the range of a coarse bin.

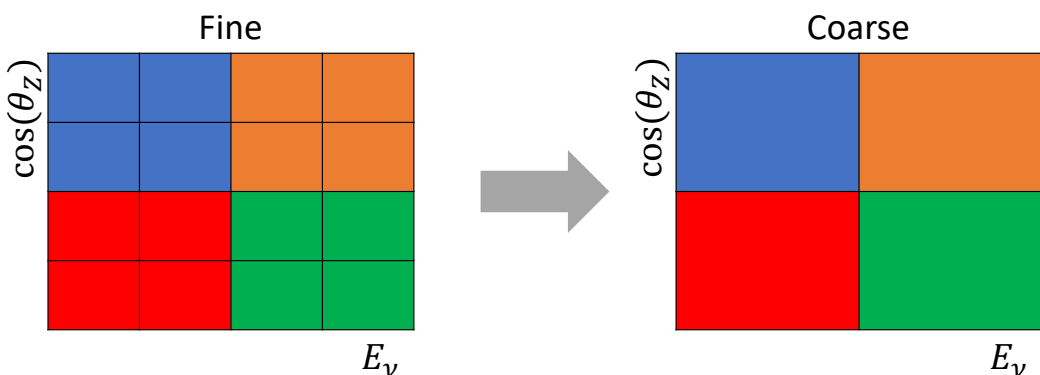


Figure 7.2: Illustration of the averaging procedure for $N = 2$. The oscillation probabilities calculated on the finer left binning are averaged to obtain the oscillation probabilities in the coarser right binning. These averaged oscillation probabilities with the coarser binning are then applied to each event during the fit.

2623 The coarse binning is defined with 67×52 bins in true neutrino energy \times
 2624 cosine zenith. It is picked to be identical to that provided in [212]. In general, the
 2625 binning is logarithmically spaced in neutrino energy but has some hand-picked
 2626 bin edges around the matter resonance to smoothly increased the bin density.
 2627 This is to avoid smearing this region which can be well sampled by the Monte
 2628 Carlo. The cosine zenith binning is approximately linearly spaced across the
 2629 allowable range but the values of layer transitions are hit precisely: -0.8376 (core-
 2630 mantle) and -0.4464 (mantle/transition zone). Bins are spread further apart for
 2631 downgoing events as this is a region unaffected by the fast oscillation wavelengths
 2632 and reduces the total number of calculations required to perform the calculation.

2633 The choice of N is justified based on two studies. Firstly, the variation of event
 2634 rates of each sample is studied as a function of N . For a given set of oscillation
 2635 parameters thrown from the PDG prior constraints (detailed in Table 2.1), the
 2636 oscillation probabilities are calculated using a given value of N . Each sample
 2637 is re-weighted and the event rate is stored. The value of N is scanned from
 2638 1, which corresponds to no averaging, to 19, which corresponds to the largest
 2639 computationally viable subdivision binning. The event rate of each sample at
 2640 large N is expected to converge to a stationary value due to the fine binning fully
 2641 sampling the small-scale structure. Figure 7.3 illustrates this behaviour for the
 2642 SubGeV_elike_0dcy sample for 9 different throws of the oscillation parameters.

2643 Denoting the event rate for one sample for a given throw t at each N by λ_t^N ,
 2644 the average over all considered N values ($\bar{\lambda}_t = \frac{1}{24} \sum_{N=1}^{24} \lambda_t^N$) is computed. The
 2645 variance in the event rate at each N is then calculated as

$$\text{Var}[\lambda^N] = \frac{1}{N_{\text{throws}}} \sum_{t=1}^{N_{\text{throws}}} \left(\lambda_t^N - \bar{\lambda}_t \right)^2 - \left[\frac{1}{N_{\text{throws}}} \sum_{t=1}^{N_{\text{throws}}} \left(\lambda_t^N - \bar{\lambda}_t \right) \right]^2. \quad (7.4)$$

2646 In practice, the following procedure is undertaken. For a particular throw,
 2647 the difference between the event rate at a particular choice of N and the mean
 2648 of the distribution is calculated. This is illustrated in Figure 7.4. This value
 2649 is then calculated for all the 2000 throws, generating a distribution of $\lambda_t^N - \bar{\lambda}_t$.

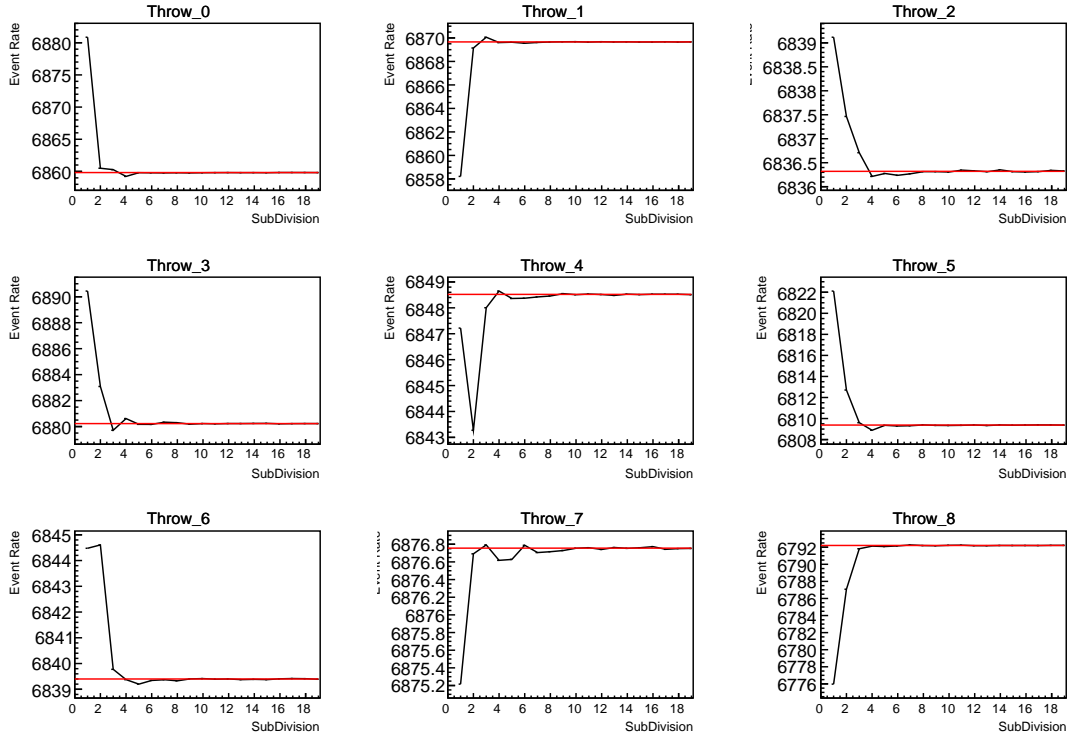


Figure 7.3: Event rate of the SubGeV_elike_0dcy sample as a function of the number of sub-divisions per coarse bin. Each subplot represents the event rate of the sample at a different oscillation parameter set thrown from the PDG priors detailed in Table 2.1. The red line in each subplot represents the mean of the event rate over the different values of sub-divisions for that particular oscillation parameter throw.

2650 This is repeated for each of the values of N considered within this study. The
 2651 distributions of this value, for $N = \{1, 5\}$, are given in Figure 7.5. As expected,
 2652 the distribution gets narrower and tends towards zero for the higher values of N .

2653 The aim of the study is to find the lowest value of N such that this variance
 2654 is below 0.001. This utilises the width of the distributions given in Figure 7.5.
 2655 This is the typical threshold used by T2K fitters to validate systematic imple-
 2656 mentation so has been set as the same criteria. The results of this study for
 2657 each atmospheric sample used within this thesis are illustrated in Figure 7.6 for
 2658 2000 throws of the oscillation parameters. As can be seen, the variance is below
 2659 the threshold at $N = 10$, and is driven primarily by the SubGeV_mulike_1dcy
 2660 and SubGeV_elike_0dcy samples.

2661 The second study to determine the value of N is as follows. The likelihood
 2662 for each sample is computed against an Asimov data set created with Asimov A

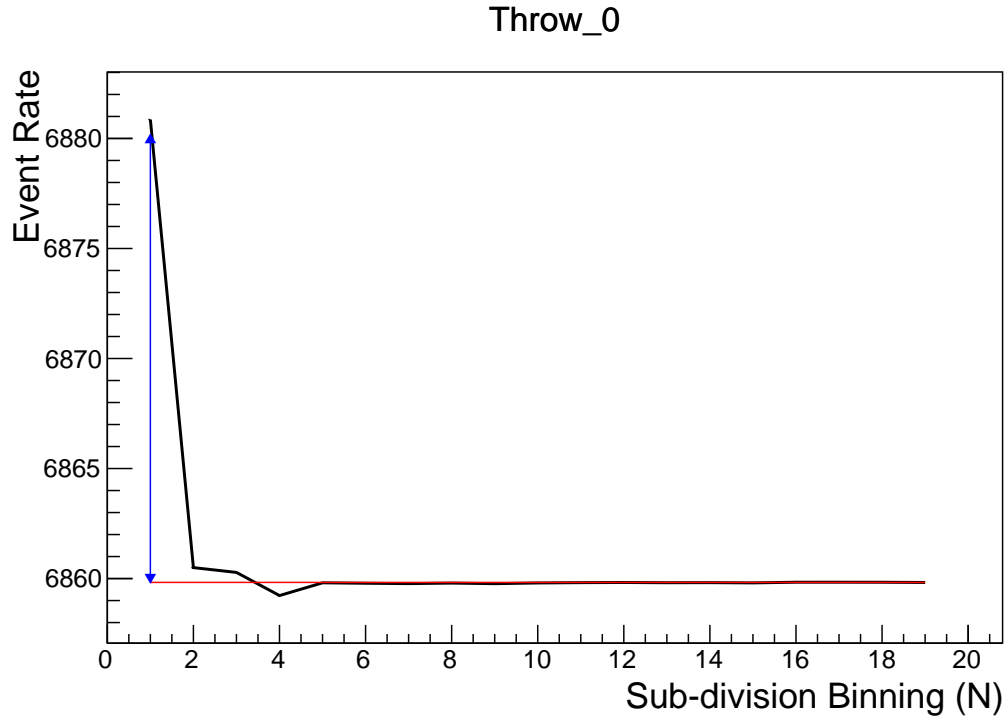


Figure 7.4: Event rate of the SubGeV_elike_0dcy sample, for a particular oscillation parameter throw, as a function of the number of sub-divisions, N , per coarse bin. The difference between the mean event rate (red), $\bar{\lambda}$, and the event rate at $N = 1$, $\lambda^{N=1}$ is defined as $\lambda^N - \bar{\lambda}$ and illustrated by the blue arrow.

oscillation parameters (Table 2.2). Following Equation 7.4, the variance of the log-likelihood over all considered N is computed. The results are shown in Figure 7.7.

A choice of $N = 10$ sub-divisions per coarse bin has a variance in both event rate and log-likelihood residuals less than the required threshold of 0.001. The largest value of the likelihood variance is of order 10^{-7} , corresponding to an error on the log-likelihood of about 3×10^{-4} which is small enough to be negligible for the oscillation analysis.

Figure 7.8 illustrates the effect of the smearing using $N = 10$. The fast oscillations in the sub-GeV upgoing region have been replaced with a normalisation effect whilst the large matter resonance structure remains.

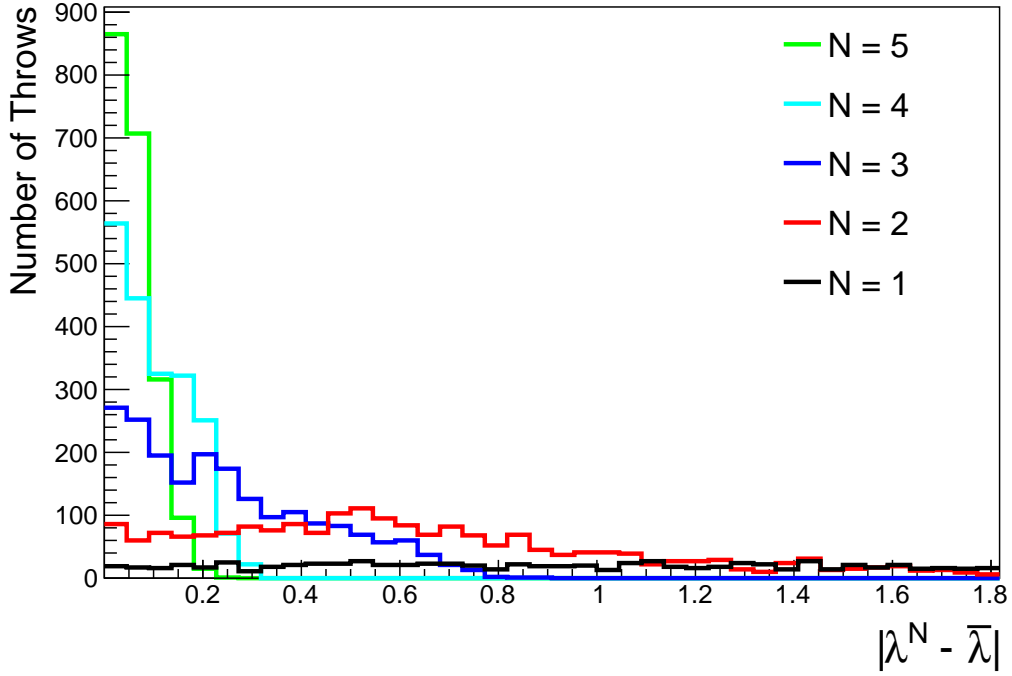


Figure 7.5: The distribution of $\lambda^N - \bar{\lambda}$ for various values of N . As expected, the distribution gets narrower for larger values of N .

2673 7.2 Calculation Engine

2674 As previously discussed in section 7.1, the calculation of oscillation probabilities
 2675 is performed at run-time. Consequently, the time per calculation is crucial for fit
 2676 performance. The initial fitting framework used for this analysis was developed
 2677 with ProbGPU [213]. This is a GPU-only implementation of the prob3 engine
 2678 [214]. It is primarily designed for neutrino propagation in a beam experiment
 2679 (single layer of constant density) with the atmospheric propagation code not
 2680 being used prior to the analysis in this thesis.

2681 Another engine, CUDAProb3 [215], has been interfaced with the fitting frame-
 2682 work used in this analysis. This interfacing was done by the author of this
 2683 thesis. It has been specifically optimised for atmospheric neutrino oscillation
 2684 calculation so does not contain the code to replace the beam oscillation calculation.
 2685 The engine utilises object-orientated techniques as compared to the functional
 2686 implementation of ProbGPU. This allows the energy and cosine zenith arrays to

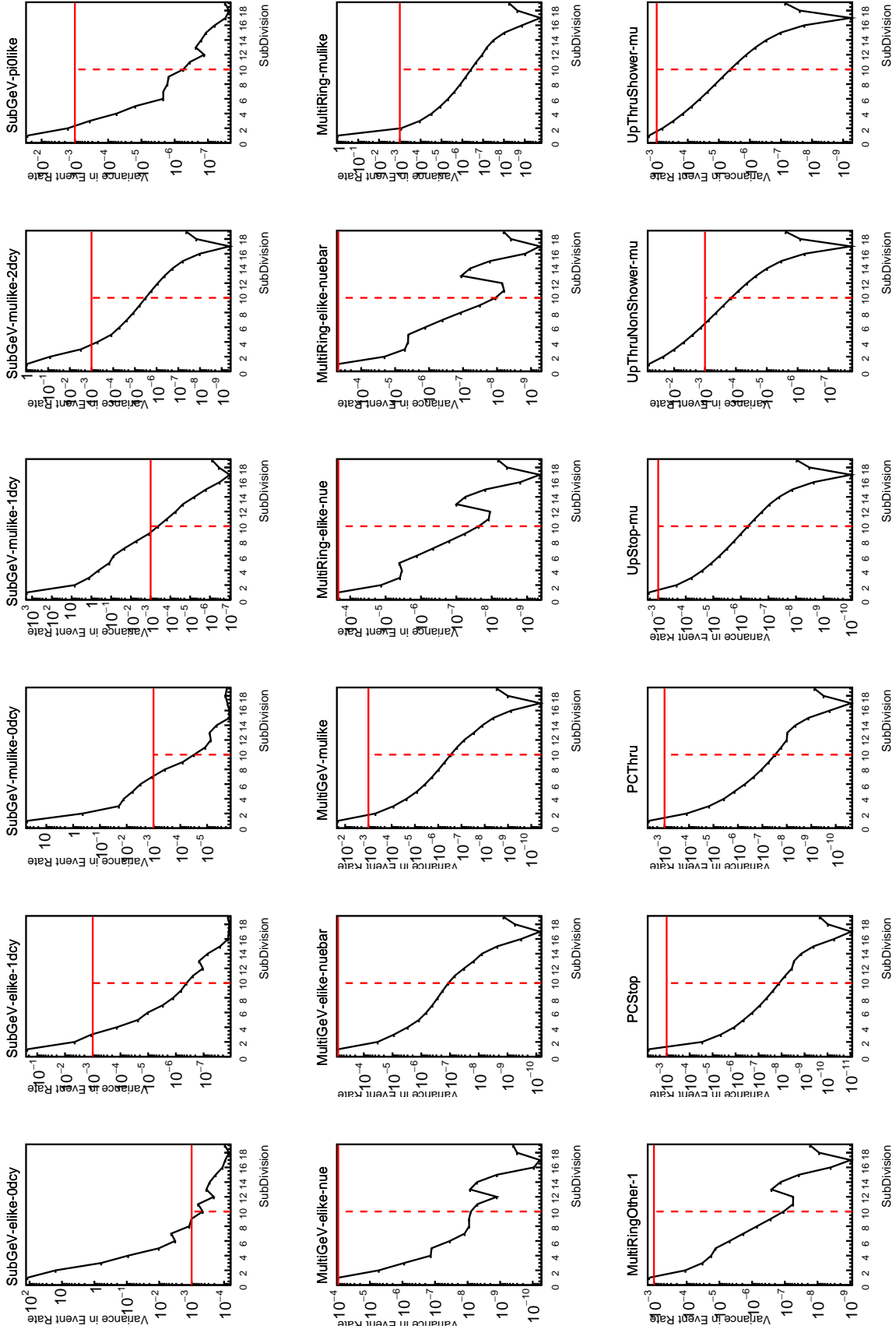


Figure 7.6: Variance of event rate for each atmospheric sample as a function of the number of sub-divisions per coarse bin. The solid red line indicates the 0.1% threshold and the dashed red line indicates the variance at a sub-division $N = 10$.

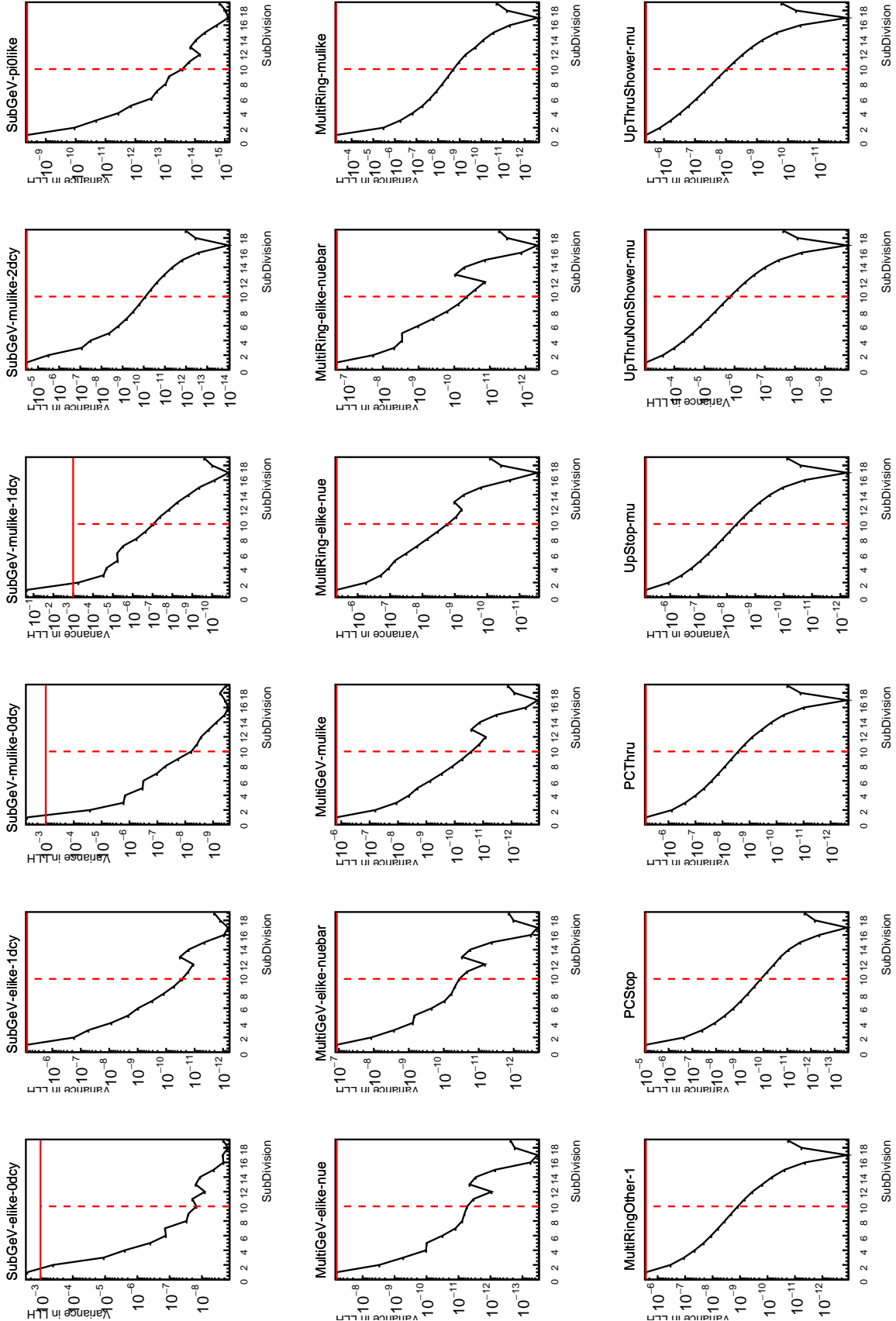


Figure 7.7: Variance of sample likelihood, when compared to 'Asimov data' set at Asimov A, for each atmospheric sample as a function of the number of sub-divisions per coarse bin. The solid red line indicates the 0.1% threshold and the dashed red line is a graphical indication of the variance at a sub-division $N = 10$.

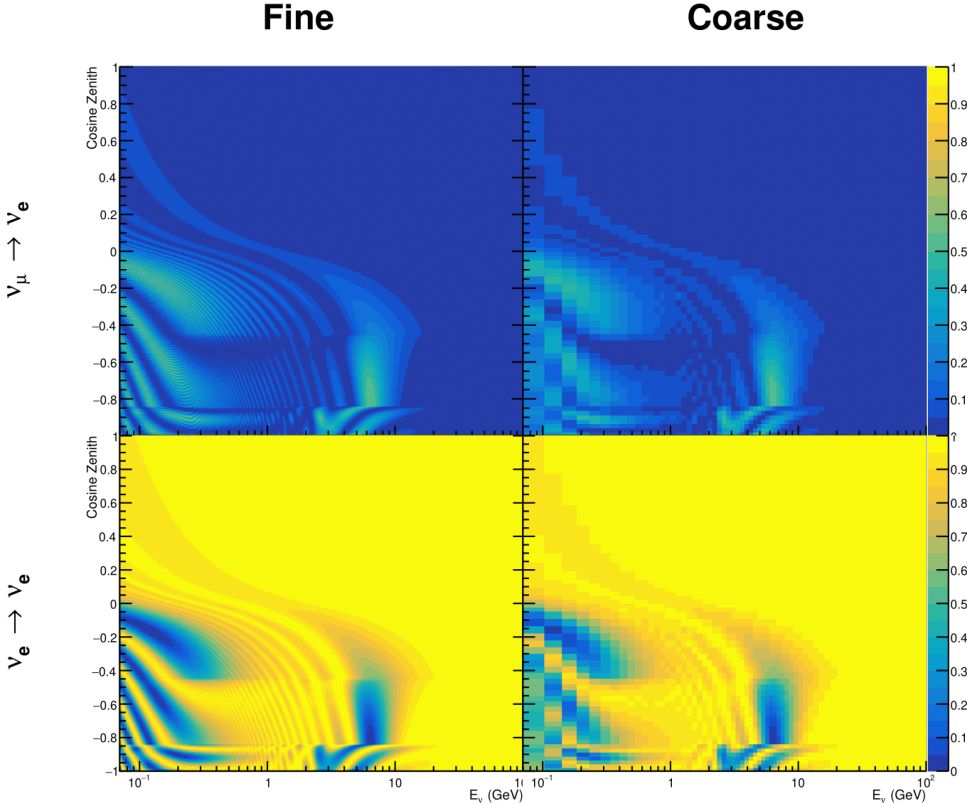


Figure 7.8: The oscillation probability, $P(\nu_\mu \rightarrow \nu_e)$ (top row) and $P(\nu_e \rightarrow \nu_e)$ (bottom row), given as a function of neutrino energy and zenith angle. The left column gives the “fine” binning used to calculate the oscillation probabilities and the right column illustrates the “coarse” binning used to reweight the Monte Carlo events. The fine binning choice is given with $N = 10$, which was determined to be below the threshold from Figure 7.6 and Figure 7.7.

be kept on GPU memory, rather than having to load these arrays onto GPU memory for each calculation. Reducing the memory transfer between CPU and GPU significantly reduces the time required for calculation. This can be seen in Figure 7.9, where the GPU implementation of CUDAProb3 is approximately three times faster than the ProbGPU engine.

Another significant advantage of CUDAProb3 is that it contains a CPU multi-threaded implementation which is not possible with the ProbGPU or prob3 engines. This eliminates the requirement for GPU resources when submitting jobs to batch systems. As illustrated in Figure 7.9, the calculation speed depends on the number

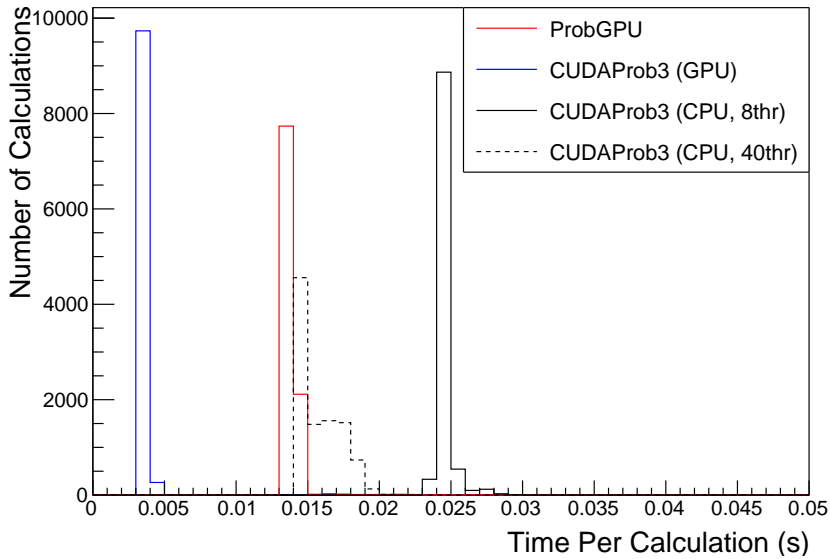


Figure 7.9: The calculation time taken to both calculate the oscillation probabilities and fill the “coarse” oscillograms, following the technique given in section 7.1, for the CUDAProb3 and ProbGPU (Red) calculation engines. CUDAProb3 has both a GPU (Blue) and CPU (Black) implementation, where the CPU implementation is multi-threaded. Therefore, 8-threads (solid) and 40-threads (dashed) configurations have been tested. Prob3, which is a CPU single-thread implementation has a mean step time of 1.142s.

of available threads. Using 8 threads (which is typical of the batch systems being used) is approximately twice as slow as the ProbGPU engine implementation, but would allow the fitting framework to be run on many more resources. This fact is utilised for any SK-only fits but GPU resources are required for any fits which include beam samples due to the ProbGPU requirement. Based on the benefits shown by the implementation in this section, efforts are being placed into including linear propagation for beam neutrino propagation into the engine [216].

7.3 Matter Density Profile

For an experiment observing neutrinos propagating through the Earth, a model of the Earth’s density profile is required. The model used within this analysis is based on the Preliminary Reference Earth Model (PREM) [80], as illustrated in Figure 2.8. Table 2.3 documents the density and radii of the layers used within the constant density approximation used by the SK-only analysis [79]. The

density measurements provided in the PREM model are provided in terms of mass density, whereas neutrino oscillations are sensitive to the electron number density. This value can be computed as the product of the chemical composition, or the Z/A value, and the mass density of each layer. Currently, the only way to measure the chemical composition value for layers close to the Earth's core is through neutrino oscillations. The chemical composition of the upper layers of the Earth's Mantle and the Transition zone is well known due to it being predominantly pyrolite which has a chemical composition value of 0.496 [217]. The chemical composition dial for the core layers is set to a value of 0.468, as calculated in [218]. As this value is less well known, it is assigned a Gaussian error with a standard deviation equivalent to the difference in chemical composition in core and mantle layers. Figure 7.10 illustrates the effect of moving from the $Z/A = 0.5$ method which is used in the official SK-only analysis to these more precise values.

The beam oscillation probability in this thesis uses a baseline of 295km, density 2.6g/cm^3 , and chemical composition 0.5 as is done by the official T2K-only analysis [219].

For a neutrino with given $E_\nu, \cos(\theta_Z)$, the oscillation probability calculation engine must be passed a list of the matter regions that the neutrino traversed, with the path length and fixed density in each region. However, a neutrino passing through the earth experiences a range of radii, and thus a range of densities, in each region. In the SK-only analysis, the earth density model used is piecewise-constant, thereby ignoring this effect. For this thesis, the density values for the calculation engine are found by averaging the earth density along the neutrino's path in each layer,

$$\langle \rho \rangle_i = \frac{1}{t_{i+1} - t_i} \int_{t_i}^{t_{i+1}} \rho(t) dt \quad (7.5)$$

where t_i are the intersection points between each layer and t is the path length of the trajectory across the layer. This leads to an improved approximation. For this averaging, the simplification of the PREM model developed in [220] is

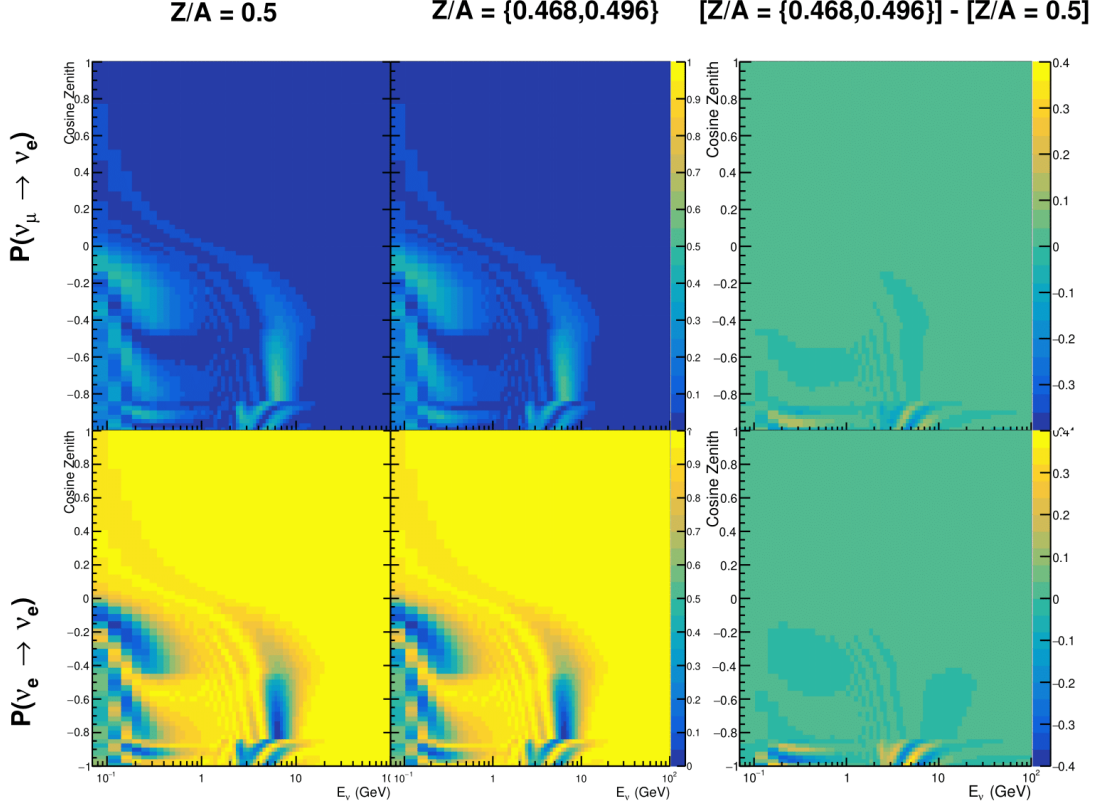


Figure 7.10: The oscillation probability, $P(\nu_\mu \rightarrow \nu_e)$ (top row) and $P(\nu_e \rightarrow \nu_e)$ (bottom row), given as a function of neutrino energy and zenith angle. The left column gives probabilities where the constant $Z/A = 0.5$ approximation which is used in the official SK-only analysis. The middle column gives the probabilities where $Z/A = [0.468, 0.498]$ values are used, as given in Table 2.3. The right column illustrates the difference in oscillation probability between the two different techniques.

used. The layers of the prem model are combined into four to reduce calculation time, with a quadratic fit to each section. This fit was not performed by the author of the thesis and is documented in [212]. The coefficients of the quadratic fit to each layer are given in Table 7.1 with the final distribution illustrated in Figure 7.11. The quadratic approximation is clearly much closer to the PREM model as compared to the constant density approximation.

The effect of using the quadratic density per $\cos(\theta_Z)$ model is highlighted in Figure 7.12. The slight discontinuity in the oscillation probability around $\cos(\theta_Z) \sim -0.45$ in the fixed density model, which is due to the transition to

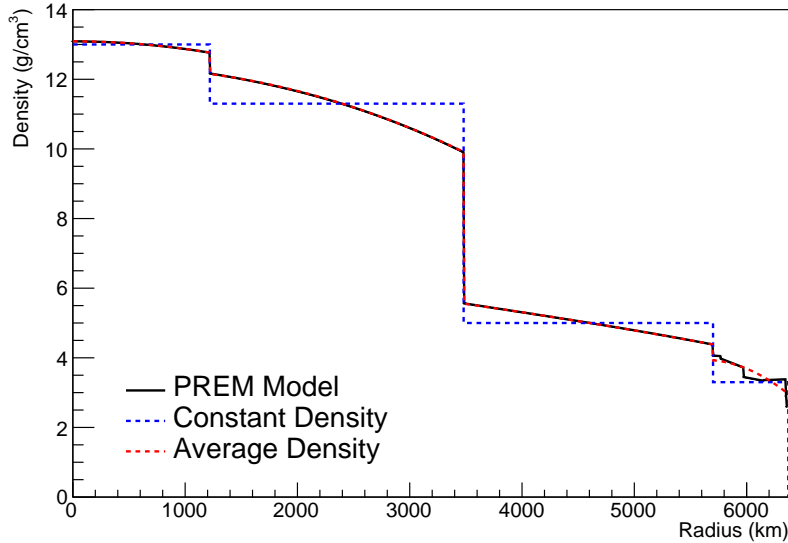


Figure 7.11: The density of the Earth given as a function of the radius, as given by the PREM model (Black), the constant density four-layer approximation (Blue), as used in the official SK-only analysis, and the quadratic approximation of the PREM model (Red).

Layer	Outer Radius [km]	Density [g/cm ³]
Inner Core	1220	$13.09 - 8.84x^2$
Outer Core	3480	$12.31 + 1.09x - 10.02x^2$
Lower Mantle	5701	$6.78 - 1.56x - 1.25x^2$
Transition Zone	6371	$-50.42 + 123.33x - 69.95x^2$

Table 7.1: The quadratic polynomial fits to the PREM model for four assumed layers of the PREM model. The fit to calculate the coefficients is given in [212], where $x = R / R_{\text{Earth}}$.

mantle layer boundary, has been reduced. This is expected as the difference in the density across this boundary is significantly smaller in the quadratic density model as compared to the constant density model. Whilst the difference in density across the other layer transitions is reduced, there is still a significant difference. This means the discontinuities in the oscillation probabilities remain but are significantly reduced. However, as the quadratic density approximation matches the PREM model well in this region, these discontinuities are due to the Earth model rather than an artifact of the oscillation calculation.

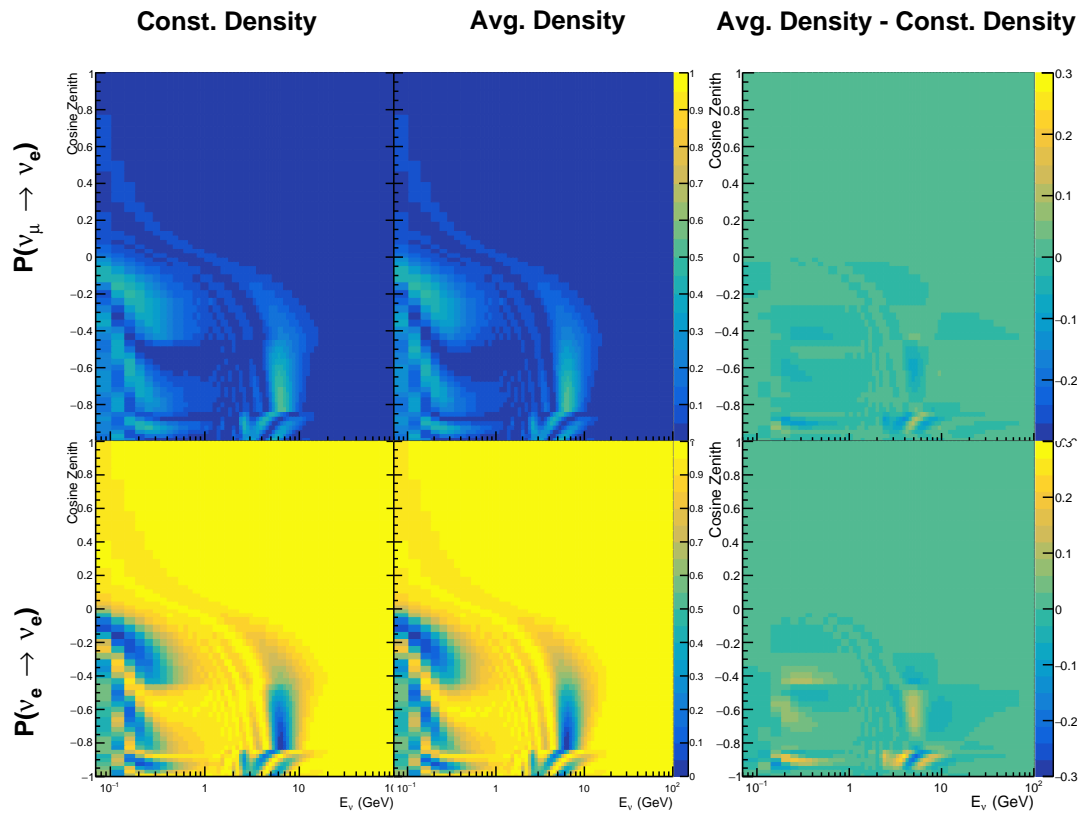


Figure 7.12: The oscillation probability, $P(\nu_\mu \rightarrow \nu_e)$ (top row) and $P(\nu_e \rightarrow \nu_e)$ (bottom row), given as a function of neutrino energy and zenith angle. The left column gives probabilities where the four-layer constant density approximation is used. The middle column gives the probabilities where the density is integrated over the trajectory, using the quadratic PREM approximation, for each $\cos(\theta_Z)$ is used. The right column illustrates the difference in oscillation probability between the two different techniques.

2754 7.4 Production Height Averaging

2755 As discussed in section 2.5, the height at which the cosmic ray flux interacts
 2756 in the atmosphere is not known on an event-by-event basis. The production
 2757 height can vary from the Earth’s surface to $\sim 50\text{km}$ above that. The SK-only
 2758 analysis methodology (described in section 7.1) for including the uncertainty
 2759 on the production height is to include variations from the Honda model when
 2760 pre-calculating the oscillation probabilities prior to the fit. This technique is not
 2761 possible for this analysis which uses continuous oscillation parameters that can
 2762 not be known prior to the fit. Consequently, an analytical averaging technique
 2763 was developed in [212]. The author of this thesis was not responsible for the
 2764 derivation of the technique but has performed the implementation and validation
 2765 of the technique for this analysis alone.

2766 Using the 20 production heights per Monte Carlo neutrino event, provided
 2767 as 5% percentiles from the Honda flux model, a production height distribution
 2768 $p_j(h|E_\nu, \cos \theta_Z)$ is built for each neutrino flavour $j = \nu_e, \bar{\nu}_e, \nu_\mu, \bar{\nu}_\mu$. In practice, a
 2769 histogram is filled with 20 evenly spaced bins in production height h between
 2770 0 and 50km. The neutrino energy and cosine zenith binning of the histogram
 2771 are the same as that provided in section 7.1. The average production height,
 2772 $\bar{h} = \int dh \frac{1}{4} \sum_j p_j(h|E_\nu, \cos(\theta_Z))$, is calculated. This assumes a linear average over
 2773 the four flavours of neutrino which are considered to be generated in cosmic ray
 2774 showers. The production height binning of this histogram is then translated into
 2775 $\delta t(h) = t(\bar{h}) - t(h)$, where $t(h)$ is the distance travelled along the trajectory.

2776 For the i^{th} traversed layer, the transition amplitude, $D_i(t_{i+1}, t_i)$, is computed.
 2777 The time-ordered product of these is then used as the overall transition amplitude
 2778 via

$$A(t_{n+1}, t_0) = D_n(t_{n+1}, t_n) \dots D_1(t_2, t_1) D_0(t_1, t_0), \quad (7.6)$$

2779 where,

$$\begin{aligned} D_n(t_{n+1}, t_n) &= \exp[-iH_n(t_{n+1} - t_n)] \\ &= \sum_{k=1}^3 C_k \exp[ia_k(t_{n+1} - t_n)] \end{aligned} \quad (7.7)$$

2780 is expressed as a diagonalised time-dependent solution to the Schrodinger
 2781 equation. The 0th layer is the propagation through the atmosphere and is the
 2782 only term that depends on the production height. Using the substitution $t_0 =$
 2783 $t(\bar{h}) - \delta t(h)$, it can be shown that

$$D_0(t_1, t_0) = D_0(t_1, \bar{h})D_0(\delta t). \quad (7.8)$$

2784 Thus Equation 7.6 becomes

$$\begin{aligned} A(t_{n+1}, t_0) &= D_n(t_{n+1}, t_n) \dots D_1(t_2, t_1)D_0(t_1, \bar{h})D(\delta t) \\ &= A(t_{n+1}, \bar{h}) \sum_{k=1}^3 C_k \exp[ia_k \delta t], \\ &= \sum_{k=1}^3 B_k \exp[ia_k \delta t]. \end{aligned} \quad (7.9)$$

2785 The oscillation probability averaged over production height is then calculated
 2786 as

$$\begin{aligned} \bar{P}(\nu_j \rightarrow \nu_i) &= \int d(\delta t) p_j(\delta t | E_\nu, \cos \theta_Z) P(\nu_j \rightarrow \nu_i) \\ &= \int d(\delta t) p_j(\delta t | E_\nu, \cos \theta_Z) A(t_{n+1}, t_0) A^*(t_{n+1}, t_0) \\ &= \sum_{km} (B_k)_{ij} (B_m)^*_{ij} \int d(\delta t) p_j(\delta t | E_\nu, \cos \theta_Z) \exp[i(a_k - a_m) \delta t] \end{aligned} \quad (7.10)$$

2787 It is important to note that the exact value of \bar{h} used does not matter as the
 2788 values of δt would change to compensate for any modification to the value of \bar{h} .

2789 In practice, implementation in CUDAProb3 [215] is relatively straightforward
 2790 as the majority of these terms are already calculated in the standard oscillation
 2791 calculation. Figure 7.13 illustrates the results of the production height averaging.

2792 As expected, the main effect is observed in the low-energy downward-going
 2793 and horizontal-going events. Upward-going events have to travel the radius
 2794 of the Earth, $R_E = 6371\text{km}$, where the production height uncertainty is a small
 2795 fraction of the total path length.

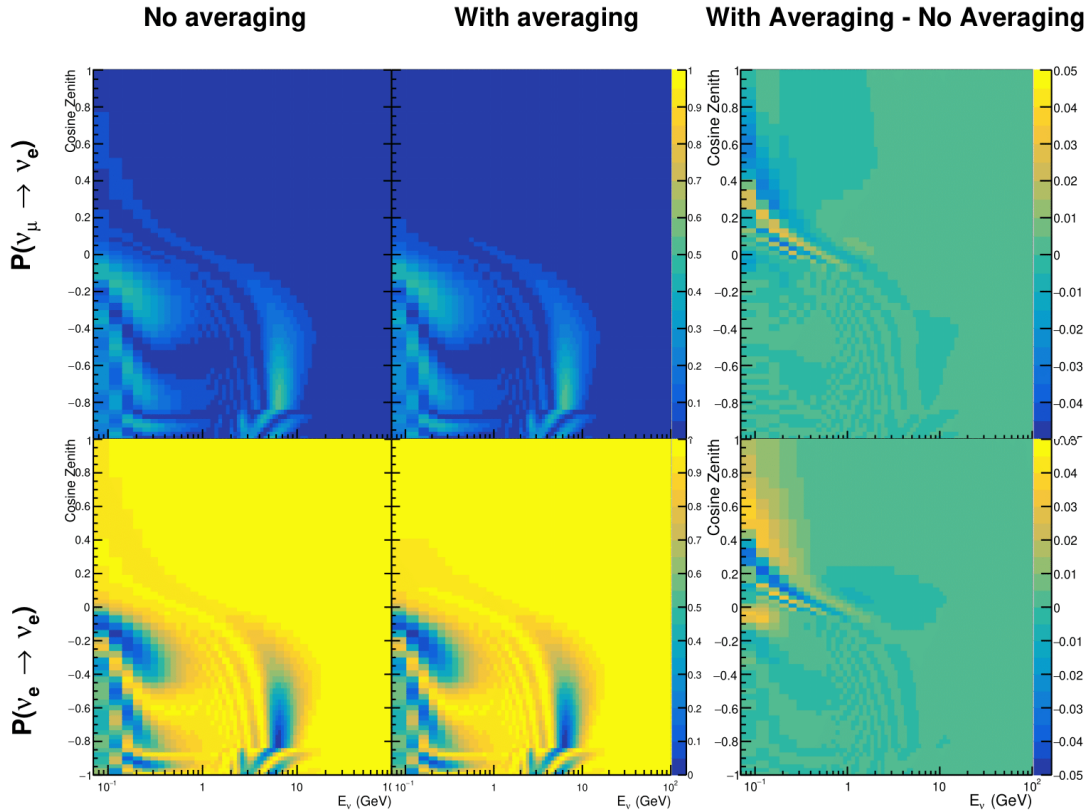


Figure 7.13: The oscillation probability, $P(\nu_\mu \rightarrow \nu_e)$ (top row) and $P(\nu_e \rightarrow \nu_e)$ (bottom row), given as a function of neutrino energy and zenith angle. The left column gives probabilities where a fixed production height of 25km is used. The middle column gives the probabilities where the production height is analytically averaged. The right column illustrates the difference in oscillation probability between the two different techniques.

8

2796

2797

Oscillation Analysis

2798 Using the samples and systematics defined in chapter 6, this chapter documents
2799 a simultaneous beam and atmospheric oscillation analysis from the T2K and SK
2800 experiments. The MaCh3 Bayesian MCMC framework introduced in chapter 4
2801 is used for all studies performed within this thesis.

2802 The MaCh3 framework used throughout this thesis has been validated through
2803 many tests. The code which handles the beam far detector samples was developed
2804 by the author and validated by comparison to the 2020 T2K analysis [75]. The
2805 sample event rates and likelihood evaluations of beam samples generated by
2806 the framework used within this thesis were compared to those from the T2K
2807 analysis by the author of this thesis. Variations of the sample predictions were
2808 compared at $\pm 1\sigma$ and $\pm 3\sigma$ and good agreement was found in all cases. A similar
2809 study, led by Dr. C. Wret was used to validate the near detector portion of
2810 the code [205]. The implementation of the atmospheric samples within MaCh3
2811 was completed and cross-checked by the author of this thesis against the P-
2812 Theta framework (Introduced in section 3.2). Both fitters are provided with
2813 the same inputs and can therefore cross-validate each other. These validations
2814 compared the event rate and likelihood calculation. Documentation of all the
2815 above validations can be found in [205].

2816 8.1 Monte Carlo Prediction

2817 Using the three sets of dial values (generated, pre-BANFF, and post-BANFF tunes)
 2818 defined in subsection 6.4.3, the predicted event rates for each sample are defined
 2819 in Table 8.1. The oscillated (AsimovA defined in Table 2.2) and un-oscillated
 2820 event rates are calculated for each tune.

Sample	Total Predicted Events					
	Generated		Pre-fit		Post-fit	
	Osc	UnOsc	Osc	UnOsc	Osc	UnOsc
SubGeV- <i>elike</i> -0dcy	7121.0	7102.6	6556.8	6540.0	7035.2	7015.7
SubGeV- <i>elike</i> -1dcy	704.8	725.5	693.8	712.8	565.7	586.0
SubGeV- <i>mulike</i> -0dcy	1176.5	1737.2	1078.6	1588.1	1182.7	1757.1
SubGeV- <i>mulike</i> -1dcy	5850.7	8978.1	5351.7	8205.1	5867.0	9009.9
SubGeV- <i>mulike</i> -2dcy	446.9	655.2	441.6	647.7	345.9	505.6
SubGeV- <i>pi0like</i>	1438.8	1445.4	1454.9	1461.1	1131.1	1136.2
MultiGeV- <i>elike</i> -nue	201.4	195.6	201.1	195.3	202.6	196.7
MultiGeV- <i>elike</i> -nuebar	1141.5	1118.3	1060.7	1039.5	1118.5	1095.7
MultiGeV- <i>mulike</i>	1036.7	1435.8	963.1	1334.1	1015.2	1405.9
MultiRing- <i>elike</i> -nue	1025.1	982.2	1026.8	984.3	1029.8	986.4
MultiRing- <i>elike</i> -nuebar	1014.8	984.5	991.0	962.0	1008.9	978.5
MultiRing- <i>mulike</i>	2510.0	3474.4	2475.6	3425.8	2514.6	3480.4
MultiRingOther-1	1204.5	1279.1	1205.8	1280.3	1207.4	1281.0
PCStop	349.2	459.2	338.4	444.7	346.8	456.1
PCThru	1692.8	2192.5	1661.5	2149.8	1689.2	2187.8
UpStop-mu	751.2	1295.0	739.7	1271.6	750.4	1293.0
UpThruNonShower-mu	2584.4	3031.6	2577.9	3019.4	2586.8	3034.0
UpThruShower-mu	473.0	488.6	473.2	488.7	473.8	489.4
FHC1Rmu	328.0	1409.2	301.1	1274.7	345.1	1568.0
RHC1Rmu	133.0	432.3	122.7	396.2	135.0	443.9
FHC1Re	84.6	19.2	77.4	18.2	93.7	19.7
RHC1Re	15.7	6.4	14.6	6.1	15.9	6.3
FHC1Re1de	10.5	3.2	10.3	3.1	8.8	2.9

Table 8.1: The Monte Carlo predicted event rate of each far detector sample used within this analysis. Three model parameter tunes are considered, as defined in subsection 6.4.3. Un-oscillated and oscillated predictions are given, where the oscillated predictions assume Asimov A oscillation parameters provided in Table 2.2.

2821 Generally, the samples which target CCQE interaction modes observe a
 2822 decrease in prediction when using the pre-fit dial values. This is in accordance
 2823 with the Monte Carlo being produced assumed $M_A^{QE} = 1.21\text{GeV}$ [164] whilst

the pre-fit dial value is set to $M_A^{QE} = 1.03\text{GeV}$ as suggested by [203]. Furthermore, the predicted event rates of samples that target CCRES interaction modes are significantly reduced when considering the post-BANFF fit. This follows the observations in subsection 6.4.3. The strength of the accelerator neutrino experiment can be seen in the remarkable difference between the oscillated and unoscillated predictions in the FHC1Rmu and RHC1Rmu samples. There is a very clear decrease in the expected event rate between the oscillated and un-oscillated predictions which is not as obvious as in the atmospheric samples. This is due to the fact that the beam energy is tuned to the maximum disappearance probability which is not the case for the naturally generated atmospheric neutrinos.

8.1.1 Likelihood Scans

Using the definition of the likelihood presented in section 6.5, the response of each sample to a variation of a particular parameter can be studied. Figure 8.1 presents the variation of all the samples (beam and atmospheric) at the far detector to the oscillation parameters of interest: δ_{CP} , $\sin^2(\theta_{13})$, $\sin^2(\theta_{23})$, and Δm_{32}^2 . These plots are colloquially called ‘likelihood scan’ (or ‘log-likelihood scans’). The process of making these plots is as follows. An Asimov data set (following technique detailed in section 6.5) is built using the AsimovA oscillation parameters and pre-fit systematic tune. The Monte Carlo is then reweighted using the value of the oscillation parameter at each point on the x-axis of the scan. The likelihood is then calculated between the Asimov data and Monte Carlo prediction and plotted. This process identifies which samples drive the determination of the oscillation parameters in the joint fit.

Due to the caveat of fixed systematic parameters and the correlations between oscillation parameters being ignored when creating these likelihood scans, the value of $\chi^2 = 1$ (or $-2 \times \ln(\text{Likelihood}) = 1$) does not equate to the typical 1σ sensitivity. However, it does give an indication of which samples respond the strongest to a variation in a particular oscillation parameter. The point at

2852 which the likelihood tends to zero illustrates the value of the parameter used
 2853 to build the Asimov data prediction.

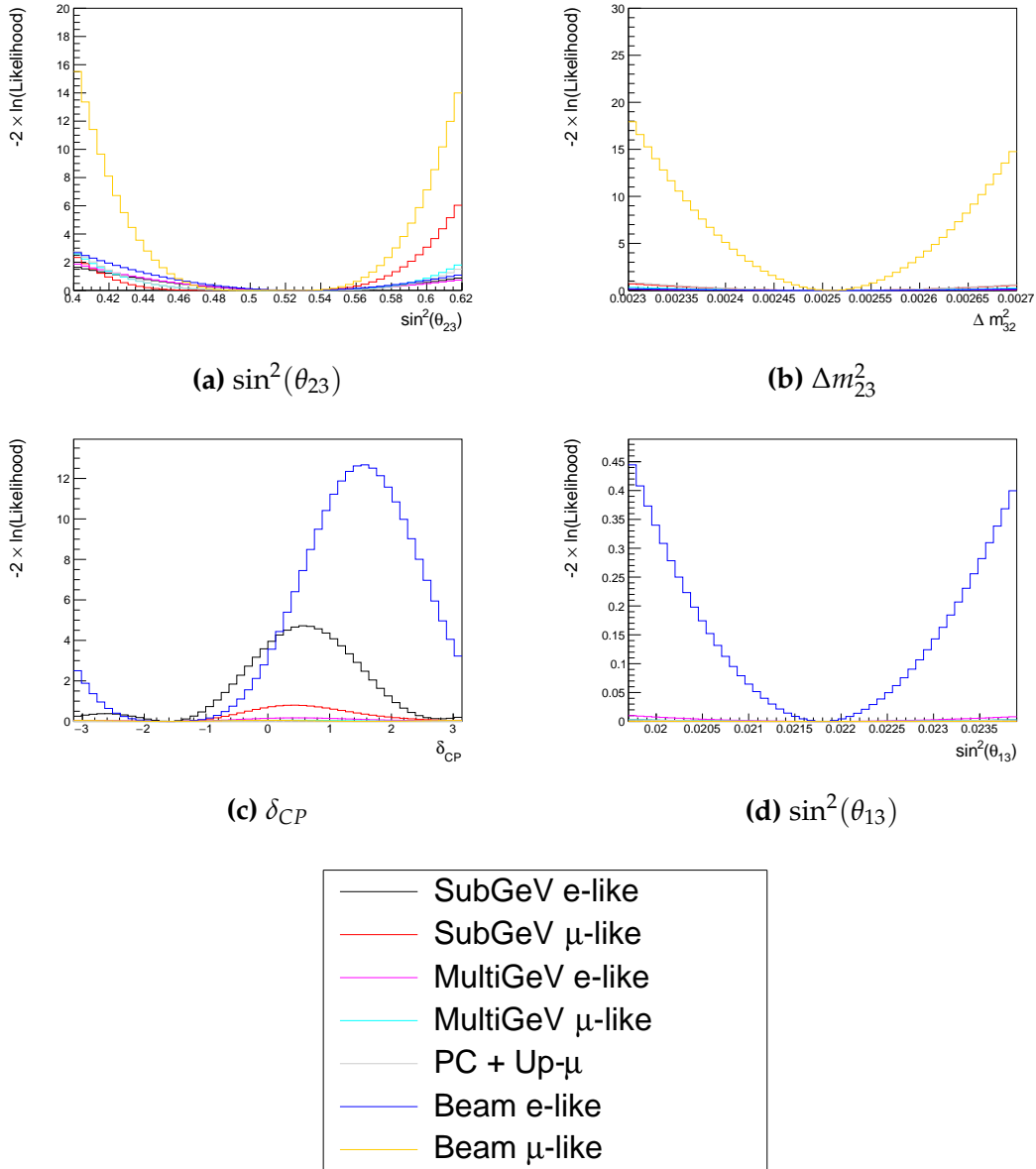


Figure 8.1: The response of the likelihood, as defined in section 6.5, illustrating the response of the samples to a variation of an oscillation parameter.

2854 The sensitivity to $\sin^2(\theta_{23})$ is mostly dominated by the beam muon-like
 2855 samples. The response of an individual atmospheric sample is small but non-
 2856 negligible such that the summed response over all atmospheric samples becomes
 2857 comparable to that of the muon-like beam samples. Consequently, the sensitivity

of the joint fit to $\sin^2(\theta_{23})$ would be expected to be greater than the beam-only analysis. The only sample which respond to the $\sin^2(\theta_{13})$ oscillation parameter is the electron-like beam samples. Consequently, no increase in sensitivity beyond that of the T2K-only analysis would be expected from the joint fit. Regardless, the sensitivity of the beam sample is significantly weaker than the external reactor constraint so prior knowledge will dominate any measurement that is included within this thesis. The Δm_{21}^2 and $\sin^2(\theta_{12})$ parameters are not considered as there is simply no sensitivity in any sample considered within this analysis. The response to Δm_{32}^2 is completely dominated by the beam muon-like samples. This is because the beam neutrino energy can be specifically tuned to match the maximal disappearance probability. Despite this, improvements to the $|\Delta m_{32}^2|$ sensitivity may be expected due to additional mass hierarchy determination added by the atmospheric samples.

Two-dimensional scans of the appearance ($\sin^2(\theta_{13})$ - δ_{CP}) and disappearance ($\sin^2(\theta_{23})$ - Δm_{32}^2) parameters are illustrated in Figure 8.2 and Figure 8.3, respectively. The caveat of fixed systematic parameters and correlations between other oscillation parameters being neglected still apply.

The appearance log-likelihood scans show the distinct difference in how the beam and atmospheric samples respond. The beam samples have an approximately constant width of the 2σ and 3σ contours, throughout all ranges of δ_{CP} . The response of the atmospheric samples to $\sin^2(\theta_{13})$ is very strongly correlated to the value of δ_{CP} being evaluated, with the strongest constraints around $\delta_{CP} \sim 1$. Consequently, this difference allows some of the degeneracy in a beam-only fit to be broken. Comparing the beam-only and joint fit likelihood scans, the 2σ continuous contour in δ_{CP} for beam samples is broken when the atmospheric samples are added. This may result in a stronger sensitivity to δ_{CP} . Similarly, the width of the 3σ contours also becomes dependent upon the value of δ_{CP} . Whilst these are encouraging results for the joint fit, these are not sensitivity measurements as the systematic parameters are fixed and the correlation between oscillation parameters is neglected. An interesting point to

note is that the atmospheric samples have little sensitivity to $\sin^2(\theta_{13})$ on their own, as evidenced in Figure 8.1, but can improve sensitivity to the parameter when combined within the simultaneous fit.

The response of the atmospheric samples in Figure 8.2 shows an interesting behaviour when considering the application of the reactor constraint. At higher values of $\sin^2(\theta_{13})$, two lobes appear around $\delta_{CP} \sim -\pi/2$ and $\delta_{CP} \sim 2.4$. If this distribution was projected onto the δ_{CP} axis, these lobes would mean the posterior distribution would have a significant dip between these values. However, the region of $\sin^2(\theta_{13})$ near the reactor constraint ($\sin^2(\theta_{13}) = (2.18 \pm 0.08) \times 10^{-2}$) is flatter across the range of δ_{CP} . Therefore, if we were to project only this region onto the δ_{CP} axis, the dip between the peaks would not be as significant. If this behaviour was to be seen in the results of a fit, these marginalisation effects would actually conspire to reduce the sensitivity to δ_{CP} if the reactor constraint was to be applied.

The disappearance log-likelihood scans in $\sin^2(\theta_{23})$ - Δm_{32}^2 space (Figure 8.3) show the expected behaviour when considering the one-dimensional scans already discussed. The uncertainty on the width of $|\Delta m_{32}^2|$ is mostly driven by the beam-only sensitivities. However, the width of this contour in the inverted mass region ($\Delta m_{32}^2 < 0$) is significantly reduced due to the ability of the atmospheric samples to select the correct (normal) mass hierarchy. The width of the uncertainty in $\sin^2(\theta_{23})$ is also reduced compared to the beam-only sensitivities, with a further decrease in the inverted hierarchy region due to the better mass hierarchy determination.



Figure 8.2: Two-dimensional log-likelihood scan of the appearance ($\sin^2(\theta_{13})$ - δ_{CP}) parameters showing the response of the beam samples (top left), atmospheric samples (top right) and the summed response (bottom). The Asimov A oscillation parameters, defined in Table 2.2, are known to be the true point (Black Cross). The position of the smallest log-likelihood is highlighted with the triangle. Prior uncertainty terms of the oscillation parameters are neglected. The two(three) sigma contour levels are illustrated with the dashed(solid) red line.

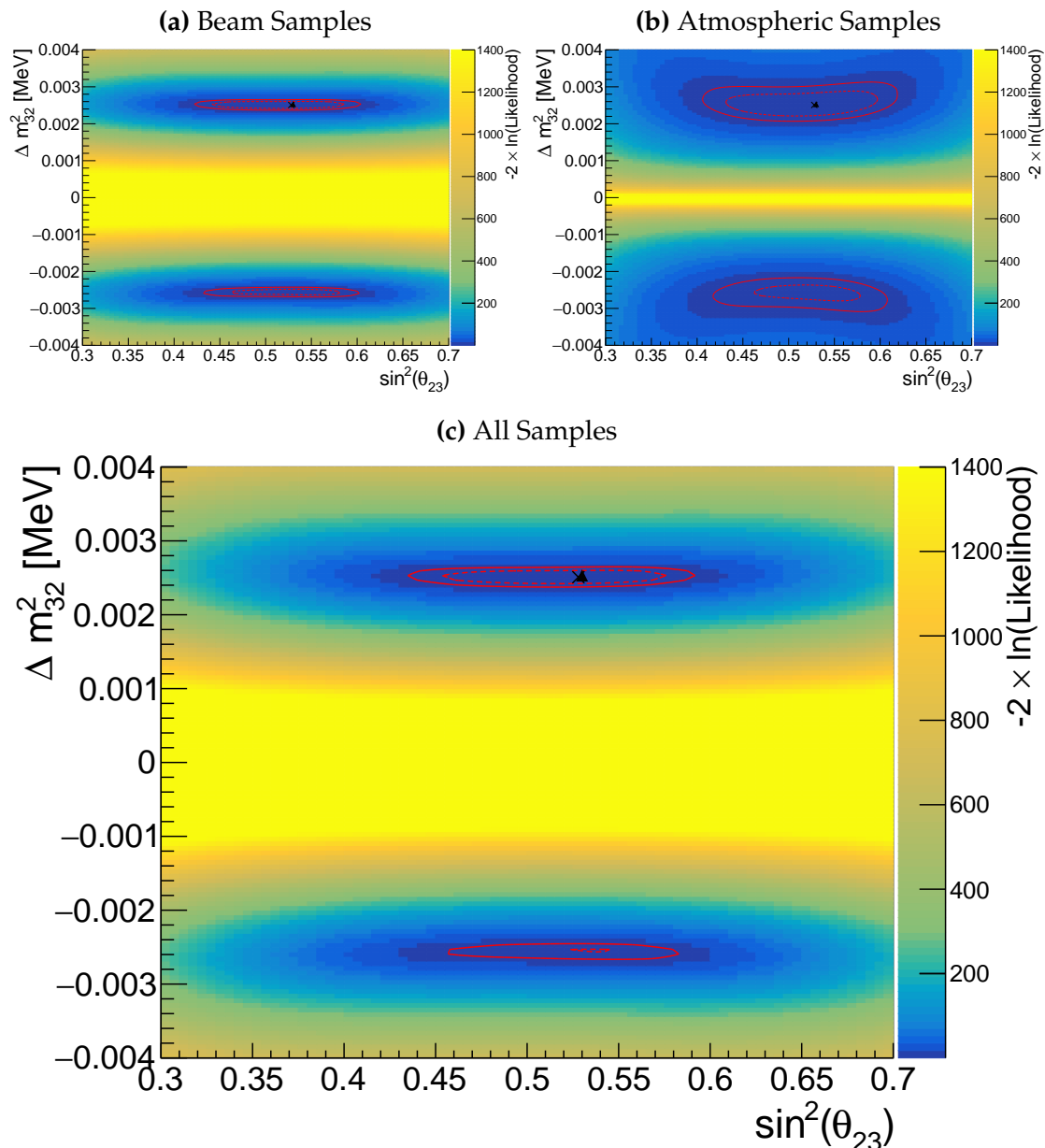


Figure 8.3: Two-dimensional log-likelihood scan of the disappearance ($\sin^2(\theta_{23})$)- Δm_{32}^2) parameters showing the response of the beam samples (top left), atmospheric samples (top right) and the summed response (bottom). The Asimov A oscillation parameters, defined in Table 2.2, are known to be the true point (Black Cross). The position of the smallest log-likelihood is highlighted with the triangle. Prior uncertainty terms of the oscillation parameters are neglected. The two(three) sigma contour levels are illustrated with the dashed(solid) red line.

The likelihood scans illustrated thus far only consider the sensitivity of this analysis for a fixed set of true oscillation parameters, namely Asimov A defined in Table 2.2. Whilst computational infeasible to run many fits at different parameter sets, it is possible to calculate the likelihood response to different Asimov data sets. Figure 8.4 and Figure 8.5 illustrate how the sensitivity changes for differing true values of δ_{CP} and $\sin^2(\theta_{23})$, respectively. For both of these plots, the other oscillation parameters are fixed at their Asimov A values. Consequently, the caveat of fixed systematic parameters and correlations between other oscillation parameters being neglected still applies.

To explain how these plots are made, consider Figure 8.4. This plot is built by considering multiple one-dimensional log-likelihood scans, each creating an Asimov data with the value of δ_{CP} taken from the x-axis. The likelihood to a particular Asimov data set is calculated after reweighting the Monte Carlo prediction to each value of δ_{CP} on the y-axis.

Figure 8.4 illustrates the sensitivity to δ_{CP} . Notably, the 1σ intervals contain regions in the off-diagonal for which the beam and atmospheric samples have broken and discontinuous contours. This indicates that there are regions of δ_{CP} which are degenerate. For example, for the x-axis value of $\delta_{CP} = 0$, the beam samples sensitivity would include two discontinuous regions excluded from the 1σ interval: $\delta_{CP} \sim 0$ and $\delta_{CP} \sim \pi$. The offset in δ_{CP} between the beam and atmospheric samples allows the joint fit to have increased sensitivity in these regions. Consequently, the difference between the beam-only and joint beam-atmospheric fit should be studied using multiple Asimov data sets.

Despite the increased sensitivity at 1σ , the 2σ intervals from the joint fit are more similar to the two independent sensitivities and the off-diagonal degeneracies mostly remain. This indicates that the joint fit has the strength to aid parameter determination but can not entirely break the degeneracies in δ_{CP} at higher confidence levels.

Figure 8.5 illustrates a similar analysis as above, although the value of $\sin^2(\theta_{23})$ is varied and δ_{CP} is fixed to the Asimov A parameter value. Due to the beam

²⁹⁴¹ parameters and baseline being tuned to specifically target this oscillation parameter, the average sensitivity of the beam samples is stronger than the atmospheric
²⁹⁴² samples. However, the degeneracy around maximal mixing ($\sin^2(\theta_{23}) = 0.5$) is
²⁹⁴³ significantly more peaked in the beam samples compared to the atmospheric
²⁹⁴⁴ samples. This behaviour is strengthened when considering the 2σ intervals, to the
²⁹⁴⁵ point where two distinct discontinuous regions of the 2σ intervals exist around
²⁹⁴⁶ the Asimov point $\sin^2(\theta_{23}) \sim 0.41, 0.6$. Given the caveat of only considering
²⁹⁴⁷ likelihood scans, the joint analysis would mostly eliminate the discontinuous
²⁹⁴⁸ intervals in these regions. This means that the joint fit could feasibly have an
²⁹⁴⁹ increased preference for the correct octant hypothesis.
²⁹⁵⁰

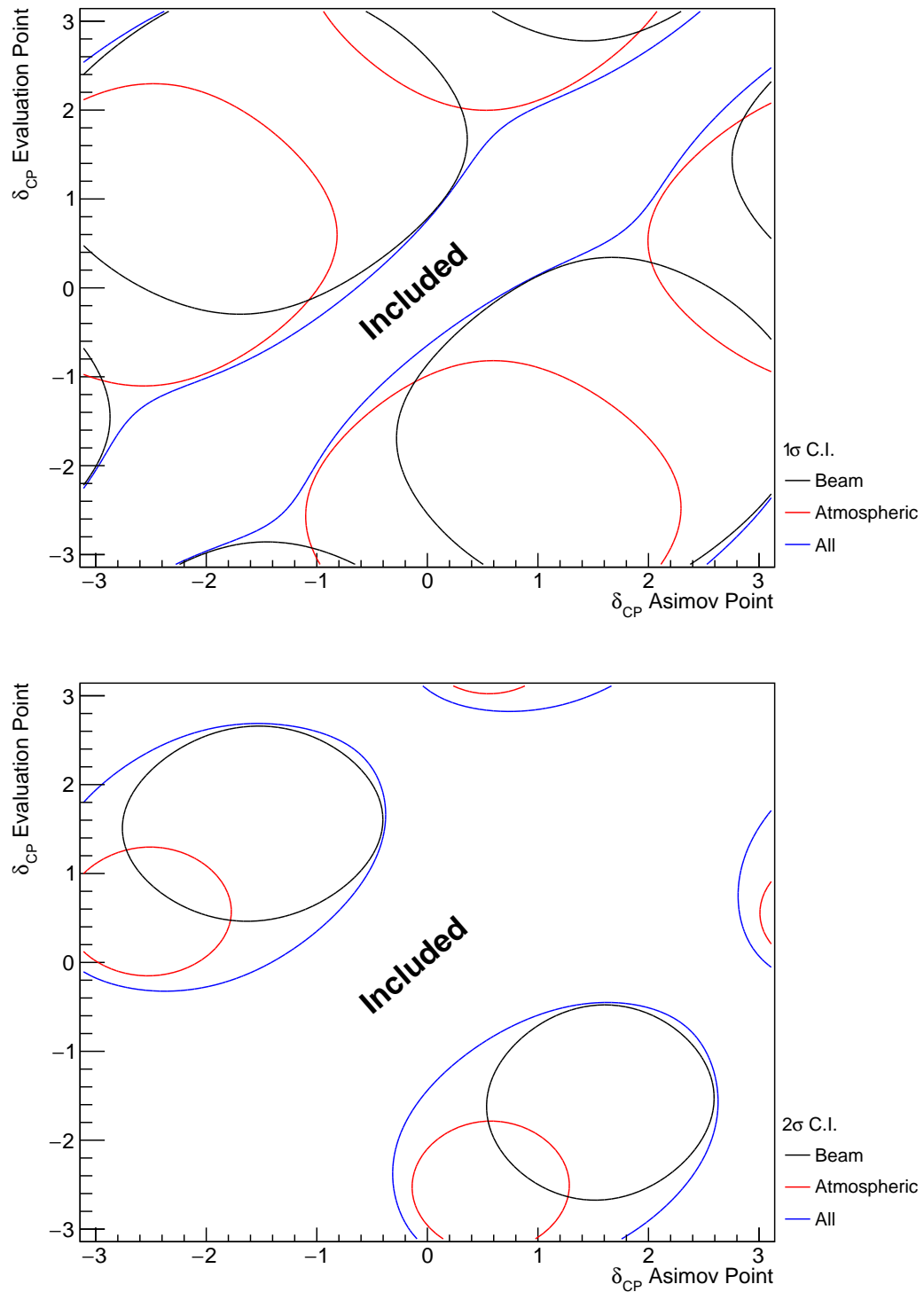


Figure 8.4: A series of one-dimensional likelihood scans over δ_{CP} , where an Asimov data set is built for each value of δ_{CP} on the x-axis and the likelihood is evaluated for each value of δ_{CP} on the y-axis. The diagonal represents the minimum log-likelihood and defines the region included within the 1σ (Top) and 2σ (Bottom) confidence intervals. The beam (black) and atmospheric (red) samples are individually plotted and the joint fit (blue) is the sum of the two.

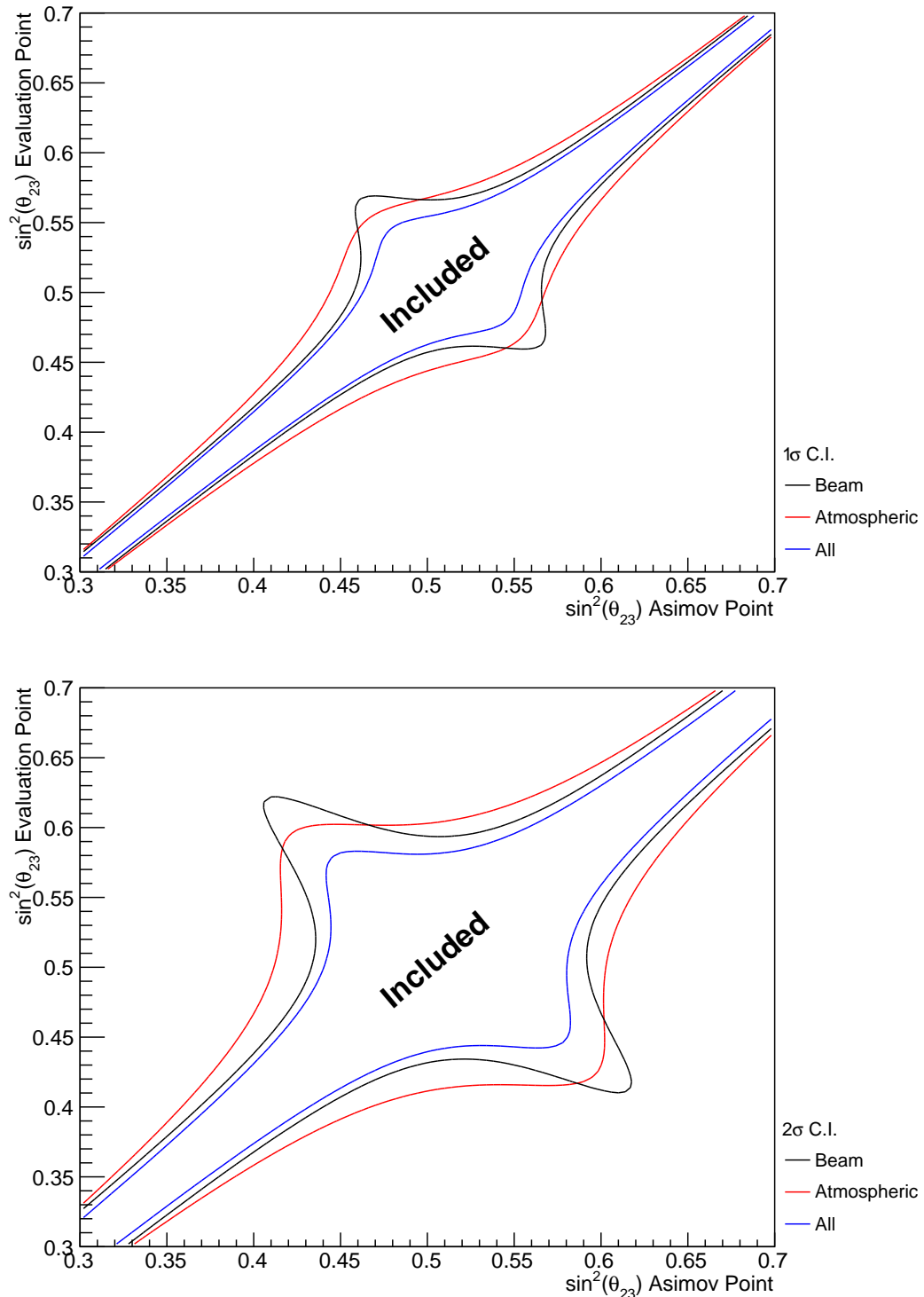


Figure 8.5: A series of one-dimensional likelihood scans over $\sin^2(\theta_{23})$, where an Asimov data set is built for each value of $\sin^2(\theta_{23})$ on the x-axis and the likelihood is evaluated for each value of $\sin^2(\theta_{23})$ on the y-axis. The diagonal represents the minimum log-likelihood and defines the region included within the 1σ (Top) and 2σ (Bottom) confidence intervals. The beam (black) and atmospheric (red) samples are individually plotted and the joint fit (blue) is the sum of the two.

Alongside oscillation parameters (Figure 8.1), the sensitivity to systematic parameters can also be studied for the joint fit. As some of these parameters are correlated between the beam and atmospheric events, the response of the atmospheric samples can modify the constraint. This means the systematics can have additional constraints than what they would from a beam-only analysis. Therefore, the response from the beam and the atmospheric samples to various systematic parameters has been compared in Figure 8.6. The Asimov data set has been created using the AsimovA oscillation parameter and the pre-fit systematic tune. For example, the systematic parameter controlling the effective axial mass coupling in CCQE interactions, M_A^{QE} , is clearly dominated by the ND constraint. An example where the response of the atmospheric sample is approximately similar to the near detector constraint is the 2p2h_Cto0 normalisation systematic. This systematic models the scaling of the 2p2h interaction cross-section on a carbon target to an oxygen target. There are also systematics which have no near detector constraint. For example, the systematic parameters which describe the normalisation of the NC1Gamma and NCOther interaction modes. The atmospheric samples are significantly more sensitive to these systematics than the beam samples due to their similar interaction contributions but relatively higher statistics (Table 8.1). As an example of how the atmospheric samples can help constrain systematic parameters used within the T2K-only analysis, these NC background events in beam electron-like samples will be considerably more constrained with the additional sensitivity of atmospheric samples. This would be expected to reduce the overall uncertainty of the beam electron-like event rates in the joint analysis compared to the beam-only studies. This could modify the sensitivity of the beam samples due to the more constrained background events.

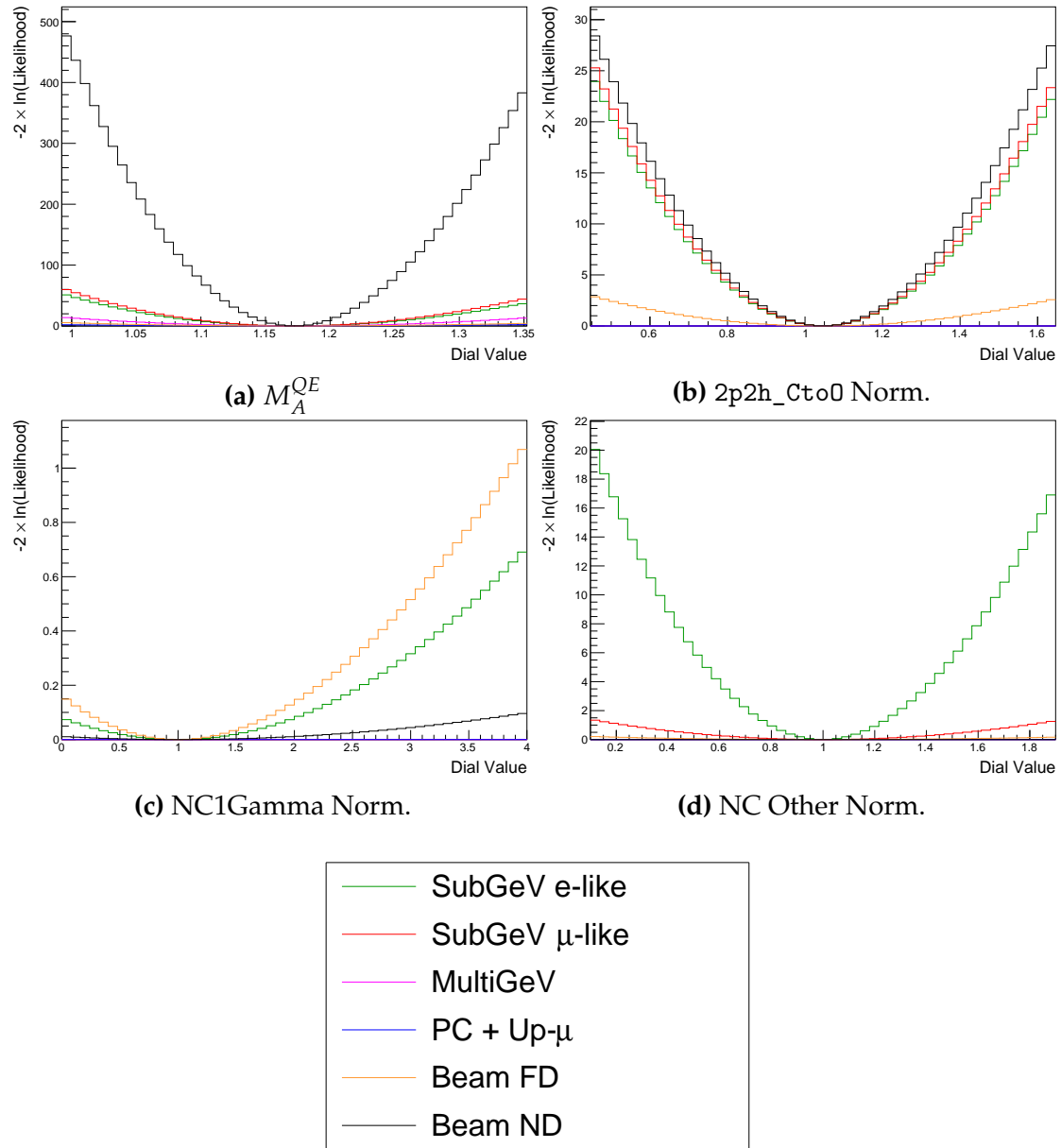


Figure 8.6: The response of the likelihood, as defined in section 8.2, illustrating the response of the samples to the various cross-section systematic parameters.

2976 8.2 Sensitivities

2977 The sensitivities of the joint T2K and SK oscillation analysis are presented in
2978 the form of Asimov fits. This technique builds an Asimov data set (follow-
2979 ing section 6.5) using the AsimovA oscillation parameters and post-BANFF
2980 systematic tune.

2981 In practice, the Asimov fits presented within this analysis are modified from
2982 the above definition. An Asimov prediction of both beam and atmospheric far
2983 detector samples is fit whilst the true data is used for near detector samples.
2984 The Asimov predictions at the far detector are built using the BANFF tuning (as
2985 discussed in section 3.2). These modifications mean that the results are equivalent
2986 to performing a far detector Asimov fit using inputs from the BANFF data fit.
2987 Consequently, this allows the results to be cross-checked with the results from
2988 the P-Theta analysis. The comparison has been performed and is documented in
2989 [221]. No significant discrepancies were found between the fitters.

2990 This section proceeds with the following studies. Firstly, the sensitivity of
2991 the atmospheric samples after the T2K cross-section has been applied to the low-
2992 energy events is detailed in subsection 8.2.1. This includes studying the choice of
2993 applying the 2020 PDG reactor constraint [76] to the atmospheric samples, which
2994 is documented in subsection 8.2.2. Additionally, the effect of applying the near-
2995 detector constraints onto the atmospheric samples is discussed in subsection 8.2.3.
2996 The main result is the sensitivity of the simultaneous beam and atmospheric fit.
2997 The sensitivities, both with and without the application of the reactor constraint,
2998 are presented in subsection 8.2.4 and subsection 8.2.5, respectively. To indicate
2999 the benefit of the joint analysis, the sensitivities are compared to the 2020 T2K
3000 sensitivities [75, 186] in subsection 8.2.6 and subsection 8.2.7. As shown in
3001 subsection 8.1.1, the response of the beam and atmospheric samples change
3002 depending upon the true set of oscillation parameters assumed. Therefore,
3003 subsection 8.2.8 documents the sensitivities at an alternative oscillation parameter

³⁰⁰⁴ set. It is important to note that these results have been published at the Neutrino
³⁰⁰⁵ 2022 conference on behalf of the T2K and SK collaborations [111].

3006 8.2.1 Atmospheric-Only Sensitivity Without Reactor Constraint

3007 This section presents the results of an Asimov fit using samples from the near
 3008 detector and only atmospheric samples from the far detector. The results are
 3009 presented as one-dimensional or two-dimensional histograms which have been
 3010 marginalised over all other parameters using the technique outlined in sub-
 3011 section 4.3.1. Each histogram displays the posterior probability density and
 3012 illustrates the credible intervals, calculated using the technique in subsection 4.3.2.
 3013 For these fits in this subsection, a flat penalty term is used for $\sin^2(\theta_{13})$ such the
 3014 reactor constraint is not applied. The Asimov data is generated assuming the
 3015 AsimovA oscillation parameter set defined in Table 2.2 and the post-BANFF
 3016 systematic parameter tune.

Without Reactor Constraint, Both Hierarchies

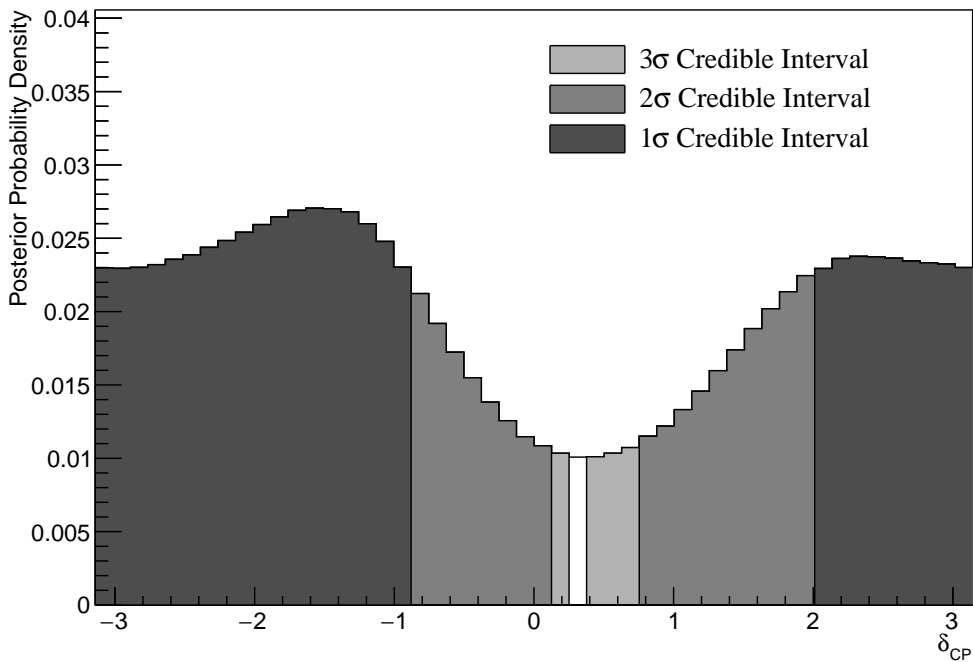


Figure 8.7: The one-dimensional posterior probability density distribution in δ_{CP} , marginalised over both hierarchies, from the SK atmospheric-only fit. The reactor constraint is not applied.

3017 Figure 8.7 illustrates the posterior probability density for δ_{CP} , marginalised
 3018 over both hierarchies. If instead, only steps in the normal hierarchy were
 3019 considered, the shape of the contours would change. The fit favours the known

3020 oscillation parameter ($\delta_{CP} = -1.601$) although the posterior probability is very
 3021 flat through the range of $-\pi < \delta_{CP} < -1$ and $2 < \delta_{CP} < \pi$. There is also a region
 3022 around $\delta_{CP} \sim 0.4$ which is disfavoured at 2σ . This indicates that the SK samples
 3023 can rule out some parts of the CP conserving parameter space reasonably well,
 3024 near $\delta_{CP} \sim 0.4$, when the true value of $\delta_{CP} \sim \pi/2$.

Without Reactor Constraint, Both Hierarchies



Figure 8.8: The one-dimensional posterior probability density distribution in Δm_{32}^2 , marginalised over both hierarchies, from the SK atmospheric-only fit. The reactor constraint is not applied.

3025 The posterior probability density in Δm_{32}^2 is given in Figure 8.8. This dis-
 3026 tribution includes steps in both the normal hierarchy (NH, $\Delta m_{32}^2 > 0$) and the
 3027 inverse hierarchy (IH, $\Delta m_{32}^2 < 0$). The highest posterior probability density is
 3028 found within the NH, which agrees with the known oscillation parameter value.
 3029 However, all of the credible intervals span both of the hierarchies hypotheses.
 3030 If instead, only steps in the normal hierarchy were considered, the shape of the
 3031 contours would change. The known oscillation parameter is $2.509 \times 10^{-3} \text{ eV}^2$,
 3032 which is contained within the 1σ credible interval.

	LO ($\sin^2 \theta_{23} < 0.5$)	UO ($\sin^2 \theta_{23} > 0.5$)	Sum
NH ($\Delta m_{32}^2 > 0$)	0.17	0.40	0.58
IH ($\Delta m_{32}^2 < 0$)	0.13	0.29	0.42
Sum	0.31	0.69	1.00

Table 8.2: The distribution of steps in an SK atmospheric-only fit, presented as the fraction of steps in the upper (UO) and lower (LO) octants and the normal (NH) and inverted (IH) hierarchies. The reactor constraint is not applied. The Bayes factors are calculated as $B(\text{NH}/\text{IH}) = 1.37$ and $B(\text{UO}/\text{LO}) = 2.24$.

Following the discussion in subsection 4.3.3, the Bayes factor for hierarchy preference can be calculated by determining the fraction of steps that fall into the NH and the IH regions, as an equal prior is placed on both hypotheses. A similar calculation can be performed by calculating the fraction of steps which fall in the lower octant (LO, $\sin^2 \theta_{23} < 0.5$) or upper octant (UO, $\sin^2 \theta_{23} > 0.5$). The fraction of steps, broken down by hierarchy and octant, are given in Table 8.2. The Bayes factor for preferred hierarchy model is $B(\text{NH}/\text{IH}) = 1.37$. Table 4.1 states this value of the Bayes factor indicates a weak preference for the normal hierarchy model. The Bayes factor for choice of octant is $B(\text{UO}/\text{LO}) = 2.24$. This is also classified as a weak preference for the UO. Both of these show that the fit is returning the correct choice of models (NH and UO) for the known Asimov A oscillation parameters defined in Table 2.2.

The 1σ credible intervals, broken down by hierarchy, and position in parameter space of the highest posterior probability density is given in Table 8.3. These are taken from the one-dimensional projections of the oscillation parameters, marginalised over all other parameters within the fit. For the known Asimov value of $\delta_{CP} = -1.601$, the 1σ credible interval rules out a region between $\delta_{CP} = -0.86$ and $\delta_{CP} = 1.96$, when marginalising over both hierarchies. The position of the highest posterior density is $\delta_{CP} = -1.57$ which is clearly compatible with the known oscillation parameter value.

The sensitivity of the atmospheric samples to $\sin^2(\theta_{13})$ is presented in Figure 8.9. The likelihood scans presented in Figure 8.1 suggest that the sensitivity

Parameter	Interval	HPD
δ_{CP} , (BH)	$[-\pi, -0.86], [1.96, \pi]$	-1.57
δ_{CP} , (NH)	$[-\pi, -0.86], [1.88, \pi]$	-1.57
δ_{CP} , (IH)	$[-\pi, -0.94], [1.96, \pi]$	-1.57
Δm_{32}^2 (BH) [$\times 10^{-3}\text{eV}^2$]	$[-3.00, -2.50], [2.35, 3.15]$	2.65
Δm_{32}^2 (NH) [$\times 10^{-3}\text{eV}^2$]	$[2.39, 3.04]$	2.64
Δm_{32}^2 (IH) [$\times 10^{-3}\text{eV}^2$]	$[-3.15, -2.45]$	-2.70
$\sin^2(\theta_{23})$ (BH)	$[0.476, 0.59]$	0.542
$\sin^2(\theta_{23})$ (NH)	$[0.476, 0.59]$	0.554
$\sin^2(\theta_{23})$ (IH)	$[0.476, 0.59]$	0.542

Table 8.3: The position of the highest posterior probability density (HPD) and width of the 1σ credible interval for the SK atmospheric-only fit. The reactor constraint is not applied. The values are presented by which hierarchy hypothesis is assumed: marginalised over both hierarchies (BH), normal hierarchy only (NH), and inverted hierarchy only (IH).

3055 to $\sin^2(\theta_{13})$ will be small. This behaviour is also seen in the fit results, where the
 3056 width of the 1σ credible intervals span the region of $\sin^2(\theta_{13}) = [0.008, 0.08]$. This
 3057 is more than an order of magnitude worse than the constraint from reactor
 3058 experiments [76].

3059 As previously discussed, the correlations between oscillation parameters are
 3060 also important to understand how the atmospheric samples respond. Figure 8.10
 3061 illustrates the two dimensional $\sin^2(\theta_{13}) - \delta_{CP}$ sensitivity, marginalised over all
 3062 other parameters. The displayed contours are calculated by marginalising over
 3063 both hierarchies. The shape of the 1σ credible interval shows that the constraining
 3064 power of the fit on δ_{CP} is dependent upon the value of $\sin^2(\theta_{13})$. Furthermore,
 3065 they show a strong resemblance to the likelihood scans illustrated in Figure 8.2.
 3066 Whilst the atmospheric samples do not strongly constrain the value of $\sin^2(\theta_{13})$,
 3067 the value of $\sin^2(\theta_{13})$ does impact the atmospheric sensitivity to δ_{CP} . A value of
 3068 $\sin^2(\theta_{13}) \sim 0.02$ would select a continuous contour over all values of δ_{CP} . This
 3069 shows the effect of the marginalisation effect previously described.

Without Reactor Constraint, Both Hierarchies



Figure 8.9: The one-dimensional posterior probability density distribution in $\sin^2(\theta_{13})$, marginalised over both hierarchies, from the SK atmospheric-only fit. The reactor constraint is not applied.

The $\sin^2(\theta_{23}) - \Delta m_{32}^2$ disappearance contours are illustrated in Figure 8.11.
 As expected, the area contained in the inverted hierarchy 1σ credible interval is slightly smaller than that in the normal hierarchy. This follows from the Bayes factor showing a weak preference for NH meaning that more of the steps will exist in the $\Delta m_{32}^2 > 0$ region. The known oscillation parameters of $\sin^2(\theta_{23}) = 0.528$ and $\Delta m_{32}^2 = 2.509 \times 10^{-3} \text{ eV}^2$ are contained within the 1σ credible interval.

Figure 8.12 illustrates the two-dimensional projections for each permutation of oscillation parameters which this analysis is sensitive to: δ_{CP} , $\sin^2(\theta_{13})$, $\sin^2(\theta_{23})$, and Δm_{32}^2 . The purpose of this plot is to illustrate the correlations between the oscillation parameters. The contours are calculated whilst marginalising over both hierarchies, however, only the NH is illustrated when plotting the Δm_{32}^2 parameter. As expected the correlations play a significant role in these sensitivity measurements, especially the choice of the $\sin^2(\theta_{13})$ constraint. The application of reactor constraint would be expected to alter both the width and position of the

Without Reactor Constraint, Both Hierarchies



Figure 8.10: The two-dimensional posterior probability density distribution in δ_{CP} – $\sin^2(\theta_{13})$, marginalised over both hierarchies, from the SK atmospheric-only fit. The reactor constraint is not applied.

3084 Δm_{32}^2 , δ_{CP} , and $\sin^2(\theta_{23})$ constraints. The majority of the octant model preference
 3085 comes from the region of $\sin^2(\theta_{13}) \sim 0.03$ such that the application of the reactor
 3086 constraint would not be expected to significantly change the octant preference.
 3087 The reactor constraint would result in lower values of $|\Delta m_{32}^2|$. Interestingly, the
 3088 distribution of steps in the δ_{CP} - $\sin^2(\theta_{13})$ plot is slightly flatter in the region of the
 3089 reactor constraint. Both the posterior distribution from this fit and the distribution
 3090 in Figure 8.2 show a region of low negative log-likelihood extending out towards
 3091 higher values of $\sin^2(\theta_{13})$ in the $\delta_{CP} \sim -\pi/2$ and $\delta_{CP} \sim 2$ region. Consequently,
 3092 the reactor constraint could feasibly reduce the sensitivity of the atmospheric
 3093 samples to δ_{CP} , due to the previously discussed marginalisation effects.

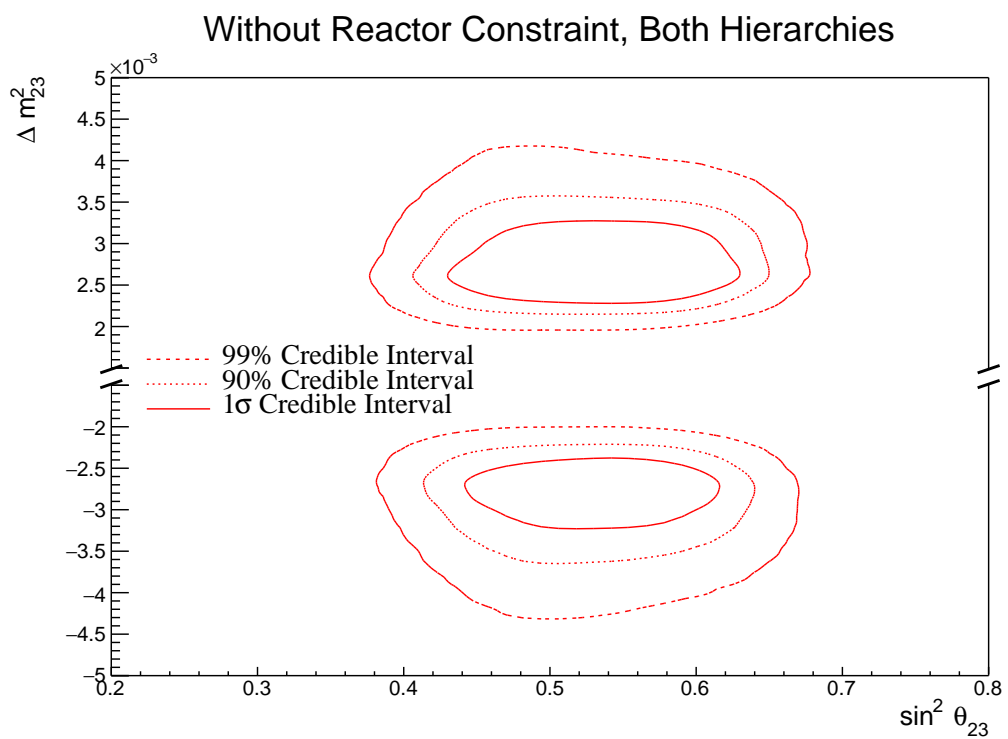


Figure 8.11: The two-dimensional posterior probability density distribution in $\Delta m_{32}^2 - \sin^2(\theta_{23})$, marginalised over both hierarchies, from the SK atmospheric-only fit. The reactor constraint is not applied.

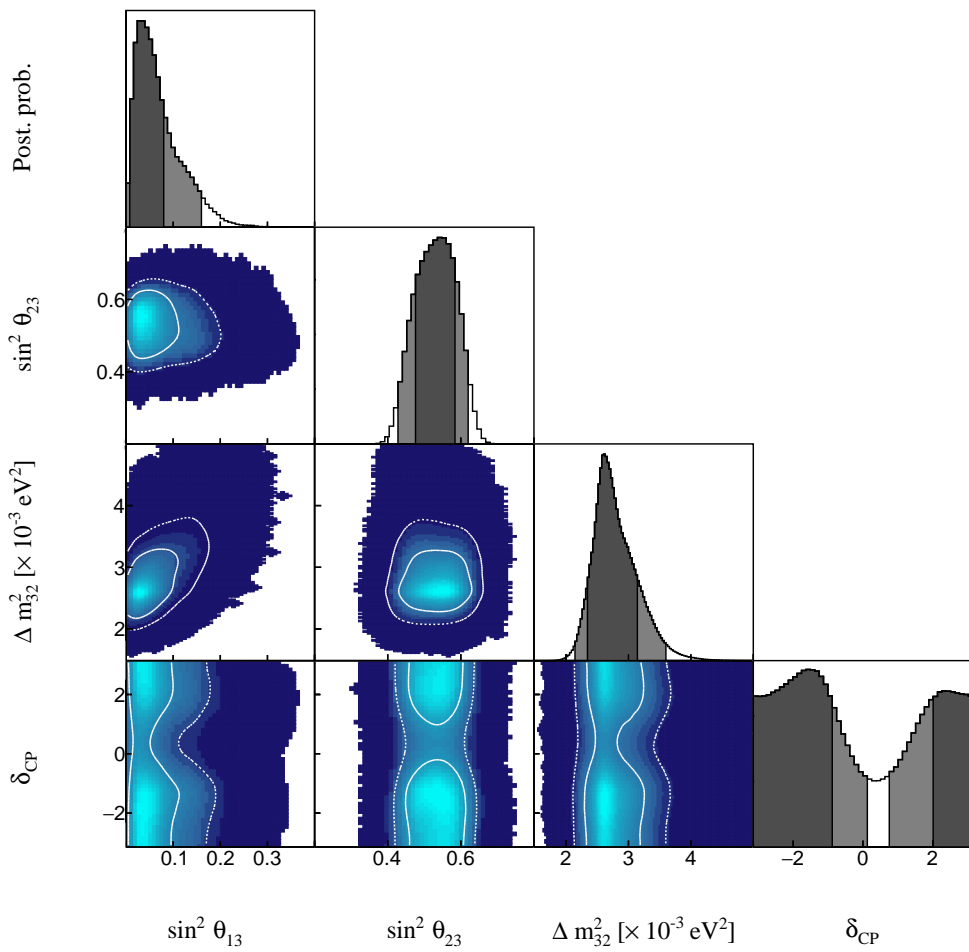


Figure 8.12: The posterior probability density distribution from the SK atmospheric-only fit. The reactor constraint is not applied. The distribution is given for each two-dimensional permutation of the oscillation parameters of interest. The one-dimensional distribution of each parameter is also given.

3094 8.2.2 Atmospheric-Only Sensitivity With Reactor Constraint

3095 The results in subsection 8.2.1 discuss the atmospheric sensitivity when the reactor
 3096 constraint is not applied. The correlations illustrated in Figure 8.12 indicate that
 3097 the marginalisation effects could contribute to differing sensitivities when the
 3098 external reactor constraint is applied. Using the technique discussed in subsec-
 3099 tion 4.1.1, the posterior distribution of the fit in subsection 8.2.1 can be reweighted
 3100 to include the reactor constraint of $\sin^2(\theta_{13}) = (2.18 \pm 0.08) \times 10^{-2}$ [76].

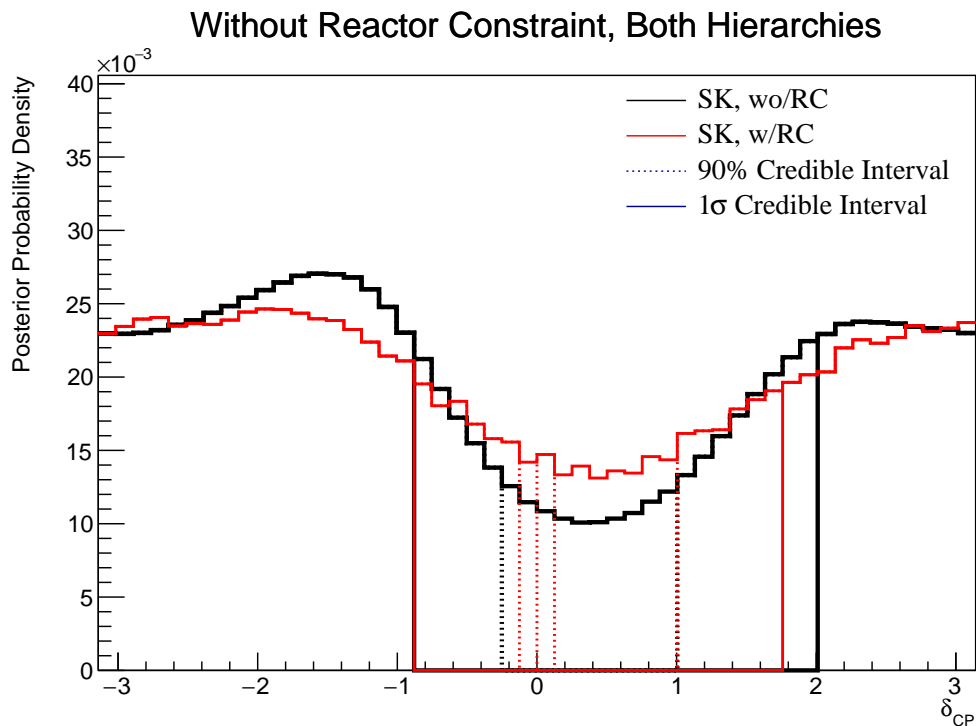


Figure 8.13: The one-dimensional posterior probability density distribution in δ_{CP} compared between the SK atmospheric-only fit (Black) and the SK atmospheric fit with the reactor constraint applied (Red). The distributions are marginalised over both hierarchies.

3101 Figure 8.13 illustrates the sensitivity to δ_{CP} of the atmospheric fit with reactor
 3102 constraint applied. The distribution is less peaked than the previous results.
 3103 This is due to the expected marginalisation effect previously discussed. The
 3104 width of the 1σ credible interval is increased when the reactor constraint is
 3105 applied, indicating less sensitivity to δ_{CP} in the region of $\sin^2(\theta_{13})$ preferred
 3106 by the reactor constraint.

Without Reactor Constraint, Both Hierarchies

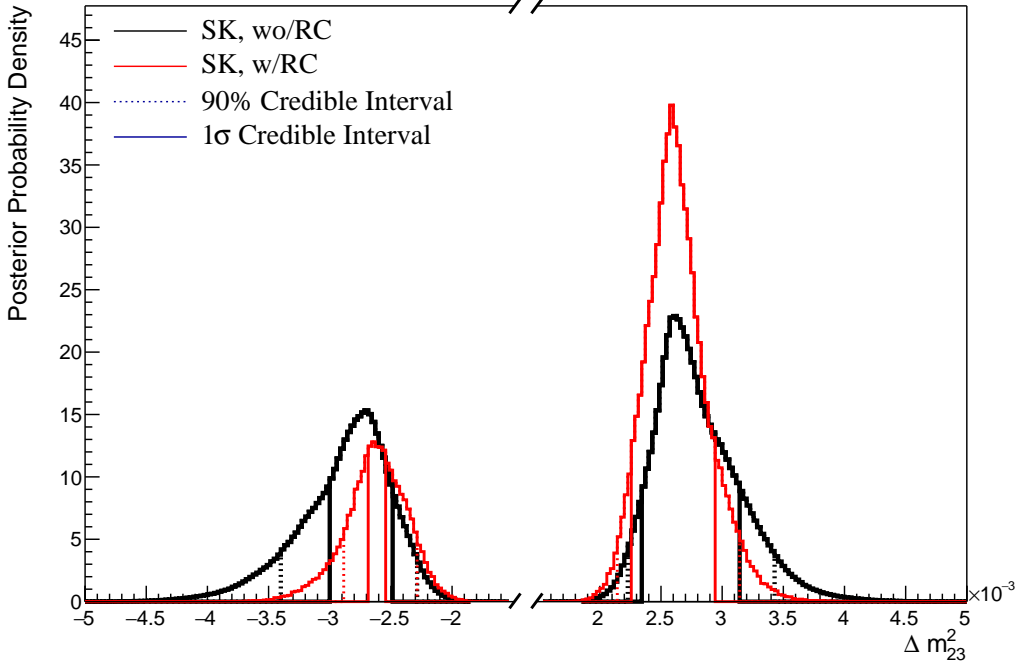


Figure 8.14: The one-dimensional posterior probability density distribution in Δm_{32}^2 compared between the SK atmospheric-only fit (Black) and the SK atmospheric fit with the reactor constraint applied (Red). The distributions are marginalised over both hierarchies.

3107 The reactor constraint increases the sensitivity of the atmospheric samples to
 3108 Δm_{32}^2 as illustrated in Figure 8.14. The 1σ credible interval in Δm_{32}^2 is determined
 3109 to be $[-2.70, -2.55] \times 10^{-3}\text{eV}^2$ and $[2.25, 2.95] \times 10^{-3}\text{eV}^2$. The width of the IH
 3110 credible interval is reduced by $\sim 70\%$ when the reactor constraint is applied. Due
 3111 to the marginalisation effects observed in Figure 8.12, the favoured region of Δm_{32}^2
 3112 moves closer to zero for both hierarchies. A clear explanation of this behaviour
 3113 is illustrated in Figure 8.15 which illustrates the posterior distribution in the
 3114 $\Delta m_{32}^2 - \sin^2(\theta_{13})$ parameters, marginalised over both hierarchies. The correlation
 3115 between Δm_{32}^2 and $\sin^2(\theta_{13})$ is such that lower values of $\sin^2(\theta_{13})$ tend towards
 3116 lower values of $|\Delta m_{32}^2|$. This moves the posterior distribution towards the known
 3117 oscillation parameter $\Delta m_{32}^2 = 2.509 \times 10^{-3}\text{eV}^2$.

3118 Table 8.4 presents the fraction of steps in each hierarchy and octant model
 3119 for the fit after the reactor constraint has been applied. The reactor constraint
 3120 significantly increases the NH preference, increasing the Bayes factor from



Figure 8.15: The two-dimensional posterior probability density distribution in Δm_{32}^2 – $\sin^2(\theta_{13})$ compared between the SK atmospheric-only fit (Black) and the SK atmospheric fit with the reactor constraint (Red). The distributions are marginalised over both hierarchies.

	LO ($\sin^2 \theta_{23} < 0.5$)	UO ($\sin^2 \theta_{23} > 0.5$)	Sum
NH ($\Delta m_{32}^2 > 0$)	0.21	0.53	0.74
IH ($\Delta m_{32}^2 < 0$)	0.08	0.18	0.26
Sum	0.29	0.71	1.00

Table 8.4: The distribution of steps in an SK atmospheric with reactor constraint fit, presented as the fraction of steps in the upper (UO) and lower (LO) octants and the normal (NH) and inverted (IH) hierarchies. The Bayes factors are calculated as $B(\text{NH}/\text{IH}) = 2.86$ and $B(\text{UO}/\text{LO}) = 2.39$.

³¹²¹ $B(\text{NH}/\text{IH}) = 1.37$ to $B(\text{NH}/\text{IH}) = 2.86$ when the reactor constraint is applied.

³¹²² This is still defined as a weak preference for NH hypothesis according to Jeffrey's

³¹²³ scale (see Table 4.1), however, it is a stronger preference than when the constraint

³¹²⁴ is not applied. The preference for the correct octant model is slightly increased

³¹²⁵ by the application of the reactor constraint which is consistent with expectation.

³¹²⁶ However, the conclusion that would be made does not significantly change.

3127 8.2.3 Application of Near Detector Constraints for Atmospheric 3128 Samples

3129 The choice of applying the near detector constraints to the low-energy atmo-
3130 spheric samples was introduced in subsection 6.4.3. This subsection illustrates
3131 the effect of that choice on the sensitivities of the atmospheric samples to the
3132 oscillation parameters. This Asimov data was generated assuming the ‘AsimovA’
3133 oscillation parameter set defined in Table 2.2 and the post-BANFF systematic
3134 parameter tune.

3135 The change in sensitivity on δ_{CP} is given in Figure 8.16. The reactor constraint
3136 is not applied in either of the fits within this comparison. The shape of the
3137 posterior is similar although less peaked at the Asimov point ($\delta_{CP} = -1.601$)
3138 and more symmetric between the regions of $\delta_{CP} = -1.601$ and $\delta_{CP} \sim 2.5$. The
3139 width of the 1σ credible intervals are approximately the same (identical to within
3140 a bin width) and the same conclusion holds for the higher credible intervals. The
3141 change in sensitivity to other oscillation parameters has been studied and no
3142 significant discrepancies were found. As expected, the sensitivities are statistics
3143 dominated and the exact choice of systematic model and constraint does not
3144 significantly affect the physics conclusions one would make from this analysis.



Figure 8.16: The one-dimensional posterior probability density distribution in δ_{CP} compared between the SK atmospheric-only fit where the near detector constraint is (Black) and is not (Red) applied. The distributions are marginalised over both hierarchies.

3145 8.2.4 Atmospheric and Beam Sensitivity without Reactor Con- 3146 straint

3147 This section presents the sensitivities of the simultaneous beam and atmospheric
 3148 analysis where the reactor constraint is not applied. Similar to the previous
 3149 studies, the Asimov data is built assuming the post-BANFF cross-section tune
 3150 and Asimov A oscillation parameters defined in Table 2.2. This fit uses all 18 near
 3151 detector beam samples, 5 far detector beam samples, and 18 atmospheric samples.
 3152 The sensitivity to δ_{CP} , marginalised over both hierarchies, is given in Figure 8.17.

Without Reactor Constraint, Both Hierarchies

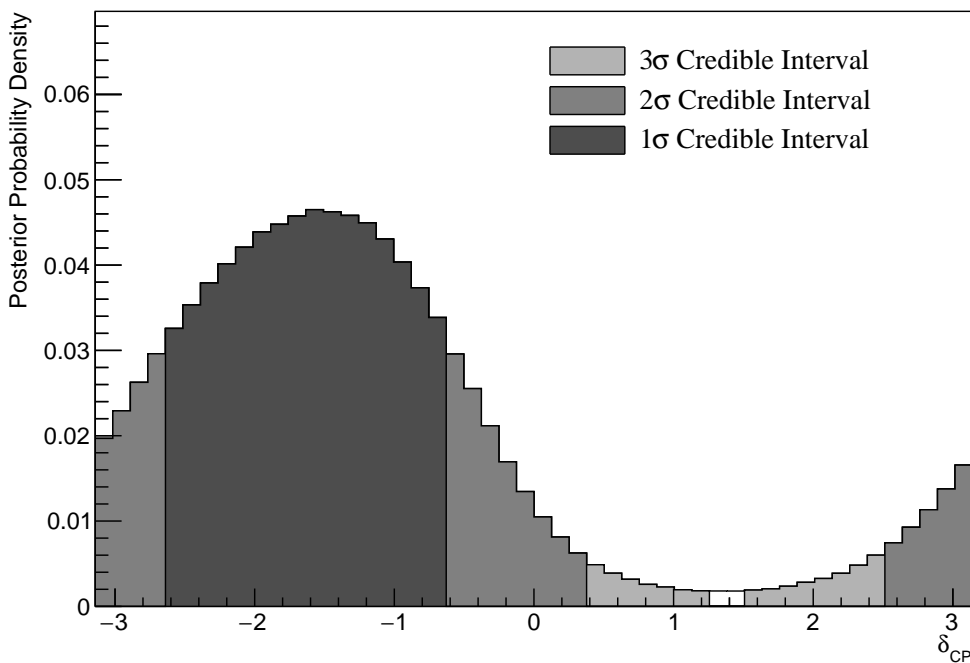


Figure 8.17: The one-dimensional posterior probability density distribution in δ_{CP} , marginalised over both hierarchies, from the joint beam and atmospheric fit. The reactor constraint is not applied.

3153 The credible intervals and highest posterior distribution for each oscillation
 3154 parameter is given in Table 8.5. The highest posterior probability density is
 3155 $\delta_{CP} = -1.58$ and is compatible with the known Asimov A value of $\delta_{CP} = -1.601$.
 3156 The CP-conserving values of $\delta_{CP} = 0, \pi, -\pi$ are disfavoured at 1 σ credible
 3157 interval. There is also a region around $\delta_{CP} = 1.4$ which is disfavoured at more
 3158 than 3 σ . Whilst these conclusions can only be made at this particular Asimov

3159 point, it does show that if the true value of δ_{CP} was CP-violating, this joint
3160 analysis would be able to disfavour CP conserving values at over 1σ without
3161 any external constraints. The highest posterior probability density does move
3162 further away from the Asimov point when only steps in the NH region are
3163 considered. This is due to the correlations between the value of δ_{CP} and the
3164 mass hierarchy, as will be later discussed.

Parameter	Interval	HPD
δ_{CP} , (BH)	$[-2.64, -0.63]$	-1.57
δ_{CP} , (NH)	$[-2.76, -0.63]$	-1.45
δ_{CP} , (IH)	$[-2.39, -0.88]$	-1.57
Δm_{32}^2 (BH) [$\times 10^{-3}\text{eV}^2$]	[2.46, 2.58]	2.49
Δm_{32}^2 (NH) [$\times 10^{-3}\text{eV}^2$]	[2.48, 2.56]	2.51
Δm_{32}^2 (IH) [$\times 10^{-3}\text{eV}^2$]	$[-2.60, -2.52]$	-2.55
$\sin^2(\theta_{23})$ (BH)	[0.48, 0.55]	0.509
$\sin^2(\theta_{23})$ (NH)	[0.48, 0.55]	0.509
$\sin^2(\theta_{23})$ (IH)	[0.48, 0.55]	0.521

Table 8.5: The position of the highest posterior probability density (HPD) and width of the 1σ credible interval for the joint beam and atmospheric fit. The reactor constraint is not applied. The values are presented by which hierarchy hypothesis is assumed: marginalised over both hierarchies (BH), normal hierarchy only (NH), and inverted hierarchy only (IH).

3165 The sensitivity to Δm_{32}^2 is illustrated in Figure 8.18, marginalised over both
3166 hierarchies. Notably, the 1σ credible interval is entirely contained within the
3167 normal hierarchy region, as illustrated in Table 8.5. This is illustrates reasonable
3168 sensitivity to the mass hierarchy model. This is also reflected in the 1σ credible
3169 intervals being approximately the same when they are made considering both
3170 hierarchies and when considering only the NH. The known oscillaton parameter
3171 is $\Delta m_{32}^2 = 2.509 \times 10^{-3}\text{eV}^2$. The normal hierarchy distribution favours this value
3172 with the highest posterior probability density of $\Delta m_{32}^2 = 2.51 \times 10^{-3}\text{eV}^2$.

3173 The fraction of steps in each of the mass hierarchy regions and octants of
3174 $\sin^2(\theta_{23})$ is given in Table 8.6. The Bayes factors are determined to be $B(\text{NH}/\text{IH}) =$

3175 3.67 and $B(\text{UO}/\text{LO}) = 1.74$. Jeffrey's scale (presented in Table 4.1) states that
 3176 this value of the hierarchy Bayes factor illustrates substantial evidence for the
 3177 normal hierarchy hypothesis. This corresponds to the correct hypothesis given
 3178 the known oscillation parameters. It is a stronger statement than the atmospheric-
 3179 only analysis can provide. It is important to note that this is a substantial
 3180 preference that requires no external constraints required. The Bayes factor for
 3181 octant determination represents a weak preference for the upper octant but does
 3182 select the correct octant model.

	LO ($\sin^2 \theta_{23} < 0.5$)	UO ($\sin^2 \theta_{23} > 0.5$)	Sum
NH ($\Delta m_{32}^2 > 0$)	0.29	0.50	0.79
IH ($\Delta m_{32}^2 < 0$)	0.08	0.13	0.21
Sum	0.37	0.63	1.00

Table 8.6: The distribution of steps in a joint beam and atmospheric fit, presented as the fraction of steps in the upper (UO) and lower (LO) octants and the normal (NH) and inverted (IH) hierarchies. The reactor constraint is not applied. The Bayes factors are calculated as $B(\text{NH}/\text{IH}) = 3.67$ and $B(\text{UO}/\text{LO}) = 1.74$.

3183 The sensitivity to $\sin^2(\theta_{23})$ is presented in Figure 8.19. There is a clear
 3184 preference for the upper octant but the peak of the distribution is relatively
 3185 flat. It peaks at $\sin^2(\theta_{23}) = 0.509$ which is in the region of the known value of
 3186 $\sin^2(\theta_{23}) = 0.528$. The difference in the highest posterior distribution and the
 3187 width of the credible interval is relatively unchanged when considering different
 3188 hierarchy models showing no strong correlation between $\sin^2(\theta_{23})$ and $|\Delta m_{32}^2|$.

3189 The sensitivity presented as a function of the appearance parameters ($\sin^2(\theta_{13}) -$
 3190 δ_{CP}) is given in Figure 8.20. As expected, the contours follow that given in
 3191 Figure 8.2, where the 2σ credible intervals have a closed contour excluding the
 3192 region around $\delta_{CP} \sim 1.2$. The width of the 3σ credible interval is also clearly
 3193 dependent upon the value of δ_{CP} . Close to the Asimov point, $\delta_{CP} = -1.601$, the
 3194 width of the 3σ credible interval approximately spans $\sin^2(\theta_{13}) = [0.013, 0.04]$.
 3195 This is reduced to a region of $\sin^2(\theta_{13}) = [0.023, 0.042]$ at the most disfavoured
 3196 value of δ_{CP} . This follows the behaviour shown in the likelihood scans. The 1σ

Without Reactor Constraint, Both Hierarchies

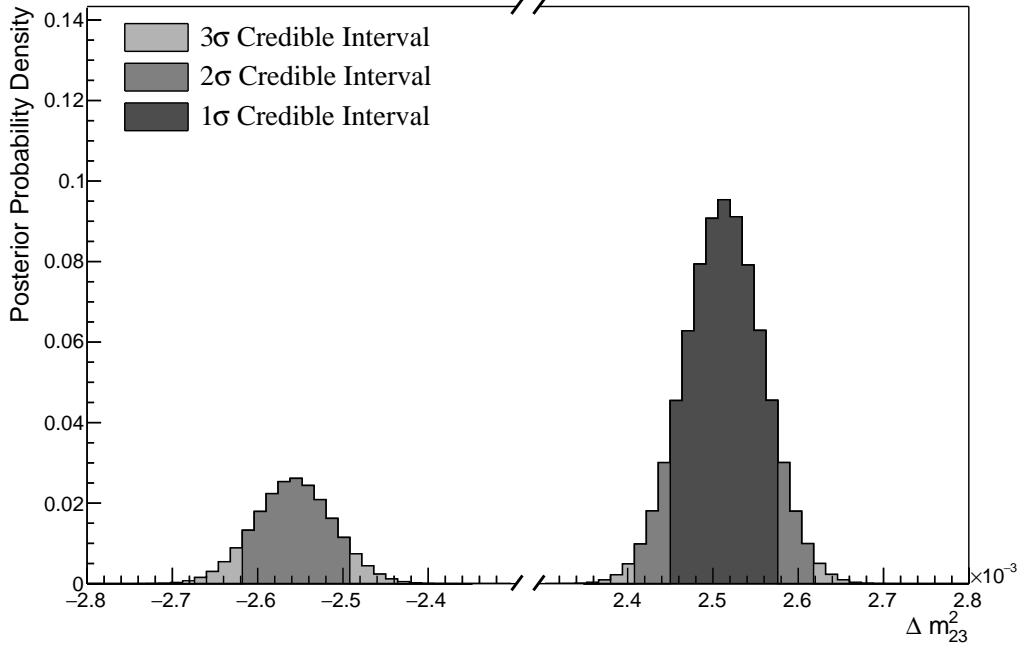


Figure 8.18: The one-dimensional posterior probability density distribution in Δm_{32}^2 , marginalised over both hierarchies, from the joint beam and atmospheric fit. The reactor constraint is not applied.

credible interval is consistent with both the known oscillation parameter and the reactor constraint ($\sin^2(\theta_{13}) = (2.18 \pm 0.08) \times 10^{-2}$). Application of the reactor constraint would be expected to decrease the width of the 1 σ credible intervals of δ_{CP} due to the triangular shape of the posterior probability.

The sensitivity in terms of the ‘disappearance’ parameters marginalised over both hierarchies is given in Figure 8.21. The area contained within the IH credible intervals is significantly smaller than those in the NH region. This is reflected in the IH credible intervals being tighter in the $\sin^2(\theta_{23})$ dimension. No significant correlation is observed between the value of $\sin^2(\theta_{23})$ and $|\Delta m_{32}^2|$.

The two-dimensional posterior distribution for each permutation of the oscillation parameters of interest is given in Figure 8.22. The most notable observation is that the $\sin^2(\theta_{13})$ and $\sin^2(\theta_{23})$ are anti-correlated. If the value of $\sin^2(\theta_{13})$ was known to be closer to the known oscillation parameter value, the preferred value of $\sin^2(\theta_{23})$ would increase furthering the preference for the UO. That

Without Reactor Constraint, Both Hierarchies

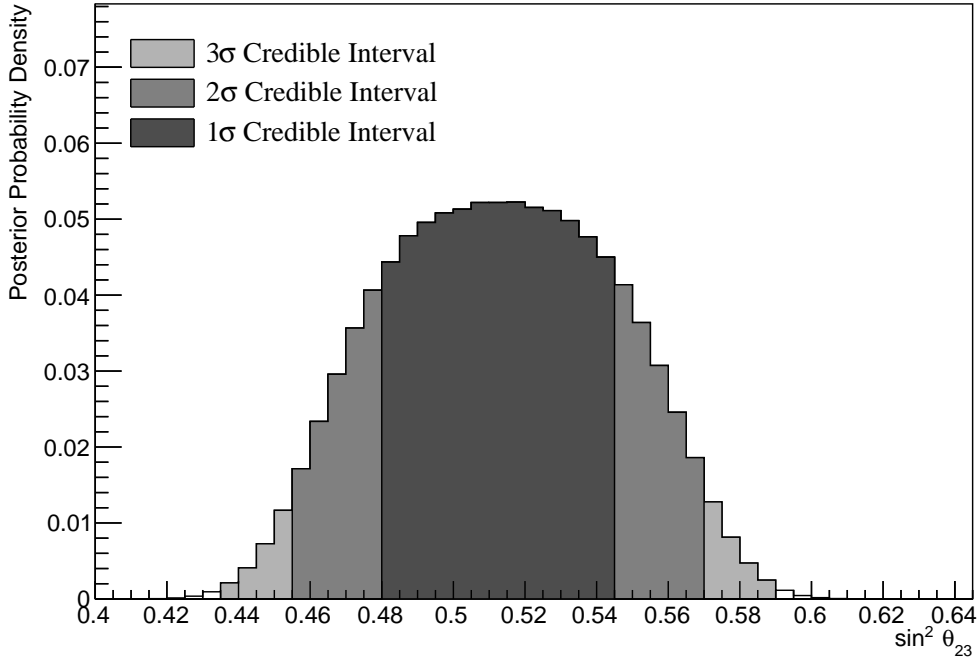


Figure 8.19: The one-dimensional posterior probability density distribution in $\sin^2(\theta_{23})$, marginalised over both hierarchies, from the joint beam-atmospheric fit. The reactor constraint is not applied.

would move the highest posterior probability closer in line with the Asimov value. This also means that the preference for the UO would be increased if the reactor constraint was to be applied.

Furthermore, the δ_{CP} and $|\Delta m_{32}^2|$ oscillation parameters are anti-correlated, such that higher values of $|\Delta m_{32}^2|$ prefer lower values of δ_{CP} . Whilst this is an interesting result on its own, the width of the Δm_{32}^2 contours also depend on $\sin^2(\theta_{13})$. This introduces another correlation effect that could modify the sensitivity to δ_{CP} once the reactor constraint is applied.

The correlation between $\sin^2(\theta_{13})$ and Δm_{32}^2 can be seen in Figure 8.23. A much larger fraction of the posterior distribution is contained in the NH for lower values of $\sin^2(\theta_{13})$. Consequently, the application of the reactor constraint would be expected to significantly increase the preference for NH.

Without Reactor Constraint, Both Hierarchies

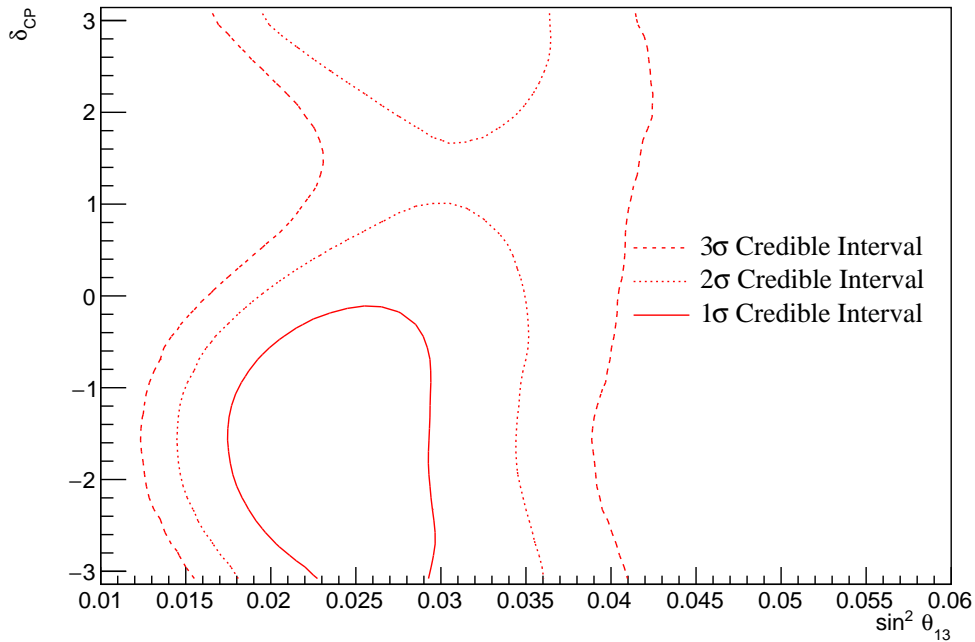


Figure 8.20: The two-dimensional posterior probability density distribution in δ_{CP} – $\sin^2(\theta_{13})$, marginalised over both hierarchies, from the joint beam and atmospheric fit. The reactor constraint is not applied.

Without Reactor Constraint, Both Hierarchies

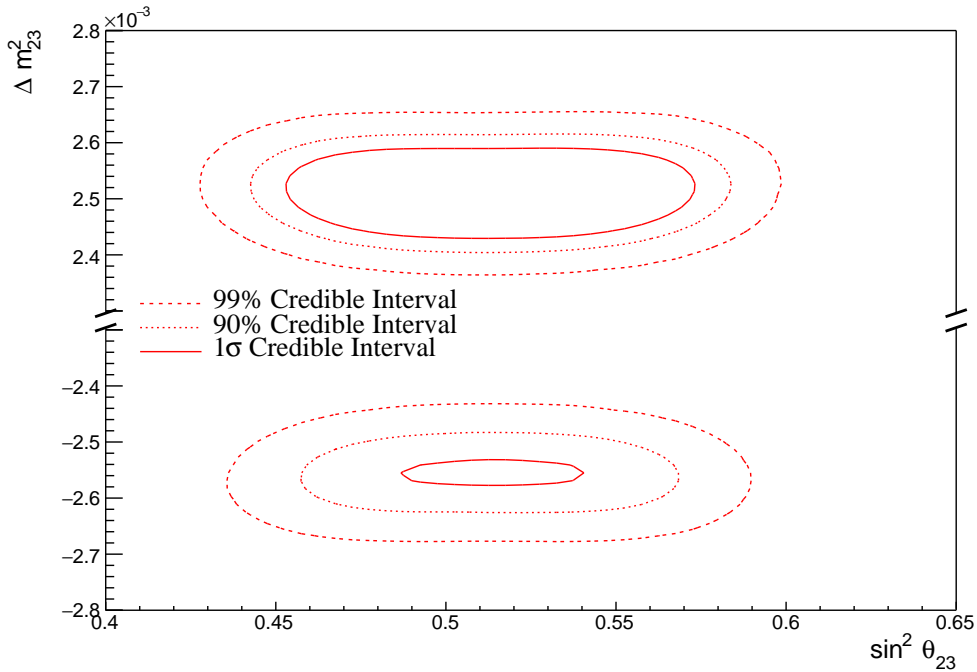


Figure 8.21: The two-dimensional posterior probability density distribution in Δm_{32}^2 – $\sin^2(\theta_{23})$, marginalised over both hierarchies, from the joint beam and atmospheric fit. The reactor constraint is not applied.

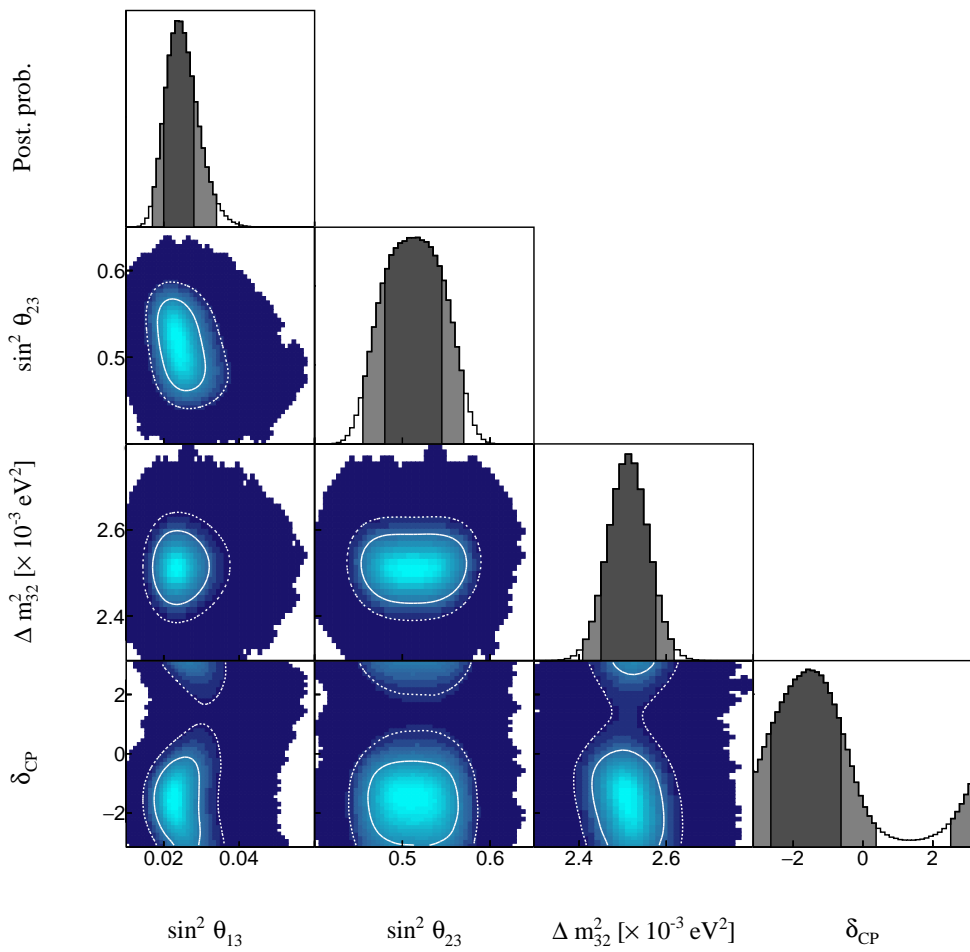


Figure 8.22: The posterior probability density distribution from the joint beam and atmospheric fit. The reactor constraint is not applied. The distribution is given for each two-dimensional permutation of the oscillation parameters of interest. The one-dimensional distribution of each parameter is also given.

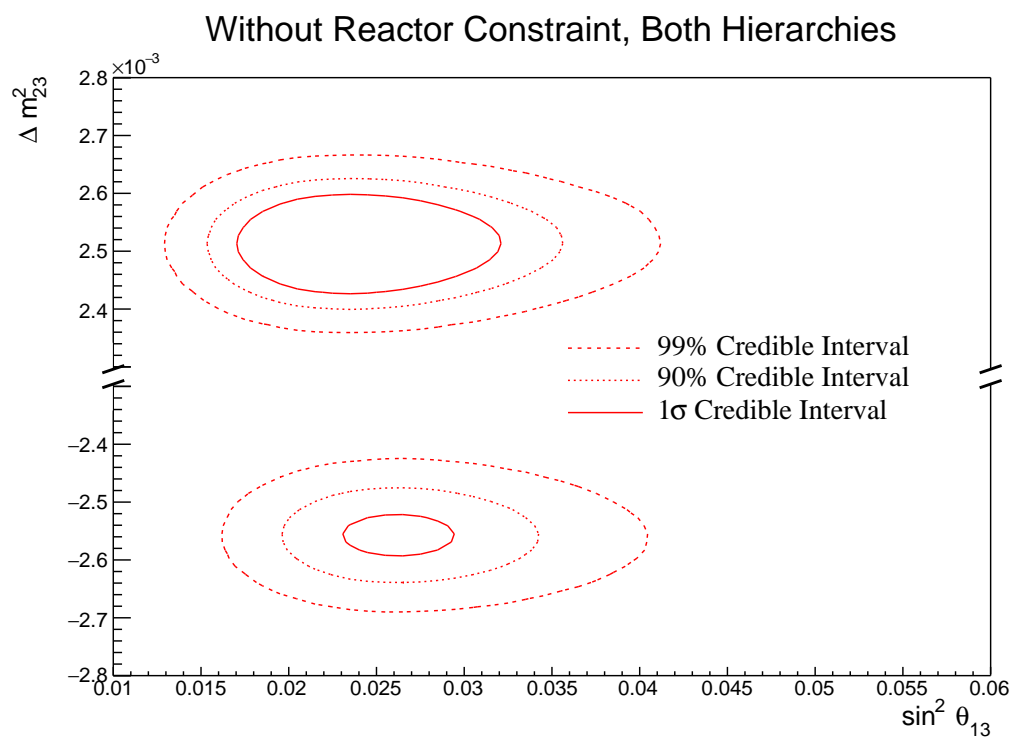


Figure 8.23: The two-dimensional posterior probability density distribution in $\Delta m_{32}^2 - \sin^2(\theta_{13})$, marginalised over both hierarchies, from the joint beam and atmospheric fit. The reactor constraint is not applied.

3223 8.2.5 Atmospheric and Beam Sensitivity with Reactor Constraint

3224 This section presents the sensitivities of the joint beam and atmospheric fit when
 3225 the reactor constraint is applied to $\sin^2(\theta_{13})$. As with the previous studies, the
 3226 Asimov data is made using the AsimovA oscillation parameter set defined in
 3227 Table 2.2 and the post-BANFF systematic parameter tune.

With Reactor Constraint, Both Hierarchies

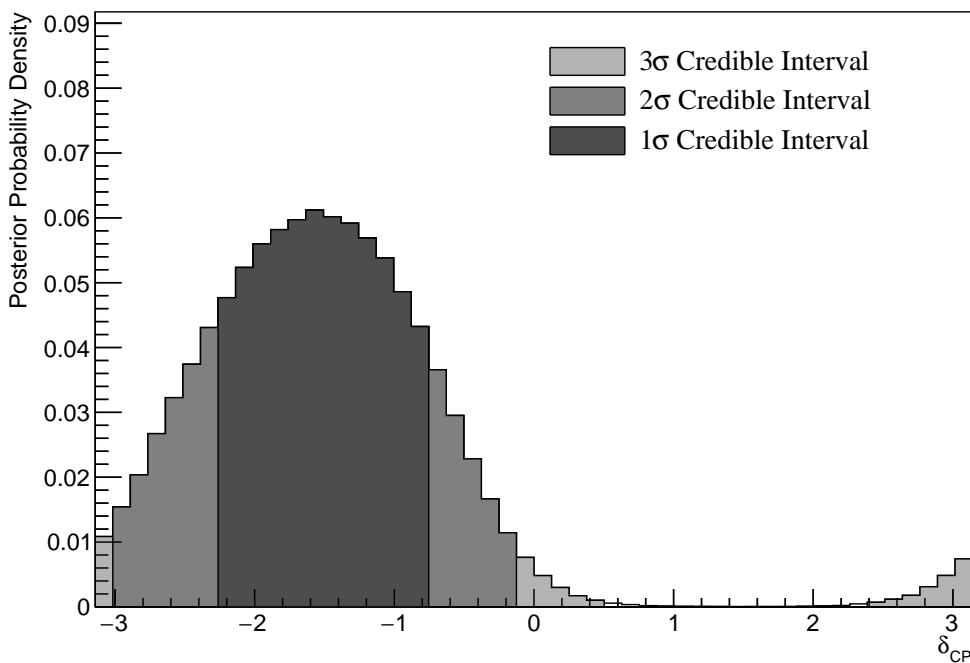


Figure 8.24: The one-dimensional posterior probability density distribution in δ_{CP} , marginalised over both hierarchies, from the joint beam and atmospheric fit where the reactor constraint is applied.

3228 Figure 8.24 illustrates the sensitivity to δ_{CP} , marginalised over both hierarchies.
 3229 The CP-conserving values of $\delta_{CP} = -\pi, 0, \pi$ are disfavoured at 2σ . Furthermore,
 3230 the 3σ credible interval excludes the region of $\delta_{CP} = [0.50, 2.39]$. Thus clearly
 3231 disfavouring the region of $\delta_{CP} = \pi/2$ at more than 3σ for this particular set
 3232 of known oscillation parameters. The width of the 1σ credible intervals and
 3233 the position of the highest posterior probability density is given in Table 8.7.
 3234 The highest posterior probability density in δ_{CP} is calculated as $\delta_{CP} = -1.57$
 3235 showing no significant biases in the determination of the known oscillation

parameters. The posterior distribution is more peaked around the known oscillation parameter value of $\delta_{CP} = -1.601$, as compared to the sensitivities when the reactor constraint is not applied (subsection 8.2.4). This follows from the correlations shown in Figure 8.20, where a lower value of $\sin^2(\theta_{13})$ results in tighter constraints on δ_{CP} .

The effect of applying the reactor constraint for δ_{CP} in the joint beam-atmospheric fit is presented in Figure 8.25. The posterior distribution from the two fits are marginalised over both hierarchies. Clearly, the reactor constraint improves the ability of the fit to select the known oscillation parameter as the shape of the distribution is much more peaked. This is also evidenced by the tightening of the 1σ and 90% credible intervals. Additionally, the disfavoured region of $1 < \delta_{CP} < 2$ is wider when the reactor constraint is applied.

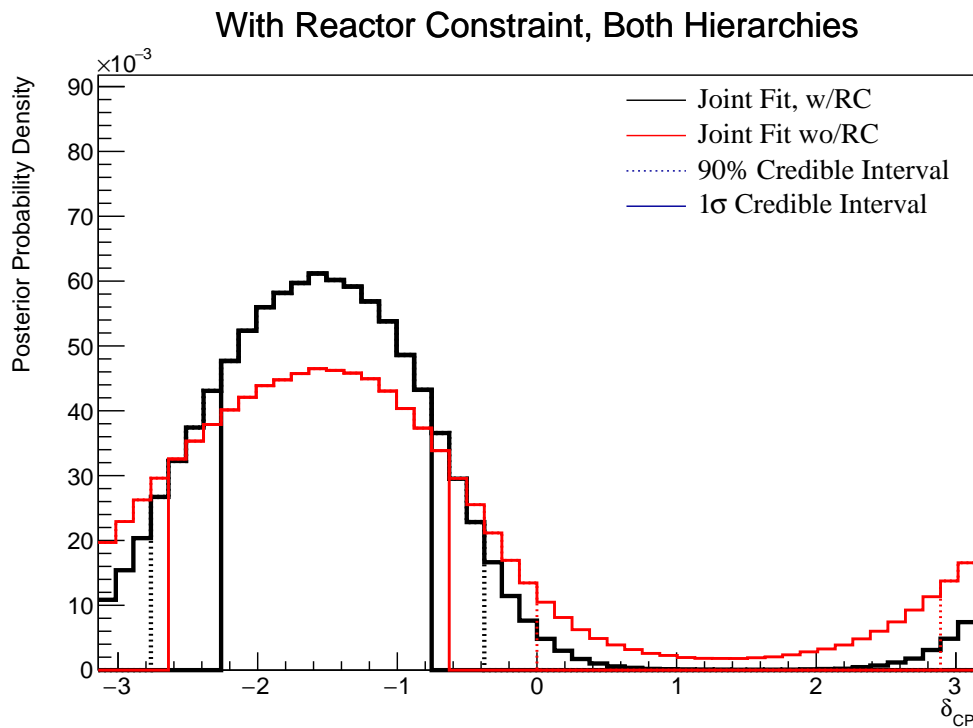


Figure 8.25: The one-dimensional posterior probability density distribution in δ_{CP} compared between the joint beam-atmospheric fit (Red) and the joint beam and atmospheric fit with the reactor constraint (Black). The distributions are marginalised over both hierarchies.

The sensitivity to $\sin^2(\theta_{23})$, marginalised over both hierarchies, is given in Figure 8.26. The highest posterior probability density is located at $\sin^2(\theta_{23}) = 0.527$

Parameter	Interval	HPD
δ_{CP} , (BH)	[-2.26, -0.75]	-1.57
δ_{CP} , (NH)	[-2.26, -0.75]	-1.57
δ_{CP} , (IH)	[-2.13, -1.00]	-1.57
Δm_{32}^2 (BH) [$\times 10^{-3}\text{eV}^2$]	[2.46, 2.52]	2.49
Δm_{32}^2 (NH) [$\times 10^{-3}\text{eV}^2$]	[2.48, 2.56]	2.51
Δm_{32}^2 (IH) [$\times 10^{-3}\text{eV}^2$]	[-2.60, -2.52]	-2.55
$\sin^2(\theta_{23})$ (BH)	[0.49, 0.55]	0.527
$\sin^2(\theta_{23})$ (NH)	[0.49, 0.55]	0.527
$\sin^2(\theta_{23})$ (IH)	[0.50, 0.56]	0.539

Table 8.7: The position of the highest posterior probability density (HPD) and width of the 1σ credible interval for the joint beam and atmospheric fit where the reactor constraint is applied. The values are presented by which hierarchy hypothesis is assumed: marginalised over both hierarchies (BH), normal hierarchy only (NH), and inverted hierarchy only (IH).

which agrees with the known value of $\sin^2(\theta_{23}) = 0.528$. The distribution clearly favours the UO with almost the entirety of the 1σ credible interval contained in the region. Figure 8.27 highlights the sensitivity of the joint fit both with and without the reactor constraint. The fit where the reactor constraint is applied selects the known value much better ($\sin^2(\theta_{23}) = 0.528$). Furthermore, the reactor constraint increases the UO preference which is evidenced by the distribution moving further away from the octant boundary. This indicates that there are marginalisation effects between the two mixing parameters. This follows from the correlation illustrated between $\sin^2(\theta_{23}) - \sin^2(\theta_{13})$ in Figure 8.22. The posterior distribution of the fit with reactor constraint is more peaked compared to the flatter distribution when the reactor constraint is not applied.

The fraction of steps contained within the two hierarchy and two octant models is given in Table 8.8. The reactor constraint significantly reduces the fraction of steps that are contained within the IH-LO region from 0.08 to 0.02, whilst significantly increasing the fraction of steps within the NH-UO region from 0.53 to 0.64. The application of the reactor constraint increases the Bayes factor

With Reactor Constraint, Both Hierarchies



Figure 8.26: The one-dimensional posterior probability density distribution in $\sin^2(\theta_{23})$, marginalised over both hierarchies, from the joint beam and atmospheric fit where the reactor constraint is applied.

from $B(\text{NH}/\text{IH}) = 3.67$ to $B(\text{NH}/\text{IH}) = 7.29$. There is a very clear preference for the NH, with the Jeffreys scale stating a substantial preference for both fits (see subsection 4.3.3). The Bayes factor for UO preference is calculated as $B(\text{UO}/\text{LO}) = 2.86$. Whilst still a weak preference, this is certainly a stronger statement than the sensitivity when the reactor constraint is not applied.

	LO ($\sin^2 \theta_{23} < 0.5$)	UO ($\sin^2 \theta_{23} > 0.5$)	Sum
NH ($\Delta m_{32}^2 > 0$)	0.24	0.64	0.88
IH ($\Delta m_{32}^2 < 0$)	0.02	0.10	0.12
Sum	0.26	0.74	1.00

Table 8.8: The distribution of steps in a joint beam and atmospheric with the reactor constraint fit applied, presented as the fraction of steps in the upper (UO) and lower (LO) octants and the normal (NH) and inverted (IH) hierarchies. The Bayes factors are calculated as $B(\text{NH}/\text{IH}) = 7.29$ and $B(\text{UO}/\text{LO}) = 2.86$.

The sensitivity to Δm_{32}^2 , with the reactor constraint applied, is presented in

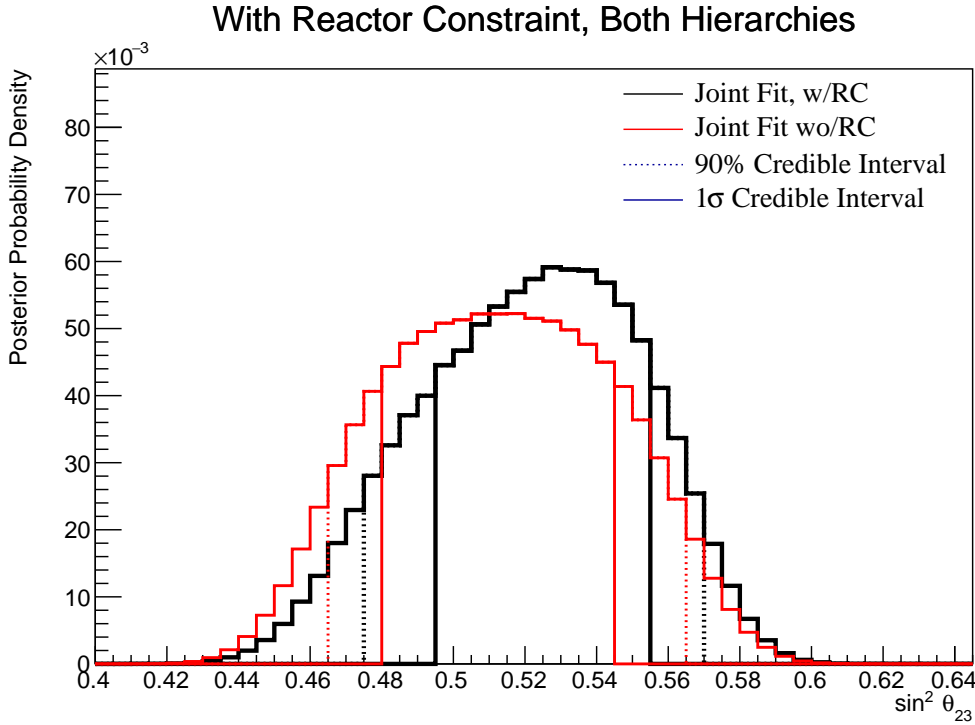


Figure 8.27: The one-dimensional posterior probability density distribution in $\sin^2(\theta_{23})$ compared between the joint beam-atmospheric fit (Red) and the joint beam and atmospheric fit with the reactor constraint (Black). The distributions are marginalised over both hierarchies.

3272 Figure 8.28. The posterior distribution is marginalised over both hierarchies. As
 3273 expected, the 1σ credible interval is entirely contained within the NH region. The
 3274 position of the highest posterior probability density is given as $2.49 \times 10^{-3} \text{ eV}^2$,
 3275 illustrating no significant bias between the fit results and the known oscillation
 3276 parameters. The application of the reactor constraint does move significantly the
 3277 position of the credible intervals but does reduce their width.

3278 The sensitivity to the appearance parameters ($\sin^2(\theta_{13}) - \delta_{CP}$) is given in
 3279 Figure 8.29. The distribution is mostly uncorrelated between the two parameters
 3280 and is centered at the known oscillation parameters. The 1σ credible interval
 3281 excludes $\delta_{CP} = 0$ and $\delta_{CP} = (-)\pi$. Furthermore, the 3σ credible intervals
 3282 exclude the region of $\delta_{CP} = \pi/2$.

3283 The sensitivity to the disappearance parameters ($\sin^2(\theta_{23}) - \Delta m_{32}^2$) is illus-
 3284 trated in Figure 8.30. As expected from the one-dimensional distribution, the 1σ
 3285 credible interval is entirely contained within the NH region. Both the NH and

With Reactor Constraint, Both Hierarchies

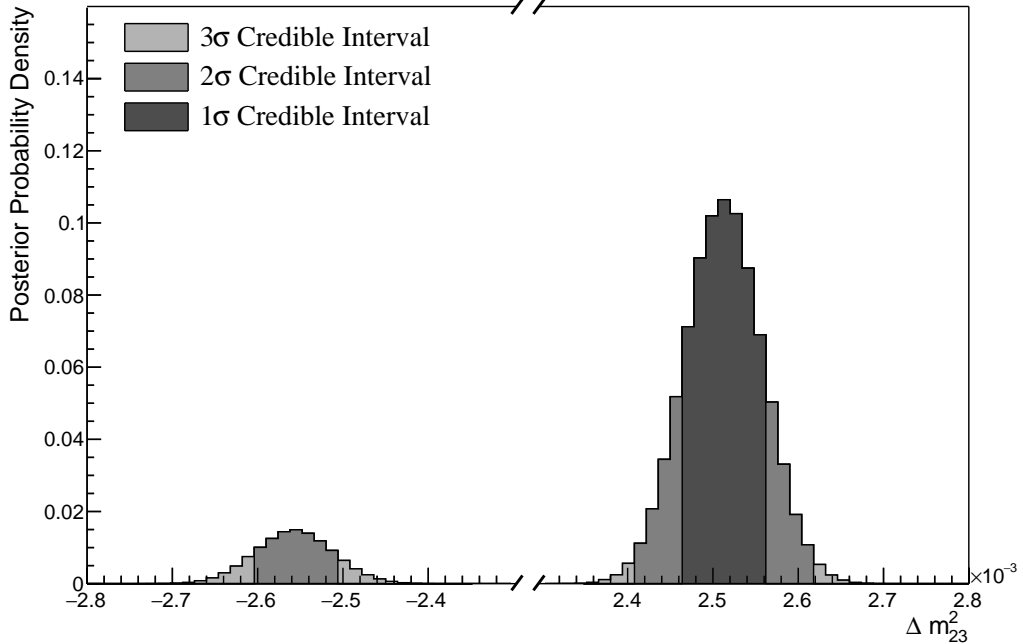


Figure 8.28: The one-dimensional posterior probability density distribution in Δm_{32}^2 , marginalised over both hierarchies, from the joint beam and atmospheric fit where the reactor constraint is applied.

3286 IH regions favour the UO, with a visually similar preference in both hierarchies.
 3287 The width of the Δm_{32}^2 1 σ credible interval does not significantly depend upon
 3288 the value or octant of $\sin^2(\theta_{23})$. This shows that there are no strong correlations
 3289 between these two parameters.

3290 Figure 8.31 illustrates the posterior distribution for each permutation of
 3291 two oscillation parameters of interest. The application of the reactor constraint
 3292 significantly reduces the correlations previously seen in Figure 8.22. There is
 3293 still a small correlation between δ_{CP} and Δm_{32}^2 . The application of the reactor
 3294 constraint has not significantly affected this correlation. The width of the 1 σ
 3295 credible interval in Δm_{32}^2 is wider for a value of $\delta_{CP} = 0$ as compared to a value
 3296 of $\delta_{CP} = \pi$. Similarly, the width of the 1 σ credible interval in δ_{CP} is smaller
 3297 for lower values of $\sin^2(\theta_{23})$.

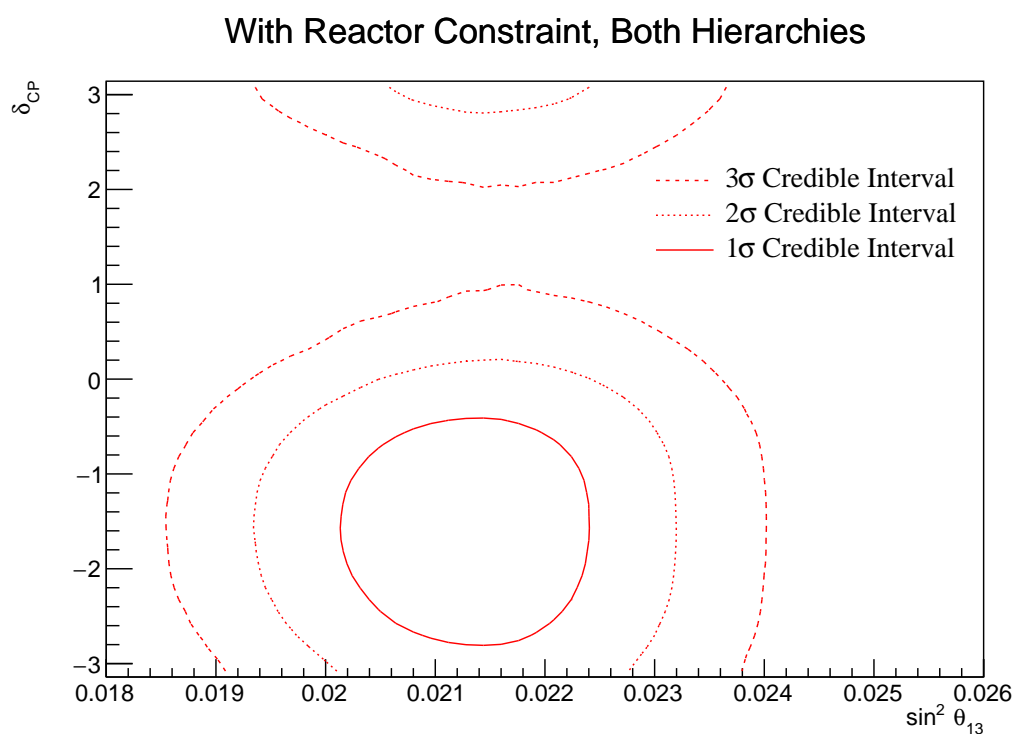


Figure 8.29: The two-dimensional posterior probability density distribution in $\delta_{CP} - \sin^2(\theta_{13})$, marginalised over both hierarchies, from the joint beam and atmospheric fit where the reactor constraint is applied.

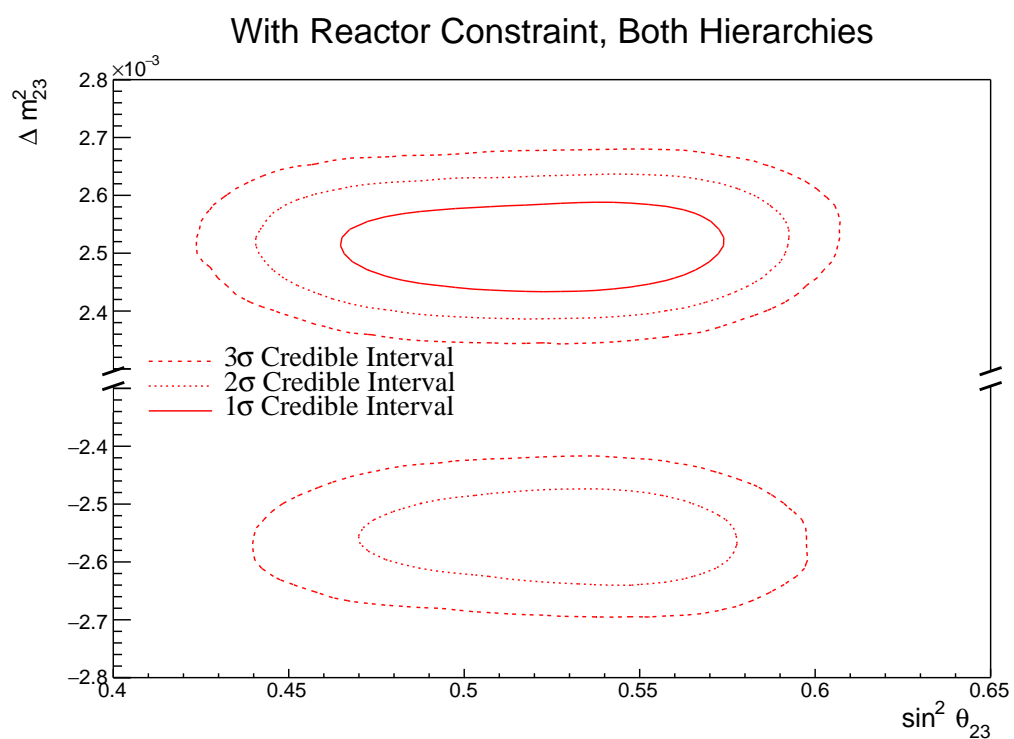


Figure 8.30: The two-dimensional posterior probability density distribution in $\Delta m_{32}^2 - \sin^2(\theta_{23})$, marginalised over both hierarchies, from the joint beam and atmospheric fit where the reactor constraint is applied.



Figure 8.31: The posterior probability density distribution from the joint beam and atmospheric fit where the reactor constraint is applied. The distribution is given for each two-dimensional permutation of the oscillation parameters of interest. The one-dimensional distribution of each parameter is also given.

3298 8.2.6 Comparison to Latest T2K Sensitivities without Reactor 3299 Constraint

3300 The benefits of the joint beam and atmospheric analysis can be determined by
 3301 comparing the sensitivities to the beam-only analysis. This section presents those
 3302 comparisons for sensitivities built using the Asimov A oscillation parameters
 3303 defined in Table 2.2 and the post-BANFF systematic tune. The reactor constraint
 3304 is not applied within either of the fits used in these comparisons.

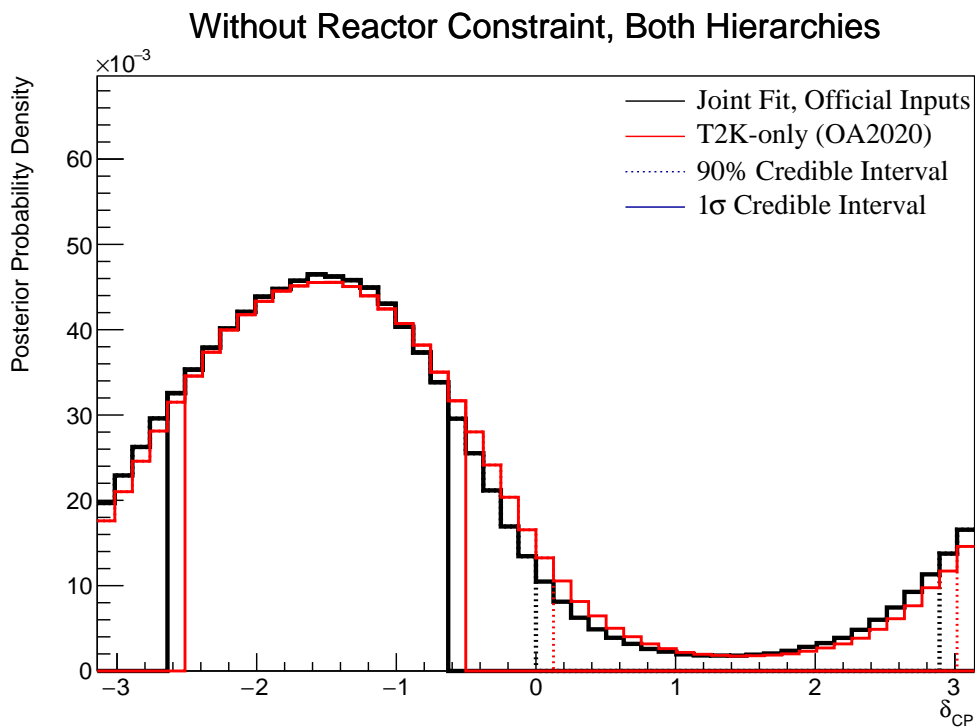


Figure 8.32: The one-dimensional posterior probability density distribution in δ_{CP} compared between the joint beam-atmospheric fit (Black) and the latest T2K sensitivities (Red) [186]. The reactor constraint is not applied in either fit. The distributions are marginalised over both hierarchies.

3305 The sensitivity, marginalised over both hierarchies, to δ_{CP} from the joint
 3306 beam-atmospheric and beam-only fits is presented in Figure 8.32. As expected
 3307 from the likelihood scans (Figure 8.4), the sensitivity to δ_{CP} is not significantly
 3308 increased. This is because the known oscillation parameter value ($\delta_{CP} = -1.601$)
 3309 lies at the position where the beam samples dominate the sensitivity compared
 3310 to the SK samples.

The sensitivity to Δm_{32}^2 of the joint beam-atmospheric fit is illustrated in Figure 8.33, where the posterior distribution has been marginalised over both hierarchies. The 1σ credible interval of the joint beam and atmospheric fit is entirely contained within the NH region. This shows the significant increase in the ability of the fit to determine the correct mass hierarchy, as compared to the beam-only analysis. This is further evidenced by the fact that the 90% credible intervals from the joint fit are also tighter in the IH region as compared to the beam-only analysis. The Bayes factor for mass hierarchy determination for the beam-only and joint beam and atmospheric are $B(\text{NH}/\text{IH}) = 1.91$ and $B(\text{NH}/\text{IH}) = 3.67$, respectively. According to Jeffrey's scale (Table 4.1), the beam-only analysis represents a weak preference for the NH hypothesis whereas the joint fit returns a substantial preference for the NH hypothesis. To summarise, the joint beam-atmospheric fit has a substantial preference for the correct hierarchy without the requirement of external constraints.



Figure 8.33: The one-dimensional posterior probability density distribution in Δm_{32}^2 compared between the joint beam-atmospheric fit (Black) and the latest T2K sensitivities (Red) [186]. The reactor constraint is not applied in either fit. The distributions are marginalised over both hierarchies.

3325 The sensitivity to $\sin^2(\theta_{23})$, marginalised over both hierarchies, for both the
 3326 beam-only and joint beam and atmospheric analysis are presented in Figure 8.34.
 3327 The peak of the posterior distribution from the joint analysis is more aligned
 3328 with the known value of $\sin^2(\theta_{23}) = 0.528$ as compared to the beam-only
 3329 analysis. This indicates that the marginalisation effects from other oscillation
 3330 parameters ($\sin^2(\theta_{13}) - \sin^2(\theta_{23})$) presented in Figure 8.22) are less prevalent in
 3331 the projection of this parameter. The Bayes factors for the beam-only and joint
 3332 beam-atmospheric fit are $B(\text{UO}/\text{LO}) = 1.56$ and $B(\text{UO}/\text{LO}) = 1.74$, respectively.
 3333 Therefore, the joint beam-atmospheric fit does prefer the UO more strongly than
 3334 the beam-only analysis, albeit slightly.

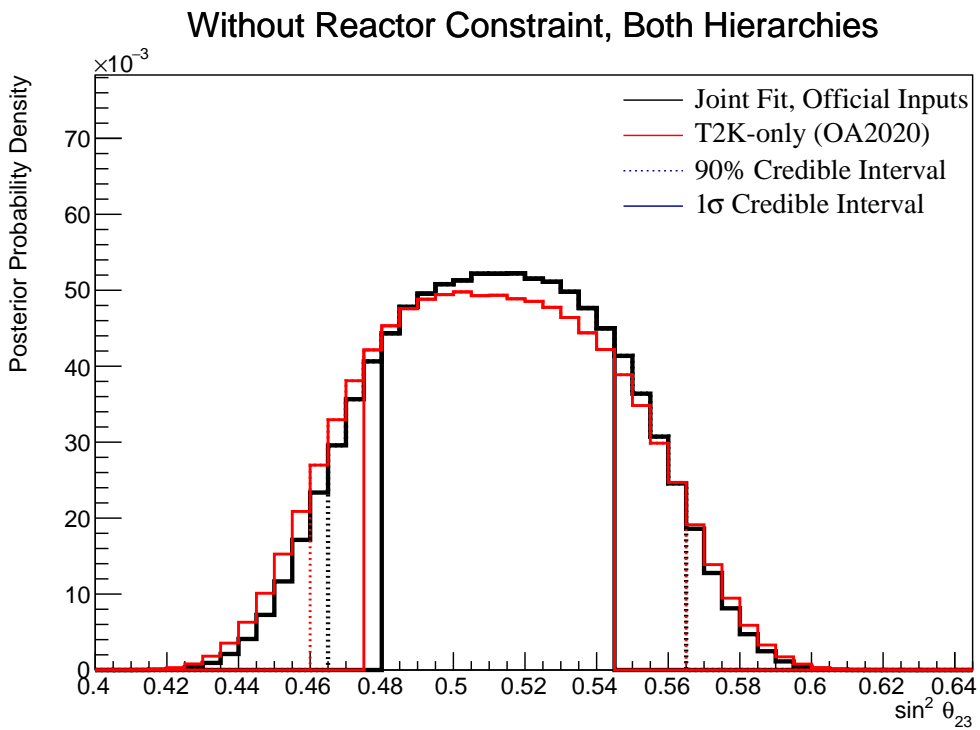


Figure 8.34: The one-dimensional posterior probability density distribution in $\sin^2(\theta_{23})$ compared between the joint beam-atmospheric fit (Black) and the latest T2K sensitivities (Red) [186]. The reactor constraint is not applied in either fit. The distributions are marginalised over both hierarchies.

3335 Whilst the beam-only and joint beam-atmospheric fits have similar sensitivity
 3336 to δ_{CP} and $\sin^2(\theta_{23})$ when projected in one-dimension, the benefit of the joint
 3337 analysis becomes more obvious when the sensitivities are presented in two-

dimensions. The sensitivity of the two fits to the appearance parameters ($\delta_{CP} - \sin^2(\theta_{13})$) are illustrated in Figure 8.35.

The width of the 99% joint fit credible interval in $\sin^2(\theta_{13})$ is squeezed in the region of $\delta_{CP} \sim 0$ compared to the beam-only analysis. This is the same behaviour that is seen in the appearance likelihood scans presented in Figure 8.2. The 1σ and 90% also exhibit slightly tighter constraints on δ_{CP} . This is most prevalent in the region of $\delta_{CP} \sim 0$ and $\sin^2(\theta_{13}) \sim 0.03$. Whilst the atmospheric samples do not have significant sensitivity to $\sin^2(\theta_{13})$ (as shown in Figure 8.1), they aid in breaking the degeneracy between the oscillation parameters allowing for tighter constraints.

The sensitivity to the disappearance parameters $\sin^2(\theta_{23}) - \Delta m_{32}^2$, marginalised over both hierarchies, is presented in Figure 8.36 for both the beam-only and joint beam-atmospheric fits. Whilst the one-dimensional sensitivity comparisons considered so far show the improvements of the joint fit, the two-dimensional projection really shows the benefit of adding the atmospheric samples to the beam samples. The area contained within the IH credible intervals is drastically reduced in the joint fit. This follows from the better determination of the mass hierarchy seen in the Bayes factor comparisons. The 1σ joint fit credible interval in the IH region more strongly favours the UO as compared to the beam-only fit. Even in the NH region, the width of the credible intervals in $\sin^2(\theta_{23})$ decrease, albeit to a smaller extent.

The change in sensitivity to $\delta_{CP} - \Delta m_{32}^2$ is illustrated in Figure 8.37. As expected, the contours presented within the IH region are much smaller in the joint fit due to the increased sensitivity to mass hierarchy determination. This culminates in a region around $\delta_{CP} \sim \pi/2$ which is excluded at 3σ . This behaviour is not present within the beam-only analysis. Consistent with the previous observations, the area contained within the IH credible intervals is significantly reduced in comparison to the beam-only analysis.

The sensitivity to Δm_{32}^2 and $\sin^2(\theta_{23})$, as a function of $\sin^2(\theta_{13})$, is presented in Figure 8.38 and Figure 8.39, respectively. These sensitivities are marginalised

Without Reactor Constraint, Both Hierarchies



Figure 8.35: The two-dimensional posterior probability density distribution in δ_{CP} – $\sin^2(\theta_{13})$ compared between the joint beam-atmospheric fit (Black) and the latest T2K sensitivities (Red) [186]. The reactor constraint is not applied in either fit. The distributions are marginalised over both hierarchies.

over both hierarchies. As expected from the previous observations, the Δm_{32}^2 contours within IH region of the joint fit are much smaller than the beam-only analysis. Notably, the joint fit IH 1σ credible intervals exclude the region around the reactor constraint. This is not a bias from the fit as the known value for Δm_{32}^2 is in the NH region. This does suggest that the application of the reactor constraint would further increase the preference for NH in the joint fit as compared to its effect on the beam-only analysis.

The beam-only and joint beam-atmospheric fits have a slightly different contour shape between the $\sin^2(\theta_{13})$ and $\sin^2(\theta_{23})$ parameters, as illustrated by Figure 8.39. The joint analysis disfavours the wrong octant hypothesis more strongly in the region of high $\sin^2(\theta_{13})$. This suggests that the application of the reactor constraint will favour the UO more strongly in the joint analysis compared to the beam-only analysis.



Figure 8.36: The two-dimensional posterior probability density distribution in Δm_{32}^2 – $\sin^2(\theta_{23})$ compared between the joint beam-atmospheric fit (Black) and the latest T2K sensitivities (Red) [186]. The reactor constraint is not applied in either fit. The distributions are marginalised over both hierarchies.

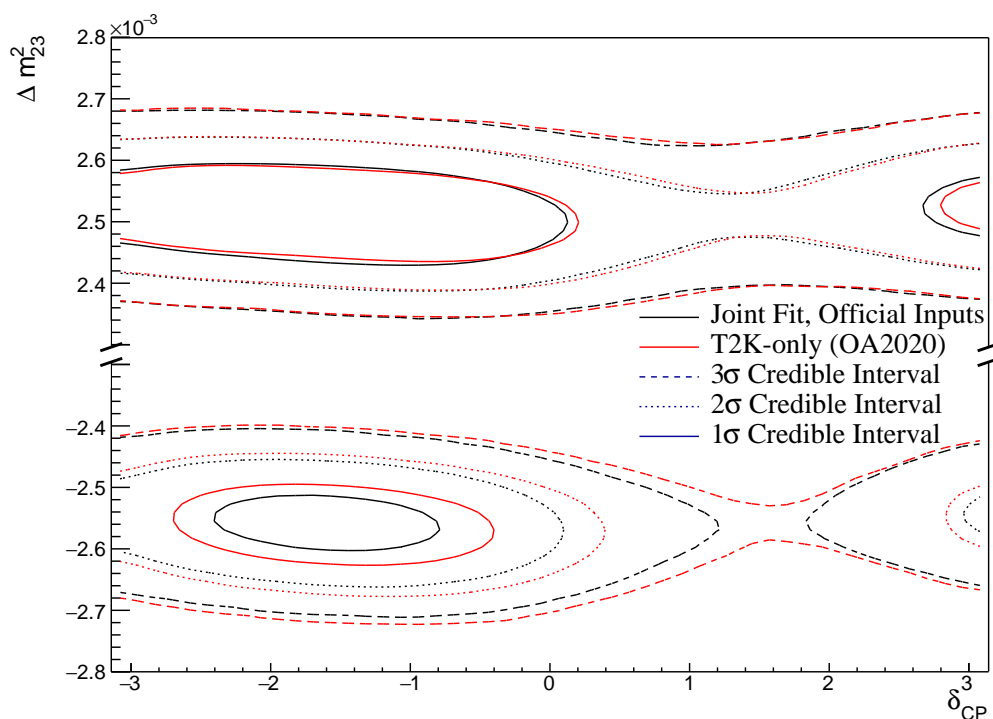


Figure 8.37: The two-dimensional posterior probability density distribution in $\Delta m_{32}^2 - \Delta_{CP}$ compared between the joint beam-atmospheric fit (Black) and the latest T2K sensitivities (Red) [186]. The reactor constraint is not applied in either fit. The distributions are marginalised over both hierarchies.

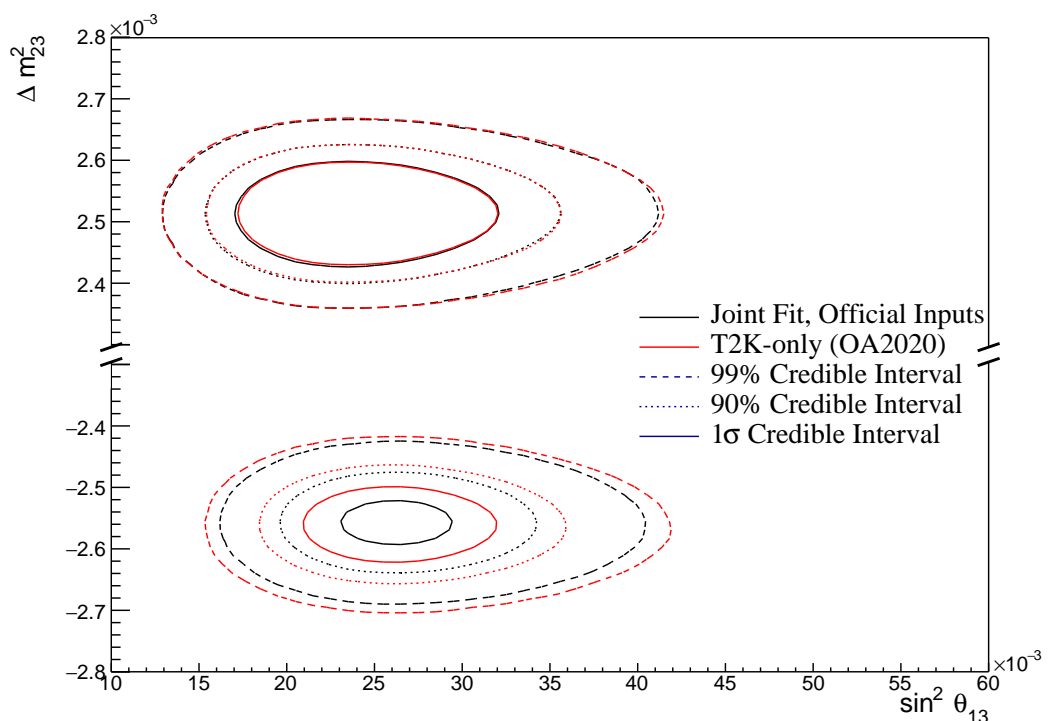


Figure 8.38: The two-dimensional posterior probability density distribution in Δm_{32}^2 – $\sin^2(\theta_{23})$ compared between the joint beam-atmospheric fit (Black) and the latest T2K sensitivities (Red) [186]. The reactor constraint is not applied in either fit. The distributions are marginalised over both hierarchies.

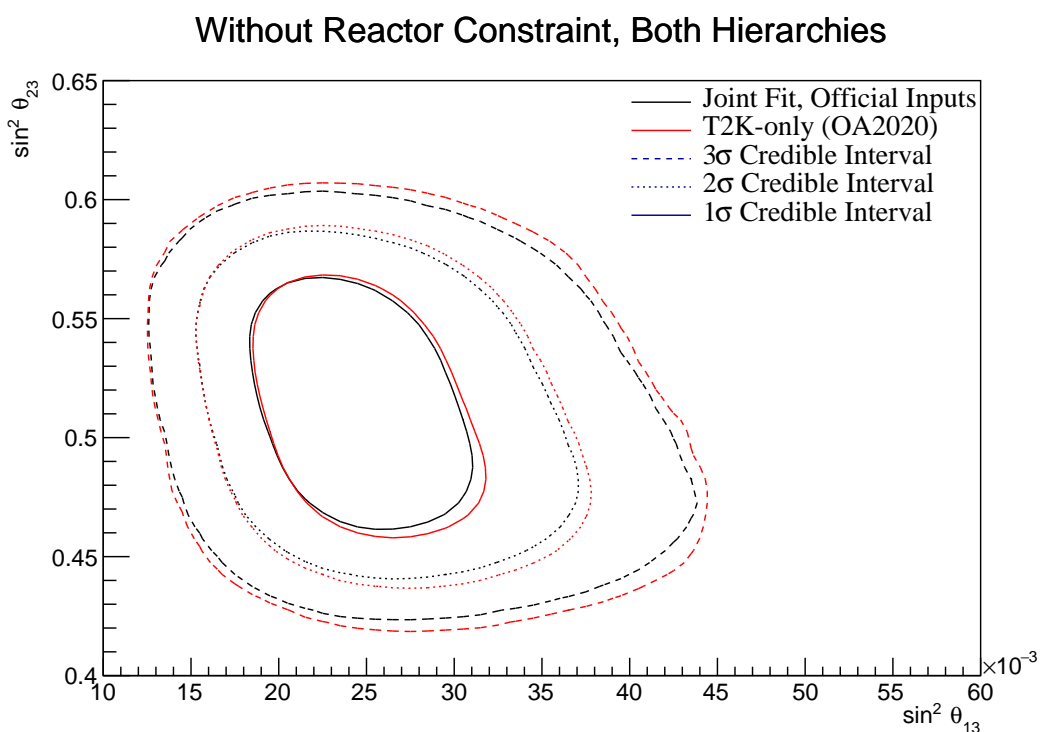


Figure 8.39: The two-dimensional posterior probability density distribution in $\sin^2(\theta_{23})$ – $\sin^2(\theta_{13})$ compared between the joint beam-atmospheric fit (Black) and the latest T2K sensitivities (Red) [186]. The reactor constraint is not applied in either fit. The distributions are marginalised over both hierarchies.

3381 8.2.7 Comparison to Latest T2K Sensitivities with Reactor Con- 3382 straint

3383 The comparison between the beam-only and joint beam-atmospheric fits are
 3384 compared in subsection 8.2.6. Those comparisons were made with the reactor
 3385 constraint not applied to either of the fits. This section illustrates the com-
 3386 parison when the reactor constraint is applied. As shown in Figure 8.38, the
 3387 application of the reactor constraint is expected to significantly increase the
 3388 joint fit's preference for the NH hypothesis, as compared to the beam-only
 3389 analysis. Figure 8.40 illustrates the sensitivities of the two fits to the disappearance
 3390 parameters ($\sin^2(\theta_{23}) - \Delta m_{32}^2$) marginalised over both hierarchies and with the
 3391 reactor constraint applied. This plot clearly illustrates the benefit of the joint
 3392 beam and atmospheric analysis. The 1σ credible interval in the IH region is
 3393 entirely removed in the joint analysis, illustrating the improved NH preference.

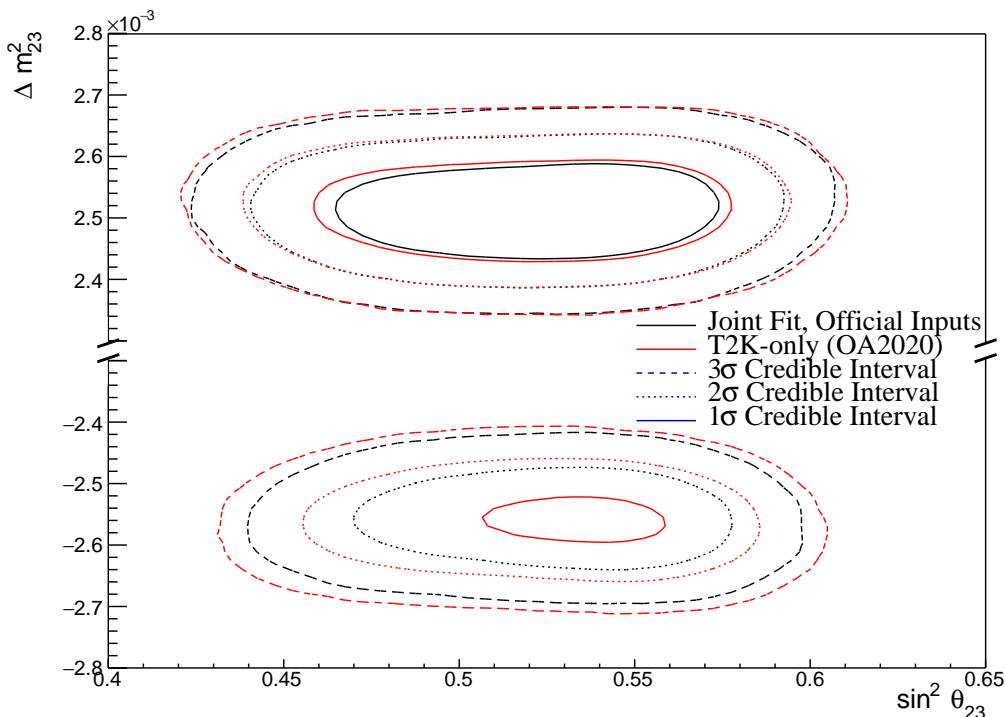


Figure 8.40: The two-dimensional posterior probability density distribution in $\Delta m_{32}^2 - \sin^2(\theta_{23})$ compared between the joint beam-atmospheric fit (Black) and the latest T2K sensitivities (Red) [186]. The reactor constraint is applied in both fits. The distributions are marginalised over both hierarchies.

3394 The credible intervals of the joint fit are also tighter in the $\sin^2(\theta_{23})$ dimension
3395 than the beam-only analysis in both mass hierarchy regions. This shows that
3396 beyond the ability of the joint fit to prefer the NH more strongly than the beam-
3397 only analysis, the precision to which it can measure $\sin^2(\theta_{23})$ is also improved.
3398 The Bayes factor for NH preference is calculated as $B(\text{NH}/\text{IH}) = 7.29$ and
3399 $B(\text{NH}/\text{IH}) = 3.41$ for the joint beam-atmospheric and beam-only analysis,
3400 respectively. Whilst both present a significant preference for the NH hypothesis
3401 (Table 4.1), the joint fit's preference is much stronger. A similar conclusion can be
3402 made regarding the Bayes factors for UO preference which are $B(\text{UO}/\text{LO}) = 2.86$
3403 and $B(\text{UO}/\text{LO}) = 2.67$ for the joint beam-atmospheric and beam-only analysis,
3404 respectively. Both of these represent a mild preference for the UO but there is
3405 a stronger preference observed in the joint analysis.

3406 The sensitivity of the beam-only and joint beam-atmospheric analyses, to the
3407 appearance parameters ($\delta_{CP} - \sin^2(\theta_{13})$), are compared in Figure 8.41. These
3408 results are marginalised over both hierarchies and include the reactor constraint
3409 on $\sin^2(\theta_{13})$. For this particular set of known oscillation parameters (AsimovA
3410 defined in Table 2.2), the beam-only analysis dominates the sensitivity. The
3411 joint fit does slightly increase the sensitivity to δ_{CP} but it does not change any
3412 conclusions that would be made.



Figure 8.41: The two-dimensional posterior probability density distribution in δ_{CP} – $\sin^2(\theta_{13})$ compared between the joint beam-atmospheric fit (Black) and the latest T2K sensitivities (Red) [186]. The reactor constraint is applied in both fits. The distributions are marginalised over both hierarchies.

3413 8.2.8 Effect of Asimov Parameter Set

3414 Figure 8.4 and Figure 8.5 show that the choice of the parameter set at which the
 3415 Asimov data is made can affect the conclusion. ‘AsimovA’ oscillation parameters
 3416 are defined at a region of δ_{CP} which is dominated by the T2K experiment. This
 3417 explains why the addition of the atmospheric samples does not significantly in-
 3418 crease the sensitivity to δ_{CP} , as illustrated in subsection 8.2.6 and subsection 8.2.7.
 3419 This section presents the sensitivities when ‘AsimovB’ oscillation parameters,
 3420 as defined in Table 2.2, are assumed (alongside the post-BANFF tune) when
 3421 building the Asimov data.

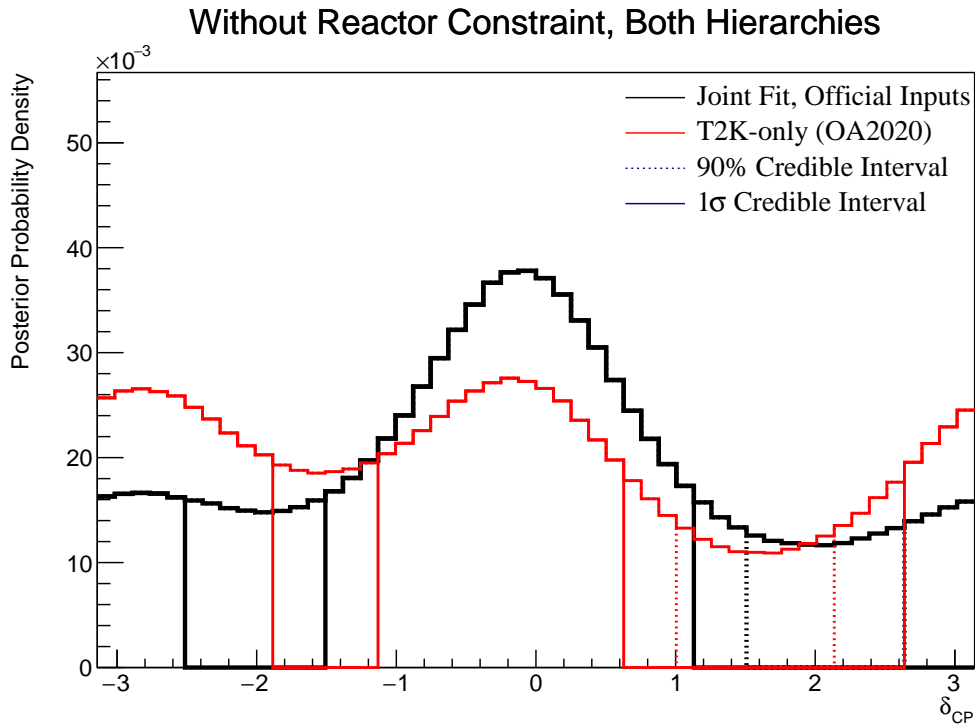


Figure 8.42: The one-dimensional posterior probability density distribution in δ_{CP} compared between the joint beam-atmospheric fit (Black) and the latest T2K sensitivities (Red) [186]. The reactor constraint is not applied in either fit. The distributions are marginalised over both hierarchies.

3422 The sensitivity to δ_{CP} for the joint beam and atmospheric fit is presented
 3423 in Figure 8.42. The results are compared to those from the beam-only analysis
 3424 in [186]. The reactor constraint is not applied in either of the fits. The known
 3425 oscillation parameter value is $\delta_{CP} = 0$. The shape of the posterior distribution

from the joint analysis is more peaked at $\delta_{CP} = 0$ as compared to the beam-only analysis which has approximately the same posterior probability density at $\delta_{CP} = 0$ and $\delta_{CP} = \pi$. This shows the ability of the joint analysis to better determine the correct phase of δ_{CP} if the true value was CP-conserving. The 1σ credible intervals and the position of the highest posterior probability density are given in Table 8.9.

Parameter	Interval	HPD
δ_{CP} , (BH)	$[-\pi, -2.51], [-1.51, 1.31]$	-0.06
δ_{CP} , (NH)	$[-1.13, 1.63]$	0.06
δ_{CP} , (IH)	$[-3.02, -1.88], [-1.76, 0.13]$	-0.44
Δm_{32}^2 (BH) [$\times 10^{-3}$ eV 2]	$[-2.60, -2.49], [2.46, 2.59]$	2.51
Δm_{32}^2 (NH) [$\times 10^{-3}$ eV 2]	$[2.47, 2.56]$	2.52
Δm_{32}^2 (IH) [$\times 10^{-3}$ eV 2]	$[-2.61, -2.52]$	-2.57
$\sin^2(\theta_{23})$ (BH)	$[0.43, 0.48], [0.55, 0.59]$	0.45
$\sin^2(\theta_{23})$ (NH)	$[0.43, 0.49], [0.55, 0.58]$	0.45
$\sin^2(\theta_{23})$ (IH)	$[0.44, 0.48], [0.54, 0.59]$	0.57

Table 8.9: The position of the highest posterior probability density (HPD) and width of the 1σ credible interval for the SK atmospheric-only fit. The reactor constraint is not applied. The values are presented by which hierarchy hypothesis is assumed: marginalised over both hierarchies (BH), normal hierarchy only (NH) and inverted hierarchy only (IH).

Naively, if just the 1σ credible interval were considered without observing the shape of the distribution, it would appear that the joint analysis would have a worse sensitivity to δ_{CP} due to the larger interval around δ_{CP} . The 1σ credible interval for the beam-only analysis is given as the range $\delta_{CP} = [-\pi, -1.88], [-1.13, 0.63]$ and $[2.64, \pi]$ which contains 56% of all values of δ_{CP} . The joint beam and atmospheric analysis contains 52% of all δ_{CP} values within the 1σ credible interval. Therefore, if the area within the 1σ credible interval were to be compared between the two fits, the joint analysis would be shown to have better precision.

This contradiction stems from the methodology in which the credible interval is calculated. The technique used in this analysis (documented in subsection 4.3.2)

3442 fills the credible interval by selecting bins in order of magnitude until 68% of the
3443 posterior density is contained. If instead, the credible interval was calculated
3444 by expanding around the highest posterior probability, the benefits of the joint
3445 fit would be more obvious. In the case where the shape of the posterior was
3446 Gaussian, these two techniques would be equivalent.

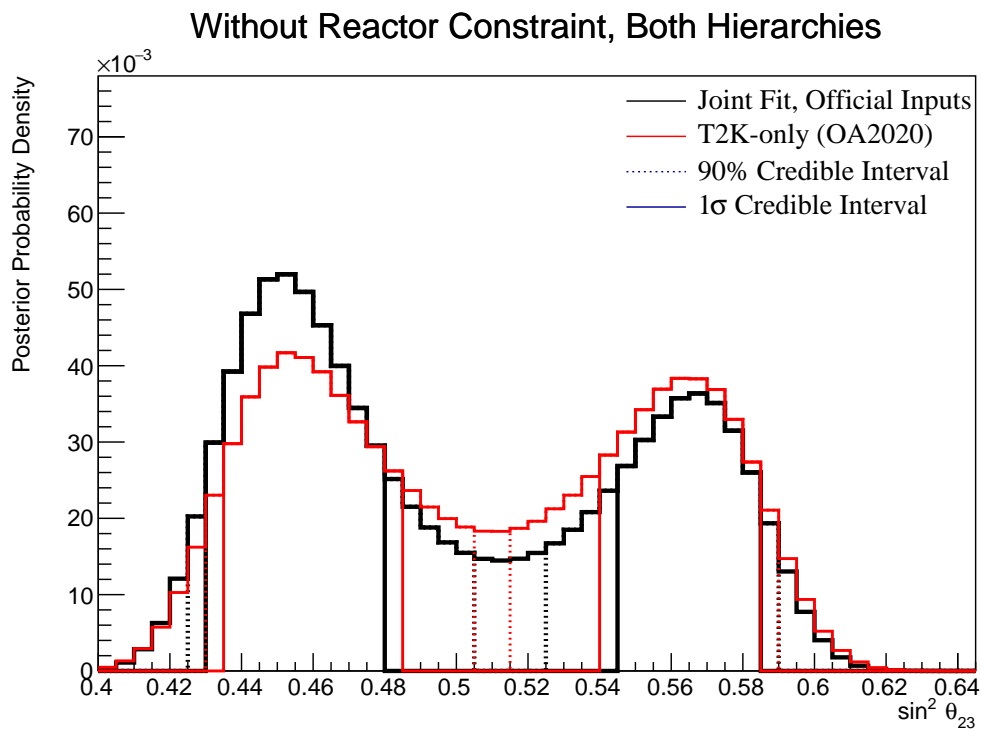


Figure 8.43: The one-dimensional posterior probability density distribution in $\sin^2(\theta_{23})$ compared between the joint beam-atmospheric fit (Black) and the latest T2K sensitivities (Red) [186]. The reactor constraint is not applied in either fit. The distributions are marginalised over both hierarchies.

3447 The sensitivity of the joint beam and atmospheric fit to $\sin^2(\theta_{23})$ is presented
3448 in Figure 8.43. The sensitivity is compared to that of the beam-only analysis
3449 in [186]. The reactor constraint is not applied in either of the fits being com-
3450 pared. The Asimov parameter value is $\sin^2(\theta_{23}) = 0.45$ and the sensitivities are
3451 marginalised over both hierarchies. Clearly, the joint beam and atmospheric
3452 fit has a much larger probability density in the region surrounding the known
3453 oscillation parameters. This shows the better octant determination of the joint
3454 analysis compared to the beam-only fit. The ratio of the posterior density at

the peak of the lower octant to the peak of the upper octant from the joint fit is 1.43 compared to 1.09 from the beam-only analysis. This shows further support for the joint analysis in correctly selecting the lower octant, which is the correct hypothesis given the known oscillation parameters.

	LO ($\sin^2 \theta_{23} < 0.5$)	UO ($\sin^2 \theta_{23} > 0.5$)	Sum
NH ($\Delta m_{32}^2 > 0$)	0.35	0.24	0.59
IH ($\Delta m_{32}^2 < 0$)	0.19	0.22	0.41
Sum	0.54	0.46	1.00

Table 8.10: The distribution of steps in a joint beam and atmospheric fit, presented as the fraction of steps in the upper (UO) and lower (LO) octants and the normal (NH) and inverted (IH) hierarchies. The reactor constraint is not applied. The Bayes factors are calculated as $B(\text{NH}/\text{IH}) = 1.43$ and $B(\text{LO}/\text{UO}) = 1.19$.

The distribution of steps, split by hierarchy and octant hypothesis, is presented in Table 8.10. The Bayes factor for hierarchy and octant determination are $B(\text{NH}/\text{IH}) = 1.43$ and $B(\text{LO}/\text{UO}) = 1.19$, respectively. The octant Bayes factor is now presented as LO/UO as the known oscillation parameter is contained within the lower octant. These values compare to $B(\text{NH}/\text{IH}) = 1.08$ and $B(\text{LO}/\text{UO}) = 0.91$ from the beam-only analysis. This shows additional evidence of the joint analysis's preference for selecting the correct octant and hierarchy hypothesis. Comparisons to the AsimovA Bayes factors presented in Table 8.6 show how the preference for the correct octant and hierarchy depend on the true value of δ_{CP} and $\sin^2(\theta_{23})$.

The sensitivity of the beam-only and joint beam-atmospheric analysis to Δm_{32}^2 is given in Figure 8.44. Both of the results are marginalised over both hierarchies and the reactor constraint is not applied in either analysis. The joint analysis has a stronger preference for the correct hierarchy (NH) which is shown by the higher Bayes factor ($B(\text{NH}/\text{IH}) = 1.43$) compared to the beam-only analysis ($B(\text{NH}/\text{IH}) = 1.08$).

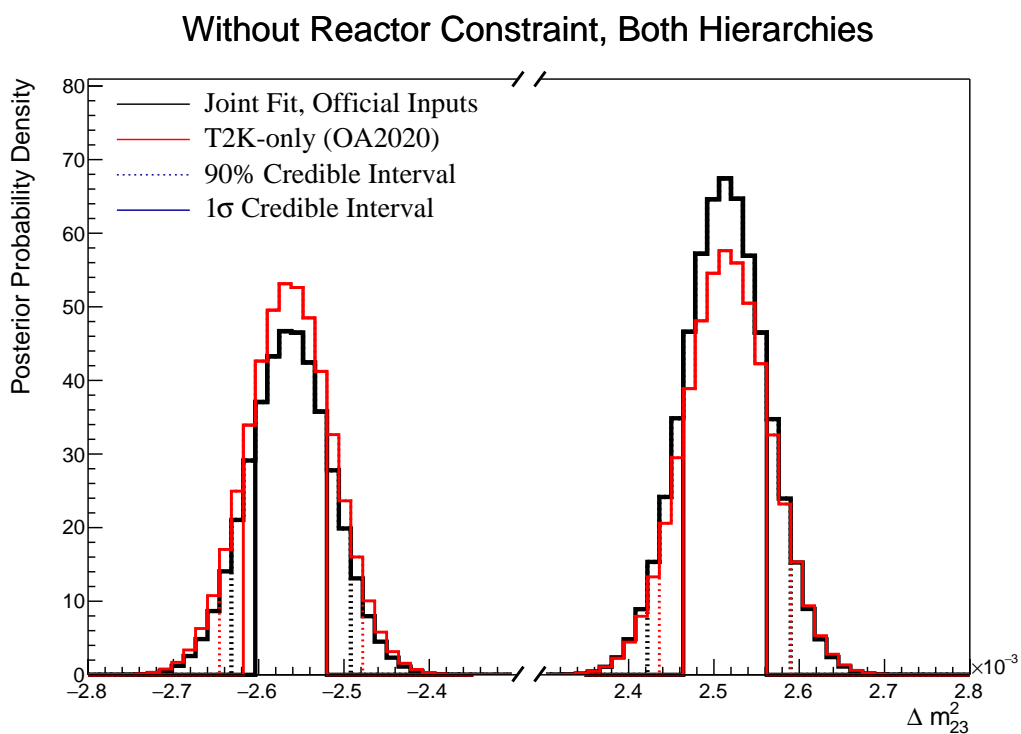


Figure 8.44: The one-dimensional posterior probability density distribution in Δm_{32}^2 compared between the joint beam-atmospheric fit (Black) and the latest T2K sensitivities (Red) [186]. The reactor constraint is not applied in either fit. The distributions are marginalised over both hierarchies.

9

3475

3476

Conclusions and Outlook

Appendices

3477

A

3478

3479

Atmospheric Sample Spectra

3480 This appendix documents the interaction mode breakdown of all the atmospheric
3481 samples used within the analysis. The generated tune of the model parameters
3482 and the Asimov A oscillation parameter set (defined in Table 2.2) are assumed.
3483 The livetime of SK-IV is taken to be 3244.4 days.

3484 A.1 Binning

3485 The lepton momentum and cosine zenith binning edges for the atmospheric
3486 samples used within this analysis are defined in Table A.1.

3487 A.2 Fully Contained Sub-GeV Samples

3488 The interaction mode breakdown of the fully contained Sub-GeV samples are
3489 shown in Figure A.1 and Figure A.2, for the samples with enriched CC0 π and
3490 CC1 π^\pm respectively.

3491 The CC0 π sample are dominated by CCQE events ($\sim 70\%$) with smaller
3492 contributions of 2p2h ($\sim 12\%$) and CC1 π ($\sim 10\%$) components. The energy peaks
3493 around 300 MeV, which is slightly below that of the T2K samples but still has
3494 significant contribution upto 1 GeV which overlaps the T2K sample energy range.

Sample	$\cos(\theta_Z)$ Bins	Momentum Bin Edges ($\log_{10}(P)$ MeV)
SubGeV-elike-0dcy	10	2.0, 2.4, 2.6, 2.8, 3.0, 3.2
SubGeV-elike-1dcy	1	2.0, 2.4, 2.6, 2.8, 3.0, 3.2
SubGeV-mulike-0dcy	10	2.0, 2.4, 2.6, 2.8, 3.0, 3.2
SubGeV-mulike-1dcy	10	2.0, 2.4, 2.6, 2.8, 3.0, 3.2
SubGeV-mulike-2dcy	1	2.0, 2.4, 2.6, 2.8, 3.0, 3.2
SubGeV-pi0like	1	2.0, 2.2, 2.4, 2.6, 2.8, 3.2
MultiGeV-elike-nue	10	3.0, 3.4, 3.7, 4.0, 5.0
MultiGeV-elike-nuebar	10	3.0, 3.4, 3.7, 4.0, 5.0
MultiGeV-mulike	10	3.0, 3.4, 5.0
MultiRing-elike-nue	10	3.0, 3.4, 3.7, 5.0
MultiRing-elike-nuebar	10	3.0, 3.4, 3.7, 5.0
MultiRing-mulike	10	2.0, 3.124, 3.4, 3.7, 5.0
MultiRing-Other1	10	3.0, 3.4, 3.7, 4.0, 5.0
PC-Stop	10	2.0, 3.4, 5.0
PC-Through	10	2.0, 3.124, 3.4, 3.7, 5.0
Upmu-Stop	10	3.2, 3.4, 3.7, 8.0
Upmu-Through-Showering	10	2.0, 8.0
Upmu-Through-NonShowering	10	2.0, 8.0

Table A.1: The reconstructed cosine zenith and lepton momentum binning assigned to the atmospheric samples. The “ $\cos(\theta_Z)$ Bins” column illustrates the number of bins uniformly distributed over the $-1.0 \leq \cos(\theta_Z) \leq 1.0$ region for fully and partially contained samples and $-1.0 \leq \cos(\theta_Z) \leq 0.0$ region for up- μ samples.

3495 The one-ring CC1 π samples, where the pion is tagged via its decay electron,
 3496 are dominated by CC1 π events ($\sim 75\%$) with a small contribution of CCM π
 3497 ($\sim 10\%$). The two-ring pion sample is mostly dominated by the NC1 π^0 via
 3498 resonances, and has several equally-sized contributions from CCQE, NC1 π^\pm via
 3499 resonances, and NC coherent pion production, where the π^0 likely comes from
 3500 nucleon and π^\pm final state interactions in the nucleus.

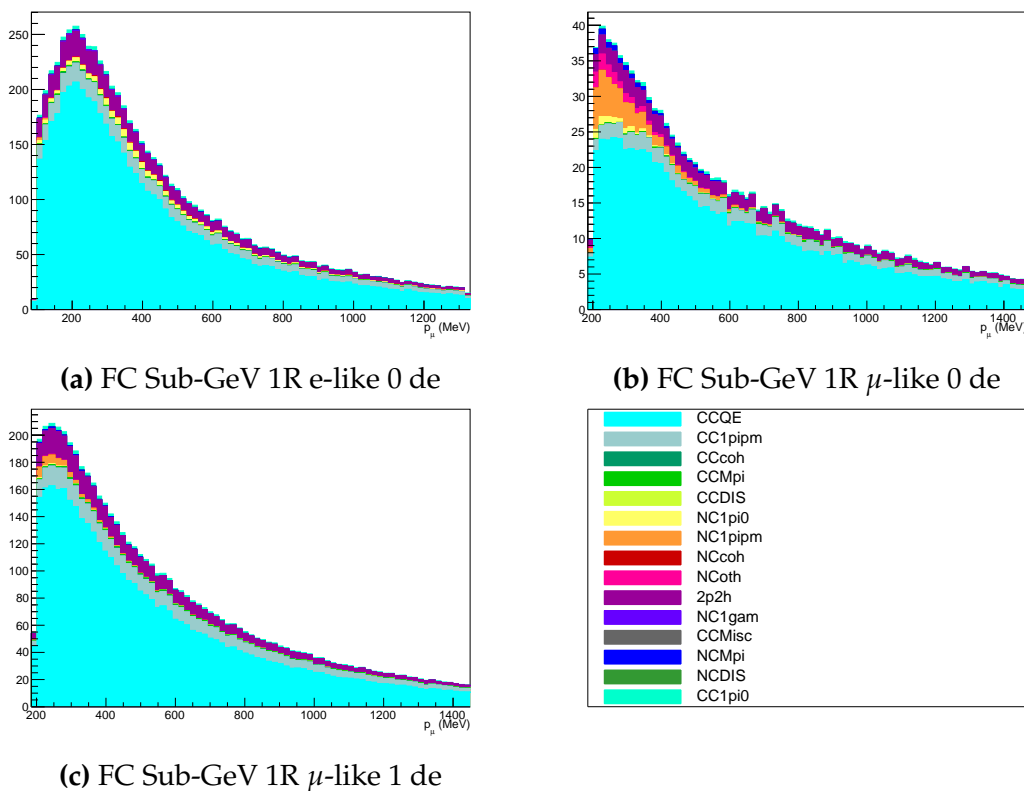


Figure A.1: Breakdown by interaction mode of the FC Sub-GeV atmospheric samples targeting CC 0π events.

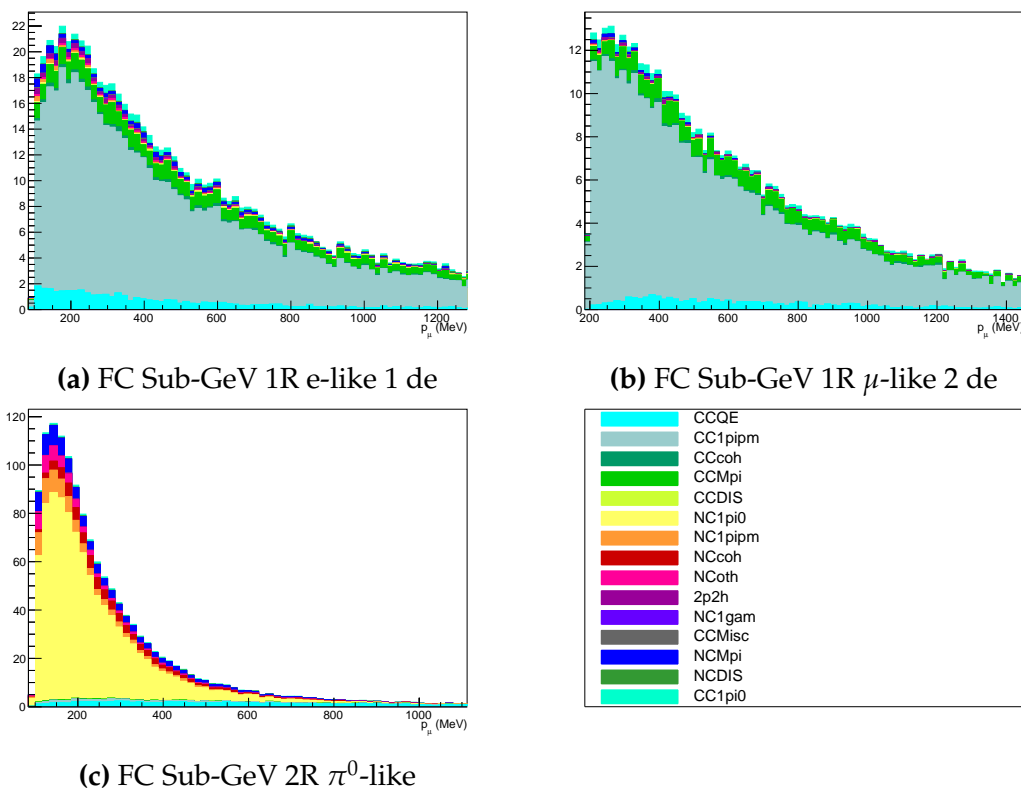


Figure A.2: Breakdown by interaction mode of the FC Sub-GeV atmospheric samples targeting single pion events.

3501 A.3 Fully Contained Multi-GeV Samples

3502 The interaction mode breakdown of fully contained multi-GeV samples is high-
 3503 lighted in Figure A.3. Due to the event selection applied in SK which targets π^+
 3504 and π^- separation, the ν_e sample mainly consists of events with pions (single pion
 3505 production or multi-pion/DIS interactions). The pion separation is explained in
 3506 Section section 6.1. This reasoning also explains the significant CCQE contribution
 3507 of the $\bar{\nu}_e$ sample. The muon-like sample is dominated by CCQE interactions with
 3508 $\sim 10 - 15\%$ 2p2h and CC1 π contribution of events.

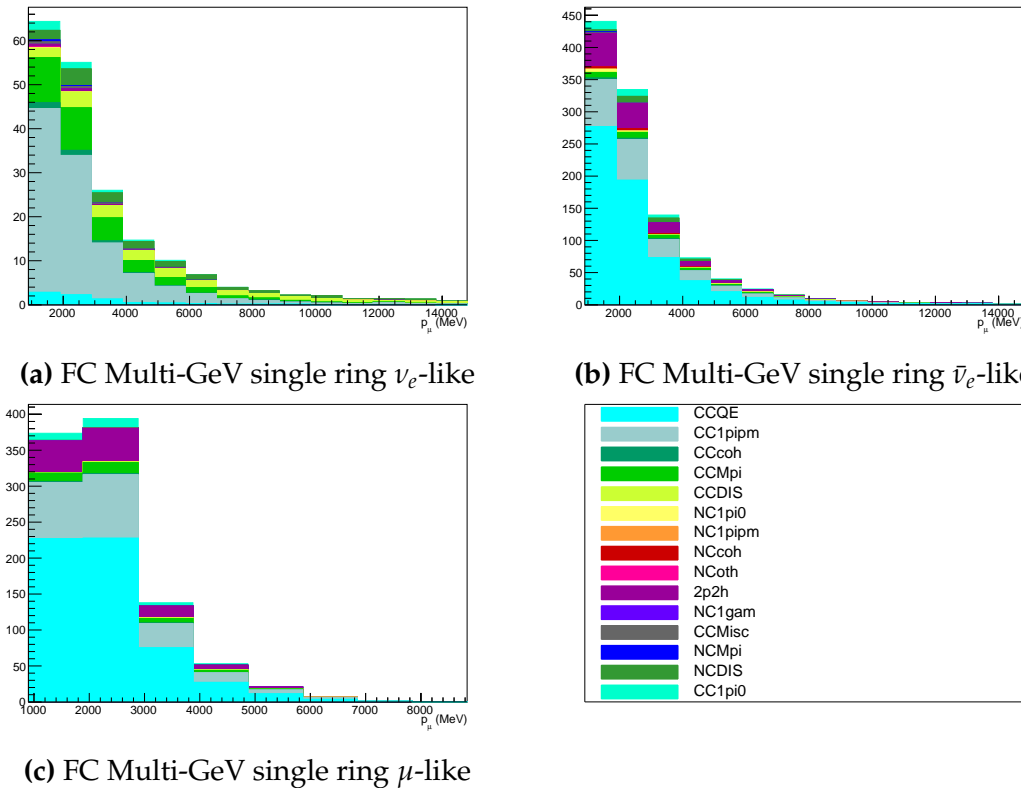


Figure A.3: Breakdown by interaction mode of the FC Multi-GeV single ring atmospheric samples.

3509 A.4 Fully Contained Multi-Ring Samples

3510 The interaction mode breakdown of fully contained multi-ring events is shown
 3511 in Figure A.4. These samples see more interaction modes contributing in general,
 3512 and there is a much larger contribution from multi-pion and DIS interaction
 3513 modes, compared to the other samples.



Figure A.4: Breakdown by interaction mode of the FC Multi-GeV multi-ring atmospheric samples.

³⁵¹⁴ A.5 Partially Contained Samples

³⁵¹⁵ The breakdown for partially contained samples is highlighted in Figure A.5.
³⁵¹⁶ As with the multi-ring samples, there is no dominating interaction mode. The
³⁵¹⁷ neutrino energies of events in this sample extend into the tens of GeV and become
³⁵¹⁸ dominated by DIS interaction modes in the high energy limit.

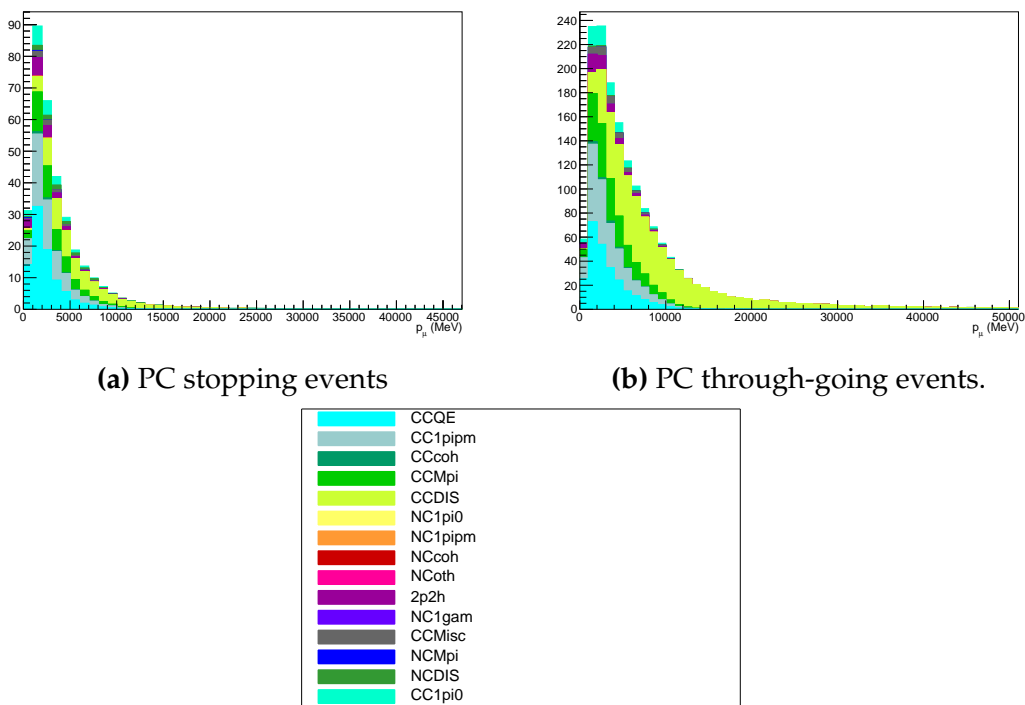


Figure A.5: Breakdown by interaction mode of the PC atmospheric samples.

3519 A.6 Upward-Going Muon Samples

3520 The breakdown for upward-going muons is illustrated in Figure A.6. These
 3521 samples are significantly dominated by DIS interactions with energies extending
 3522 up into the hundreds of GeV.

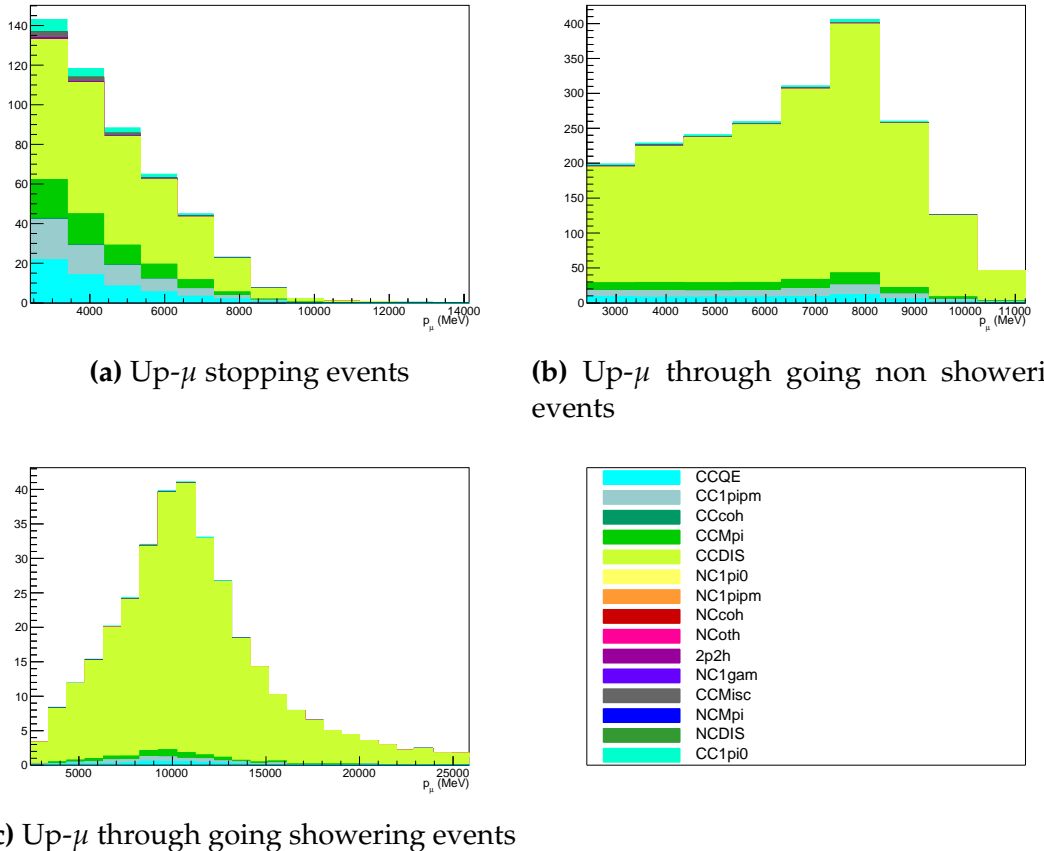


Figure A.6: Breakdown by interaction mode of the atmospheric upward going muon samples.

Bibliography

- [1] J Chadwick. "Intensitätsverteilung im magnetischen Spectrum der β -Strahlen von radium B + C". In: *Verhandl. Dtsc. Phys. Ges.* 16 (1914), p. 383. URL: <http://cds.cern.ch/record/262756>.
- [2] C D Ellis and W A Wooster. "The average energy of disintegration of radium E". en. In: *Proc. R. Soc. Lond. A Math. Phys. Sci.* 117.776 (Dec. 1927), pp. 109–123.
- [3] W. Pauli. "Dear radioactive ladies and gentlemen". In: *Phys. Today* 31N9 (1978), p. 27.
- [4] E. Fermi. "An attempt of a theory of beta radiation. 1." In: *Z. Phys.* 88 (1934), pp. 161–177.
- [5] F. Reines and C. L. Cowan. "Detection of the Free Neutrino". In: *Phys. Rev.* 92 (3 1953), pp. 830–831. URL: <https://link.aps.org/doi/10.1103/PhysRev.92.830>.
- [6] C. L. Cowan et al. "Detection of the Free Neutrino: a Confirmation". In: *Science* 124.3212 (1956), pp. 103–104. eprint: <http://science.sciencemag.org/content/124/3212/103.full.pdf>. URL: <http://science.sciencemag.org/content/124/3212/103>.
- [7] G. Danby et al. "Observation of High-Energy Neutrino Reactions and the Existence of Two Kinds of Neutrinos". In: *Phys. Rev. Lett.* 9 (1 1962), pp. 36–44. URL: <https://link.aps.org/doi/10.1103/PhysRevLett.9.36>.
- [8] K. Kodama et al. "Observation of tau neutrino interactions". In: *Physics Letters B* 504.3 (2001), pp. 218 –224. URL: <http://www.sciencedirect.com/science/article/pii/S0370269301003070>.
- [9] A. Aguilar-Arevalo et al. "Evidence for neutrino oscillations from the observation of anti-neutrino(electron) appearance in a anti-neutrino(muon) beam". In: *Phys. Rev.* D64 (2001), p. 112007. arXiv: [hep-ex/0104049](https://arxiv.org/abs/hep-ex/0104049) [hep-ex].
- [10] A. A. Aguilar-Arevalo et al. "Improved Search for $\bar{\nu}_\mu \rightarrow \bar{\nu}_e$ Oscillations in the MiniBooNE Experiment". In: *Phys. Rev. Lett.* 110 (16 2013), p. 161801. URL: <https://link.aps.org/doi/10.1103/PhysRevLett.110.161801>.
- [11] Planck Collaboration et al. "Planck 2018 results. VI. Cosmological parameters". In: *aap* 641 (Sept. 2020).
- [12] J. A. Bagger et al. "Precision electroweak measurements on the Z resonance". In: *Physics Reports* 427.5 (2006), pp. 257 –454. URL: <http://www.sciencedirect.com/science/article/pii/S0370157305005119>.
- [13] B. Pontecorvo. "Neutrino Experiments and the Problem of Conservation of Leptonic Charge". In: *Sov. Phys. JETP* 26 (1968). [Zh. Eksp. Teor. Fiz. 53, 1717(1967)], pp. 984–988.

- 3560 [14] B. Pontecorvo. "Inverse beta processes and nonconservation of lepton charge". In: Sov. Phys. JETP 7 (1958). [Zh. Eksp. Teor. Fiz.34,247(1957)], pp. 172–173.
- 3561
- 3562 [15] Makoto Kobayashi and Toshihide Maskawa. "CP-Violation in the
3563 Renormalizable Theory of Weak Interaction". In: Progress of Theoretical Physics
3564 49.2 (1973), pp. 652–657. URL: <http://dx.doi.org/10.1143/PTP.49.652>.
- 3565 [16] Nicola Cabibbo. "Unitary Symmetry and Leptonic Decays". In: Phys. Rev. Lett. 10
3566 (12 1963), pp. 531–533. URL:
3567 <https://link.aps.org/doi/10.1103/PhysRevLett.10.531>.
- 3568 [17] A Maio and. "Search for Majorana neutrinos with the SNO+ detector at
3569 SNOLAB". In: Journal of Physics: Conference Series 587 (2015), p. 012030. URL:
3570 <https://doi.org/10.1088/1742-6596/587/1/012030>.
- 3571 [18] A Yu Smirnov. "The MSW effect and solar neutrinos". In: (2003).
- 3572 [19] S.P. Mikheyev and A.Y. Smirnov. "Resonance enhancement of oscillations in
3573 matter and solar neutrino spectroscopy". In: Soviet Journal of Nuclear Physics 42 (6
3574 1985), pp. 913–917.
- 3575 [20] L. Wolfenstein. "Neutrino oscillations in matter". In: Phys. Rev. D 17 (9 1978),
3576 pp. 2369–2374. URL: <https://link.aps.org/doi/10.1103/PhysRevD.17.2369>.
- 3577 [21] Vernon D. Barger et al. "Matter Effects on Three-Neutrino Oscillations". In: Phys.
3578 Rev. D 22 (1980), p. 2718.
- 3579 [22] Y. Ashie et al. "Evidence for an Oscillatory Signature in Atmospheric Neutrino
3580 Oscillations". In: Phys. Rev. Lett. 93 (10 2004), p. 101801. URL:
3581 <https://link.aps.org/doi/10.1103/PhysRevLett.93.101801>.
- 3582 [23] Q. R. Ahmad et al. "Direct Evidence for Neutrino Flavor Transformation from
3583 Neutral-Current Interactions in the Sudbury Neutrino Observatory". In: Phys.
3584 Rev. Lett. 89 (1 2002), p. 011301. URL:
3585 <https://link.aps.org/doi/10.1103/PhysRevLett.89.011301>.
- 3586 [24] 2015 Nobel prize in Physics as listed by Nobelprize.org.
3587 https://www.nobelprize.org/nobel_prizes/physics/laureates/2015/.
3588 Accessed: 22-06-2022.
- 3589 [25] J. A. Formaggio and G. P. Zeller. "From eV to EeV: Neutrino Cross Sections
3590 Across Energy Scales". In: Rev. Mod. Phys. 84 (2012), pp. 1307–1341. arXiv:
3591 1305.7513 [hep-ex].
- 3592 [26] A Oralbaev, M Skorokhvatov, and O Titov. "The inverse beta decay: a study of
3593 cross section". In: Journal of Physics: Conference Series 675.1 (2016), p. 012003. URL:
3594 <https://doi.org/10.1088/1742-6596/675/1/012003>.
- 3595 [27] A Bellerive. "Review of solar neutrino experiments". en. In: Int. J. Mod. Phys. A
3596 19.08 (Mar. 2004), pp. 1167–1179.
- 3597 [28] Raymond Davis, Don S. Harmer, and Kenneth C. Hoffman. "Search for
3598 Neutrinos from the Sun". In: Phys. Rev. Lett. 20 (21 1968), pp. 1205–1209. URL:
3599 <https://link.aps.org/doi/10.1103/PhysRevLett.20.1205>.
- 3600 [29] Núria Vinyoles et al. "A new generation of standard solar models". In: Astrophys.
3601 J. 835.2 (Jan. 2017), p. 202.

- 3602 [30] V Gribov and B Pontecorvo. "Neutrino astronomy and lepton charge". en. In: *Phys. Lett. B* 28.7 (Jan. 1969), pp. 493–496.
- 3603 [31] K. S. Hirata et al. "Observation of ${}^8\text{B}$ solar neutrinos in the Kamiokande-II detector". In: *Phys. Rev. Lett.* 63 (1 1989), pp. 16–19. URL: <https://link.aps.org/doi/10.1103/PhysRevLett.63.16>.
- 3604 [32] W Hampel et al. "GALLEX solar neutrino observations: results for GALLEX IV". en. In: *Phys. Lett. B* 447.1-2 (Feb. 1999), pp. 127–133.
- 3605 [33] J. N. Abdurashitov et al. "Measurement of the solar neutrino capture rate with gallium metal". In: *Phys. Rev. C* 60 (5 1999), p. 055801. URL: <https://link.aps.org/doi/10.1103/PhysRevC.60.055801>.
- 3606 [34] Q R Ahmad et al. "Direct evidence for neutrino flavor transformation from neutral-current interactions in the Sudbury neutrino observatory". en. In: *Phys. Rev. Lett.* 89.1 (June 2002).
- 3607 [35] Borexino Collaboration. "Comprehensive measurement of pp-chain solar neutrinos". en. In: *Nature* 562.7728 (Oct. 2018), pp. 505–510.
- 3608 [36] B Aharmim et al. "A search for neutrinos from the SolarhepReaction and the diffuse supernova neutrino background with the Sudbury neutrino observatory". en. In: *Astrophys. J.* 653.2 (Dec. 2006), pp. 1545–1551.
- 3609 [37] M Agostini et al. "Experimental evidence of neutrinos produced in the CNO fusion cycle in the Sun". In: (2020).
- 3610 [38] G Danby et al. "Observation of high-energy neutrino reactions and the existence of two kinds of neutrinos". In: *Phys. Rev. Lett.* 9.1 (July 1962), pp. 36–44.
- 3611 [39] K. Abe et al. "T2K neutrino flux prediction". In: *Physical Review D* 87.1 (2013). URL: <https://doi.org/10.1103%2Fphysrevd.87.012001>.
- 3612 [40] D. G. Michael et al. "Observation of Muon Neutrino Disappearance with the MINOS Detectors in the NuMI Neutrino Beam". In: *Phys. Rev. Lett.* 97 (19 2006), p. 191801. URL: <https://link.aps.org/doi/10.1103/PhysRevLett.97.191801>.
- 3613 [41] G. Danby et al. "Observation of High-Energy Neutrino Reactions and the Existence of Two Kinds of Neutrinos". In: *Phys. Rev. Lett.* 9 (1 1962), pp. 36–44. URL: <https://link.aps.org/doi/10.1103/PhysRevLett.9.36>.
- 3614 [42] M. A. Acero et al. "First measurement of neutrino oscillation parameters using neutrinos and antineutrinos by NOvA". In: *Phys. Rev. Lett.* 123 (15 2019), p. 151803. URL: <https://link.aps.org/doi/10.1103/PhysRevLett.123.151803>.
- 3615 [43] K. Abe et al. "The T2K experiment". In: *Nuclear Instruments and Methods in Physics Research Section A: Accelerators, Spectrometers, Detectors and Associated Equipment* 659.1 (2011), pp. 106 –135. eprint: <http://www.sciencedirect.com/science/article/pii/S0168900211011910>.
- 3616 [44] B Abi et al. "Long-baseline neutrino oscillation physics potential of the DUNE experiment". en. In: *Eur. Phys. J. C Part. Fields* 80.10 (Oct. 2020).
- 3617 [45] Hyper-Kamiokande Proto-Collaboration et al. "Physics potential of a long-baseline neutrino oscillation experiment using a J-PARC neutrino beam and Hyper-Kamiokande". In: *Prog. Theor. Exp. Phys.* 2015.5 (May 2015), pp. 53C02–0.

- 3646 [46] Carlos Blanco, Dan Hooper, and Pedro Machado. "Constraining sterile neutrino
3647 interpretations of the LSND and MiniBooNE anomalies with coherent neutrino
3648 scattering experiments". In: *Physical Review D* 101.7 (2020). URL:
3649 <https://doi.org/10.1103%2Fphysrevd.101.075051>.
- 3650 [47] MicroBooNE Collaboration et al. *Search for an Excess of Electron Neutrino*
3651 *Interactions in MicroBooNE Using Multiple Final State Topologies*. 2021. URL:
3652 <https://arxiv.org/abs/2110.14054>.
- 3653 [48] B. Armbruster et al. "Upper limits for neutrino oscillations $\bar{\nu}_\mu \rightarrow \bar{\nu}_e$ from muon
3654 decay at rest". In: *Phys. Rev. D* 65 (11 2002), p. 112001. URL:
3655 <https://link.aps.org/doi/10.1103/PhysRevD.65.112001>.
- 3656 [49] T K Gaisser and M Honda. "Flux of Atmospheric Neutrinos". In: (2002).
- 3657 [50] G. D. Barr et al. "Three-dimensional calculation of atmospheric neutrinos". In:
3658 *Physical Review D* 70.2 (2004). URL:
3659 <https://doi.org/10.1103/physrevd.70.023006>.
- 3660 [51] M. Honda et al. "Calculation of atmospheric neutrino flux using the interaction
3661 model calibrated with atmospheric muon data". In: *Physical Review D* 75.4 (2007).
3662 URL: <https://doi.org/10.1103/physrevd.75.043006>.
- 3663 [52] M. Honda et al. "New calculation of the atmospheric neutrino flux in a
3664 three-dimensional scheme". In: *Phys. Rev. D* 70 (4 2004), p. 043008. URL:
3665 <https://link.aps.org/doi/10.1103/PhysRevD.70.043008>.
- 3666 [53] M. Honda et al. "Improvement of low energy atmospheric neutrino flux
3667 calculation using the JAM nuclear interaction model". In: *Phys. Rev. D* 83 (12
3668 2011), p. 123001. URL:
3669 <https://link.aps.org/doi/10.1103/PhysRevD.83.123001>.
- 3670 [54] A. Fasso et al. "FLUKA: status and prospects for hadronic applications". In:
3671 (2001).
- 3672 [55] Y. Ashie et al. "Measurement of atmospheric neutrino oscillation parameters by
3673 Super-Kamiokande I". In: *Physical Review D* 71.11 (2005). URL:
3674 <https://doi.org/10.1103/physrevd.71.112005>.
- 3675 [56] F Reines et al. "Evidence for high-energy cosmic-ray neutrino interactions". In:
3676 *Phys. Rev. Lett.* 15.9 (Aug. 1965), pp. 429–433.
- 3677 [57] D. Casper et al. "Measurement of atmospheric neutrino composition with the
3678 IMB-3 detector". In: *Phys. Rev. Lett.* 66 (20 1991), pp. 2561–2564. URL:
3679 <https://link.aps.org/doi/10.1103/PhysRevLett.66.2561>.
- 3680 [58] K S Hirata et al. "Observation of a small atmospheric ν_μ/ν_e ratio in Kamiokande".
3681 en. In: *Phys. Lett. B* 280.1-2 (Apr. 1992), pp. 146–152.
- 3682 [59] Z. Li et al. "Measurement of the tau neutrino cross section in atmospheric
3683 neutrino oscillations with Super-Kamiokande". In: *Physical Review D* 98.5 (2018).
3684 URL: <https://doi.org/10.1103/physrevd.98.052006>.
- 3685 [60] Kamiokande Collaboration et al. "Atmospheric neutrino oscillation analysis with
3686 external constraints in Super-Kamiokande I-IV". In: (2017).
- 3687 [61] T2K Collaboration. "Constraint on the matter-antimatter symmetry-violating
3688 phase in neutrino oscillations". en. In: *Nature* 580.7803 (Apr. 2020), pp. 339–344.

- 3689 [62] M A Acero et al. "First measurement of neutrino oscillation parameters using
3690 neutrinos and antineutrinos by NOvA". en. In: *Phys. Rev. Lett.* 123.15 (Oct. 2019),
3691 p. 151803.
- 3692 [63] M G Aartsen et al. "Measurement of atmospheric neutrino oscillations at 6–56
3693 GeV with IceCube DeepCore". In: *Phys. Rev. Lett.* 120.7 (Feb. 2018).
- 3694 [64] P Adamson et al. "Combined analysis of $\nu\mu$ Disappearance
3695 and $\nu\mu \rightarrow \nu e$ Appearance in MINOS using accelerator and atmospheric neutrinos".
3696 In: *Phys. Rev. Lett.* 112.19 (May 2014).
- 3697 [65] M. Sajjad Athar et al. "Status and perspectives of neutrino physics". In: *Progress
3698 in Particle and Nuclear Physics* 124 (2022), p. 103947. URL:
3699 <https://doi.org/10.1016/Fj.pnpp.2022.103947>.
- 3700 [66] Soo-Bong Kim, Thierry Lasserre, and Yifang Wang. "Reactor Neutrinos". In: *Adv.
3701 High Energy Phys.* 2013 (2013), pp. 1–34.
- 3702 [67] Mohammad Sajjad Athar et al. "Status and perspectives of neutrino physics". In: *Prog. Part. Nucl. Phys.* 124 (2022), p. 103947. arXiv: 2111.07586 [hep-ph].
- 3704 [68] K Abe et al. "First gadolinium loading to Super-Kamiokande". en. In: *Nucl.
3705 Instrum. Methods Phys. Res. A* 1027.166248 (Mar. 2022), p. 166248.
- 3706 [69] F. P. An et al. "Observation of Electron-Antineutrino Disappearance at Daya Bay".
3707 In: *Phys. Rev. Lett.* 108 (17 2012), p. 171803. URL:
3708 <https://link.aps.org/doi/10.1103/PhysRevLett.108.171803>.
- 3709 [70] J. K. Ahn et al. "Observation of Reactor Electron Antineutrinos Disappearance in
3710 the RENO Experiment". In: *Phys. Rev. Lett.* 108 (19 2012), p. 191802. URL:
3711 <https://link.aps.org/doi/10.1103/PhysRevLett.108.191802>.
- 3712 [71] Y. Abe et al. "Indication of Reactor $\bar{\nu}_e$ Disappearance in the Double Chooz
3713 Experiment". In: *Phys. Rev. Lett.* 108 (13 2012), p. 131801. URL:
3714 <https://link.aps.org/doi/10.1103/PhysRevLett.108.131801>.
- 3715 [72] JUNO Collaboration et al. *TAO Conceptual Design Report: A Precision Measurement
3716 of the Reactor Antineutrino Spectrum with Sub-percent Energy Resolution*. 2020. arXiv:
3717 2005.08745 [physics.ins-det].
- 3718 [73] M P Decowski. "KamLAND's precision neutrino oscillation measurements". en.
3719 In: *Nucl. Phys. B*. 908 (July 2016), pp. 52–61.
- 3720 [74] A. Gando et al. "Constraints on θ_{13} from a three-flavor oscillation analysis of
3721 reactor antineutrinos at KamLAND". In: *Phys. Rev. D* 83 (5 2011), p. 052002. URL:
3722 <https://link.aps.org/doi/10.1103/PhysRevD.83.052002>.
- 3723 [75] Patrick Dunne. *Latest Neutrino oscillation results from T2K*. 2020.
- 3724 [76] Particle Data Group et al. "Review of particle physics". en. In: *Prog. Theor. Exp.
3725 Phys.* 2020.8 (Aug. 2020).
- 3726 [77] R. L. Workman and Others. "Review of Particle Physics". In: *PTEP* 2022 (2022),
3727 p. 083C01.
- 3728 [78] K. Abe et al. "Precise Measurement of the Neutrino Mixing Parameter θ_{23} from
3729 Muon Neutrino Disappearance in an Off-Axis Beam". In: *Phys. Rev. Lett.* 112 (18
3730 2014), p. 181801. URL:
3731 <https://link.aps.org/doi/10.1103/PhysRevLett.112.181801>.

- 3732 [79] Roger Wendell. "Three Flavor Oscillation Analysis of Atmospheric Neutrinos in
3733 Super-Kamiokande". PhD thesis. University of North Carolina, 2008.
- 3734 [80] Adam M Dziewonski and Don L Anderson. "Preliminary reference Earth model".
3735 en. In: *Phys. Earth Planet. Inter.* 25.4 (June 1981), pp. 297–356.
- 3736 [81] Y Fukuda et al. "Evidence for oscillation of atmospheric neutrinos". In: *Phys. Rev.*
3737 *Lett.* 81.8 (Aug. 1998), pp. 1562–1567.
- 3738 [82] K. Abe et al. "Calibration of the Super-Kamiokande detector". In: *Nuclear*
3739 *Instruments and Methods in Physics Research Section A: Accelerators, Spectrometers,*
3740 *Detectors and Associated Equipment* 737 (2014), pp. 253–272. URL:
3741 <https://doi.org/10.1016/j.nima.2013.11.081>.
- 3742 [83] Linyan Wan. "Atmospheric Neutrino_Super-K". In: (2022). URL:
3743 <https://zenodo.org/record/6694761>.
- 3744 [84] Miao Jiang. "Study of the neutrino mass hierarchy with the atmospheric neutrino
3745 data collected in Super-Kamiokande IV". PhD thesis. Kyoto University, 2019.
- 3746 [85] S Fukuda et al. "The super-kamiokande detector". en. In: *Nucl. Instrum. Methods*
3747 *Phys. Res. A* 501.2-3 (Apr. 2003), pp. 418–462.
- 3748 [86] S. Fukuda et al. "The Super-Kamiokande detector". In: *Nuclear Instruments and*
3749 *Methods in Physics Research Section A: Accelerators, Spectrometers, Detectors and*
3750 *Associated Equipment* 501.2 (2003), pp. 418–462. eprint:
3751 <http://www.sciencedirect.com/science/article/pii/S016890020300425X>.
- 3752 [87] Y Itow et al. "The JHF-Kamioka neutrino project". In: (2001).
- 3753 [88] M Jiang et al. "Atmospheric neutrino oscillation analysis with improved event
3754 reconstruction in Super-Kamiokande IV". en. In: *Prog. Theor. Exp. Phys.* 2019.5
3755 (May 2019).
- 3756 [89] H. Kume et al. "20 inch diameter photomultiplier". In: *Nuclear Instruments and*
3757 *Methods in Physics Research* 205.3 (1983), pp. 443–449. URL:
3758 <https://www.sciencedirect.com/science/article/pii/0167508783900078>.
- 3759 [90] A. Suzuki et al. "Improvement of 20 in. diameter photomultiplier tubes". In:
3760 *Nuclear Instruments and Methods in Physics Research Section A: Accelerators,*
3761 *Spectrometers, Detectors and Associated Equipment* 329.1-2 (May 1993), pp. 299–313.
3762 URL: [https://doi.org/10.1016/0168-9002\(93\)90949-i](https://doi.org/10.1016/0168-9002(93)90949-i).
- 3763 [91] Y Nakano et al. "Measurement of the radon concentration in purified water in
3764 the Super-Kamiokande IV detector". en. In: *Nucl. Instrum. Methods Phys. Res. A*
3765 977.164297 (Oct. 2020), p. 164297.
- 3766 [92] Hamamatsu. *Hamamatsu Photonics Photomultiplier Tubes Handbook*. URL:
3767 https://www.hamamatsu.com/content/dam/hamamatsu-photonics/sites/documents/99\SALES\LIBRARY/etd/PMT_handbook_v4E.pdf.
- 3769 [93] K Abe et al. "First gadolinium loading to Super-Kamiokande". en. In: *Nucl.*
3770 *Instrum. Methods Phys. Res. A* 1027.166248 (Mar. 2022), p. 166248.
- 3771 [94] John F. Beacom and Mark R. Vagins. "Antineutrino Spectroscopy with Large
3772 Water Čerenkov Detectors". In: *Phys. Rev. Lett.* 93 (17 2004), p. 171101. URL:
3773 <https://link.aps.org/doi/10.1103/PhysRevLett.93.171101>.

- 3774 [95] Ll Marti et al. "Evaluation of gadolinium's action on water Cherenkov detector
3775 systems with EGADS". en. In: *Nucl. Instrum. Methods Phys. Res. A* 959.163549
3776 (Apr. 2020), p. 163549.
- 3777 [96] Ll Marti et al. "Evaluation of gadolinium's action on water Cherenkov detector
3778 systems with EGADS". In: (2019).
- 3779 [97] Mark Vagins. *Solar/DSNB Neutrino_SK-Gd*. 2022.
- 3780 [98] John Focht. PhD thesis. Massachusetts Institute of Technology, 2004.
- 3781 [99] T. Tanimori et al. "Design and performance of semi-custom analog IC including
3782 two TACs and two current integrators for 'Super-Kamiokande'". In: *IEEE*
3783 *Transactions on Nuclear Science* 36.1 (1989), pp. 497–501.
- 3784 [100] J. Hosaka et al. "Solar neutrino measurements in Super-Kamiokande-I". In: *Phys.*
3785 *Rev. D* 73 (11 2006), p. 112001. URL:
3786 <https://link.aps.org/doi/10.1103/PhysRevD.73.112001>.
- 3787 [101] H Nishino et al. "High-speed charge-to-time converter ASIC for the
3788 Super-Kamiokande detector". en. In: *Nucl. Instrum. Methods Phys. Res. A* 610.3
3789 (Nov. 2009), pp. 710–717.
- 3790 [102] S. Yamada et al. "Commissioning of the New Electronics and Online System for
3791 the Super-Kamiokande Experiment". In: *IEEE Transactions on Nuclear Science* 57.2
3792 (2010), pp. 428–432.
- 3793 [103] Satoru Yamada et al. "New online system without hardware trigger for the
3794 Super-Kamiokande experiment". In: *2007 IEEE Nuclear Science Symposium
3795 Conference Record*. Honolulu, HI, USA: IEEE, Oct. 2007.
- 3796 [104] Giada Carminati. "The new wide-band solar neutrino trigger for
3797 super-kamiokande". In: *Phys. Procedia* 61 (2015), pp. 666–672.
- 3798 [105] P A Čerenkov. "Visible radiation produced by electrons moving in a medium
3799 with velocities exceeding that of light". In: *Phys. Rev.* 52.4 (Aug. 1937),
3800 pp. 378–379.
- 3801 [106] I Frank and Ig Tamm. "Coherent visible radiation of fast electrons passing
3802 through matter". In: *Selected Papers*. Berlin, Heidelberg: Springer Berlin
3803 Heidelberg, 1991, pp. 29–35.
- 3804 [107] The T2K Collaboration. "Letter of Intent: Neutrino Oscillation Experiment at
3805 JHF". In: *KEK Proposal* (2001). eprint:
3806 <http://neutrino.kek.jp/jhfnu/loi/loi.v2.030528.pdf>.
- 3807 [108] Y Itow et al. "The JHF-Kamioka neutrino project". In: (June 2001). arXiv:
3808 [hep-ex/0106019](https://arxiv.org/abs/hep-ex/0106019) [hep-ex].
- 3809 [109] The K2K Collaboration and S H Ahn. "Detection of Accelerator-Produced
3810 Neutrinos at a Distance of 250 km". In: (Feb. 2001). arXiv: [hep-ex/0103001](https://arxiv.org/abs/hep-ex/0103001)
3811 [hep-ex].
- 3812 [110] The T2K Collaboration. "Tokai-to-Kamioka (T2K) Long Baseline Neutrino
3813 Oscillation Experiment Proposal". In: *KEK Proposal* (2006). eprint: {{<http://j-parc.jp/researcher/Hadron/en/pac\0606/pdf/p11-Nishikawa.pdf>} }.
- 3815 [111] Christophe Bronner. *Accelerator Neutrino I_Recent results from T2K*. 2022.

- 3816 [112] K. Abe et al. "Observation of Electron Neutrino Appearance in a Muon Neutrino
3817 Beam". In: *Phys. Rev. Lett.* 112 (6 2014), p. 061802. eprint:
3818 <https://link.aps.org/doi/10.1103/PhysRevLett.112.061802>.
- 3819 [113] T. Fukuda et al. "Proposal for precise measurement of neutrino-water
3820 cross-section in NINJA physics run". Proposal for J-PARC and KEK. 2017.
- 3821 [114] T. Ovsianikova et al. "New experiment WAGASCI to measure cross sections of
3822 neutrino interactions in water and hydrocarbon using J-PARC beam". In: *Physics*
3823 of Particles and Nuclei 48.6 (2017), pp. 1014–1017. eprint:
3824 <https://doi.org/10.1134/S1063779617060478>.
- 3825 [115] M. Antonova et al. "Baby MIND: a magnetized segmented neutrino detector for
3826 the WAGASCI experiment". In: *Journal of Instrumentation* 12.07 (2017), p. C07028.
3827 eprint: <http://stacks.iop.org/1748-0221/12/i=07/a=C07028>.
- 3828 [116] K. Abe et al. "First measurement of the charged current $\bar{\nu}_\mu$ double differential
3829 cross section on a water target without pions in the final state". In: *Phys. Rev. D*
3830 102 (1 2020), p. 012007. URL:
3831 <https://link.aps.org/doi/10.1103/PhysRevD.102.012007>.
- 3832 [117] K Abe et al. "Measurements of $\bar{\nu}_\mu$ and $\bar{\nu}_\mu + \nu_\mu$ charged-current cross-sections
3833 without detected pions or protons on water and hydrocarbon at a mean
3834 anti-neutrino energy of 0.86 GeV". In: *Progress of Theoretical and Experimental*
3835 *Physics* 2021.4 (Mar. 2021). URL: <https://doi.org/10.1093/ptep/ptab014>.
- 3836 [118] K. Matsuoka et al. "Design and performance of the muon monitor for the T2K
3837 neutrino oscillation experiment". In: *Nuclear Instruments and Methods in Physics*
3838 *Research Section A: Accelerators, Spectrometers, Detectors and Associated Equipment*
3839 624.3 (2010), pp. 591 –600. eprint:
3840 <http://www.sciencedirect.com/science/article/pii/S016890021002098X>.
- 3841 [119] K Abe et al. "Improved constraints on neutrino mixing from the T2K experiment
3842 with 3.13×10^{21} protons on target". en. In: *Phys. Rev. D*. 103.11 (June 2021).
- 3843 [120] Tomislav Vladisavljevic. *Predicting the T2K neutrino flux and measuring oscillation*
3844 *parameters*. 1st ed. Springer theses. Cham, Switzerland: Springer Nature, Sept.
3845 2020.
- 3846 [121] D Beavis, A Carroll, and I Chiang. "Long baseline neutrino oscillation
3847 experiment at the AGS. Physics design report". In: (Apr. 1995).
- 3848 [122] P.-A. Amaudruz et al. "The T2K fine-grained detectors". In: *Nuclear Instruments*
3849 and *Methods in Physics Research Section A: Accelerators, Spectrometers, Detectors and*
3850 *Associated Equipment* 696 (Dec. 2012), pp. 1–31. URL:
3851 <https://doi.org/10.1016/j.nima.2012.08.020>.
- 3852 [123] N. Abgrall et al. "Time projection chambers for the T2K near detectors". In:
3853 *Nuclear Instruments and Methods in Physics Research Section A: Accelerators,*
3854 *Spectrometers, Detectors and Associated Equipment* 637.1 (May 2011), pp. 25–46. URL:
3855 <https://doi.org/10.1016/j.nima.2011.02.036>.
- 3856 [124] S. Assylbekov et al. "The T2K ND280 off-axis pi-zero detector". In: *Nuclear*
3857 *Instruments and Methods in Physics Research Section A: Accelerators, Spectrometers,*
3858 *Detectors and Associated Equipment* 686 (Sept. 2012), pp. 48–63. URL:
3859 <https://doi.org/10.1016/j.nima.2012.05.028>.

- 3860 [125] D Allan et al. "The electromagnetic calorimeter for the T2K near detector
3861 ND280". In: *Journal of Instrumentation* 8.10 (2013), P10019–P10019. URL:
3862 <https://doi.org/10.1088%2F1748-0221%2F8%2F10%2Fp10019>.
- 3863 [126] *UA1 magnet sets off for a second new life*. 2022. URL: <https://cerncourier.com/a/ua1-magnet-sets-off-for-a-second-new-life/>.
- 3865 [127] F. Vannucci. "The NOMAD Experiment at CERN". In: *Advances in High Energy
3866 Physics* 2014 (2014), pp. 1–20. URL: <https://doi.org/10.1155/2014/129694>.
- 3867 [128] S. Aoki et al. "The T2K Side Muon Range Detector (SMRD)". In: *Nuclear
3868 Instruments and Methods in Physics Research Section A: Accelerators, Spectrometers,
3869 Detectors and Associated Equipment* 698 (Jan. 2013), pp. 135–146. URL:
3870 <https://doi.org/10.1016/j.nima.2012.10.001>.
- 3871 [129] K. Suzuki et al. "Measurement of the muon beam direction and muon flux for the
3872 T2K neutrino experiment". In: *Progress of Theoretical and Experimental Physics*
3873 2015.5 (2015), pp. 53C01–0. URL: <https://doi.org/10.1093%2Fptep%2Fptv054>.
- 3874 [130] S. Brooks et al. *Handbook of Markov Chain Monte Carlo*. CRC Press, 2011.
- 3875 [131] W. R. Gilks, S. Richardson, and D. J. Spiegelhalter. *Markov Chain Monte Carlo in
3876 Practice*. Chapman & Hall/CRC Interdisciplinary Statistics, 1995.
- 3877 [132] Clarence Wret. "Minimising systematic uncertainties in the T2K experiment using
3878 near-detector and external data". PhD thesis. Imperial College London, 2018.
- 3879 [133] Kirsty Elizabeth Duffy. "Measurement of the Neutrino Oscillation Parameters
3880 $\sin^2 \theta_{23}$, Δm_{32}^2 , $\sin^2 \theta_{13}$, and δ_{CP} in Neutrino and Antineutrino Oscillation at T2K".
3881 PhD thesis. Oriel College, University of Oxford, 2016.
- 3882 [134] C. Bojeckho and A. Kabooth. "Muon neutrino disappearance simultaneous fit of
3883 ND280 and SK with Run 1+2+3 data using Markov Chain Monte Carlo Analysis".
3884 In: *T2K Technical Note* 140 (2013).
- 3885 [135] Thomas Bayes Rev. "An essay toward solving a problem in the doctrine of
3886 chances". In: *Phil. Trans. Roy. Soc. Lond.* 53 (1764), pp. 370–418.
- 3887 [136] Artur Sztuc. "Standard and Non-Standard Neutrino-Antineutrino Oscillation
3888 Analyses and Event Reconstruction Studies using Markov Chain Monte Carlo
3889 Methods at T2K". PhD thesis. Imperial College London, 2021.
- 3890 [137] N. Metropolis et al. "Equation of State Calculations by Fast Computing
3891 Machines". In: *Journal of Chemical Physics* 21.6 (1970).
- 3892 [138] W. K. Hastings. "Monte Carlo Sampling Methods Using Markov Chains and
3893 Their Applications". In: *Biometrika* 57.1 (1970).
- 3894 [139] Joanna Dunkley et al. "Fast and reliable Markov chain Monte Carlo technique for
3895 cosmological parameter estimation". en. In: *Mon. Not. R. Astron. Soc.* 356.3 (Jan.
3896 2005), pp. 925–936.
- 3897 [140] Harold Jeffreys. *The Theory of Probability*. Oxford Classic Texts in the Physical
3898 Sciences. 1939.
- 3899 [141] Robert E Kass and Adrian E Raftery. "Bayes factors". en. In: *J. Am. Stat. Assoc.*
3900 90.430 (June 1995), pp. 773–795.

- 3901 [142] T.T. Böhlen et al. "The FLUKA Code: Developments and Challenges for High
3902 Energy and Medical Applications". In: *Nuclear Data Sheets* 120 (2014), pp. 211
3903 –214. eprint:
3904 <http://www.sciencedirect.com/science/article/pii/S0090375214005018>.
- 3905 [143] René Brun et al. *GEANT: Detector Description and Simulation Tool; Oct 1994*. CERN
3906 Program Library. Long Writeup W5013. Geneva: CERN, 1993. eprint:
3907 <http://cds.cern.ch/record/1082634>.
- 3908 [144] K. Abe et al. "T2K neutrino flux prediction". In: *Phys. Rev. D* 87 (1 2013),
3909 p. 012001. URL: <https://link.aps.org/doi/10.1103/PhysRevD.87.012001>.
- 3910 [145] C. Zeitnitz and T.A. Gabriel. "The GEANT-CALOR interface and benchmark
3911 calculations of ZEUS test calorimeters". In: *Nuclear Instruments and Methods in
3912 Physics Research Section A: Accelerators, Spectrometers, Detectors and Associated
3913 Equipment* 349.1 (1994), pp. 106 –111. eprint:
3914 <http://www.sciencedirect.com/science/article/pii/0168900294906130>.
- 3915 [146] A. Fiorentini et al. "Flux Prediction and Uncertainty Updates with NA61 2009
3916 Thin Target Data and Negative Focussing Mode Predictions". In: *T2K Technical
3917 Note* 217 (2017).
- 3918 [147] N. Abgrall et al. "Measurements of cross sections and charged pion spectra in
3919 proton-carbon interactions at 31 GeV/ c ". In: *Physical Review C* 84.3 (2011). URL: <https://doi.org/10.1103/physrevc.84.034604>.
- 3920 [148] N. Abgrall et al. "Measurement of production properties of positively charged
3921 kaons in proton-carbon interactions at 31 GeV/ c ". In: *Physical Review C* 85.3 (2012). URL: <https://doi.org/10.1103/physrevc.85.035210>.
- 3922 [149] N. Abgrall et al. "Pion emission from the T2K replica target: Method, results and
3923 application". In: *Nuclear Instruments and Methods in Physics Research Section A:
3924 Accelerators, Spectrometers, Detectors and Associated Equipment* 701 (2013), pp. 99
3925 –114. eprint:
3926 <http://www.sciencedirect.com/science/article/pii/S016890021201234X>.
- 3927 [150] M. Apollonio et al. "Forward production of charged pions with incident protons
3928 on nuclear targets at the CERN Proton Synchrotron". In: *Phys. Rev. C* 80 (3 2009),
3929 p. 035208. eprint: <https://link.aps.org/doi/10.1103/PhysRevC.80.035208>.
- 3930 [151] B. Blau et al. "The superconducting magnet of AMS-02". In: *Nuclear Physics B -
3931 Proceedings Supplements* 113.1-3 (Dec. 2002), pp. 125–132. URL:
3932 [https://doi.org/10.1016/s0920-5632\(02\)01831-5](https://doi.org/10.1016/s0920-5632(02)01831-5).
- 3933 [152] S. Haino et al. "Measurements of primary and atmospheric cosmic-ray spectra
3934 with the BESS-TeV spectrometer". In: *Physics Letters B* 594.1-2 (July 2004),
3935 pp. 35–46. URL: <https://doi.org/10.1016/j.physletb.2004.05.019>.
- 3936 [153] NASA. *U.S. Standard Atmosphere, 1976*. 1976.

- 3943 [154] S. Roesler, R. Engel, and J. Ranft. "The Monte Carlo Event Generator
3944 DPMJET-III". In: *Advanced Monte Carlo for Radiation Physics, Particle Transport*
3945 *Simulation and Applications*. Springer Berlin Heidelberg, 2001, pp. 1033–1038. URL:
3946 <https://doi.org/10.1007/978-3-642-18211-2\166>.
- 3947 [155] Koji Niita et al. "PHITS—a particle and heavy ion transport code system". In:
3948 *Radiation Measurements* 41.9-10 (Oct. 2006), pp. 1080–1090. URL:
3949 <https://doi.org/10.1016/j.radmeas.2006.07.013>.
- 3950 [156] T Sanuki et al. "Measurements of atmospheric muon spectra at mountain
3951 altitude". In: *Physics Letters B* 541.3-4 (2002), pp. 234–242. URL:
3952 <https://doi.org/10.1016%2Fs0370-2693%2802%2902265-7>.
- 3953 [157] P. Achard et al. "Measurement of the atmospheric muon spectrum from 20 to
3954 3000 GeV". In: *Physics Letters B* 598.1-2 (2004), pp. 15–32. URL:
3955 <https://doi.org/10.1016%2Fj.physletb.2004.08.003>.
- 3956 [158] Kazufumi Sato. *Atmospheric Neutrino_Reviews on neutrino fluxes (low E atm nu)*.
3957 2022.
- 3958 [159] Yoshinari Hayato and Luke Pickering. "The NEUT neutrino interaction
3959 simulation program library". In: *The European Physical Journal Special Topics* 230.24
3960 (Oct. 2021), pp. 4469–4481. URL:
3961 <https://doi.org/10.1140/epjs/s11734-021-00287-7>.
- 3962 [160] Yoshinari Hayato. "A Neutrino Interaction Simulation Program Library NEUT".
3963 In: *Acta Physica Polonica B* 40.9 (2009).
- 3964 [161] C.H. Llewellyn Smith. "Neutrino reactions at accelerator energies". In: *Physics*
3965 *Reports* 3.5 (1972), pp. 261 –379. eprint:
3966 <http://www.sciencedirect.com/science/article/pii/0370157372900105>.
- 3967 [162] Omar Benhar, Adelchi Fabrocini, and Stefano Fantoni. "The nucleon spectral
3968 function in infinite nuclear matter". In: *Nuclear Physics A* 497 (June 1989),
3969 pp. 423–430. URL: [https://doi.org/10.1016/0375-9474\(89\)90484-3](https://doi.org/10.1016/0375-9474(89)90484-3).
- 3970 [163] R. Bradford et al. "A New Parameterization of the Nucleon Elastic Form Factors".
3971 In: *Nuclear Physics B - Proceedings Supplements* 159 (2006). Proceedings of the 4th
3972 International Workshop on Neutrino-Nucleus Interactions in the Few-GeV
3973 Region, pp. 127 –132. eprint:
3974 <http://www.sciencedirect.com/science/article/pii/S0920563206005184>.
- 3975 [164] A. A. Aguilar-Arevalo et al. "First measurement of the muon neutrino charged
3976 current quasielastic double differential cross section". In: *Physical Review D* 81.9
3977 (2010). URL: <https://doi.org/10.1103%2Fphysrevd.81.092005>.
- 3978 [165] R. Gran et al. "Neutrino-nucleus quasi-elastic and 2p2h interactions up to 10
3979 GeV". In: *Phys. Rev. D* 88 (11 2013), p. 113007. eprint:
3980 <https://link.aps.org/doi/10.1103/PhysRevD.88.113007>.
- 3981 [166] Ch. Berger and L. M. Sehgal. "Lepton mass effects in single pion production by
3982 neutrinos". In: *Phys. Rev. D* 76 (11 2007), p. 113004. URL:
3983 <https://link.aps.org/doi/10.1103/PhysRevD.76.113004>.
- 3984 [167] Ch. Berger and L. M. Sehgal. "Partially conserved axial vector current and
3985 coherent pion production by low energy neutrinos". In: *Phys. Rev. D* 79 (5 2009),
3986 p. 053003. eprint: <https://link.aps.org/doi/10.1103/PhysRevD.79.053003>.

- 3987 [168] Torbjörn Sjöstrand. "High-energy-physics event generation with PYTHIA 5.7 and
3988 JETSET 7.4". In: *Computer Physics Communications* 82.1 (Aug. 1994), pp. 74–89.
3989 URL: [https://doi.org/10.1016/0010-4655\(94\)90132-5](https://doi.org/10.1016/0010-4655(94)90132-5).
- 3990 [169] Christophe Bronner and Mark Hartz. "Tuning of the Charged Hadrons
3991 Multiplicities for Deep Inelastic Interactions in NEUT". In: *Proceedings of the 10th*
3992 *International Workshop on Neutrino-Nucleus Interactions in Few-GeV Region*
3993 (*NuInt15*). Journal of the Physical Society of Japan, Dec. 2016. URL:
3994 <https://doi.org/10.7566/jpsc.12.010041>.
- 3995 [170] M. Glück, E. Reya, and A. Vogt. "Dynamical parton distributions revisited". In:
3996 *The European Physical Journal C* 5.3 (1998), pp. 461–470. URL:
3997 <https://doi.org/10.1007%2Fs100529800978>.
- 3998 [171] Arie Bodek and Un-ki Yang. *Axial and Vector Structure Functions for Electron- and*
3999 *Neutrino- Nucleon Scattering Cross Sections at all Q^2 using Effective Leading order*
4000 *Parton Distribution Functions*. 2010. URL: <https://arxiv.org/abs/1011.6592>.
- 4001 [172] Arie Bodek and Un-Ki Yang. "Update to the Bodek-Yang Unified Model for
4002 Electron- and Neutrino- Nucleon Scattering Cross Sections". In: (2010). URL:
4003 <https://arxiv.org/abs/1012.0261>.
- 4004 [173] Sowjanya Gollapinni. "Neutrino Cross section Future". In: (2016). URL:
4005 <https://arxiv.org/abs/1602.05299>.
- 4006 [174] E. S. Pinzon Guerra et al. "Using world π^\pm -nucleus scattering data to constrain
4007 an intranuclear cascade model". In: *Phys. Rev. D* 99 (5 2019), p. 052007. URL:
4008 <https://link.aps.org/doi/10.1103/PhysRevD.99.052007>.
- 4009 [175] S. Agostinelli et al. "GEANT4: A Simulation toolkit". In: *Nucl. Instrum. Meth.*
4010 A506 (2003), pp. 250–303.
- 4011 [176] R. Brun et al. "GEANT3". In: (Sept. 1987).
- 4012 [177] et al. A. Himmel. "Super-Kamiokande events and data quality studies for T2K
4013 Runs 5 and 6". In: *T2K Technical Note* 219 (2015).
- 4014 [178] et al. S. Berkman. "fiTQun: A New Reconstruction Algorithm for Super-K". In:
4015 *T2K Technical Note* 146 (2013).
- 4016 [179] R.B. Patterson et al. "The extended-track event reconstruction for MiniBooNE".
4017 In: *Nuclear Instruments and Methods in Physics Research Section A: Accelerators,*
4018 *Spectrometers, Detectors and Associated Equipment* 608.1 (2009), pp. 206–224. URL:
4019 <https://doi.org/10.1016%2Fj.nima.2009.06.064>.
- 4020 [180] M. Shiozawa. "Reconstruction algorithms in the Super-Kamiokande large water
4021 Cherenkov detector". In: *Nuclear Instruments and Methods in Physics Research*
4022 *Section A: Accelerators, Spectrometers, Detectors and Associated Equipment* 433.1-2
4023 (Aug. 1999), pp. 240–246. URL:
4024 [https://doi.org/10.1016/s0168-9002\(99\)00359-9](https://doi.org/10.1016/s0168-9002(99)00359-9).

- 4025 [181] K. Abe et al. "Search for <mml:math
4026 xmlns:mml="http://www.w3.org/1998/Math/MathML"
4027 display="inline"><mml:mi>C</mml:mi><mml:mi>P</mml:mi></mml:math>
4028 Violation in Neutrino and Antineutrino Oscillations by the T2K Experiment with
4029 <mml:math xmlns:mml="http://www.w3.org/1998/Math/MathML"
4030 display="inline"><mml:mn>2.2</mml:mn><mml:mo>x</mml:mo><mml:msup><mml:mn
4031 Protons on Target". In: *Physical Review Letters* 121.17 (Oct. 2018). URL:
4032 <https://doi.org/10.1103/physrevlett.121.171802>.
- 4033 [182] K. Abe et al. "Measurements of neutrino oscillation in appearance and
4034 disappearance channels by the T2K experiment with<mml:math
4035 xmlns:mml="http://www.w3.org/1998/Math/MathML"
4036 display="inline"><mml:mn>6.6</mml:mn><mml:mo>x</mml:mo><mml:mn>1</mml:mn
4037 on target". In: *Physical Review D* 91.7 (Apr. 2015). URL:
4038 <https://doi.org/10.1103/physrevd.91.072010>.
- 4039 [183] F and James. "MINUIT: Function Minimization and Error Analysis Reference
4040 Manual". In: (1998). CERN Program Library Long Writeups. URL:
4041 <https://cds.cern.ch/record/2296388>.
- 4042 [184] Xiaoyue Li and Michael Wilking. "FiTQun Event Selection Optimization". In:
4043 *T2K Technical Note* 319 (2017).
- 4044 [185] Shimpei Tobayama. "An Analysis of the Oscillation of Atmospheric Neutrinos".
4045 PhD thesis. British Columbia U., 2016.
- 4046 [186] et al. D. Barrow. "Super-Kamiokande Data Quality, MC, and Systematics in Run
4047 10". In: *T2K Technical Note* 399 (2020).
- 4048 [187] A. Maghrabi, A. Aldosari, and M. Almutairi. "Correlation analyses between solar
4049 activity parameters and cosmic ray muons between 2002 and 2012 at high cutoff
4050 rigidity". In: *Advances in Space Research* 68.7 (Oct. 2021), pp. 2941–2952. URL:
4051 <https://doi.org/10.1016/j.asr.2021.05.016>.
- 4052 [188] K. Abe et al. "Atmospheric neutrino oscillation analysis with external constraints
4053 in Super-Kamiokande I-IV". In: *Phys. Rev. D* 97 (7 2018), p. 072001. eprint:
4054 <https://link.aps.org/doi/10.1103/PhysRevD.97.072001>.
- 4055 [189] J. Beringer et al. "Review of Particle Physics". In: *Phys. Rev. D* 86 (1 2012),
4056 p. 010001. URL: <https://link.aps.org/doi/10.1103/PhysRevD.86.010001>.
- 4057 [190] S. Nakayama K. Iyogi and Y. Obayashi. "T2K data acquisition and FC event
4058 selection at Super-Kamiokande". In: *T2K Technical Note* 027 (2011).
- 4059 [191] LeeKaPik. "Study of the neutrino mass hierarchy with the atmospheric neutrino
4060 data observed in Super-Kamiokande". PhD thesis. Tokyo University, 2012.
- 4061 [192] R. Wendell et al. "Atmospheric neutrino oscillation analysis with subleading
4062 effects in Super-Kamiokande I, II, and III". In: *Phys. Rev. D* 81 (9 2010), p. 092004.
4063 URL: <https://link.aps.org/doi/10.1103/PhysRevD.81.092004>.
- 4064 [193] J. Hosaka et al. "Three flavor neutrino oscillation analysis of atmospheric
4065 neutrinos in Super-Kamiokande". In: *Phys. Rev. D* 74 (3 2006), p. 032002. URL:
4066 <https://link.aps.org/doi/10.1103/PhysRevD.74.032002>.

- 4067 [194] Laura Munteanu et al. "Constraining the Flux and Cross Section Models with
4068 Data from ND280 using FGD1 and FGD2 for the 2020 Oscillation Analysis". In:
4069 *T2K Technical Note 395* (2020).
- 4070 [195] P. Bartet et al. " ν_μ CC event selections in the ND280 tracker using Run 2+3+4
4071 data". In: *T2K Technical Note 212* (2015).
- 4072 [196] Will Parker. "Constraining Systematic Uncertainties at T2K using Near Detector
4073 Data". PhD thesis. Royal Holloway University of London, 2020.
- 4074 [197] V. Berardi et al. " $\bar{\nu}_\mu$ event selection in the ND280 tracker using Run 5c and Run 6
4075 anti-neutrino beam data". In: *T2K Technical Note 246* (2015).
- 4076 [198] James Missert. "TN-318: Fit to Super-K Atmospheric Neutrino Data for
4077 Optimization of the fitQun Fiducial Volume Cuts and Estimation of Detector
4078 Uncertainties". In: *T2K Technical Note 318* (2017).
- 4079 [199] et al. J. Chakrani. "NIWG model and uncertainties for 2021 oscillation analysis".
4080 In: *T2K Technical Note 414* (2022).
- 4081 [200] Morgan Wascko. "T2K Status, Results, and Plans". *Neutrino* 2018. 2018.
- 4082 [201] et al. Tomislav Vladisavljevic. "Flux Prediction and Uncertainty with
4083 NA61/SHINE 2009 Replica-Target Data (TN354 version 3.3)". In: *T2K Technical
4084 Note 354* (2020).
- 4085 [202] G Ambrosini et al. "K/ π production ratios from 450 GeV/c protons on
4086 beryllium". en. In: *Phys. Lett. B* 420.1-2 (Feb. 1998), pp. 225–232.
- 4087 [203] et al. Edward Atkin. "NIWG model and uncertainties for 2019-2020 oscillation
4088 analysis". In: *T2K Technical Note 344* (2019).
- 4089 [204] et al. D. Barrow. "Flux and interaction models for the initial T2K-SK atmospheric
4090 joint fit studies". In: *T2K Technical Note 422* (2022).
- 4091 [205] et al. D. Barrow. "SK atmospheric T2K beam joint fit technical note, MaCh3
4092 details". In: *T2K Technical Note 426* (2022).
- 4093 [206] A. A. Aguilar-Arevalo et al. "Measurement of ν_μ and $\bar{\nu}_\mu$ induced neutral current
4094 single π^0 production cross sections on mineral oil at $E_\nu \sim \mathcal{O}(1 \text{ GeV})$ ". In: *Phys.*
4095 *Rev. D* 81 (1 2010), p. 013005. eprint:
4096 <https://link.aps.org/doi/10.1103/PhysRevD.81.013005>.
- 4097 [207] Patrick de Perio and James Imber. "Super-K Systematic Uncertainties for RUN1-4
4098 Joint ν_e and ν_μ Analyses". In: *T2K Technical Note 186* (2014).
- 4099 [208] Patrick de Perio and James Imber. "Update of SK ν_e systematic error for 2012a
4100 oscillation analysis". In: *T2K Technical Note 107* (2012).
- 4101 [209] Cris Vilela Daniel Barrow. *T2K-SK Detector Matrix Uncertainties - MaCh3*
4102 *Integration*. <https://git.t2k.org/t2k-sk/t2ksk-detcovmat/-/tree/feature/MaCh3Integration>. Accessed: 22-06-2022.
- 4104 [210] Roger Barlow and Christine Beeston. "Fitting using finite Monte Carlo samples".
4105 en. In: *Comput. Phys. Commun.* 77.2 (Oct. 1993), pp. 219–228.
- 4106 [211] J S Conway. *Incorporating nuisance parameters in likelihoods for multisource spectra*.
4107 2011.

- 4108 [212] et al. D. Barrow. "Oscillation probability calculation for the T2K+SK atmospheric
4109 joint fit". In: *T2K Technical Note* 425 (2022).
- 4110 [213] R G Calland, A C Kaboth, and D Payne. "Accelerated event-by-event neutrino
4111 oscillation reweighting with matter effects on a GPU". In: 9.04 (Apr. 2014),
4112 P04016–P04016. URL: <https://doi.org/10.1088/1748-0221/9/04/p04016>.
- 4113 [214] R. Wendell. <http://www.phy.duke.edu/raw22/public/Prob3++/>.
- 4114 [215] Felix Kallenborn et al. "Massively parallel computation of atmospheric neutrino
4115 oscillations on CUDA-enabled accelerators". In: *Computer Physics Communications*
4116 234 (2019), pp. 235–244. URL: <https://www.sciencedirect.com/science/article/pii/S0010465518302790>.
- 4117 [216] Liban Warsame. *MaCh3 Analysis Progress*. URL: <https://indico.fnal.gov/event/50217/contributions/241232/attachments/155318/202209/MaCh3ProgressforDUNELBL\underscoreMay17%20%282%29.pdf>.
- 4118 [217] Simon Bourret, João A B Coelho, and Véronique Van Elewyck and. "Neutrino
4119 oscillation tomography of the Earth with KM3NeT-ORCA". In: *Journal of Physics: Conference Series* 888 (2017), p. 012114. URL:
4120 <https://doi.org/10.1088/1742-6596/2F888%2F1%2F012114>.
- 4121 [218] C. Rott, A. Taketa, and D. Bose. "Spectrometry of the Earth using Neutrino
4122 Oscillations". In: *Scientific Reports* 5.1 (Oct. 2015). URL:
4123 <https://doi.org/10.1038/srep15225>.
- 4124 [219] Kaoru Hagiwara, Naotoshi Okamura, and Ken ichi Senda. "The earth matter
4125 effects in neutrino oscillation experiments from Tokai to Kamioka and Korea". In:
4126 *Journal of High Energy Physics* 2011.9 (Sept. 2011). URL:
4127 [https://doi.org/10.1007/jhep09\(2011\)082](https://doi.org/10.1007/jhep09(2011)082).
- 4128 [220] Dave Typinski. *Earth Gravity*.
4129 <http://www.typnet.net/Essays/EarthGravGraphics/EarthGrav.pdf>.
4130 Accessed: 24-06-2022.
- 4131 [221] D. Barrow. *T2K Beam + SK Atmospheric Joint Fit*. 2022.